3.2 First-Principles Calculation of Material Properties

Theoretical Study on Dynamical Processes at Surfaces and Interfaces using Density Functional Theory and Machine Learning Methods

Yoshitada MORIKAWA
Department of Precision Engineering, Graduate School of Engineering, Osaka University
2-1 Yamadaoka, Suita, Osaka 565-0871

In this fiscal year, we investigated several systems which are important in both fundamental science and applications. Thermal stability of heterogeneous catalysts, along with high activity and selectivity, plays a central role in the catalyst design for industrial applications,1 − 4 e.g., three-way catalyst (TWC) converters to purify emission of exhaust gases or fuel cells. However, the thermal instability originated from the agglomeration (sintering) of metal nanoparticles (NPs) over time under operating condition is the major concern, especially for the catalyst with metal NPs in small sizes. Self-regenerable metal NPs on the oxide surface show great potential to overcome this problem. Metal oxide NPs are highly anchored on the oxide support under oxidative conditions with strong metal − support interaction (MSI) leading to the sintering resistance, while they are subsequently reduced back to active metallic NPs under reductive conditions. This approach is often employed to prepare the ultrastable TWCs in which the platinum-group metal (PGM) NPs are exposed to the high-temperature reduction − oxidation (redox) fluctuations of exhaust gas. PGM-O − M bonds (M is the metal of the support surface) formed in oxidative atmospheres can suppress sintering effectively. We investigated a machine-learning enhanced density functional theory study of $\mathrm{Pd}_x\mathrm{O}_y$ nanoparticles supported on a $\mathrm{Sr_3Ti_2O_7}$ (001) surface and demonstrate that supported oxidized Pd particles fulfill the conditions for the self-regenerative catalysts [1].

We also elucidated the surface facet dependence on the oxygen adsorption and oxidized surface morphology of the diamond (111) and (100) surfaces to give insights that will improve the polishing, etching, and fabrication of diamond devices [2]. Furthermore, We perform machine learning molecular dynamics simulations to gain an atomic-level understanding of the dependence of the graphitization and thermal degradation behavior of diamond to the (111) and (100) surface facets.[3] The interatomic potential is constructed using graph neural network model, trained using energies and forces from spin-polarized van der Waals-corrected density functional theory calculations. Our results show that the C(111) surface is more susceptible to thermal degradation, which occurs from 2850 K through synchronized bilayer exfoliation mechanism. In comparison, the C(100) surface thermally degrade from a higher temperature of 3680 K through the formation of sp1 carbon chains and amorphous sp2-sp3 carbon network. Due to the dangling bonds at the step edges, the stepped surfaces are more susceptible to thermal degradation compared to the corresponding flat surfaces, with the stepped C(111) and C(100) surfaces thermally degrading from 1810 K to 3070 K, respectively. We propose potential applications of this study in diamond tool wear suppression, diamond polishing, and production of graphene directly from the diamond surface.

We also conducted collaboration with experimental groups. Using $ab-initio$ calculations of the XPS chemical shift, we identified chemical species on plasma-treated polytetrafluoroethylene (PTFE) surfaces.[4]

We also conducted theoretical calculations on the energies of oxygen reduction and hydrogen insertion reactions with oxygen-deficient perovskite oxides and we demonstrated that the oxygen vacancy ordering in $Sr(Fe_{1-x}Co_x)O_y$ (SFCO) epitaxial films can be stabilized by increasing the Co content ($x \geq 0.3$) and revealed that it plays a key role in promoting proton accommodation into the SFCO lattice. Our results provide guidelines for controlling material properties through the insertion and extraction of hydrogen and for designing and exploring hydrogen-insertion materials.[5]

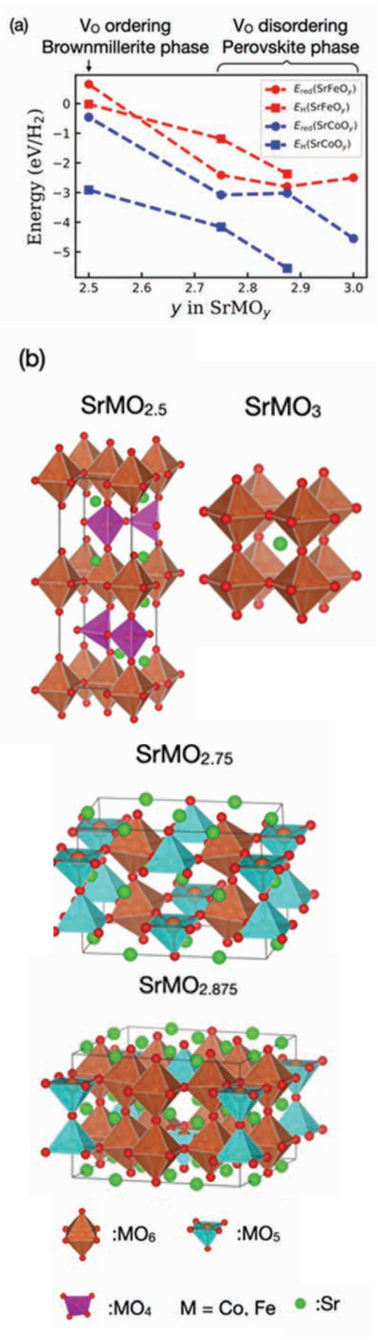

Figure 1: Theoretical investigation of oxygen reduction and protonation of $SrFeO_y$ and $SrCoO_y$. (a) Oxygen reduction energy (E_{red}) and hydrogen insertion energy (E_H) of $SrMO_y$ (M = Fe and Co) as a function of oxygen stoichiometry(y). (b-e) Crystal structures of $SrMO_y$.

References

[1] T. N. Pham, B. A. Choi Tan, Y. Hamamoto, K. Inagaki, I. Hamada, and Y. Morikawa, ACS Catal. **14**, 1443-1458 (2024).

[2] J. I. G. Enriquez, T. Yamasaki, M. Michiuchi, K. Inagaki, M. Geshi, I. Hamada, Y. Morikawa, J. Phys. Chem. C **128**, 6294-6308 (2024).

[3] J. I. G. Enriquez, H. H. Halim, T. Yamasaki, M. Michiuchi, K. Inagaki, M. Geshi, I. Hamada, Y. Morikawa, Carbon **226**, 119223 (2024).

[4] M. Nishino, K. Inagaki, Y. Morikawa, K. Yamamura, and Y. Ohkubo, Appl. Surf. Sci. **655**, 159369 (2024).

[5] Y. Isoda, T. N. Pham, R. Aso, S. Nakamizo, T. Majima, S. Hosokawa, K. Nitta, Y. Morikawa, Y. Shimakawa, and D. Kan, Nature Commun. **16**, 56 (2025).

FTQC Algorithm Implementation for Quantum Chemistry: A Hybrid approach with Quantum- and Super-computer

Yu-ichiro Matsushita
Department of Physics,
The University of Tokyo, Hongo, Tokyo 113-8626

In recent years, quantum computers have been attracting attention in the field of material calculations due to their ability to solve problems that are difficult for conventional supercomputers. In this work, we used the hybrid computing approach combining the supercomputer "ohtaka" at The University of Tokyo and Quantinuum's quantum computer to perform quantum chemistry calculations. A particularly noteworthy achievement was the successful execution of FTQC (Fault-Tolerant Quantum Computing) algorithms for ground state calculation on a real quantum computer using quantum error detection codes, marking the world's first attempt. The calculation target of this study is composite defects in aluminum nitride (AlN) to reveal the great potential as a promising quantum bit material. The successful implementation of FTQC algorithms in this study demonstrated their efficacy in generating highly accurate material property values through quantum chemistry calculations.

For this study, the calculation model involved around 300 atoms, and initial calculations were performed using Density Functional Theory (DFT) on the "ohtaka" supercomputer at The University of Tokyo. A downfolding method was employed to reduce the problem size without sacrificing precision, focusing on the most challenging regions of the system that required high-accuracy calculations. Subsequently, Quantinuum's trapped-ion quantum computer "H1-1" was used to execute FTQC algorithms on the refined model, and quantum error detection codes (Iceberg codes) were applied to mitigate the effects of quantum noise, leading to highly accurate results.

The outcome of this study demonstrated that FTQC algorithms function with high accuracy, successfully determining both the ground and excited states of composite defects, which are promising as quantum bit materials. The FTQC algorithm used in the calculations was the probabilistic imaginary time evolution (PITE) method, which was developed by our group. The PITE method has been mathematically proven to accelerate quantum chemistry calculations, and its successful implementation in this research confirms its potential.

Moreover, the study revealed that composite defects in AlN possess highly unique quantum properties, including spin triplet and spin singlet states, which are particularly valuable for quantum bit applications. This discovery expands the diversity of quantum bit materials. The calculations showed that, compared to an ideal FTQC machine, the current quantum computer hardware can achieve 98% of the ideal FTQC machine's precision. (See Fig.1)

As quantum computers continue to improve, the practical application of FTQC algorithms is expected to accelerate the development of quantum chemistry calculations and materials informatics. The results of this research were released in a press release and idely disseminated.

References

[1] H. Nishi, *et. al.*, Phys. Rev. Applied **23**, 034016 (2025).

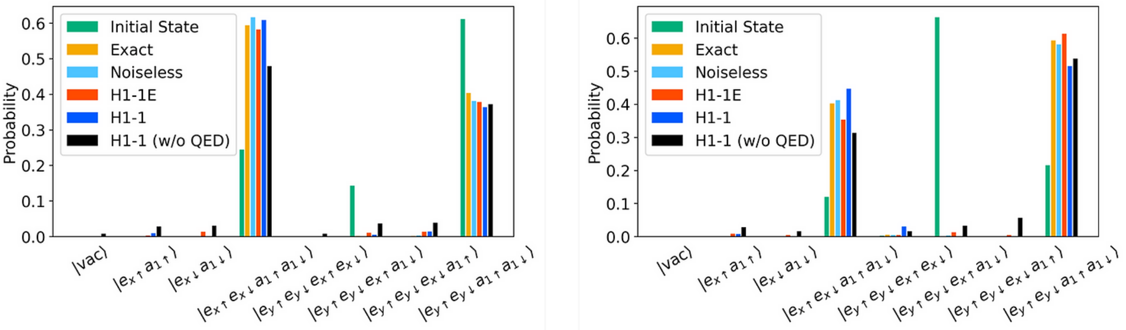

Fig. 1, Execution results on a real quantum computer. The results for the ground state (left figure) and the excited state (right figure). In each figure, the initial state is shown in green, the exact imaginary time evolution method in yellow, the ideal quantum computer without noise in light blue, the simulation results with the noise model in red, the results from the real quantum computer using quantum error detection codes in blue, and the results from the real quantum computer without using quantum error detection codes in black.

Analyses on local properties at complex structures via ab-initio-based methods/ Analyses on correlation between material properties and atomic structures in complex structures via ab-initio-based methods

Satoshi WATANABE
Department of Materials Engineering, the University of Tokyo
7-3-1 Hongo, Bunkyo-ku, Tokyo, 113-8656

1 Introduction

Understanding local properties in complex structures—such as amorphous phases, surfaces, interfaces, and defects—is crucial for advancing new information devices and energy systems. To this end, we have conducted simulations based on ab initio methods, particularly density functional theory (DFT) and machine learning potentials (MLPs).

As research has progressed, the correlation between atomic structures and local properties has become increasingly important. Recently, we have focused our studies on elucidating these correlations. Below, we introduce two of our results from fiscal year 2024.

2 Construction of machine learning potentials for alloy cluster catalysts

High entropy alloys (HEAs), containing five or more elements, have attracted significant attention as potential candidates for various applications. However, identifying optimal HEAs through DFT calculations is computationally expensive due to the vast compositional space. To address this, we constructed machine learning potentials (MLPs) for efficient catalyst discovery [1].

Our target was catalysts for the CO_2 reduction reaction (CO_2RR), where activity and selectivity are closely linked to the adsorption energies of CO molecules and H atoms. We trained MLPs to predict these energies, using DFT data on optimized structures, total energies, and adsorption energies for nine promising elements (Ag, Au, Co, Cu, Ni, Ir, Pd, Pt, Rh). Training data were sourced from both in-house calculations and publicly available data [2, 3, 4].

Unlike previous studies that focused on flat slab models, we constructed MLPs applicable to cluster models, as non-flat surfaces often exhibit superior catalytic activity. Our MLPs achieved mean absolute errors typically below 60 meV for adsorption energies and total energies (per atom), even for clusters of varying size and shape and up to five elements.

Using these MLPs, we identified HEA compositions with the H and CO adsorption energies within desirable ranges for catalysis. This work provides a strong foundation for high-throughput screening of alloy compositions and cluster geometries, addressing current limitations in DFT calculations for HEA clusters.

3 Thermal conductivities of AlN crystals with vacancies

Aluminum nitride (AlN) is widely used in electronic devices, where heat dissipation critically affects performance. Since fabrication processes inevitably introduce defects, it is important to understand how these defects—and their charge states—impact thermal conductivity. While DFT offers high predictive accuracy, it is computationally intensive. Conventional MLPs cannot handle multiple defect charge states, so we previously developed a scheme [5] based on high-dimensional neural network potentials (NNP) [6] to address this.

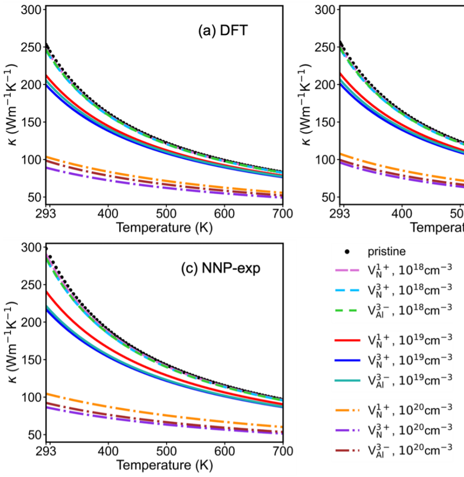

Figure 1: Comparisons of thermal conductivities between pristine AlN and defect-laden AlN predicted using the optimal lattice constants by (a) DFT, (b) NNP and using the experimental lattice constants by (c) NNP. Reprinted from Ref. [7].

In this study [7], we applied this scheme to investigate the effects of nitrogen vacancies in +1 and +3 charge states (V_N^{1+} and V_N^{3+}) and aluminum vacancies in −3 charge state (V_{Al}^{3-}) on the lattice dynamics of AlN. The 2nd and 3rd-order interatomic force constants were calculated using the finite displacement method via the PHONOPY [8] and thirdorder.py [9] codes, respectively. The thermal conductivities were calculated using the AlmaBTE package [10]. The constructed NNP exhibited excellent accuracy, with root mean square errors of 3.55 meV/atom (training) and 3.48 meV/atom (testing) for total energies, and about 69 meV/Å for atomic forces. Phonon bands, phonon scattering rates, and thermal conductivity (κ) predicted by the NNP were in good agreement with DFT results. The results on κ are shown in Fig. 1. We found that V_N^{3+} most significantly reduces κ, followed by V_{Al}^{3-} and then V_N^{1+}. Our findings contradict earlier speculations based solely on mass differences and highlight the critical role of structural distortions in phonon scattering.

References

[1] K. Miyamoto, K. Shimizu, A. K. A. Lu, and S. Watanabe: e-J. Surf. Sci. Nanotechnol., in press.

[2] J. K. Pedersen, T. A. A. Batchelor, and A. Bagger: ACS Catal.**10** (2020) 2169.

[3] K. Tran and Z. W. Ulissi: Nat. Catal. **1** (2018) 696.

[4] M. Scheidgen, et al.: J. Open Source Softw. **8** (2023) 5388.

[5] K. Shimizu, et al.: Phys. Rev. B **106** (2022) 054108.

[6] J. Behler and M. Parrinello: Phys. Rev. Lett. **98** (2007) 146401.

[7] Y. Dou, et al.: Phys. Rev. Mater. **9** (2025) 034601.

[8] A. Togo and I. Tanaka: Scr. Mater. **108** (2015) 1.

[9] A. Togo, L. Chaput, and I. Tanaka: Phys. Rev. B **91** (2015) 094306.

[10] J. Carrete, et al.: Comput. Phys. Commun. **220** (2017) 351.

Development of a first-principles computational method for functional materials

Fumiyuki ISHII, Naoya YAMAGUCHI, Rifky SYARIATI,
Hana Pratiwi KADARISMAN, Shohei MIURA,
Yaotang ZHANG, Yedija Yusua Sibuea TEWENG, Jin INOUE, Sota, YAMATE
Khusnul YAKIN, Wardah AMALIA, Shigetomo YANASE,
Syifa Fauzia Hariyanti PUTURI, Ahmad GHIFFARI, Salsabila Amanda PUTRI
Nanomaterials Research Institute, Kanazawa University
Kanazawa, 920-1192, Japan

1. *High-throughput computational screening of 2D thermoelectric materials*[1]

The pursuit of efficient thermoelectric energy conversion has gained momentum as a solution for waste heat recovery and environmental sustainability. Despite existing repositories documenting electronic characteristics of two-dimensional materials and conventional thermoelectric compounds, a significant knowledge gap persists regarding transverse transport phenomena, specifically anomalous Hall and Nernst conductivities in magnetic 2D systems. To bridge this deficiency, we employed computational high-throughput screening via first-principles density functional theory coupled with Boltzmann transport formalism. Among the investigated systems, transition metal trihalide monolayers emerged as exemplary candidates, with comprehensive analysis of 240 structural variants revealing that $\mathrm{PdBr_3}$ and $\mathrm{PtBr_3}$ ferromagnetic films demonstrate quantized anomalous Hall transport in both pristine and charge-doped configurations. Spin-orbit interactions induce modest energy gaps (approximately 35 meV and 12 meV for $\mathrm{PdBr_3}$ and $\mathrm{PtBr_3}$ respectively), establishing these systems as topological Chern insulators characterized by non-trivial Berry curvature distributions and contrasting Chern indices across the chemical potential range.

Our computational analysis uncovered remarkable anomalous Nernst responses in these layered compounds, with $\mathrm{PdBr_3}$ exhibiting peak coefficients of -54.1 $\mu V/K$ while $\mathrm{PtBr_3}$ demonstrates values reaching -23.3 $\mu V/K$ under ambient conditions with appropriate hole carrier concentrations. The exceptional magnitude of these coefficients stems from the interplay between thermally-driven charge currents and topologically-protected Hall responses, facilitated by the distinctive band topology in proximity to the chemical potential. The tunability of coefficient polarity through electronic doping, together with the enhancement provided by van Hove critical points, positions these materials as attractive platforms for advanced energy conversion technologies, especially in internet-of-things applications demanding versatile thermal energy scavenging capabilities.

2. *Anomalous Nernst effect in* $CrGeTe_3$[2]

We have performed first-principles calculations to investigate the anomalous Nernst effect in ferromagnetic $\mathrm{CrGeTe_3}$ thin films and understand the origin of large anomalous transverse thermoelectric effects in two-dimensional ferromagnetic materials. We focused on how Berry curvature contributes to anomalous Hall conductivity, particularly examining the role of nodal lines—degenerate points in the band structure that become small band gaps when spin-orbit coupling is introduced. In monolayer $CrGeTe_3$, we discovered a circular nodal line in the conduction band energy range of 0.43–0.58 eV, which oscillates with six minima and maxima around the Γ point in k-space.

When we included spin-orbit coupling in the calculations, the nodal line created small band gaps that generated large Berry curvatures, resulting in significant anomalous transverse thermoelectric conductivity α_{xy}. We found peaks in both anomalous Hall conductivity σ_{xy} and anomalous transverse thermoelectric conductivity α_{xy} around $\mu = 0.32$ eV, with magnitudes reaching approximately 10 $(\mu\mathrm{V/K})(e^2/h)$. These findings suggest that ferromagnetic $CrGeTe_3$ thin films exhibit promising anomalous Nernst effects originating from the nodal line structure, making them potential candidates for thermoelectric applications that leverage transverse temperature gradients.

3. *Layer-Resolved Anomalous Hall Effect in Thin Films and Heterointerfaces: First-Principles Study*[3]
This research presents a comprehensive first-principles computational study of the anomalous Hall effect (AHE) with layer-by-layer decomposition in various thin film and heterointerface systems. The research team from Kanazawa University developed an advanced computational methodology that combines local Berry phase approaches [4] with hybrid Wannier functions to analyze the contribution of individual layers to the anomalous Hall conductivity in metallic systems. By calculating Berry phases (Berry curvature) on two-dimensional Brillouin zone meshes and constructing hybrid Wannier functions on the same mesh, the researchers successfully achieved layer-resolved decomposition of the anomalous Hall effect in complex material systems. The computational investigations encompassed single metallic systems including Fe thin films, Cr thin films, and $SrRuO_3$ thin films, as well as ferromagnetic/nonmagnetic heterostructures such as Fe/W and $SrRuO_3/SrIrO_3$. The results revealed characteristic features of layer-resolved anomalous Hall conductivity, demonstrating enhanced conductivity near interfaces and significant contributions from specific layers, which correspond well with important experimental observations in metallic systems. Additionally, the study provided insights into the spatial distribution of the anomalous Hall effect in antiferromagnetic materials, offering new perspectives on topological properties and improving understanding of transport phenomena in complex systems through examination of individual layer contributions.

References

[1] R. Syariati, S.A. Wella, E. Suprayoga, M.S. Muntini, and F. Ishii, J. Phys.: Condens. Matter **37** 025602 (2025).

[2] K. Shibata, E. Suprayoga, R. Syariati, and F. Ishii, *in preparation*.

[3] F. Ishii, H. Kadarisman, Y. Morishima, and N. Yamaguchi, *in preparation*.

[4] H. Sawahata, N. Yamaguchi, S. Minami, and F. Ishii, Phys. Rev. B **107** 024404(2023).

Development of first-principles calculation code RSPACE and design of highly functional interface

Tomoya ONO
Graduate School of Engineering, Kobe University
Rokkodai-cho, Nada, Kobe 657-8501

Silicon carbide (SiC) is a wide-bandgap semiconductor that has attracted considerable attention as a promising material for next-generation power electronics devices, including the **metal-oxide-semiconductor field-effect transistor (MOSFET)**. However, the high channel resistance at the thermally oxidized SiC/SiO_2 interface degrades the performance of SiC MOSFETs, which occurs by the reduction of field-effect mobility, compared to that in the bulk material. Post-oxidation annealing processes using nitrogen-based gases substantially improve this mobility degradation at the interface. In our studies, we utilized the first-principle electronic structure calculations and investigated mobility degradation mechanisms that originate from sources distinct from conventional trap states. Previously, we reported that the conduction band edge (CBE) states exhibit discontinuities in the inversion layer at atomic step edges, which are induced by the Coulomb interaction of oxygen atoms in the SiO_2 layer [1]. In the present study, we extended our analysis to the effect under a more realistic low nitrogen concentration, approximately one-third of which was used in our previous calculations and comparable to the values reported in recent experiments.

In this study, the computations were performed using the **RSPACE code**, which employs a real-space finite-difference approach for density functional theory (DFT) calculations [2]. We considered various slab supercell models of 4H-SiC(0001)/SiO_2 interfaces; Fig. 1 illustrates an example of the atomic-scale structure. The model consists of a SiO_2 region (thickness: 8.2 Å) and a 4H-SiC substrate comprising seven SiC bilayers (thickness: 17.5 Å), where quasi-cubic (k) and hexagonal (h) sites are alternately stacked along the [0001] direction. Furthermore, the computational models are categorized based on both the SiC-side interface (*i.e.* whether the topmost Si layer corresponds to a k site or an h site) and the SiO_2-side structure (*i.e.* whether the interface layer faces a one-fold or three-fold Si-O structure); then, the models are referred to as k1, k3, h1, and h3 interfaces, respectively. For the nitrided region, similar to our previous work [1], we incorporated nitrogen atom defects with a density of 1.22×10^{15} atoms/cm^2.

In this work, we investigated the accumulation of the charge density of the CBE states by using the partial charge (PC) densities defined below:

$$\rho_{\mathrm{PC}} = \sum_{i,k} \left| \int \Psi^*_{i,k}(\boldsymbol{r}) \phi_k(\boldsymbol{r}) d\boldsymbol{r} \right|^2 \times \theta(\epsilon_{i,k} - \epsilon_F)\theta(\epsilon_{max} - \epsilon_{i,k})\Delta_k, \quad (1)$$

where ϵ_F is the Fermi level, θ is the Heaviside function, and $\phi_k(x, y, z)$ is the wavefunction of the CBE states obtained by the thin film models. $\epsilon_{\mathrm{max}}(=\epsilon_F+1.65$ eV), which is the maximum energy of the energy window, is chosen so that the energy window contains the CBE states inside the SiC substrate. The calculated PC before and after annealings are plot-

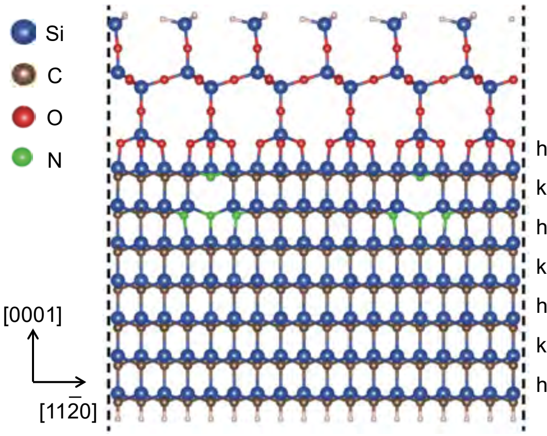

Figure 1: Slab supercell structure of the 4H-SiC/SiO_2 interface after NO annealing. An example is the h3-type model, characterized by a hexagonal (h) site at the SiC interface and a three-fold structure of Si–O bonds.

ted in Fig. 2. The PC values after partial nitridation are insensitive to the change of the nitrided regions. They are lower than those before NO annealing, owing to the screening of the Coulomb interaction from the oxygen atoms by the nitrided layer. However, the partial charge at the interface after partial nitridation remains larger than that after full nitridation, indicating that the effect of NO annealing may be limited.

In addition, we have calculated the carrier scattering property at the interface. The transmission spectrum for the h-type interfaces is shown in Fig. 3.

References

[1] M. Uemoto, N. Funaki, K. Yokota, T. Hosoi, and T. Ono, Appl. Phys. Express **17**, 011009 (2024).

[2] K. Hirose, T. Ono, Y. Fujimoto, and S. Tsukamoto, *First-Principles Calculations in Real-Space Formalism, Electronic Configurations and Transport Properties of Nanostructures* (Imperial College, London, 2005).

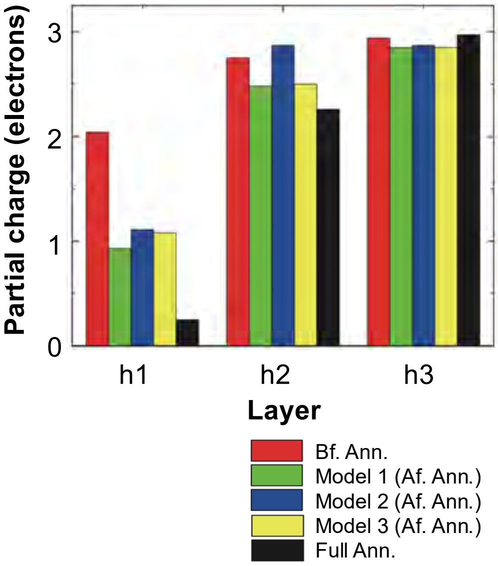

Figure 2: Partial charge densities [Eq. (1)] of the CBE states for various interface structures. Before annealing ("bf. ann.") refers to the pristine h3-type interface model. Model 1 represents the annealed ("af. ann.") structure illustrated in Fig. 1. Model 2 and Model 3 correspond to similar h-type interfaces incorporating nitrogen atoms at different sites. "Full Ann." denotes the model in which all considerable sites are nitrided, as studied in our previous work [1].

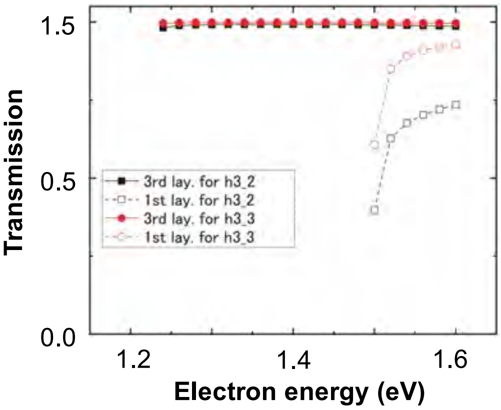

Figure 3: Transmission of h-type interfaces at 1st layer and 3rd layer channels.

Density functional theory study of adsorption and reaction of molecules on solid surfaces and interfaces

Ikutaro Hamada

Department of Precision Engineering, Graduate School of Engineering,

The University of Osaka (aka Osaka Universit)y, 2-1 Yamadaoka, Suita, Osaka 565-0871

Understanding the microscopic details of adsorption and reaction of molecules on surfaces of solid and low-dimensional materials is of critical importance as they play key roles in fundamental chemical processes, such as wetting, as well as technologically relevant ones, such as heterogenous catalytic reactions. We performed density-functional theory (DFT) simulations on organic molecules on a semiconductor surface [1,2], graphene adsorption on a metal surface, bilayers composed of the hydrogen boride (HB) sheets [3], water adsorption on the edges of the HB sheet [4], chemical reactions of various molecules on the HB sheet surface, using different DFT codes including STATE [5] and Quantum-ESPRESSO [6]. Below, I describe the key findings obtained mainly using the system B of the supercomputer facility at ISSP.

We investigated the organic molecules such as C_{60} and PTCDA on the Si(111)(7×7) surface and succeeded in determining their adsorption states, including adsorption sites, corresponding adsorption energies, and vibrational modes. We also investigated graphene on the Rh(111) surface and succeeded in reproducing the Moiré pattern of graphene observed in the experiment. Furthermore, we succeeded in characterizing the adsorption states of single atoms the on graphene/Rh(111) system. For the HB sheets, we clarified the vibrational properties of the HB sheet and bilayers composed of HB sheets and DB sheets using the recently developed computationally efficient package [7] and contributed to the characterization of the experimental vibrational spectroscopy. Furthermore, we investigated the adsorption and reaction of a water molecule at the surface and edge of the HB sheet and found that water dissociation is more facile near the edge region, not on the surface, and suggest that hydrolysis reaction observed in the experiment take place near the edge of the HB sheet. Finally, the carbon dioxide conversion to methane and ethane [8] on the HB sheet is currently under intense investigation and will be published in the near future.

References

[1] Y. Park, I. Hamada, A. Hammud, E. W. Meijer, M. Wolf, T. Kumagai, and A. Shiotari, Nat. Commun. **15**, 6709 (2024).

[2] B. Cirera, S. Liu, Y. Park, I. Hamada, M.

Wolf, A. Shiotari, and T. Kumagai, Phys. Chem. Chem. Phys. **26**, 21325-21331 (2024).

[3] S.-I. Ito, K. I. M. Rojas, Y. Yasuda, N. Noguchi, K. Fukuda, M. Hikichi, Z. Kang, M. Yuan, R. Tsuji, O. Oki, S. Roy, Y. Hikita, I. Matsuda, M. Miyauchi, I. Hamada, and T. Kondo, J. Phys. Chem. Lett. **15**, 10965-10976 (2024).

[4] K. I. M. Rojas, Y. Morikawa, and I. Hamada, Phys. Rev. Materials **8**, 114004 (2024).

[5] STATE documentation, https://state-doc.readthedocs.io/

[6] P. Giannozzi et al., J. Phys. Condens. Matter 21, 395502 (2009).

[7] K. I. M. Rojas, Y. Morikawa, and I. Hamada, J. Open Source Softw. **10**, 7855 (2025).

[8] T. Goto, S.-I. Ito, S. L. Shinde, I. Matsuda, and I. Hamada, H. Hosono, and T. Kondo, Commun. Chem. **5**, 118 (2022).

Development of Anharmonic Phonon Property Database Using First-Principles Calculations

Masato OHNISHI

The Institute of Statistical Mathematics,

Research Organization of Information and Systems, Tachikawa, Tokyo 190-0014, Japan

In recent years, data-driven materials development has been rapidly advancing. For inorganic materials in particular, in addition to conventional databases such as the Materials Project, large and newly released databases like DeepMind GNoME (2023) [1], META OMat24 (2024) [2], and Microsoft MatterK (2025) [3] have also become available. However, these databases often lack thermal property data or cover only a limited materials space. Moreover, thermal properties can vary significantly depending on factors such as impurities and carrier concentration, highlighting the need for thermal property databases constructed through theoretical calculations under well-defined conditions.

In this study, we developed automation software for calculating anharmonic phonon properties, named auto-kappa (Fig. 1), which enables the computation of mode-dependent phonon lifetimes, temperature-dependent thermal conductivities, and spectral thermal conductivities. Using this software, we constructed the anharmonic phonon property database through high-throughput first-principles calculations. As a result, we obtained

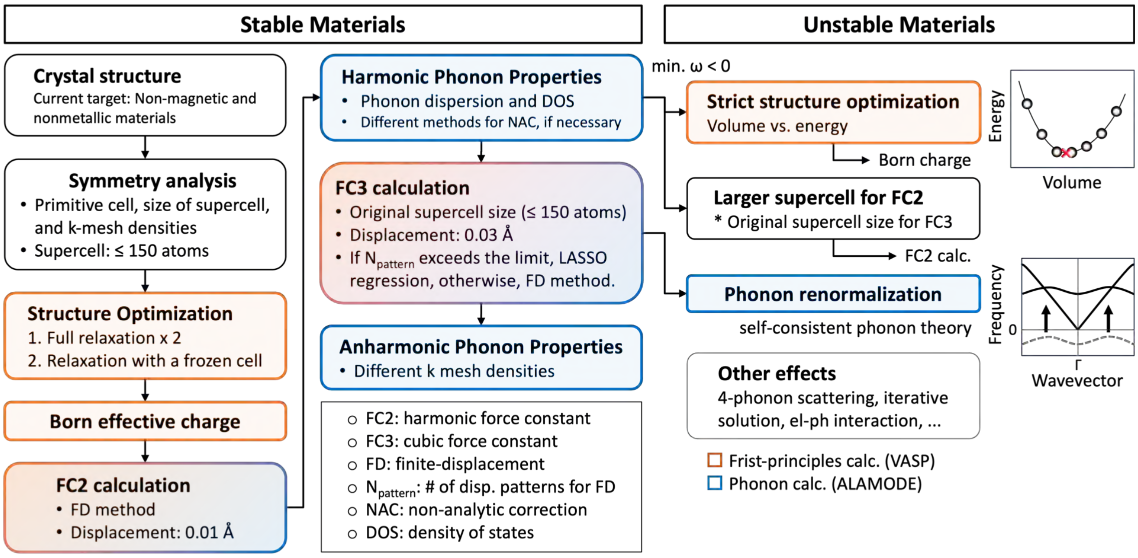

Fig. 1. Automated workflow for anharmonic phonon properties.

anharmonic phonon properties for over 6,000 inorganic materials. Leveraging this dataset, we demonstrated deep-learning scaling laws and screened for materials with high and low thermal conductivity from the GNoME database, which contains over 230,000 novel compounds. This work has been recently submitted to npj Computational Materials and arXiv. The developed software and database will be made publicly available upon the publication of the paper. The database is expected to be utilized in materials development across a diverse range of fields, including not only thermal properties but also mechanical, electronic, electrical, magnetic, and optical properties.

References

[1] Merchant, A. et al. Scaling deep learning for materials discovery. Nature 624, 80–85 (2023).

[2] Barroso-Luque, L. et al. Open Materials 2024 (OMat24) Inorganic Materials Dataset and Models. arXiv (2024) doi:10.48550/arxiv.2410.12771.

[3] Li, J. et al. Probing the Limit of Heat Transfer in Inorganic Crystals with Deep Learning. arXiv (2025) doi:10.48550/arxiv.2503.11568.

Analysis of thermal transport in disordered systems

Junichiro SHIOMI
Department of Mechanical Engineering,
The University of Tokyo, Hongo 7-3-1, Bunkyo-ku, Tokyo 113-8656, Japan

We investigated thermal transport behaviour in various complex systems. This year, we focused on the heat transport property of $FeCl_3$-graphite intercalation compounds and thermal transport suppression due to impurity addition in bulk disordered systems like amorphous silicon.

1. $FeCl_3$-graphite intercalation compounds

This study extends previous research on graphite and its intercalation with $FeCl_3$ to further elucidate the thermal conductivity behavior across different intercalation stages. In this context, "Stage-n" denotes the number of graphene layers between adjacent intercalant layers. Using non-equilibrium molecular dynamics (NEMD) simulations, we previously observed a non-monotonic trend in thermal conductivity, characterized by an initial decrease followed by an increase. Our findings suggest a transition from a coherent transport regime at lower stages to an incoherent regime at higher stages. Notably, Stage-3 exhibits an unexpected increase in thermal conductivity compared to Stage-2, before subsequently decreasing. To investigate the underlying mechanisms, we performed Spectral Energy Density (SED) analysis to extract phonon dispersion relations as a function of frequency and wavevector. This enabled the calculation of key thermal properties, including phonon mean free path and coherence length. The observed reduction in mean free paths and an increase in coherence lengths (Fig. 1a, b) relative to pristine graphite provide insight into the suppression of thermal conductivity in $FeCl_3$-intercalated graphite.

2. Impurity addition in bulk a-Si

In this study, NEMD simulations were performed on amorphous silicon (a-Si) to investigate the impact of impurities on thermal transport. In amorphous materials, thermal conduction is governed by both propagating modes (propagons) and non-propagating modes (diffusons), making it challenging to characterize the effect of impurities on vibrational modes [1,2]. Impurities were introduced by randomly substituting Si atoms with heavier Si isotopes at varying atomic concentrations (at%). The calculated thermal conductivity values (Fig. 2a) reveal a reduction of 10–20% at 10 at% impurity concentration, aligning with experimental observations. Density of states calculations confirmed that this reduction is not due to a decrease in the speed of sound caused by mass effects. Interestingly, the Allen-Feldman theory [2], which predicts similar thermal conductivity for pure and impure amorphous systems, fails to capture this suppression. Further analysis using normal mode decomposition (NMD) method (Fig. 2b) suggests that impurity scattering does not significantly suppress relaxation times. However, participation ratio (PPR) calculations based on eigenmodes (Fig. 2c) indicate increased mode localization with impurity addition, which likely contributes to the observed thermal conductivity suppression

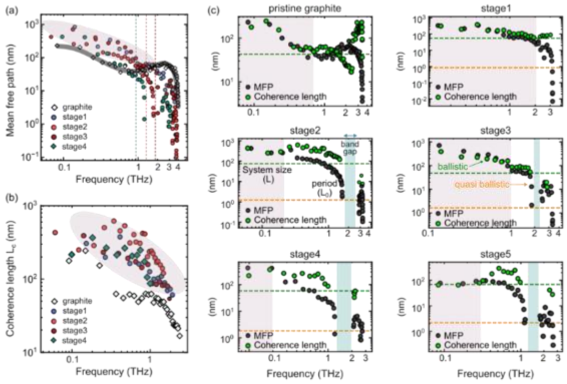

Fig. 1. Comparison of a) mean free path and b) coherence length with respect to frequency between stages 1-4 and pristine graphite. c) Expanded plots for direct comparison of mean free path and coherence length for each stage and pristine graphite

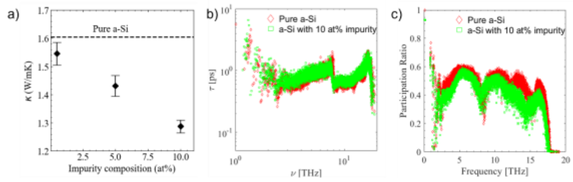

Fig. 2 a) Thermal conductivity variation with respect to the composition of heavy Si, b) Relaxation time as a function of frequency and c) Participation ratio as a function of frequency for pure a-Si and a-Si with 10 at% of heavy Si. The above results were obtained for heavy Si with mass twice that of pure Si.

References

[1] J.M. Larkin et al., Phy. Review B., 89, 144303 (2014)

[2] P. B. Allen et al., Philosophical Magazine, 79, 11-12 (1999)

Reduction of Rare Metals in Fuel Cell and Formic Acid Decomposition Catalysts

Norihito Sakaguchi

Center for Advanced Research of Energy and Materials, Faculty of Engineering,

Hokkaido University, Sapporo, Hokkaido 060-8628

We investigated the effects of adsorbates on the adsorption energy and diffusion barrier of single Pt atoms and Pt dimers supported on the light-element doped graphene using first-principles calculations based on density functional theory (DFT). We also investigated the catalytic selectivities of the single Pt atoms supported on the light-element doped graphene in formic acid decomposition reactions. We have also studied the adsorption states of a CO monolayer on Ag(111) surfaces.

First, we investigated the adsorption energy and diffusion barrier of single Pt atoms and Pt dimers supported on the light-element doped graphene. We performed the total energy and electronic structure calculations using the Vienna Ab initio Simulation Package (VASP). We installed a parallelized VASP with Intel® MPI Library and Intel® Math Kernel Library. We showed that the adsorption energy and diffusion barrier of single Pt atoms and Pt dimers drastically change by the adsorption of atoms and molecules.[1] In some cases, the diffusion barrier of the single Pt atoms and Pt dimers becomes less than 0.1 eV. However, the effects of adsorbates were complex, and a systematic understanding of their effects was not available.

We investigated the catalytic selectivities of the single Pt atoms supported on the light-element doped graphene in formic acid decomposition reactions. We considered four reaction pathways: two for hydrogen production and two for water production. We found that the light-element dopants in graphene can significantly change the catalytic selectivities.

We investigated the adsorption states of a CO monolayer on Ag(111) surfaces.[2] The obtained adsorption energy and adsorption structure show good agreement with experimental results. We also revealed that structural fluctuation can occur very easily with small activation barriers. This result explains the experimentally observed structural fluctuation in low-temperature conditions.

References

[1] Y. Kunisada, N. Sakaguchi, Catalysts and Catalysis 66 (2024) 259.

[2] M. Kimura, Y. Kunisada, Y. Sugimoto, Adv. Mater. Interfaces in press

Development of First-Principles GWΓ Method

Yoshifumi NOGUCHI

Department of Applied Chemistry and Biochemical Engineering, Graduate School of Engineering, Shizuoka University, Johoku 3-5-1, Hamamatsu, Shizuoka 432-8561, Japan

Considering first-order three-point vertex function ($\Gamma = 1 + iGGW$), we have developed a first-principles GWΓ method, which intrinsically goes beyond a conventional GW approximation [1], with the three-point vertex function approximated as unity ($\Gamma = 1$). To demonstrate the computational accuracy of the GWΓ method and contributions of newly added higher-order terms (or first-order three-point vertex functions) to the GW one-electron self-energy operator, we simulated the B1s, C1s, N1s, O1s, and F1s core-electron binding energies (BEs) of 19 small molecules, and directly compared them with the available experimental data without any artificial shifts. Table I lists mean absolute errors (MAEs) of the LDA Kohn-Sham orbital energies, and GW and GWΓ quasiparticle energies. It is well-known that LDA results significantly underestimate experimental BEs by approximately 20-34 eV. Herein, this underestimation was improved by simply replacing the LDA exchange-correlation potential with the GW one-electron self-energy operator; however, an error of several eV would remain. The shortcomings of GW method for the BEs were similar to those previously reported [2]. Additionally, the errors of GW method were reduced by the GWΓ method to 1.09-1.78 eV for B1s, C1s, N1s, O1s, and F1s BEs [3]. Because the present GW and GWΓ methods were executed with a one-shot (not self-consistent) version, the use of LDA one-electron wave functions was not sufficiently localized to describe the core-electron, thus potentially leading to errors in the GWΓ methods.

Table I. MAE of LDA, GW, and GWΓ (in eV)

	LDA	GW	GWΓ
B1s	20.21	3.71	1.09
C1s	25.19	5.14	1.35
N1s	28.35	6.94	1.60
O1s	31.97	7.80	1.78
F1s	34.33	5.78	0.45

References

[1] M. S. Hybertsen and S. G. Louie, Phys. Rev. Lett. **55**, 1418 (1985).

[2] M. J. van Setten, R. Costa, F. Viñes, and F. Illas, J. Chem. Theory Comput. **14**, 877 (2018).

[3] K. Yoneyama, Y. Noguchi, and K. Ohno, J. Chem. Phys. **161**, 154102 (2024).

Electrochemical reaction analysis using density functional calculation + implicit solvation model 6

Jun HARUYAMA

Pioneering Research Institute, RIKEN, 2-1 Hirosawa, Wako, Saitama 351-0198

Hydrogen energy conversion technologies such as fuel cells and water electrolysis devices are essential for realizing sustainable society. The investigation of fast hydrogen transport materials has attracted concerns. Recently, Ba–Li oxyhydride, $Ba_{1.75}LiH_{2.7}O_{0.9}$ (BLHO), shows the ionic conductivity of 10^{-5}–10^{-7} S/cm with activation energy of c.a. 103 kJ/mol at low temperatures ($T \leq 300$ °C, T is temperature) and 10^{-2} S/cm at high temperatures (300 °C $< T$), which conducting career has been certified as hydride ion (negative charge hydrogen, H^{-}). [1] In this study, we investigate H^{-} diffusion mechanism by first-principles molecular dynamics (FPMD) simulations.

To reproduce the occupancy ratios, the crystal structures of BLHO at low- (β) and high-temperature (δ) phases were modeled as 2×4×1 and 4×4×1 supercells as shown in Figs. 1 (a) and (b), respectively. We performed FPMD simulations with Perdew–Burke–Ernzerhof (PBE) exchange-correlation functional [2] by Vienna Ab initio Simulation Package (VASP) [3] in thermal equilibrium conditions (T = 500, 700, 900, and 1100 K) for several hundred ps. Then, the self-diffusion coefficient D, Lindemann indices (the indicators of liquid-solid transition), [4] and van Hove time correlation functions [5] of H were calculated from FPMD trajectories.

From the mean square displacements (MSD) of H atoms, we obtained *ab* plane and *c*-axis decomposed D values. The former values are plotted in Fig. 1 (c). The diffusion process in *ab* plane corresponds to the H^{-} hopping between anion equatorial sites. The estimated values of D are consistent with that obtained by the quasi-elastic neutron scattering (QENS) analysis (3–4×10^{-7} cm^2/s). [1] However, the activation energies E_a estimated from D values are 0.52–0.55 eV for both phases, which values are different from the estimated values from experimental ionic conductivity, E_a =1.0 eV (300 °C $< T$), but consistent with the analyses of elastic and inelastic neutron scattering intensities, E_a =0.6 eV (300 °C $< T$). [1] From the comparison, it is indicated that the rate-determining process of conductivity is not the *ab*-plane diffusion, but rather to the c-axis diffusion, ion movement at crystallite interfaces, or collective motions that cannot be accounted for our short time scale simulations.

Moreover, the Lindemann indices were calculated for Ba, Li, O, and H atoms as shown in Fig. 1 (d). We found that the Lindemann index of H exceeds the threshold for a solid-liquid transition (= 0.1) at high temperatures above 700 K, which suggests the sublattice melting of anion equatorial sites and the superionic conduction of H^- in BLHO. We will discuss c-axis dynamics, collective motion, and diffusion mechanism of H^- from the time correlation function in future studies.

References

[1] F. Takeiri, A. Watanabe, K. Okamoto, D. Bresser, S. Lyonnard, B. Frick, A. Ali, Y. Imai, M. Nishikawa, M. Yonemura, T. Saito, K. Ikeda, T. Otomo, T. Kamiyama, R. Kanno, and G. Kobayashi, *Nat. Mater.* **21**, 325 (2022).

[2] J.P. Perdew, K. Burke, and M. Ernzerhof, *Phys. Rev. Lett.* **77**, 3865 (1996).

[3] G. Kresse and J. Hafner, *Phys. Rev. B* **47**, 558 (1993); G. Kresse and J. Furthmüller, *Phys. Rev. B* **54**, 11169 (1996); G. Kresse and J. Furthmüller, *Comput. Mat. Sci.* **6** , 15 (1996).

[4] X. He, Y. Zhu, and Y. Mo, *Nat. Comm.* **8**, 15893 (2017).

[5] Y. Zhou, M. Karplus, K. D. Ball, and R. Stephen Berry, *J. Chem. Phys.* **116**, 2323 (2002).

[6] K. Momma and F. Izumi, *J. Appl. Crystallogr.* **44**, 1272 (2011).

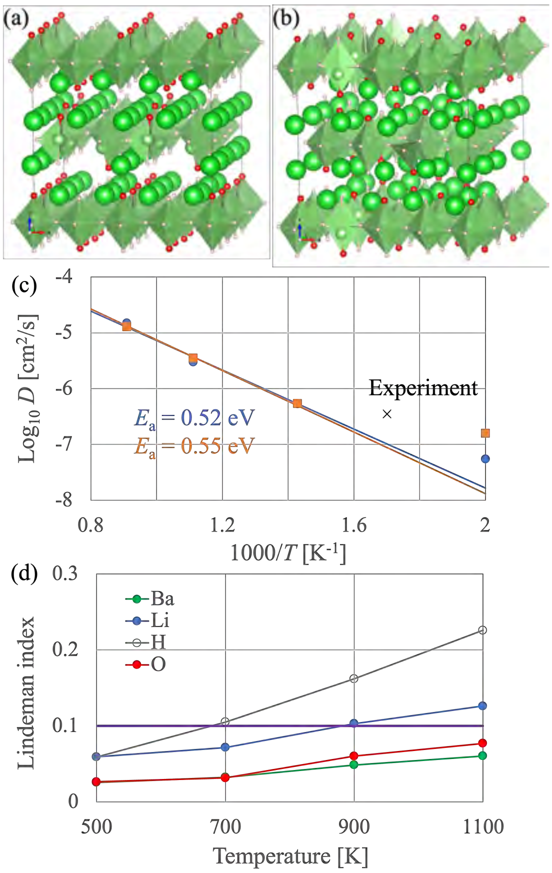

Figure 1: (a) β- and (b) δ-phase BLHO models. The VESTA package [6] was used to visualize the structures. (c) Diffusion coefficients D as a function of inverse temperature. The blue and orange squares represent β- and δ-phase values, respectively. The black cross mark represents D obtained by QENS analysis. [1] The blue and orange lines represent linear relation corresponds to the activation energies of 0.52 and 0.55 eV, respectively. (d) Lindeman indices as a function of temperature. The green, blue, gray, and red circles represent the Lindeman indices of Ba, Li, H, and O atoms, respectively. The black line is the criterion of liquid-solid transition.

Theoretical Studies on New Types of Electron Trap Defects Originated from Localized Floating States in a-SiN towards Flash Memories Application

Kenji SHIRAISHI

Institute for Materials and Systems for Sustainability,

Nagoya University, Furo-cho, Chikusa-ku, Nagoya, Aichi 464-8601

Catching and emitting electronic charges in a localized region of a material corresponds to writing and reading information data in memory devices. This could in principle be done by ordinary gap states. Yet, such states are generally prone to act as permanent traps for charge carriers mainly because of structural reconstructions occurring upon carrier trapping and/or emitting: This makes the capture and release events uncontrollable and even resulting in a degradation of the sought memory function. The localized floating states (LFS) identified, analyzed and characterized in this work is free from such structural reconstruction, not giving rise to any bonding or antibonding state but becoming reversible charge hosting and releasing centers. In our specific work on non-stoichiometric SiN systems, these LFSs exist in cavities free from structural or electronic defects. They arise just because of the networking of amorphous SiN when the amount of Si exceeds the reference one of Si_3N_4, resulting in empty spaces surrounded by an excess of four-fold coordinated Si atoms. Their active role in accepting up to two electrons has been rationalized in terms of well assessed bond descriptors, allowing for a quantitative interpretation of the peculiarity of LFS. Moreover, the preferred occupation of LFSs with respect to regular antibonding states populating the LUMO band by additional electrons can be explained in terms of local electrostatic potential, resulting more attractive of at least a factor of two in comparison with other unoccupied states, with these empty cavities acting as a sort of virtual cation able to attract the supplied electrons. Moreover, we show that the relative amount of Si and N is a way to control the arising of these states and to minimize the presence of other defects such as DBs, generally responsible for degradation, with direct practical consequences for the realization of devices. This stoichiometry tuning enhances device performance function of flash memory devices and guidelines for their design [1].

References

[1] T. Nagahashi, H. Karasawa, R. Horiike, A. Oshiyama and K. Shiraishi, IEEE Electron Devices Technology and Manufacturing (EDTM) 2025 – in press.

Clarification of Hole Trap at GaN/SiO$_2$ Interfaces and Fabrication of GaN-MOSFET

Kenji SHIRAISHI

Institute for Materials and Systems for Sustainability,

Nagoya University, Furo-cho, Chikusa-ku, Nagoya, Aichi 464-8601

Experiments in the past suggest that hole traps at GaN/SiO$_2$ interfaces are reduced with heavily Mg-doped GaN epitaxial layers [1,2], but its physical origin is unclear. In this study, we investigate by first-principles calculations the interaction between substitutional Mg atoms at Ga sites (MgGa) and O vacancy (V_O) in a nanometer-scale Ga-oxide (GaO$_x$) interfacial layer which is inevitably formed at GaN/SiO$_2$ interface, and clarify the physical reason why Mg passivates hole traps. Our calculations show that MgGa and V_O become stable by forming 2MgGa-V_O complex in GaO$_x$. In addition, while V_O form deep hole traps in the band gap of GaN, Mg attachment to V_O makes the hole-trap level shift upward substantially (Fig. 2) and thus 2MgGa-V_O induces no hole traps [3]. These results indicate that hole traps originated from V_O are passivated by the formation of a complex of MgGa atoms and V_O.

References

[1] H. Mizobata, Y. Wada, M. Nozaki, T. Hosoi, T. Shimura, and H. Watanabe, Appl. Phys. Express **13**, 081001 (2020).

[2] K. Tomigahara, M. Hara and H. Watanabe, Appl. Phys. Express **17**, 081002 (2024).

[3] S. Hattori, A. Oshiyama, K. Shiraishi, Applied Physics Letters **125**, 161601 (2024).

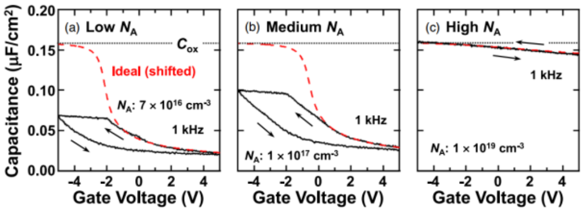

Fig.1: Experimental results of hole trap reduction by Mg incorporation. Hole trap reduction can be seen in case of heavily Mg incorporation. [Ref.1]

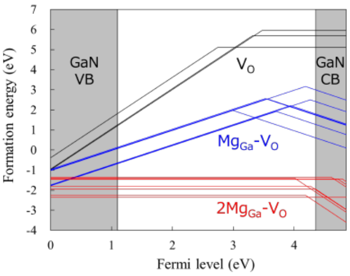

Fig.2: Formation energy diagram of Mg-V_O systems.

Clarification of Microscopic Mechanisms of Semiconductor Epitaxial Growth and Device-Interface Formation by Large-Scale Quantum-Theory-Based Computations#

Atsushi Oshiyama*

Institute of Materials and Systems for Sustainability, Nagoya University

Furo-cho, Chikusa-ku, Nagoya 464-8601

In the fiscal year of 2024, on the basis of the total-energy electronic-structure calculations and molecular dynamics simulations within the density-functional theory (DFT), we have studied the epitaxial growth of wide-gap semiconductors, atomic and electronic structures of semiconductor-insulator interfaces, and mechanisms of atomic diffusion in semiconductors. The main computational tools are our RSDFT (Real Space DFT) code and CPMD (Car-Parrinello Molecular Dynamics) code as well as VASP code. Specifically, we have clarified 1) that oxygen vacancy which is the major origin of hole traps at GaN/SiO$_2$ interfaces is passivated by doping either Mg[1] or B[2] impurities, contributing to better performance of MOS devices, 2) that implanted Mg atoms migrate in GaN via the carrier recombination processes, hereby sit at the Ga site and work as acceptors [3], 3) that in amorphous SiN which is a core part of the 3D NAND flash memory, peculiar electron states called localized floating states are nurtured in its internal space and work as charge centers, thereby making the amorphous the robust memory unit [4]. I will explain the issue 3) below.

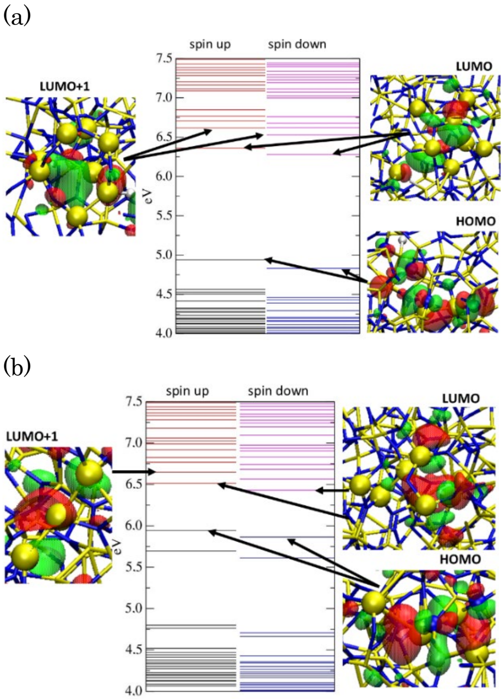

Figure: Panels (a) and (b) show the Kohn-Sham electronic levels and the related orbitals of the three hydrogenated systems r=1.22, 1.125 and 1.10, respectively. The atom color code is blue for N and yellow for Si with most relevant atoms highlighted as balls. The energy levels are colored in black (occupied states) and red (empty states) for α spin-up states and blue (occupied states) and magenta (empty states) for β spin-down states. The orbitals are shown at isosurface values of ±5x10^{-2} 1/Å$^{3/2}$ corresponding to 30% of the full amplitude; red and green colors refer to positive and negative amplitudes, respectively.

Amorphous silicon nitride (a-Si_xN_y) is a premier element for a wealth of applications. In particular, it has replaced Si floating gates in flash-memory technology and now become indispensable materials which sustain our data-driven society. Device performance is tuned by changing its stoichiometry with respect to the standard x=3, y=4 (Si_3N_4) composition. Si rich (N poor) materials are usually used in the industry. Also hydrogen atoms are incorporated to guarantee the device operation. The mechanism of the memory function, i.e., which electron states are responsible for the read/write operation, is totally unknown, however.

Following the experimental information about the stoichiometry, we have prepared 3 amorphous samples with r = 1.22, 1.125 and 1.10 where r = [amount of N] / [amount of Si]: In our supercell model these correspond to (153Si+187N), (160Si+180N) and (162Si+178N), respectively. Hydrogen atoms (1 to 3, corresponding to the experimental situation) are added to mimic the hydrogenated systems. The amorphous samples were made by the melt-quench technique: At T=2500K each 3 system is well equilibrated for at least 50 ps and becomes liquid; then the systems were cooled down to 300K with the cooling rate of 9.56 K/ps, and kept at 300K for 150 ps; finally the systems are annealed to 0K and reach the optimized geometries.

In the obtained amorphous samples without hydrogenation, several point defects such as 3-fold coordinated Si (dangling bond), 5 fold coordinated Si as well as 2-fold N appear. The four-fold coordinated Si shows a very interesting feature: The geometries of SiN_4, Si-Si-N_3 and Si-SiN_2)-Si induce an interesting electron states near the conduction band minimum and even in the gap; the states are distributed in the backyard of the 4-folded coordinated Si, floating in the interstitial region of the material (*floating states*). Upon hydrogenation, the under- and over-coordinated point defects are passivated, but these floating states survive and generate gap states. The calculated Kohn-Sham orbitals in hydrogenated amorphous are shown in Figure. An important thing which we have found is that such gap state captures and emits an electron without any bond reconstruction, indicating the reversible capture and emission, in other words, the durable read and write process. We argue this floating state guarantees the function of current flash memories.

(The group id for this work is k0042)

in collaboration with Kenji Shiraishi, Mauro Boero and other young students.

*Present address: CIES, Tohoku University

Related publications

[1] S. Hattori, A. Oshiyama, and K. Shiraishi, Appl. Phys. Lett. **125**, 161601 (2024).

[2] Y. Zhao, A. Oshiyama and K. Shiraishi, Appl. Phys. Exp. submitted (2025).

[3] Y. Zhao, K. Shiraishi, T. Narita, and A. Oshiyama, Phys. Rev. B **110**, L081201 (2024).

[4] M. Boero, K. Shiraishi, T. Nagahashi, F. Nanataki, and A. Oshiyama, Phys. Rev. Mat., submitted (2025)

Analyses on electronic structure and magnetic anisotropy in high-performance spintronics magnetic materials and parallelization development/application in quasi-particle self-consistent *GW*

Tatsuki ODA[1,2], Rinku MAJUMDER[2], Jakub LUTSINEC[2], Akatov ARTUR[2], Takumi KATSUTA[2], Haruya Niwa[2], Hikaru Yamaguchi[2], Masao OBATA[1,2]

[1]*Institute of Science and Engineering, Kanazawa University, Kanazawa, Ishikawa 920-1192*

[2]*Graduate School of Natural Science and Technology, Kanazawa University, Kanazawa, Ishikawa, 920-1192*

We have studied electronic structure in several systems of non-magnetic or magnetic material by means of the density functional theory (DFT) or the quasi-particles self-consistent *GW* (QSGW) [1]. Concerned with the latter calculation, we have successfully optimized the time-consuming parts in the code for reducing the computational time. We have also developed the evaluation scheme in the calculation of magnetic anisotropy energy (MAE) in the density functional theory (DFT) code.

(A) MAE in the alloy containing heavy elements

Promising candidates for recording media, such as FePt alloys, have large magnetic anisotropy energy. This calculation aims to analyze the origin of MAE in a multilayer system of Pt/Fe/Pt. For this aim, in addition to a procedure of direct total energy calculation, the analysis for seeking the origins of anisotropy has been required. We have developed a new approach of force theorem method.

(B) Halide perovskites by QSGW

Halide perovskites are attracting attention because their bandgap and optical properties can be adjusted by varying the halogen composition. The present case is an application to $CH_3NH_3PbI_3$ and analyze its optical properties. Additionally, we investigated the effects of spin-orbit interaction (SOI) and structural changes on both the electronic states and several optical spectra using the exchange-correlation potential obtained from the QSGW calculations.

(C) Transparent superconductor by QSGW

Transition-metal-oxide $LiTi_2O_4$ is one of transparent superconductor and it is only superconductor in spinel oxides. Until now, the approach from the density functional theory (DFT) has revealed its electronic structures and provided frameworks to its superconductivity. The present calculation investigated its electronic states using the QSGW. The resulting one-particle electronic structure is nicely consistent with the transparency for visible light observed in the optical measurement. We investigate the spectra of electron energy loss spectroscopy as well as the optical spectra obtained from the dielectric polarization function. As a result, the former indicates a strong quasi-plasmon peak in the low frequency range [2].

(D) Fe_3X (X=Pd, Pt) by QSGW

We investigated electronic structures and generalized susceptibilities in cubic Fe_3X (X=Pd, Pt) alloys [3]. These systems are well known as magnetic shape memory alloy. Compared with those of the DFT method with generalized gradient approximation, the energy band structure indicates both an energy level shift to the high energy side and a narrow bandwidth in the minority-spin state. Employing the rigid band approximation, the profile of generalized susceptibility was found to indicate the peak positions at some modulation vectors. These modulations may be assigned to the instability of the cubic symmetry phase in the martensitic phase transition observed in the experiment.

(E) Ni_2MnX (X=Al, Mn, In) by QSGW

According to the QSGW, our group has found the Ni e_g orbitals appear just on the Fermi level in the cubic (austenite) phase of Ni_2MnX [4]. This appearance could be lead to martensite phase transition combined by the band Jahn-Teller effect. We investigated the electronic structures of Ni2MnX (X=Al, Ga, In) series using the QSGW [4]. Their narrow bandwidth appearing at the Fermi level in the minority-spin state has not been reproduced by the approaches of DFT and DFT+U methods.

(F) Migration of twin boundary

Migration of the twin boundary in a modulated martensite phase of the magnetic shape memory alloy Ni_2MnGa is significant to understand the magnetic shape memory effects. This work explored the migration mechanism of the nano-twin boundaries among the layers by first-principles calculations. We systematically analyzed intermediate structures throughout the migration path using the DFT approach [5]. We identified some key factors using the systems of 10M and 14M modulated phases. As a result, we obtained a concise barrier energy formula as empirical one. The resulting energy for barriers was found to be enough so low as a permission of the transition by the thermal energy.

References

[1] T. Kotani, J. Phys. Soc. Jpn. **83**, 094711 (2014); *ecalj*: https://github.com/tkotani/ecalj/.

[2] T. Oda *et al.*, submitted in the conference, SCES 2025.

[3] A. Akatov *et al.*, Sci. Rep. Kanazawa Univ. **68**, 83 (2025).

[4] J. Luštinec *et al.*, J. Magn. Soc. Jpn. **48**, 94 (2024).

[5] R. Majumder *et al.*, accepted in the proceedings CCP2023.

Development of Ceramic Protective Coating to Suppress Corrosion and Hydrogen Embrittlement of Metallic Materials

Yuji Kunisada
Center for Advanced Research of Energy and Materials, Faculty of Engineering,
Hokkaido University, Sapporo, Hokkaido 060-8628

In order to develop efficient hydrogen permeation barriers, we investigated the formation energies and diffusion properties of hydrogen impurities in the vicinity of the cationic dopants and interfaces between different ceramic materials,[1] with the aid of the first-principles calculation based on the density functional theory (DFT). We also investigated the behaviors of hydrogen impurities at the interface between ceramic and metallic materials.

We investigated the formation energies and diffusion barriers of hydrogen impurities near the cationic dopants in the α-Al_2O_3 and α-Al_2O_3/α-Cr_2O_3 interface using The Vienna Ab initio Simulation Package (VASP). We installed a parallelized VASP with Intel® MPI Library and Intel® Math Kernel Library. We found that hydrogen impurities can form chemical bonds with coordinated oxygen atoms near transition metal dopants in α-Al_2O_3. Such chemical bonds can be observed at the stable sites in the α-Al_2O_3 region as well as in the α-Cr_2O_3 region. Those are because transition metal cations near hydrogen impurities can stably accept excess electrons associated with forming OH bonds.[2] The range in which this stabilization of hydrogen impurities occurs depends on the element of transition metal cation and varies from a few to 15 Å. Therefore, dilute transition metal cation dopants can affect the stability of hydrogen impurities.

We also investigated the behaviors of hydrogen impurities at the interface between ceramic and metallic materials. The behaviors of hydrogen impurities at the interface between ceramics and metallic materials significantly affect the diffusion properties of hydrogen impurities and the exfoliation properties of ceramic coating films. We considered α-Al_2O_3/Fe interfaces. Since the α-Al_2O_3/Fe interface is incommensurate, we revealed that the formation energies of hydrogen impurities vary depending on its site. We also found that hydrogen impurities are more stable in the interface region than in the bulk region.

References

[1] Y. Kunisada, R. Sano, N. Sakaguchi, Int. J. Hydrog. Energy 97 (2025) 1327.

[2] T. Watanabe, Y. Kunisada, N. Sakaguchi, ChemPhysChem 20 (2019) 1369.

First-principles study on electron transport properties of heterostacking of graphene and graphitic carbon nitride

Yoshiyuki EGAMI
Division of Applied Physics, Faculty of Engineering, Hokkaido University
Kita 13, Nishi 8, Kita-ku, Sapporo, Hokkaido 060-8628

Graphene, a typical two-dimensional material, is expected to find a wide range of applications because of its outstanding electrical conductivity, thermal conductivity, and mechanical strength. To apply graphene to electronic and optical devices, a great deal of effort has been devoted to the development of techniques to widen its band gap. Although graphene has many potential applications, the optimum band gap size for each application is often different. Therefore, research into methods that can adjust the band gap after synthesis is highly desirable.

In this study, we investigated the electronic transport properties of heterostructures composed of atomic layer materials. Specifically, we aimed to modulate the electronic structure and transport properties of heterostructures formed by van der Waals stacking (heterostacking) with graphene and graphitic carbon nitride using first principles calculations. First-principles simulations were carried out using the "RSPACE" code based on the real-space finite-difference formalism[1, 2]. Our goal is to design semiconductor materials with low effective mass and tunable band gap in the range of about 0.2 eV to 1.0 eV using graphene and carbon nitride heterostacking. As a method of tuning, the application of an external electric field and mechanical pressure are considered, and the resulting changes in electronic structure and transport properties are simulated.

First, in graphene/C_3N heterostacking, it was found that simple stacking alone has little effect on the respective band structures. However, by applying pressure and an electric field perpendicular to the layers, the band gap size could be continuously controlled in the range of about 0.01 eV to 0.4 eV, while maintaining the small effective mass derived from graphene. On the other hand, in graphene/C_3N_4 heterostacking, continuous bandgap control from about 0.01 eV to 0.75 eV was shown to be possible by simply applying pressure. Furthermore, electron transport calculations reveal that in the AA-stacking model, the applied pressure causes reflection of incident electrons within the heterostructure region, which significantly affects the electron transmission probability and can even lead to a completely OFF state.

References

[1] K. Hirose *et al.*: First-principles calculations in real-space formalism (Imperial College Press, 2005).

[2] Y. Egami, S. Tsukamoto and T. Ono: Phys. Rev. Res. **3**, 013038 (2021).

Molecular dynamics simulations of thermal diffusion field around laser irradiated nanoparticle with LSPR electric field

Kiyoto KAWAI[1], Hiroki GONOME[1]

[1]*Graduate School of Science and Engineering,*

Yamagata University, Jonan, Yonezawa, Yamagata 992-8510

Plasmonic nanoparticles (NPs) have attracted enormous attention because of their unique optical, chemical, electric, and catalytic properties. They have been widely applied in various fields including plasmonics, sensing, catalysis, and biomedical fields [1]. For these applications, detailed thermal reaction properties of NPs are important to optimized design. In this study, we evaluate the thermal diffusion field around laser irradiated Au NP by using molecular dynamics simulations. The laser absorbance was set as 1.92 eV/ps on NP. The electric field (EF) distribution was pre-calculated by COMSOL Multiphysics and applied as no EF, static EF, and cyclic EF conditions. Figure 1 shows orientation distribution of water molecules. In the static EF case, weak crystallization of water molecules occurred and enhanced thermal diffusion in water solvent. Figure 2 shows the energy difference between translation and rotation energy of water molecules. In the case of cyclic EF case, the energy difference was smaller than other cases. It suggests the cyclic EF promote conversion translation energy to rotation energy of water molecules. The thermal diffusion in cyclic EF case was enhanced because the rotation motion has more contribution to thermal diffusivity in water solvent than translation motion.

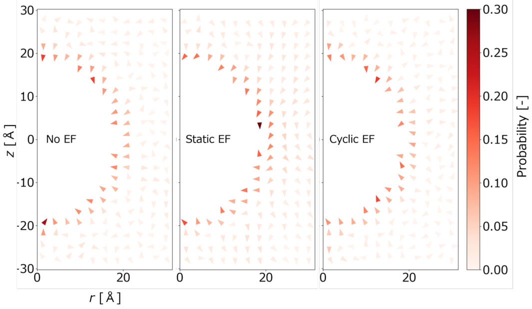

Fig. 1: Orientation of water molecules.

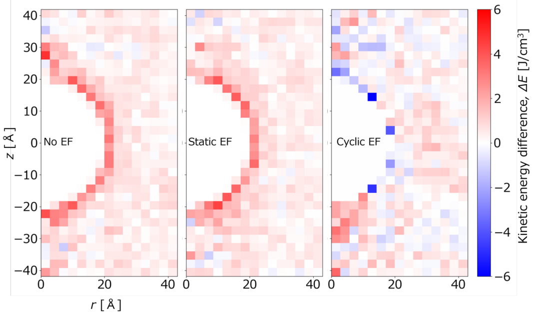

Fig. 2: Kinetic energy difference between translation and rotation of water molecules.

References

[1] J. E. Park, M. Kim, J. Hwang, and J. Nam, Small methods, **1**, 1600032 (2017).

First-principles study of mechanical properties on alloys

Naoki UEMURA

Department of Mechanical and Electrical Systems Engineering,
Faculty of Engineering, Kyoto University of Advanced Science,
18, Yamanouchi-Gotandacho, Ukyo-word, Kyoto, 615-8577

We have studied magnesium alloys with long-period stacking ordered (LPSO) structures by performing first-principles calculations based on density functional theory (DFT) using the VASP code. As a representative material of LPSO-Mg alloys, we calculated the generalized stacking fault energy (GSFE) on the basal and prismatic planes of Mg-Zn-Y alloys with LPSO structure [1]. This year, we investigated the dependence of the GSFE of Mg–Zn–Y with LPSO structure on normal strain and found that the GSFE on the prismatic plane is more sensitive to normal strain than the basal plane [2].

Following the approach proposed by Ogata *et al.* [3], in which the maximum derivative of the GSFE curve is defined as the ideal shear strength, we estimated the ideal shear strengths of both hcp-Mg and the 10H LPSO structure in Mg–Zn–Y alloys based on the tangent at the first inflection point of their respective GSFE curves (Fig. 1). Considering the presence of solute clusters in the LPSO structure, it is reasonable to assume that the ideal shear strength of LPSO is slightly higher than that of hcp-Mg. Experimentally, uniaxial micro-compression and nanoindentation tests along the [0001] axis of single-crystal magnesium have reported stress values ranging from 600 to 1200 MPa [4]. In micropillar tests of single-crystalline 18H LPSO in Mg–Zn–Y alloys, the stress at the first pop-in event was reported to be 750 MPa [5]. Although the ideal shear strength does not account for the nucleation of dislocations, interfaces, or defects and is therefore higher than the experimental values, it serves as an upper limit for the material's intrinsic strength.

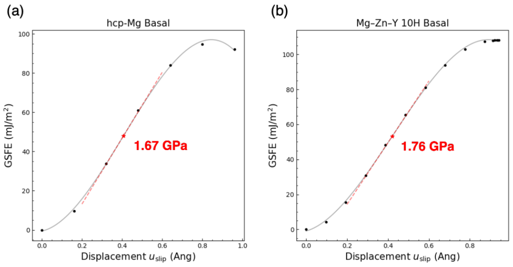

Fig. 1: Ideal shear strengths estimated from the GSFE curves of (a) hcp-Mg and (b) 10H LPSO.

References

[1] N. Uemura *et al.*, Mater. Trans. **65** 1080 (2024).

[2] N. Uemura *et al.*, in preparation.

[3] S. Ogata *et al.*, Science **298** 807 (2002).

[4] S. L. Shang *et al.*, Acta. Mater. **67** 168 (2014).

[5] W. S. Chuang *et al.*, J. Alloys Compd. **772** 288 (2019).

Analysis of defect structures and ion migration using first-principles calculations and machine learning

Koji SHIMIZU
Research Center for Computational Design of Advanced Functional Materials,
National Institute of Advanced Industrial Science and Technology, Umezono, Tsukuba,
Ibaraki 305-8568

Understanding the correlation between local structures, including defects, and ion conduction mechanisms in solid electrolytes is essential for advancing all-solid-state battery development. Despite advances in computational techniques and resources enabling the study of more complex models, first-principles calculations based on density functional theory (DFT) remain computationally expensive, which limits large-scale analyses. Machine learning potentials (MLPs) trained on first-principles data offer a promising approach to balance accuracy and computational efficiency.

The author has applied MLPs to investigate the structure and lithium-ion conduction properties of crystalline, glassy, and crystallized glass forms of Li_3PS_4 [1]. This project explores the impact of additive incorporation on the solid electrolyte properties of Li_3PS_4. A diverse set of atomic configurations was generated, and a DFT-based training dataset was constructed. An equivariant graph neural network potential [2] was employed to train the MLP, enabling molecular dynamics (MD) simulations.

Additionally, the author studied the effects of hydrogen incorporation on the fracture behavior of aluminum during tensile MD simulations, revealing hydrogen segregation near grain boundaries and its role in strength degradation and fracture [3]. To explore high-entropy alloys as potential catalysts, a ML model was developed to predict the adsorption energies of hydrogen and carbon monoxide on cluster alloys with various compositions and geometries, demonstrating their potential for catalytic applications through high-throughput screening [4].

References

[1] K. Shimizu, P. Bahuguna, S. Mori, A. Hayashi, and S. Watanabe, J. Phys. Chem. C **128**, 10139 (2024).

[2] Y. Park, J. Kim, S. Hwang, and S. Han. J. Chem. Theory Comput. **20**, 4857 (2024).

[3] Y. Liu, K. Shimizu, and S. Watanabe, submitted.

[4] K. Miyamoto, K. Shimizu, A.K.A. Lu, and S. Watanabe, e-J. Surf. Sci. Nanotechnol. Accepted.

Numerical evaluation of the effect of twist angle on phonon hydrodynamics in twisted 2D materials

Xu Bin

Department of Mechanical Engineering,

The University of Tokyo, 7-3-1, Hongo, Bunkyo-ku, Tokyo 113-8656

Two-dimensional materials, particularly transition metal dichalcogenides (TMDs), are widely used in electronics, photonics, and thermoelectrics due to their exceptional physical and chemical properties. Recently, stacked 2D materials with slight twist angles have shown unique properties, but the effect of twist angle on interfacial thermal conductance remains unclear. Although some simulation studies suggest that thermal conductivity decreases as the twist angle increases, experimental verification is lacking. Therefore, this study aims to systematically investigate the impact of twist angle on thermal conduction in bilayer TMDs through time-domain thermoreflectance (TDTR) experiments and molecular dynamics simulations, providing theoretical support for the design of thermoelectric materials and thermal management systems.

As shown in Fig.1, We employed the TDTR technique to measure the interlayer thermal conductance (TC) of twisted bilayer TMDs ($MoS_2$and WS_2) with varying twist angles. The samples were fabricated using a sequential pick-up method to ensure clean interfaces, and the twist angle was precisely controlled. The TDTR measurements revealed a significant decrease in thermal conductance as the twist angle increased,

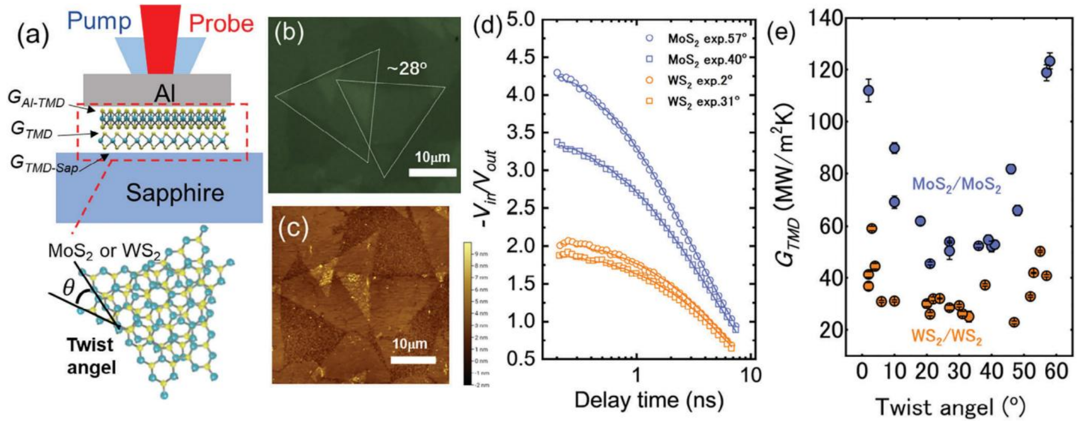

Figure 1. Time-domain thermoreflectance (TDTR) measurement for measuring thermal conductance (TC) of twisted bilayer TMD. a) Schematic of the TDTR system and sample. b) Optical microscopy and c) AFM images of twisted bilayer MoS_2 with a twist angle of 28°. d) Representative temperature decay profile (–Vin/Vout) of twisted bilayer MoS_2 and WS_2. e) TC between bilayers MoS_2 and WS_2 $(\mathrm{G_{TMD}})$ under different twist angles.

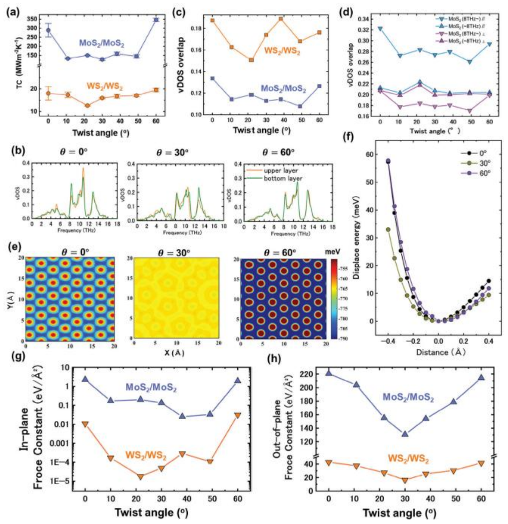

Figure 2. MD simulations of interfacial heat conduction in twisted bilayer TMDs. a) Thermal conductance (TC) of MoS_2 and WS_2 bilayers at different twist angles. b) vDOS of the upper and bottom layers in twisted MoS_2 bilayers. c) vDOS overlap of upper and bottom layers in WS_2 and MoS_2. d) vDOS overlap in low (≈8 THz) and high (8 THz~) frequency ranges for in-plane (//) and out-of-plane (⊥) directions. e) Displacement energy of twisted MoS_2 along in-plane and f) out-of-plane directions. g) Second-order force constant of MoS_2 and WS_2 along in-plane and h) out-of-plane directions across twist angles from 0° to 60°.

with a more pronounced variation observed in MoS_2 compared to WS_2. These experimental findings provided the first direct evidence of twist-angle dependence on TC in bilayer TMDs

Figure 2 investigates the relationship between twist angle and interfacial thermal conductance through molecular dynamics (MD) simulations. The simulation results show that thermal conductance decreases as the twist angle increases, with a more significant variation observed in MoS2, which aligns with the experimental findings. By analyzing the vibrational density of states (vDOS) and interlayer interactions, the study reveals that interfacial heat conduction is closely related to the overlap of interlayer interactions and vibrational frequencies. The simulations further show that the changes in vDOS due to atomic reconstruction in the twisted structure are a key factor affecting thermal conductance.

Reference

[1] B. Xu, M. An, S. Masubuchi, Y. Li, R. Guo, T. Machida, and J. Shiomi, Heat conduction modulation in incommensurate twisted stacking of transition-metal dichalcogenide, Adv. Funct. Materials, 2422761 (2025)

First-principles calculation of optical control on semiconductor transport properties

Shunsuke A. Sato

Department of Physics, Tohoku University, Sendai 980-8578, Japan

We have studied light-induced electron dynamics in semiconductors based on microscopic calculations grounded in quantum mechanics. For this study, we employed two theoretical frameworks. The first is first-principles electron dynamics calculations based on time-dependent density functional theory (TDDFT) [1]. Practical calculations were performed using the SALMON code [2] and the Octopus code [3]. The second method is the quantum master equation approach with a tight-binding Hamiltonian, for which we employed a home-made code [4].

In addition to applications in attosecond science of transition metal dichalcogenides [5], we used first-principles calculations to study the transport properties of bulk silicon in the THz regime under the presence of MIR laser fields. For this purpose, we employed the Wigner distributions of ions to account for phonon scattering contributions through an ab initio approach [6]. Based on this approach, we can investigate the transient optical and transport properties of silicon with phonon-assisted indirect gap transitions. As a result of these calculations, we computed the light-induced anomalous Hall effect in silicon. Currently, we are investigating the microscopic origin of this phenomenon.

Using the quantum master equation approach, we have also investigated light-induced electron dynamics in GaAs, a prototypical wide-gap semiconductor. Based on pump-probe simulations employing two light pulses, we found that the optical and transport properties of GaAs are significantly affected by the coupling between intra- and interband transitions. While the contributions from solely intraband and interband transitions have been investigated separately, the effects of their coupling remain to be clarified. We are currently conducting a microscopic analysis of the induced transient optical and transport properties based on this coupling.

These studies are expected to provide a fundamental understanding of the optical and transport properties of semiconductors in nonequilibrium regimes, advancing technological applications toward optoelectronic devices.

References

[1] Erich Runge and E. K. U. Gross, Phys. Rev. Lett. 52, 997 (1984).

[2] M. Noda, et al., Comput. Phys. Commun. 235, 356 (2019).

[3] N. Tancogne-Dejean, et al., J. Chem. Phys. 152, 124119 (2020)

[4]https://github.com/shunsuke-sato/tight_binding_spds

[5] A. Zong, et al., arXiv:2407.00772 [cond-mat.str-el]

[6] K. Lively, S. A. Sato, G. Albareda, A. Rubio, Aaron Kelly, Phys. Rev. Research 6, 013069 (2024)

Exploration of Stable Structure in $K_2NdTa_5O_{15}$ using First-Principles Phonon Calculations

Hodaka ABE, Sou YASUHARA

School of Materials and Chemical Technology,

Institute of Science Tokyo, Ookayama, Meguroku, Tokyo 152-8550

Antiferroelectrics are promising materials for the next-generation ceramics capacitors because they can exhibit high ε_r under high electric fields due to a field-induced antipolar-to-polar phase transition. Here, we focused on antiferroelectric $K_2NdM_5O_{15}$ (M=Nb^{5+}, Ta^{5+}), which exhibit relatively high permittivity ε_r~800. We have experimentally demonstrated that controlling the Nb/Ta ratio is effective in shifting the phase transition temperature and stabilising the antiferroelectric phase around room temperature, but the microscopic mechanism is still unclear. To elucidate key factors determining the modulation of phase stability by changing the Nb/Ta ratio, we derived the stable structure of $K_2NdTa_5O_{15}$ based on first-principles phonon calculations and compared it with that of $K_2NdNb_5O_{15}$.

In this study, VASP and Phonopy codes were used for density functional calculations and finite difference phonon calculations, respectively. To deduce phase transition pathway from the high-symmetry structure, we first calculated phonon dispersion of $K_2NdTa_5O_{15}$ with the aristotype $P4/mbm$ structure (Fig.1(a)). Stable structure exploration was carried out by performing structural relaxation for low-symmetry structures with displacements along phonon modes with imaginary frequencies.

Figure 1(b) shows the stable structure of $K_2NdTa_5O_{15}$ derived from the phonon calculations. While $K_2NdNb_5O_{15}$ has two types of structural distortion, NbO_6 octahedral tilting distortion and antipolar distortion due to intraoctahedral displacement of Nb, the stable structure of $K_2NdTa_5O_{15}$ has only tilting distortion of TaO_6 octahedra and the antipolar distortion is inactivated. Suppression of the second order Jahn-Teller effect in the Ta system with higher d-level is thought to have caused a such change in the stable structure.

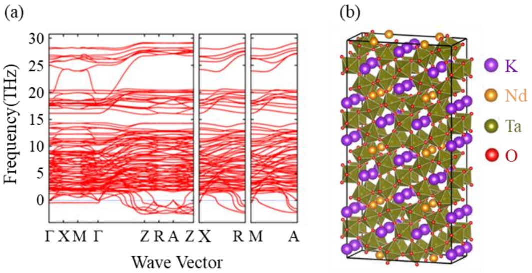

Fig.1 (a) Phonon dispersion curves of $K_2NdTa_5O_{15}$ with the aristotype $P4/mbm$ structure. (b) The stable structure of $K_2NdTa_5O_{15}$ derived from phonon calculations.

References

[1] H. Abe, S. Yasuhara, T. Tsurumi and T. Hoshina: J. Ceram. Soc. Jpn. **131**[7], 189(2023)

Investigation on single ion motions for a polarization switching in a wurtzite-type $LiGaO_2$

Sou YASUHARA

School of Materials and Chemical Technology,

Institute of Science Tokyo, Ookayama, Meguroku, Tokyo 152-8550

A wurtzite-type materials have gathered much attention since a discovery of ferroelectricity in a wurtzite-type structure of Sc doped AlN in 2019[1]. Exploring new wurtzite-type materials is essential for understanding polarization switching mechanisms. We now focus on $LiGaO_2$ with a distorted wurtzite-type structure, which distortion is originated from a difference of ionic radii between Li^+ and Ga^{3+}. In this study, we carried out first principles calculations for evaluating a polarization switching in $LiGaO_2$ focusing on single ion motions during a polarization switching.

The density functional theory calculations were carried out using the projector augmented wave method as implemented in the VASP. The modified Predew-Burke-Ernzerhof generalized gradient approximation was utilized as an exchange correlation functional. The k-point mesh was 8×8×8. The cutoff energy and convergence energy were 550 eV and 1.0×10^{-7} eV, respectively. The formation energy of $LiGaO_2$ with structural modifications of Li or Ga ion sites was calculated. Li or Ga positions were altered from -0.15 to 0.15 in the atomic position of $LiGaO_2$ structure.

A calculation result as a color map is shown in Fig. 1. As a result, a case of opposite polarization state of Li and Ga ions were unstable. In addition, a promising way to the polarization switching is that both Li and Ga ions move at the same time. We further carried out an evaluation of a Li or Ga motion in a super cell structure (2 x 2 x 1). The energy difference during the movements of Ga and Li were 0.42 eV/f.u. and 0.26 eV/f.u., respectively. This result indicates that single cation movements are less favor for the polarization switching in $LiGaO_2$.

References

[1] S. Fichtner, N. Wolff, F. Lofink, L. Kienle, and B. Wagner, J. Appl. Phys. **125**, 114103 (2019).

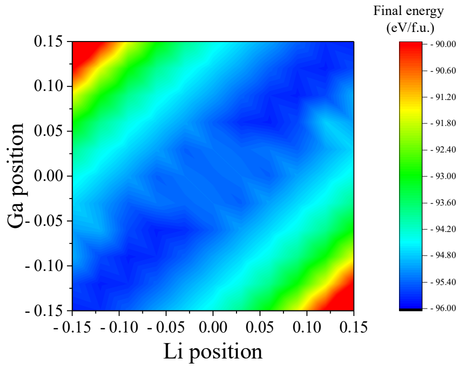

Fig. 1 A color map of calculation results of final energy in $LiGaO_2$ as a function of Ga/Li position.

First-Principles Molecular-Dynamics Study of Structural and Electronic Properties of Disordered Materials under Extreme Conditions

Fuyuki SHIMOJO

Department of Physics, Kumamoto University, Kumamoto 860-8555

Since disordered materials do not exhibit long-range order as observed in crystals, simulations with larger system sizes are required to investigate their static and dynamic properties. For this purpose, machine-learning interatomic potentials (MLIPs) based on artificial neural networks trained on accurate first-principles molecular dynamics (MD) data are useful.

We have developed a method using a robust MLIP that enables stable MD simulations for systems of tens of thousands of atoms under high-temperature and high-pressure conditions for highly covalent materials [1]. In the present study, we apply this method to SiO_2 glass under decompression to simulate the transformation from the sixfold- to fourfold-coordinated structures, which is accompanied by permanent densification. A system consisting of about 30,000 atoms was simulated from 60 to 0 GPa at room temperature with the MLIP. The calculations were performed in steps of 5 GPa down to 20 GPa, and then in steps of 2 GPa thereafter. The simulation time for each pressure was longer than 10 ps. At 14 GPa, where the transformation occurred most significantly, the calculation was extended to 2.7 ns. Figure 1 shows the calculated pressure dependence of the coordination number for Si. A drastic change in the coordination number is observed between 16 and 10 GPa. These results indicate that the MLIP successfully reproduces the structural transformation in SiO_2 glass. The transformation was found to proceed via a relatively unstable fivefold-coordinated state, and the fourfold-coordinated phase grows logarithmically with time.

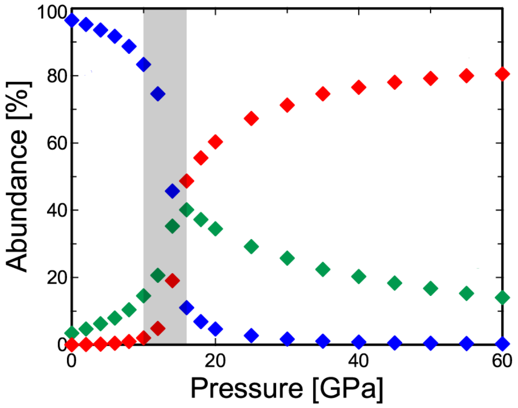

Fig. 1: Pressure dependence of calculation results for distribution of coordination number for Si. The blue, green, and red symbols represent the abundance of fourfold-, fivefold-, and sixfold-coordinated Si atoms, respectively.

References

[1] D. Wakabayashi et al., J. Phys. Soc. Jpn. **92**, 074002 (2023).

GW + BSE photoabsorption spectra of transition metal doped TiO_2 and excited-state TD*GW*-MD simulation of CH_4 + Ni

Kaoru OHNO

Yokohama National University, Tokiwadai, Hodogaya-ku, Yokohama 240-8501

To explore quasiparticle (QP) energy gaps and photoabsorption spectra of rutile TiO_2 with nonmagnetic transition metal (Zr, Mo, Zn, Cd) impurities, we conducted a Γ-point only *GW* + Bethe–Salpeter equation (BSE) calculation on a 72 (or 71) atom supercell using our all-electron mixed basis program, TOMBO [1]. Zn and Cd impurities must coexist with oxygen vacancy to maintain charge neutrality. Mo, Zn, or Cd doped rutile TiO_2 exhibits optical absorption and catalytic activity under visible light (Fig. 1). The resulting QP energy gaps and photoabsorption energies are fairly in good agreement with experimental and theoretical data currently available. As the most important condition for the applicability of the Γ-point only approach in the *GW* + BSE frame-work is that the Γ-point only *GW* calculation should reproduce a reasonable band gap.

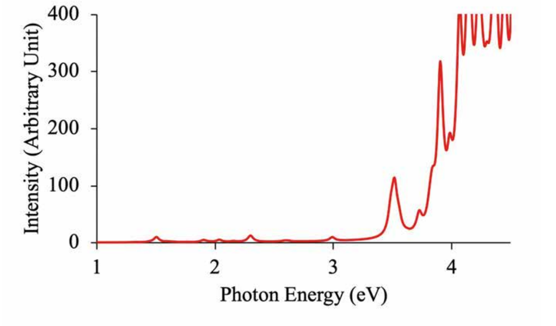

Fig. 1 Photoabsorption Spectra of Mo-doped TiO_2

We have also performed excited-state time-dependent *GW* (TD*GW*) molecular dynamics simulation for the photolysis of CH_4 + Ni using TOMBO [2]. We demonstrated that only the H ejection away from the Ni side (Fig. 2) facilitates the formation of a hydrogen molecule with the quasiparticle level corresponding to it having an energy close to the negative ionization potential of an isolated H_2 molecule. This is achieved at a PAE of 8.4 eV which is lower compared to 10.2 eV of pristine methane without Ni [3].

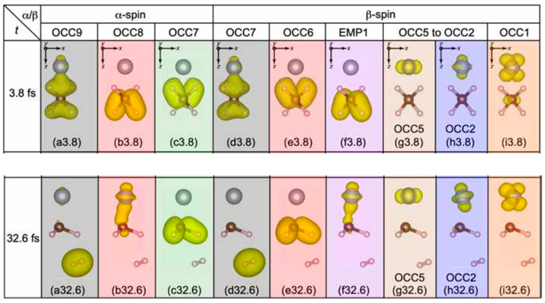

Fig. 2 Density $|\varphi|^2$ of QP levels at 3.8 fs and 32.8 fs.

References

[1] K. Ohno, R. Sahara, T. Nanri, and Y. Kawazoe, Comput. Cond. Matter **41**, e00977 (2024).

[2] A. Manjanath, R. Sahara, Y. Kawazoe, and K. Ohno, Nanomaterials, **14**, 1775 (2024).

[3] A. Manjanath, R. Sahara, K. Ohno, and Y. Kawazoe, J. Chem. Phys. **160**, 184102 (2024).

Understanding Fast Ion Conduction in Inhomogeneous Materials

Shusuke KASAMATSU
Academic Assembly (Faculty of Science),
Yamagata University, Kojirakawa, Yamagata-shi, Yamagata 990-8560

Functional materials including glasses, solid solutions, and their interfaces contain many types of inhomogeneities at the nanoscale that contribute to their performance in various applications. However, quantifying such inhomogeneities from experiments is often challenging because of the lack of nanoscale probes that can characterize local atomistic environments. First-principles quantification of such systems is also often intractable due to limitations in simulation time or the number of configurations that can be calculated within a reasonable amount of time. To overcome this limitation, we have been employing machine learning surrogate models to speed up first-principles calculations. Here, we report examination of (a) intermediate-range order/disorder in the prototypical network glass system GeO_2, and (b) dopant order/disorder in heavily doped perovskite oxides and its impact on proton conduction.

(a) Intermediate range order in GeO_2 glass [1]-- The atomistic structure of glasses have been of fundamental interest for over a century; although short-range order has often been clarified as being similar to crystalline motifs, intermediate-range order whose existence is implied by small-wavevector diffraction peaks is yet to be unambiguously characterized in real space. Although reverse Monte Carlo (RMC) fitting of diffraction data is often used to construct three-dimensional models, its reliability is sometimes questionable because diffraction data only contains two-body correlations which are not enough to fix the three-dimensional structure. Here, we performed melt-quench simulations in a 3240-atom cell using a neural network potential trained on first-principles data to construct a model of vitreous GeO_2. The structure factor calculated from the obtained model is in good agreement with experiment. Intermediate-range features were characterized using ring distributions and persistent homology, and it was found that the simulated model shows a stronger ordering compared to that obtained by RMC modeling. That is, the underlying density functional approximation in first-principles calculations determines the preferred network assembly more strictly than conventional RMC modeling, even when multiple diffraction data is used in the fitting. This shows the promise and necessity of simulations using machine learning potential based on first-principles data for accurate determination of the glass structure and its physical properties.

(b) Proton conduction in heavily Sc-doped $BaZrO_3$ [2]--Acceptor-doped perovskite oxides are of interest for application in proton ceramic fuel cells. Acceptor doping is necessary for the introduction of protons into the material, but it has been observed that increased doping leads to a decline in the proton conductivity. This is often explained by trapping of protons by the dopant. However, it was recently discovered that Sc doping leads to continuous conductivity increase up to the solubility limit of ~60 atomic percent. Here we performed Monte Carlo simulation using our abICS code to determine the Sc configuration in the material, followed by molecular dynamics simulation to explain how the detrimental effect of proton trapping is avoided. As seen in Fig. 1, our simulations revealed that a conduction path along the network of Sc dopants is formed, enabling long-range diffusion without detrapping from the dopant.

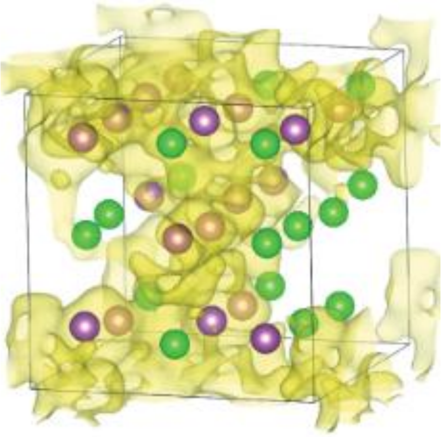

Fig. 1: Proton concentration isosurface in Sc-doped $BaZrO_3$. The Sc and Zr atoms are shown as purple and green spheres, and Ba and O atoms are omitted for clarity. From Ref. [1], reproduced under CC-BY 4.0 license.

References

[1] K. Matsutani et al., J. Chem. Phys. 161, 204103 (2024).

[2] S. Fujii et al., Sci. Technol. Adv. Mater. 25, 2416383 (2024).

Advancement of methods for predicting dielectric properties and structure exploration of materials

Shinji TSUNEYUKI
Department of Physics, The University of Tokyo
Hongo, Bunkyo-ku, Tokyo 113-0033

In preparation for developing electronic and communication devices for the 5G and beyond 5G era, it is necessary to understand and predict the dielectric properties of various materials, including crystals, amorphous materials, and polymers. In particular, the dielectric properties in the sub-terahertz to terahertz (THz) range have recently become possible to measure with high precision. However, these properties are difficult to understand due to the contribution of various physical phenomena such as electronic responses, anharmonic lattice vibrations, molecular rotation, molecular (and intermolecular) polarization, and structural relaxation. The strong anharmonic nature and slow relaxation also make computer simulations extremely challenging.

This study aims to develop and demonstrate the fundamental technology for structural simulation and first-principles simulation of permittivity of molecular materials including polymers which are technically more challenging and strongly demanded by industry. This year, we conducted (1) calculations of highly efficient permittivity calculation methods in the sub-terahertz to terahertz range for molecular liquids with complex structures, large thermal fluctuations, and slow relaxation and (2) data-assimilated structure exploration using X-ray diffraction data from materials composed of multiple crystals.

Permittivity of molecular liquids

The dielectric constant of liquids and polymer materials with large atomic displacements in the THz range can be calculated from the auto-correlation function of the system's dipole moments using molecular dynamics methods (MD). However, to determine the dielectric constant down to the sub-THz range, simulations lasting nanoseconds are required, and performing all of this using first-principles MD is extremely difficult from a cost perspective. On the other hand, fast classical MD using fixed charges cannot accurately evaluate dipole moments. To address this, we have developed a machine learning model of the Wannier center (MLWC), which represents the center of mass of electron distributions corresponding to chemical bonds and lone pairs, and have developed a method for calculating permittivity using this model.

This year, we applied this method to alcohol [1], propylene glycol, and its polymers [2] and demonstrated that it is possible to perform high-precision calculations of permittivity and light absorption coefficients in the sub-THz to THz range, including temperature dependence. For the latter, we successfully demonstrated the high transferability of the model by applying it to oligomers with higher polymerization degrees using a model learned from propylene glycol dimers.

Data assimilation structure exploration

Structure prediction using simulations has been helpful for discovering new crystals and studying amorphous and liquid materials, which are difficult to analyze by experiments. However, there are limitations due to the combinatorial explosion caused by increased atoms and the slowness of structural relaxation. To address these issues, we have developed a data-assimilated structural exploration method incorporating X-ray or neutron diffraction data into simulations to perform structural exploration efficiently. Since last year, we have been working on extending this method to cases where diffraction experimental samples contain multiple crystals, or prior estimation of lattice parameters is difficult.

This year, we confirmed that by applying the method in multiple stages, we can reproduce all crystal structures, even from powder XRD data containing three polymorphs of SiO_2 [3]. Among these three crystal phases is Coesite, which contains 48 atoms in the unit cell, demonstrating that data-assimilated structure exploration is effective for determining complex crystal structures.

References

[1] T. Amano, T. Yamazaki, and S. Tsuneyuki, Phys. Rev. B 110, 165159 (2024).

[2] T. Amano, T. Yamazaki, N. Matsumura, Y. Yoshimoto, S. Tsuneyuki, arXiv:2410.22718, to appear in Phys. Rev. B.

[3] Y. Kubo, R. Sato, Y. Zhao, T. Ishikawa, and S. Tsuneyuki, J. Chem. Phys. 161, 214113 (2024).

Design and Understanding of the Activity and Stability of Promising Electrocatalysis via Precise Catalysis Theory and AI

HAO LI

Advanced Institute for Materials Research (WPI-AIMR),
Tohoku University, Sendai, 980-8577

We have studied the development of new catalytic theories and ML-based models, as well as the design of effective catalysts for industrially significant reactions, by integrating precise theoretical models, high-level computations, machine learning (ML), and experimental validation.

This year, we utilized supercomputing resources to perform high-throughput density functional theory (DFT) calculations and machine-learning force field (MLFF)-accelerated molecular dynamics (MD) simulations to provide predictive insights into the activity and stability of electrocatalysts. This “theory-experiment-theory” cycle ensures that theoretical predictions not only guide experimental research but are also refined by experimental feedback, making it possible to identify catalyst materials with improved performance efficiently. Beyond this, to relieve the computational burden of DFT and AIMD, novel ML models are designed to learn from high-fidelity theoretical datasets and accurately predict energies and forces for new structures. Leveraging the synergy between physics-based insights and data-driven methods, we aim to develop catalysts that are not only highly active and cost-effective but also robust for long-term operation. Through this integrated approach, the work presented here outlines a path toward optimizing industrially significant electrocatalytic reactions and demonstrates the broader potential of combining fundamental theory with cutting-edge ML techniques.

During the project period, **46 papers** were published in leading journals, including JACS, Angew. Chem., Nature Commun., etc., under this ISSP supercomputer support. Some notable works will be discussed in the following:

1. Why Do Weak-Binding M–N–C Single-Atom Catalysts Possess Anomalously High Oxygen Reduction Activity? (JACS; Hao Li as the Last and Corresponding Author)

In this work, we integrated a pH-field coupled microkinetic model with detailed experimental electron state analyses to verify a novel key step in the oxygen reduction reaction (ORR) pathway of weak-binding SACs - the oxygen adsorption at the metal – nitrogen bridge site (**Fig. 1**). This step significantly altered the adsorption scaling relations, electric field responses, and solvation effects, further impacting the key kinetic reaction barrier from HOO* to O* and pH-dependent performance. Synchrotron spectra analysis further provides evidence for the new weak-binding M–N–C model, showing an increase in electron density on the antibonding π orbitals of N atoms in weak-binding M–N–C catalysts and confirming the presence of N–O bonds. These findings redefine the understanding of weak-binding M–N–C catalyst behavior, opening up new perspectives for their application in clean energy.

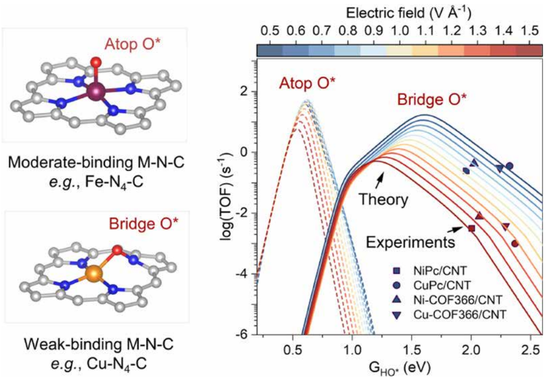

Fig. 1. A pH-field coupled microkinetic model with detailed experimental electron state analyses.

2. Hydrogen Binding Energy Is Insufficient for Describing Hydrogen Evolution on Single-Atom Catalysts (Angewandte Chemie; Hao Li as the Last and Corresponding Author)

We investigate the effects of HO*/O* poisoning and H* coverage on SACs with varied metal centers and coordination environments using pH-dependent surface Pourbaix diagrams at the reversible hydrogen electrode (RHE) scale and microkinetic modeling. Our findings reveal that HO* poisoning, realistic H* adsorption strengths at active metal sites, and the potential HER activity at the coordinating N-sites are crucial factors that should be considered for accurate descriptor development. Experimental validation using a series of M-phthalocyanine/CNT catalysts (M = Co, Ni, Cu) confirms the theoretical predictions, with excellent agreement in exchange current densities and the role of N-sites in Ni/Cu-phthalocyanine/CNT catalysts. This work provides answers to a long-lasting debate on HER descriptors by establishing ΔG_{H*} and ΔG_{HO*} as a combined HER descriptor for SACs (**Fig. 2**), offering new guidelines for catalyst design.

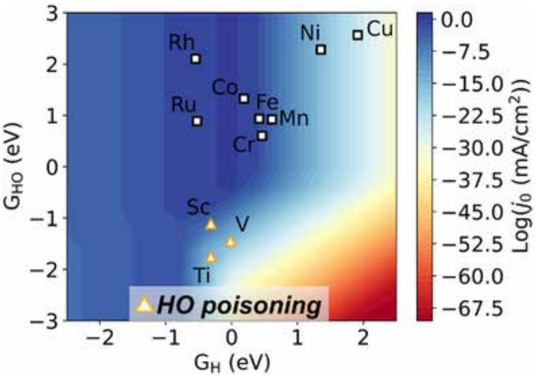

Figure 2. New microkinetic modeling predicts HER at M-N-C SACs.

References

[1] D. Zhang, F. She, J. Chen, L. Wei*, and H. Li*, J. Am. Chem. Soc. **147**, 6076–6086 (2025).

[2] S. Ye, F. Liu, F. She, J. Chen, D. Zhang, A. Kumatani, H. Shiku*, L. Wei*, and H. Li*, Angew. Chem. Int. Ed, e202425402 (2025).

Free-energy evaluation of alloys

Yoshihiro GOHDA
Department of Materials Science and Engineering, Institute of Science Tokyo
J2-22, Nagatsuta-cho 4259, Midori-ku, Yokohama 226-8501, Japan

Aiming construction of first-principles phase diagrams, we are trying to develop methods to evaluate free energies of metallic alloys. The free energy is decomposed into a few contributions, including the phonon effects and the configrational entropy as the most important ones. Moreover, other components and couplings among various contributions significantly affects phase equilibria, e.g., phase transition temperatures. Indeed, the spin-phonon coupling changes the Curie temperature of bcc Fe more than 500 K [1].

In this project, we developed a method to perform first-principles phonon calculations to evaluate Gibbs free energies efficiently [2]. In our volume integral of pressure (VIP) method, multiple phonon calculations with varying the volume are avoided in incorporating the effect of thermal expansion. This feature makes the Gibbs-energy evaluation possible for high-temperature austenite phases that is in general difficult for conventional volume-varied approaches, by combining the VIP method with the self-consistent phonon (SCPh) method [3] implementd in the ALAMODE code [4]. In applications to bcc Ti [2], we demonstrated that the electron-phonon coupling changes the austenite-martensite phase-transition tempearature more than 200 K as shown in Fig. 1. We also applied the VIP method to Ti-Al alloys that require huge computational costs.

Conventional CALPHAD approach largely relies on experimental data. In some cases, mixing enthalpies are additionally evaluated from first principles [5]. Evaluation of free energies from first principles should further expand possible range of Gibbs-energy database to experimentally unavailable cases. As one of approaches to achive the goal above, we also developed a method to include the spin-electron coupling in the evaluation of exchange-coupling parameters [6].

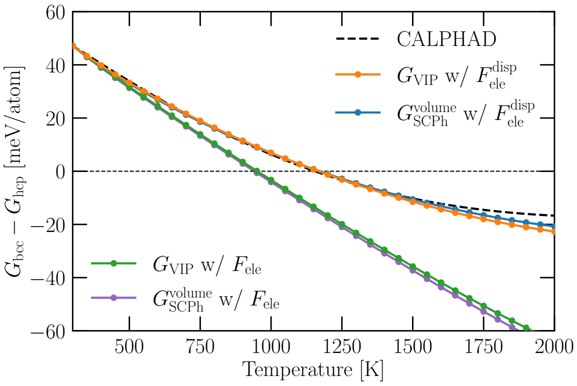

Figure 1: Difference in the Gibbs free energy between bcc and hcp Ti from 300 K to 2000 K. The origin of the DFT calculations is shifted to the CALPHAD data at 300 K, i.e., changes from 300 K are evaluated from first principles. Superscripts “disp” indicate that calculations include the electron-phonon coupling as effects of vibrational atomic displacements.

[1] T. Tanaka and Y. Gohda, npj Comput. Mater. **6**, 184 (2020).

[2] K. Hashimoto, T. Tanaka, and Y. Gohda, arXiv:2405.14823 (2024).

[3] T. Tadano and S. Tsuneyuki, Phys. Rev. B **92**, 054301 (2015).

[4] T. Tadano, Y. Gohda, and S. Tsuneyuki, J. Phys.: Condens. Matter **26**, 225402 (2014).

[5] S. Enomoto, S. Kou, T. Abe, and Y. Gohda, J. Alloys Compd. **950**, 169849 (2023).

[6] T. Tanaka and Y. Gohda, arXiv:2410.11256 (2024).

Development of the optimization method for the long-range correlation factor in the first-principles wave-function theory

Masayuki OCHI
Department of Physics, Osaka University
1-1 Machikaneyama-cho, Toyonaka, Osaka 560-0043

We have developed a first-principles electronic structure calculation software using the transcorrelated (TC) method [1, 2]. The TC method is a many-body wave function theory, where Hamiltonian is similarity-transformed with the Jastrow correlation factor. By this transformation, electron correlation effects are efficiently considered. In particular, one-electron orbitals in the Jastrow-Slater-type wave function can be optimized in the same manner as the Hartree–Fock (HF) method, to say, by solving a one-body self-consistent-field (SCF) equation. It is advantageous that the computational cost for this process is the same order as that for the HF method [3].

We have developed our computational code TC++, which was published on github [4, 5]. One can perform TC calculations using TC++ by reading some output files dumped by DFT calculation using the Quantum-Espresso package [6]. TC++ supports the following functionalities: HF, TC, and biorthogonal TC (BITC) calculations, SCF and band calculations, solids and homogeneous electron gas, a plane-wave-basis set, and norm-conserving pseudopotentials. Calculation is MPI-parallelized for the k-point and band indices.

In this year, we have implemented the interface between TC++ and first-principles quantum-Monte-Carlo code CASINO [7]. By using CASINO, one can optimize the Jastrow correlation factor using the variational Monte Carlo (VMC) method. TC++ can read the optimized Jastrow parameters, and then perform TC++ calculation using those parameters. At present, TC++ can deal with electron-electron Jastrow factors with the RPA-type and polynomial-type. By performing test calculations using ISSP supercomputers, we verified that (1) stable optimization of TC+VMC was achieved and (2) polynomial Jastrow factors improve the accuracy of calculated lattice constants.

References

[1] S. F. Boys and N. C. Handy, Proc. R. Soc. London Ser. A **309**, 209 (1969); *ibid.* **310**, 43 (1969); *ibid.* **310**, 63 (1969); *ibid.* **311**, 309 (1969).

[2] N. C. Handy, Mol. Phys. **21**, 817 (1971).

[3] M. Ochi, K. Sodeyama, R. Sakuma, and S. Tsuneyuki, J. Chem. Phys. **136**, 094108 (2012).

[4] https://github.com/masaochi/TC

[5] M. Ochi, Comput. Phys. Commun. **287**, 108687 (2023).

[6] https://www.quantum-espresso.org/

[7] https://vallico.net/casinoqmc/

First-principles materials design of perovskite semiconductors toward improving photocatalytic performance

Seiichiro L. TEN-NO
Graduate School of System Informatics, Kobe University
Rokkodai-Cho, Nada-Ku, Kobe 657-8501

Divalent cation doping into perovskite photocatalyst $SrTiO_3$ [1]

Perovskite oxide $SrTiO_3$ (STO) is a typical semiconductor photocatalyst for overall water splitting under ultraviolet. The defect control during synthesis is crucial for promoting photocatalytic activities as well as other photocatalysts. The recent experiment [2] shows that Al-doped STO (STO:Al) enables a quantum efficiency of almost unity in the ultraviolet range.

To achieve the materials design using efficient dopants for higher-performance photocatalysts, we have studied the electronic structure and formation energy of doped STO using the first-principles analysis based on the density functional theory (DFT). The supercell method is adopted to describe point defects including oxygen vacancy and substitutional doping, where several supercell models, namely, $2 \times 2 \times 3$, $2 \times 2 \times 4$, $3 \times 3 \times 3$, and $3 \times 3 \times 4$ supercell of the primitive cell of PTO, are considered to take into account the finite size effects. The DFT calculations were performed within the PBE+U functional using PAW method as implemented in VASP [3]. The Hubbard U was set to be $U = 4.36$ eV for the 3d orbitals at the Ti sites, which reproduces the relative position of defect levels to the valence and conduction band. We focus on the oxygen vacancy (V_O) and substitutional doping for the nearest Ti site. Since the V_O works as the n-type doping and introduces 2 electron carriers, we consider divalent and trivalent cations, D^{2+} and T^{3+}, with a similar ionic radius to Ti^{4+} to introduce hole carriers: D = Mg, Ni, Zn, and T = B, Al, Ga, In, Tl, Sc.

The projected density of states (PDOS) for STO:V_O shows that the defect level composed of Ti-3d appears just below the conduction bands as a donor level. This defect level can degrade the photocatalytic activities since it works as a recombination center. On the other hand, D_{Ti} and $2T_{Ti}$ doping can remove the defect level owing to the p-type doping, while the dopant levels composed of Ni-3d appear for Ni_{Ti} doping. Therefore, the photocatalytic degradation is expected to be prevented for D = Mg, Zn, and T = B, Al, Ga, In, Tl, Sc.

Furthermore, we calculated the dopant formation energy for the D_{Ti} and $2T_{Ti}$ doping, which shown in Figure 1. Here each chemical potential is evaluated from the phase equilibrium of STO, and dopant chemical potentials are evaluated from the phase equilibrium of their oxides. Mg/Zn_{Ti} and $2Ga/Sc_{Ti}$ doping are easy to form according to the formation energy. Therefore, Mg/Zn_{Ti} and $2Ga/Sc_{Ti}$ doping can be expected to be efficient dopants for high-performance photocatalytic STO. These numerical results are consistent with the experimental ones: the photocatalytic activity of synthesized STO:Mg and Zn samples are enhanced compared to pristine STO sample.

Efficient dopants for perovskite photocatalyst $PbTiO_3$

Perovskite oxide $PbTiO_3$ (PTO) is a photocatalyst for overall water splitting as well as ferroelec-

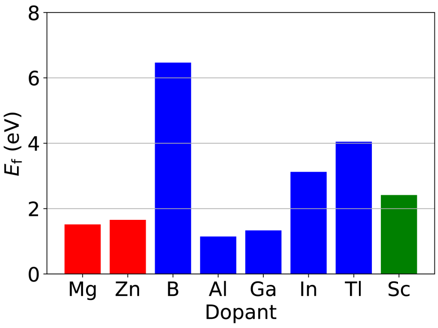

Figure 1: Dopant formation energy for each D_{Ti} and $2T_{\mathrm{Ti}}$ doping.

tric material. Similar to other photocatalysts such as STO:Al, the enhancement of photocatalytic activities is expected by the defect control using efficient dopants [4]. We have investigated the electronic structure of doped PTO using the first-principles calculations based on DFT. The $3\times3\times3$ supercell of the primitive cell of STO is used to describe point defects including oxygen vacancy and substitutional doping. The DFT calculations were performed within the PBE+U functional using PAW method as implemented in VASP [3]. The Hubbard U was set to be $U = 4.75$ eV for the 3d orbitals at the Ti sites, which reproduces the relative position of defect levels to the valence and conduction band. We also focus on the V_O) and divalent cation (D) substitution of the nearest Ti site. We consider divalent cations D^{2+} with a similar ionic radius to Ti^{4+} to introduce hole carriers: D = Mg, Ni, Zn. The oxygen sites around Ti are distinguished by the apical and in-plane oxygens (O_{ap} and O_{in}) due to the tetragonal crystal structure.

Figure 2 shows the PDOS for PTO:V_{Oap} and PTO:Mg. The presence of V_{Oap} introduces the defect level composed of Ti-3d below the conduction bands. In contrast, the Mg substitution of the nearest Ti (Mg_{Ti}) removes the defect level and the band gap is recovered. This tendency is the same as V_{Oin}, which is not shown here. Therefore, the divalent cation substitution is expected to enhance the photocatalytic activity similar to STO case. The investigation of the other divalent cation substitution and evaluation of the doping formation energy will be future works.

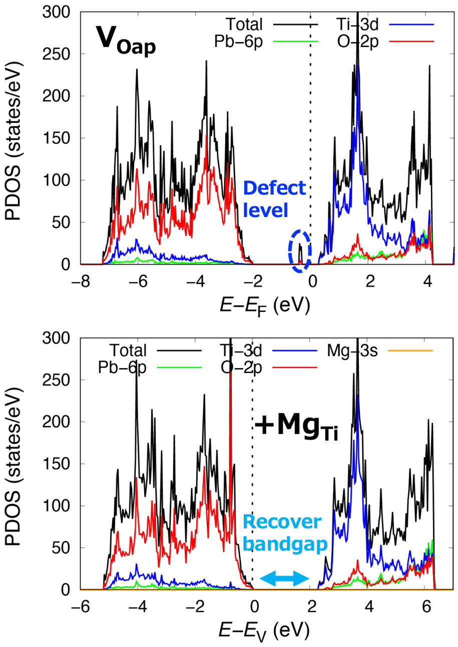

Figure 2: PDOS for PTO:V_{Oap} and PTO:Mg.

Calculation conditions

We have performed hybrid (MPI+OpenMP) parallel computing using, where the parallelization over bands and k-points is used by VASP version 6.4.2.

References

[1] K. Nishiguchi, T. Takayama, S. Takasuka, Y. Harashima, M. Fujii, and S. L. Ten-no: J. Phys. Chem. Lett. 2025, 16, 11, 2823–2830.

[2] T. Takata *et. al.*: Nature **581**, 413 (2020).

[3] G. Kresse *et. al.*: Phys. Rev. B **47**, 558 (1993); Phys. Rev. B **49**, 14251 (1994); Computational Materials Science **6** (1996) 15–50; Phys. Rev. B **54**, 11169 (1996).

[4] G. Wan *et. al.*: J. Am. Chem. Soc. 2022, 144, 20342–20350.

Microscopic structure of water/CeO_2 interface

Akira NAKAYAMA
Department of Chemical System Engineering,
The University of Tokyo, Tokyo 113-8656, JAPAN

1. Introduction

At interfaces between metal-oxide and water or alcohols, molecules in the liquid phase undergo dissociative adsorption due to acid-base sites on the surface. The ionic species generated by dissociation diffuse via proton hopping and recombine with surface hydroxyl groups. For such complex systems involving bond dissociation and formation, we constructed a neural network potential (NNP) using training data obtained by DFT calculations. Using this NNP, we performed large-scale, long-time molecular dynamics (NNP-MD) simulations to analyze the interfacial structure and dynamics.

2. Results and Discussion

Through NNP-MD simulations of the CeO_2/water interface, we successfully analyzed, with sufficient statistical reliability, the dissociation rate of water molecules at the interface and the diverse proton hopping mechanisms and its frequencies. Furthermore, when attempting to model proton hopping based on kinetics, we found that proton relay at the interface depends on the timescale of the solvent network dynamics. Therefore, it is difficult to construct meaningful kinetic models using reaction rates that ignore this time dependence, i.e., the so-called “memory effect.” To address this, we proposed a semi-Markov model in which the reaction rate is not treated as a constant, but rather depends on the time interval since the previous reaction. This approach idealizes the point of temporal reference for changes in the surrounding environment as the immediately preceding reaction. The fact that the results of kinetic Monte Carlo (KMC) simulations using this rate constant successfully reproduce those of the NNP-MD simulations demonstrates the importance of non-Markovian dynamics at the interface. As a result, we were able to establish a coarse-grained analysis method for the long-time reaction dynamics captured by NNP-MD [1].

In this work, the CP2K program package was used for DFT-MD simulations, and the PLUMED program was employed to perform the enhanced sampling simulations. The DeePMD-kit was used to construct NNPs

References

[1] Kobayashi, T.; Ikeda, T.; Nakayama, *Chem. Sci.* **2024**, *15*, 6816–6832.

Thermal Expansion and Phase Stability of BF_3 (B = Sc, Y, La, Al, Ga, In): A First-Principles Study

Yasuhide MOCHIZUKI

Department of Materials Science and Engineering,

Tokyo Institute of Technology, Ookayama, Meguro-ku, Tokyo 152-8550

Much attention has been paid to ScF3 because of its simple crystal structure and negative thermal expansion (NTE) over a wide temperature range [1]. No other binary trifluoride has the same crystal structure and exhibits NTE in as wide a temperature range as ScF_3. There has hitherto been no sufficient explanation for this reason. Herein, to discuss the phase stability and the NTE behavior of ScF_3, the 6 binary trifluorides BF_3 (B = Sc, Y, La, Al, Ga, In) are thoroughly compared by using the *ab initio* molecular-dynamics (AIMD) calculations with the on-the-fly machine-learning technique [Fig. 1(a–d)], first-principles lattice-dynamics calculations, and electronic-structure analyses based on group-representation theory and the band-unfolding method [Fig. 1(e, f)]. Our calculation results reveal that (i) the $a^-a^-a^-$

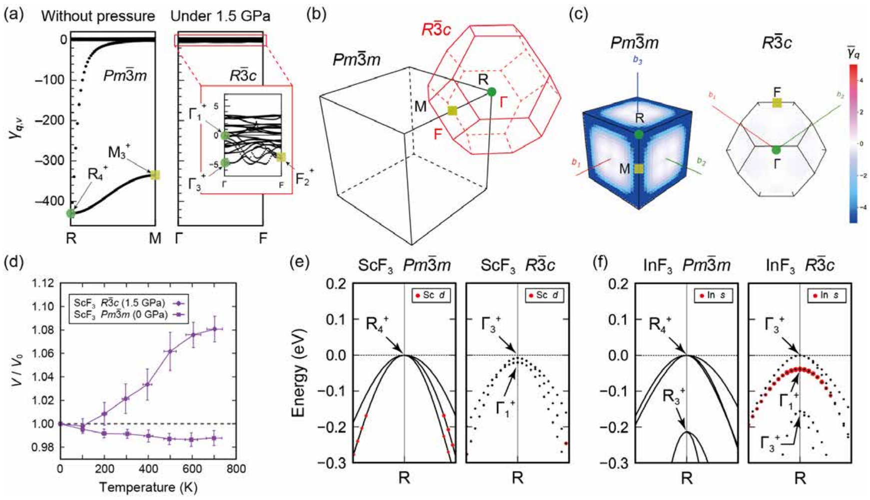

FIG. 1. (a) Dispersions of $\gamma_{q,\nu}$ of the $Pm\bar{3}m$ without pressure and $R\bar{3}c$ phases under 1.5 GPa for ScF_3. (b) The visualized first Brillouin zone of $Pm\bar{3}m$ and $R\bar{3}c$. (c) The distributions of averaged $\gamma_{q,\nu}$ in the first Brillouin zone of $Pm\bar{3}m$ and $R\bar{3}c$ phases. (d) Equilibrium lattice volumes of the $Pm\bar{3}m$ phases without pressure and $R\bar{3}c$ phases under 1.5 GPa for ScF_3 extracted from the AIMD calculations. (e, f) Calculated electronic band structures with and without the octahedral rotational distortions for (e) ScF_3 and (f) InF_3 by using the HSE06 hybrid functional in the vicinity of VBM.

octahedral rotational distortion (ORD) in ScF_3 increases the frequency of the crucial phonons for realizing NTE, leading to a weakening of the NTE behavior under hydrostatic pressure; (ii) the group-representation theory predicts the emergence of ORDs triggered by the second-order Jahn–Teller effect in cubic ScF_3, YF_3, AlF_3, GaF_3, and InF_3; (iii) cubic ScF_3 and YF_3 do not possess ORD without pressure due to their slight orbital overlap between the cations and anions; (iv) ScF_3 has a delicate balance between the repulsive force term and the energy stabilization term, induced by the octahedral rotational phonon modes; and (v) metastable cubic YF_3 and LaF_3 exhibit NTE behaviors. Our findings would provide an understanding of a material-design principle for realizing NTE [2].

Our first-principles calculations were performed by using the computing resources of Research Center for Com- putational Science at ISSP (System B).

References

[1] B. K. Greve, K. L. Martin, P. L. Lee, P. J. Chupas, K. W. Chapman, and A. P. Wilkinson, *J. Am. Chem. Soc.* **132**, 15496 (2010).

[2] H. Koiso, S. Yoshida, T. Nagai, T. Isobe, A. Nakajima, and Y. Mochizuki, *Phys. Rev. B* **110**, 064104 (2024).

Substrate can enhance thermal transport of two-dimensional materials

Jie Sun
Graduate school of Engineering,
The University of Tokyo, Hongo 7-3-1, Bunkyo-ku, Tokyo 113-8656, Japan

Two-dimensional (2D) materials are promising candidates for next-generation electronics, yet their intrinsic thermal conductivity (κ) is often suppressed when supported on substrates due to enhanced phonon scattering. While interface engineering efforts have largely focused on improving heat dissipation, mitigating the loss of intrinsic κ remains an open challenge. In this work, we investigate whether κ can be preserved—or even enhanced—on a substrate by accounting for complex phonon behaviors, including four-phonon (4ph) scattering and wave-like transport effects, which are particularly significant in low-κ materials. Employing machine learning interatomic potentials trained with moment-tensor potentials (MTPs), we simulate anharmonic thermal transport in graphene and germanene with high accuracy and efficiency. Surprisingly, we find that substrate contact can increase κ, albeit through distinct mechanisms in each material.

Thermal conductivity is calculated using the Wigner-Boltzmann transport equation, which captures both particle-like and coherent phonon transport. Accurate structural and vibrational properties are obtained from first-principles DFT calculations, which serve as training data for the MTP models. These models enable efficient extraction of high-order interatomic force constants via HIPHIVE. While substrate interactions are included during training to reflect realistic environments, they are excluded from final IFCs to isolate the intrinsic transport characteristics of the 2D layers.

To minimize lattice mismatch between the two-dimensional (2D) materials and the Au substrate, we constructed supercells with matched in-plane lattice vectors, effectively reducing intralayer strain. Graphene was modeled using a 2×2×1 supercell on Au, resulting in negligible strain (0.042%) and a consistent in-plane lattice constant of 4.92 Å, with an interlayer spacing of 3.36 Å. In contrast, germanene—with its buckled structure and lower symmetry—required a larger $\sqrt{13}\times\sqrt{13}\times1$ supercell to maintain stability. This configuration yields minor strains of 0.10% and 0.13% along the a and b directions, respectively, with an in-plane lattice constant of 14.36 Å and a vertical spacing of 2.73 Å. Top views of the relaxed heterostructures are shown in Figures 1(a) and 1(b).

We computed the lattice thermal conductivities of both free-standing and substrate-supported configurations, with the results summarized in Figures 1(c) and 1(d). For graphene at 300 K, the thermal conductivity increases from 1288 W/mK (free-standing) to 1644 W/mK on Au and remains elevated at higher temperatures. This unexpected enhancement challenges the conventional notion that substrates degrade thermal transport in 2D materials. The improved conductivity is attributed to reduced four-phonon scattering in the supported graphene, stemming from symmetry breaking of the flexural (ZA) phonon mode. When only three-phonon scattering is considered, the substrate shortens phonon lifetimes and reduces κ, as seen in Figure 1(e). However, including four-phonon scattering reveals longer lifetimes in the supported structure (Figure 1(f)), resulting in higher κ. Substrate-induced electron-phonon coupling was found to have a negligible impact on thermal transport.

For germanene, the intrinsic thermal conductivity decreases from 2.45 W/mK (free-standing) to 0.82 W/mK at 300 K when both three- and four-phonon interactions are included, with an additional coherent contribution of 0.3 W/mK. Upon contact with Au, particle-like transport is further suppressed, while coherent conductivity increases significantly—to 1.35 W/mK at 300 K and 1.92 W/mK at 600 K—compared to only 0.77 W/mK in the free-standing case. Figures 1(g) and 1(h) illustrate this mode-dependent enhancement of wave-like phonon transport. These findings point to a promising strategy for thermal management in nanoscale devices by leveraging phonon coherence through substrate interactions.

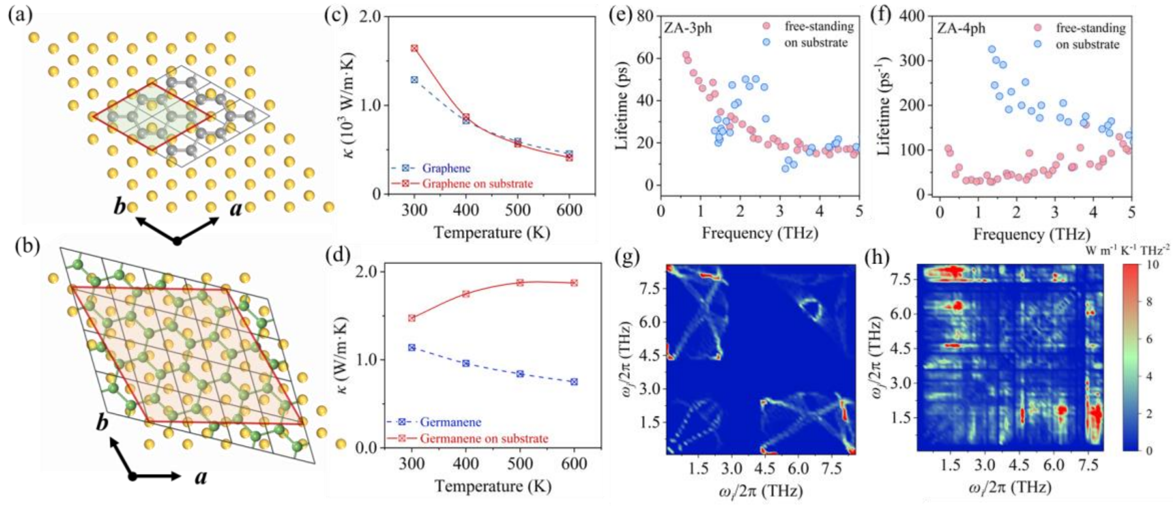

Figure 1. Top views of (a) graphene and (b) germanene on Au substrate. Thermal conductivity of free-standing and on-substrate (c) graphene and (d) germanene. Phonon lifetime of ZA mode from 0-5 THz considering (e) three-phonon and (f) four-phonon scattering in free-standing and on-substrate graphene. Mode-dependent wave-like phonon transport in (g) free-standing and (h) on-substrate germanene.

Theoretical study of grain boundary structures and segregation behavior of impurities

Kazutoshi INOUE
Advanced Institute for Materials Research, Tohoku University
Katahira 2-1-1, Aoba-ku, Sendai, Miyagi 980-8577

A comprehensive understanding of grain boundary (GB) structures is important to control their practical applications. However, the corpus of knowledge concerning GB structures remains limited even in MgO, which is a versatile compound with a high natural abundance.

In this study, we found a transitional structure from symmetric to asymmetric units at the MgO $\Sigma 5(210)$ GB by atomic resolution scanning transmission electron microscopy. In order to reveal the mechanism of the structural transition, we performed theoretical calculations to determine the stable structure of MgO and its variation with the segregation of impurities. It has been demonstrated that the simulated annealing technique using molecular dynamics (MD) simulation is an effective method to explore possible structures by cooling down models from high temperature. In order to screen potential stable and meta-stable atomic configurations by GB energy, the simulated annealing process has been repeated hundreds of times. The Buckingham force field is utilized to account for ionic charges and Coulomb forces. All MD simulations was performed using the LAMMPS package. Then, the pristine and Ca-segregated GB models were computed using the projector augmented wave method implemented in the VASP code using CPU nodes in System B. The generalized gradient approximation is employed for exchange-correlation interactions, with the formulation parameterized by Perdew, Burke, and Ernzerhof. All models were thoroughly optimized with an energy and force convergence threshold of 10^{-5} eV and 0.05 eV/Å. A $1 \times 1 \times 4$ k-point grid and 450 eV for the energy cutoff of plane waves were established after a comprehensive convergence testing. The Nudged Elastic Band (NEB) method was employed to determine the minimum energy path for the structural transition from symmetric to asymmetric units. The NEB and related methods are algorithms that can find the minimum energy pathway between two known states by iteratively optimizing a chain of intermediate structures. Subsequently, the substitution and interstitial energies of Ca were investigated to evaluate the segregation energies.

Theoretical calculations suggested that Ca atoms have a low substitution energy in metastable structures, therefore stabilizing asymmetric structures. Moreover, although there is a favored path in the NEB calculation, the difference in the transition barriar is low, which explains why Ca induces a different structure. This finding is expected to contribute to the development of materials design at the atomic level, which will take advantage of dopant segregation around GBs.

References

[1] Q. Chen, M. Saito, K. Kawahara, A. Nakamura, K. Inoue, Y. Ikuhara, "Grain Boundary Structural Transformation and the Effect of Impurities in MgO", *under review* (2025).

Quantum transport theory based on large-scale first-principles electron transport calculations

NOBUHIKO KOBAYASHI
Department of Applied Physics, University of Tsukuba
1-1-1 Tennodai Tsukuba Ibaraki 305-8573

Quantum transport theory based on large-scale first-principles electron transport calculations is important from the viewpoint of materials science and technology. We have developed the nonequilibrium Green's function (NEGF) method and the O(N) time dependent wave-packet diffusion (TD-WPD) method on the basis of the density functional theory (DFT). We have also developed methods to predict the crystal structures of organic materials, and have applied the methods to the design of organic semiconductors.

Organic semiconductors have attracted much attention for their applications to flexible, printable, lightweight, and low-cost electronic devices. The organic crystals are assemblies of π-conjugated molecules weakly bonded by van der Waals interactions, and it is difficult to predict the crystal structures. We have developed an efficient method based on DFT to predict the crystal structures of organic semiconductors from molecular structural formulas without using experimental data. As a demonstration, we applied this method to high-mobility organic semiconductor molecules, and performed crystal structure analyses for the molecules. We successfully obtained organic crystal structures from the molecular structural formulas. The predicted stable structures agree well with the experimentally observed structures, and the transport properties are accurately estimated. [1]

We have also developed a method to determine the crystal structure of organic semiconductors by incorporating the machine learning technique into PXRD analysis as shown in Fig.1. A machine-learning model that can automatically detect the peak positions from the PXRD pattern was developed by learning the PXRD patterns calculated from the crystals of the organic compounds and their peak positions. The crystal-structure analysis is successfully performed using their peak positions and the initial structure generated from the molecular structure information. [2]

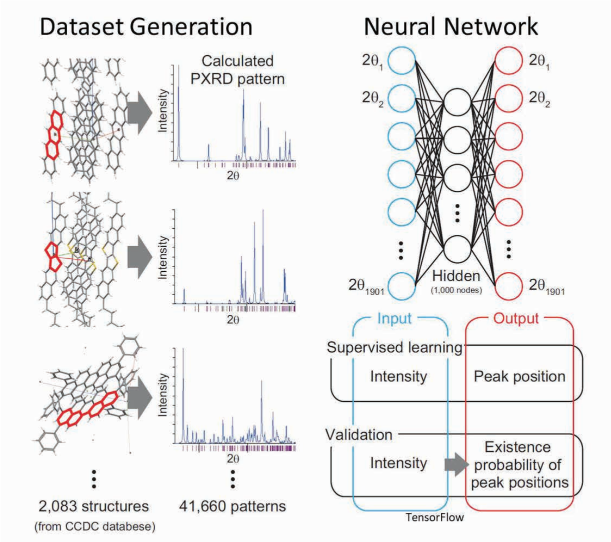

Figure 1: Machine learning model and the dataset generation process.

We have performed first-principles calculations of vertical transport in single-crystalline thin films of organic semiconductors consisting of periodically arranged molecules using a Simulation code for Atomistic Kohn-sham Equation (SAKE) developed by our group based on the DFT and NEGF formalism.[3] The transport properties are compared between single-crystalline thin film and single-molecule systems, and we reveal transport properties reflected by band dispersion and current characteristics due to good contact with organized electrode interface.

We developed the O(N) TD-WPD method for the quantum transport calculation of huge systems of up to 100 million atoms a decade ago, and have also succeeded in O(N) thermoelectric transport calculation such as Seebeck coefficient and power factor. Different from a conventional method using the electric conductivity spectrum, it obtains the coefficients directly from the correlation function between heat and electric current based on linear response theory. We apply the methodology to a two-dimensional system and confirm that the calculated results are consistent with those obtained by the conventional method. The proposed methodology provides an effective approach to evaluate the thermoelectric performance of micron-scale materials based on quantum mechanics from an atomistic viewpoint. [4]

References

[1] S. Hakata, H. Ishii, H. Takaki, T. Okamoto, J. Takeya, N. Kobayashi, *Appl. Phys. Express* 17 101001 (2024)

[2] N. Niitsu, M. Mitani, H. Ishii, N. Kobayashi, K. Hirose, S. Watanabe, T. Okamoto, J. Takeya *Appl. Phys. Lett.* 125, 013301 (2024)

[3] H.Takaki, N.Kobayashi, K.Hirose, *J. Phys.: Condens. Matter.* 32 325901(2020)

[4] H. Ishii, N. Kobayashi, K. Hirose *J. Phys. Condens. Matter.* 36 335903 (2024).

Ab initio molecular-dynamics study of CO_2 adsorption mechanisms in cement hydration process

Ikumi KANEMASU and Satoshi OHMURA

1) Premier Institute for Advanced Studies, Ehime University, Matsuyama, Ehime 790-8577

2) Department of Civil and Environmental Engineering

Hiroshima Institute of Technology, Hiroshima, Hiroshima 731-5193

It has been reported that the cement industry is the third or fourth largest emitter of carbon dioxide (CO_2) worldwide. As a result, CO_2 capture technologies in the cement industry have attracted significant attentions. To improve these technologies, detailed research on the CO_2 absorption mechanisms of cement-based materials from an atomistic perspective is required. For this reason, we have investigated the absorption properties of hydrate minerals in the cement using ab initio molecular dynamics simulations. In this study, we focused on the ettringite and tobermorite as a model of calcium silicate hydrate mineral, which formed when water reacts with cement. Figure 1 shows the structural models of ettringite and tobermorite.

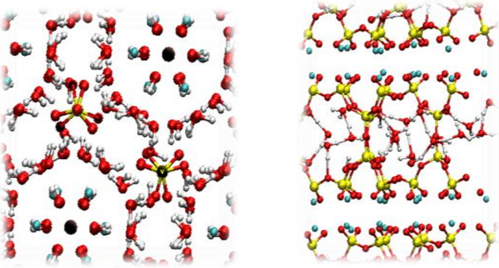

Fig. 1. Atomic configurations of ettringite and tobermorite.

We performed ab initio moelcualr dynamics simulations for these minerals + CO_2 systems. For Ettieigite-CO_2 system, It was found that CO_2 is converted to CO_2-OH (i.e., HCO_3^-), due to the presence of numerous hydroxyl groups (OH^-) in ettringite, which can react with CO_2 molecules through acid-base reactions. On the other hand, since tobermorite contains fewer hydroxyl group compared to ettringite, the formation of (HCO_3^-) is more limited.

.

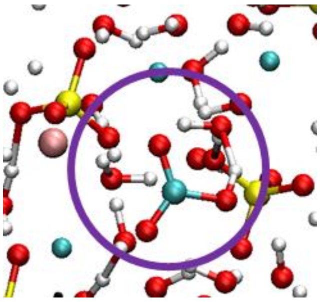

Fig. 2. HCO_3^- observed in the simulation for ettringite

References

[1] I. Kanemas, *et al.*, Cement Science and Concrete Technology **78**, 18-25 (2025).

Computational Design of Novel Functional Materials and Catalysts for Energy-related Applications

Tetsuya TAKETSUGU

Department of Chemistry, Faculty of Science

Hokkaido University, N10W8, Kita-ku, Sapporo 060-0810

The main goal of this project is to develop a number of innovative real functional materials for energy and environment-related applications using a computational approach. The density functional theory (DFT) methods as implemented in the VASP and Quantum Espresso software packages were used. The following main results were achieved:

1) We have modeled the catalytic reaction of ammonia electrooxidation in aqueous solution to produce nitrate and nitrite while generating hydrogen under ambient conditions [1]. Our DFT calculations support experimental observations and reveal the mechanism of the electrochemical oxidation of ammonia to nitrite and nitrate on a nickel oxyhydroxide (NiOOH) type of catalyst formed on the Ni foam. Different reaction pathways leading to formation of nitrate and nitrite and N_2 are studied. This research contributes to the development of a cost-effective and highly efficient catalyst for large-scale ammonia electrolysis, while shedding light on the underlying mechanism of the NiOOH catalyst.

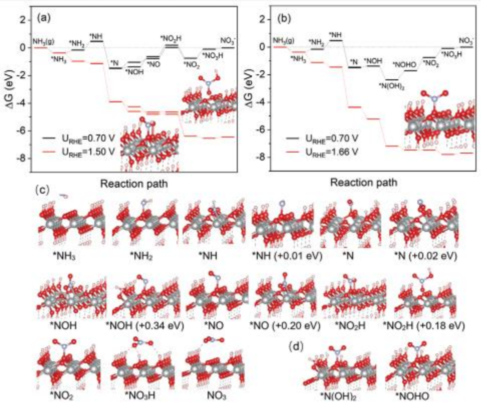

Fig. 1: Free energy diagrams for electrochemical oxidation of ammonia and the most stable structures of the reaction intermediates [1].

2) Using the extensive large-scale DFT and generic force field calculations with periodic boundary conditions (pGFN-FF) calculations we have modeled the formation of the nearly freestanding 2D gold (Au) sheets with triangular nanoscale patterns separated from the Ir(111) surface by embedded B atoms [2]. We have also unveil the structure of the buried B species and their crucial role in forming the nanostructured Au mono- and bilayers. Interfacial B atoms do not form the χ-type borophene typically observed on the

Ir(111) surface but adsorb in the Ir substrate hollow sites. Changes in the Au monolayer's band structure upon substrate decoupling indicate a transition from 3D to 2D metal bonding. The resulting Au films exhibit remarkable stability, making them practical for studying the catalytic activity of 2D gold.

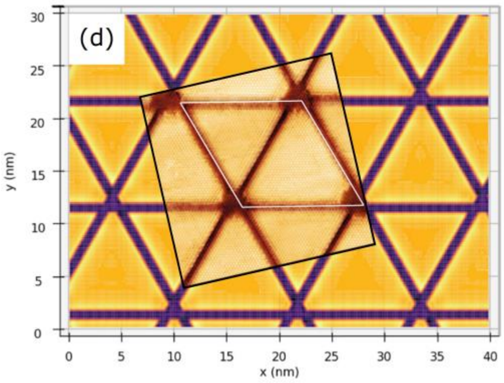

Fig 2: Nanopattern structure of monolayer gold on B/Ir(111) along with the superimposed STM image [2].

3) We performed a systematic investigation on the catalytic activities of high-spin small Fe(III) oxides for efficient hydrogen production through ammonia decomposition, using the artificial force-induced reaction method within the framework of density functional theory with the B3LYP functional. An analysis of NH_3 dehydrogenation and H_2 formation on various Fe(III) oxide sizes identifies the rate-determining steps for each reaction [3]. We found that the rate-determining step for the full NH_3 dehydrogenation on $(Fe_2O_3)_n$ (n = 1–4) is size-dependent, with the $NH* \rightarrow N* + H*$ reaction acting as the limiting step. The obtained results are valuable for designing iron trioxidebased nanosized catalysts by regulating the size of the $(Fe_2O_3)_n$ clusters to enhance H_2 production from the catalytic decomposition of ammonia.

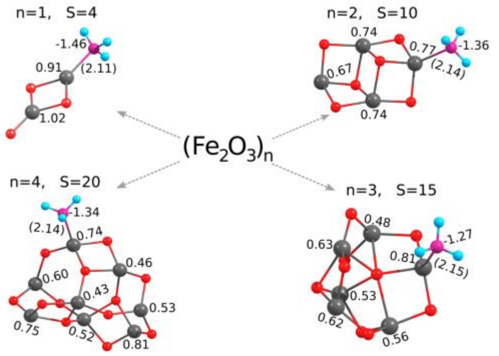

Fig 3: Optimized geometries of NH_3 adsorbed on (Fe_2O_3)n clusters for n = 1–4 [3].

References

[1] H. Liu, C.-J. Yang, C.-L. Dong, J. Wang, X. Zhang, A. Lyalin, T. Taketsugu, Z. Chen, D. Guan, X. Xu, Z. Shao, and Z. Huang, Adv. Energy Mater. **14**, 2401675 (2024).

[2] A. Preobrajenski, N. Vinogradov, D. A. Duncan, T.-L. Lee, M. Tsitsvero, T. Taketsugu, and A. Lyalin, Nat. Commun. **15**, 10518 (2024).

[3] S. Ibragimov, A. Lyalin, S. Kumar, Y. Ono, T. Taketsugu, and M. Bobrowski, J. Chem. Phys. **162**, 054305 (2025).

First-principles study of the Fano resonance in copper phthalocyanine adsorbed on Cu(100)

Yuji HAMAMOTO
Department of Communication Engineering,
Okayama Prefectural University, 111 Kuboki, Soja, Okayama 719-1197

The Fano effect is a ubiquitously observed quantum phenomenon characterized by an asymmetric resonance peak that results from the interference between continuum and discrete levels. Recent experiments based on scanning tunneling spectroscopy (STS) have demonstrated that the Fano resonance also appears in the dI/dV spectra of copper phthalocyanine (CuPc) adsorbed on the Cu(100) surface [1]. The experimental results indicate that the q-parameter, which characterizes the line shape of the Fano resonance, varies dramatically as a function of the position of the STS tip and fluorine substitution of the CuPc molecule, whereas their dependence disagrees with the theoretical expression of the q-parameter.

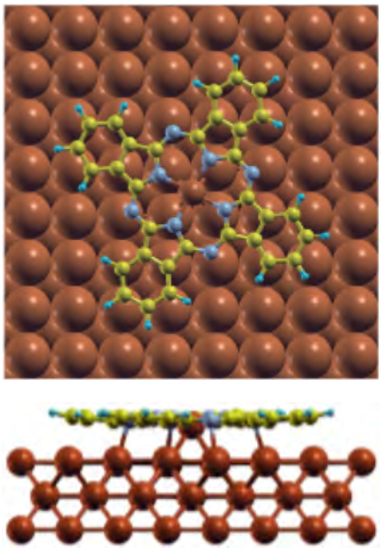

Fig. 1: Top and front views of CuPc adsorbed on Cu(100).

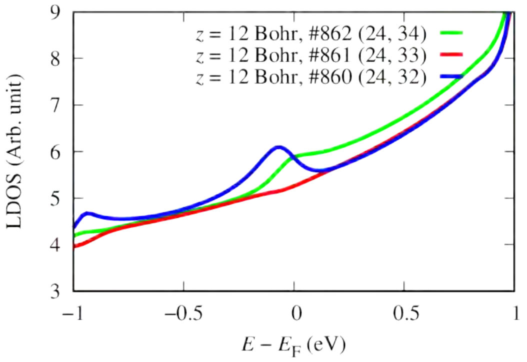

Fig. 2: LDOS obtained near the edge of the CuPc molecule adsorbed on the Cu(100) surface.

To elucidate the origin of the discrepancy, we perfume the density functional theory (DFT) calculation of the Fano resonance, using the adsorption structure obtained for CuPc on a slab model of Cu(100) [1] as shown in Fig. 1. The continuum levels of the metal surface are described by the Embedding Green's function method [2], and dI/dV is approximated by the local density of states (LDOS) near the apex of the STS tip [3].

Preliminary results for the LDOS obtained near the edge of the molecule are shown in Fig. 2, where slight signatures of a dip as well as asymmetric peaks can be observed. However, resonance peaks are almost symmetric above the molecule, in disagreement with the experimental results. This might be attributed to the fact that the generalized gradient approximation adopted in the DFT calculation fails to describe the image potential above the molecule, suppressing the interference of the surface states with molecular orbitals. For the future outlook, we plan to perform further calculations taking the image potential into account.

References

[1] H. Okuyama, S. Kuwayama, S. Hatta, T. Aruga, Y. Hamamoto, T. Shimada, I. Hamada, and Y. Morikawa, Appl. Surf. Sci. **643**, 158700 (2024).

[2] J. E. Inglesfield, J. Phys. C: Solid State Phys. **14**, 3795 (1981).

[3] J. Tersoff and D. R. Hamann, Phys. Rev. Lett. **50**, 1998 (1983).

Structure search for germanene on Ag(111) by Gaussian process regression

Yuji HAMAMOTO
Department of Communication Engineering,
Okayama Prefectural University, 111 Kuboki, Soja, Okayama 719-1197

Germanene, a germanium (Ge) analog of graphene, has been drawing growing attention because of its peculiar electronic properties due to the linear dispersions, as well as the potential application in semiconductor nanotechnology. Experimentally, germanene is grown by depositing Ge atoms on the Ag(111) surface, where a transition from Ag_2Ge alloy at low coverage to the striped phase of germanene at 1 ML has been observed. However, the existence of the Ag_2Ge alloy at the early stage casts a doubt on the formation of pure germanene. Theoretically, density functional theory calculations have been performed to analyze the electronic structures of germanene grown on Ag(111), where the formation of pure germanene is assumed in most cases, because of the structural complexity of the AgGe alloy.

To overcome the computational difficulty, we adopt GOFEE, an efficient structure search method based on the Gaussian process regression and an evolutionary algorithm [1], to investigate the possibility of alloy formation. Recently, we have applied the method to silicene on Ag(111) and successfully determined not only the well-known stable structures but also previously unknown metastable structures. We here examine the applicability of GOFEE, taking pure germanene on Ag(111) as an example. The surface is modeled with a periodically repeated $7 \times \sqrt{3}$ surface unit cell of the Ag(111) slab composed of one Ag atomic layer. A typical structure obtained by GOFEE is shown in Fig. 1, where the honeycomb lattice is significantly distorted as compared with a freestanding germanene. For the future outlook, we plan to apply this method to the GeAg alloy on Ag(111) and determine the stable structures for various stoichiometries.

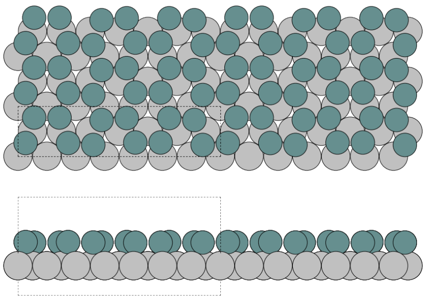

Fig. 1: Top and front views of germanene on Ag(111) obtained by GOFEE. The dotted rectangle indicates the unit cell of the system.

References

[1] M. K. Bisbo and B. Hammer, Phys. Rev. Lett. **124**, 086102 (2020).

Non-perturbative calculation of exchange coupling tensor

Tomonori TANAKA
Department of Materials Science and Engineering, Institute of Science Tokyo
Nagatsuta-cho, Yokohama 226-8501

In recent years, spintronics utilizing complex magnetic interactions found in noncollinear magnetic structures has been rapidly advancing. Meanwhile, first-principles evaluation methods for such complex magnetic interactions are still under development. Although several state-of-the-art evaluation methods exist, they are commonly based on perturbation theory, which presents issues regarding quantitative accuracy.

In this project, we first demonstrated that the non-perturbative evaluation of the exchange coupling parameters J_{ij} in the Heisenberg model [1]. Surprisingly, we find that contributions from changes in the electronic structure—which have been ignored in the perturbative methods—are necessary even in relatively small deviations from the ground magnetic state.

Although the exchange coupling parameters in the Heisenberg model remain important, they are insufficient for describing many magnetic orders and textures. Therefore, we believe that non-perturbative methods for evaluating other types of magnetic interactions are also essential. To achieve this, we have developed an efficient implementation of the spin-cluster expansion (SCE) method [2]. While the original SCE formulation theoretically allows for the description of any type of magnetic interaction within the classical spin model, its initial implementation incurred prohibitively high computational costs and was therefore impractical. We overcame this issue by utilizing constraining local magnetic fields [3].

As a demonstration, we applied the spin-cluster expansion method to a relatively simple ferromagnetic system, $L1_0-$FePt. We performed constrained-noncollinear DFT calculations using the GGA-PBE functional implemented in the VASP package. Thirty different spin configurations near the ferromagnetic state were prepared, and the corresponding total energies were collected. The SCE coefficients were then estimated using the least-squares method. For example, the exchange coupling tensor for the first-nearest-neighbor Fe-Fe pair along the x-direction, $\mathcal{J}_{1\mathrm{NN}}$, was obtained as

$$\mathcal{J}_{1\mathrm{NN}} = \begin{pmatrix} 17.81 & 0 & 0 \\ 0 & 18.30 & 0 \\ 0 & 0 & 17.67 \end{pmatrix} \mathrm{meV}. \quad (1)$$

This method enables the evaluation of non-diagonal components consisting of symmetric and antisymmetric anisotropic exchange couplings from fully self-consistent DFT calculations. We therefore plan to apply our method to systems exhibiting more complex magnetic textures.

References

[1] T. Tanaka and Y. Gohda, arXiv:2410.11256.

[2] R. Drautz and M. Fähnle, Phys. Rev. B **69**, 104404 (2004).

[3] T. Tanaka and Y. Gohda, in preparation.

Boosting Energy Efficiency in Biomass & Fuel Cell Systems: Using Ni Nanoparticles on CeO_2 for Methane Conversion

Takaya FUJISAKI

Faculty of Materials for Energy,

Shimane University, 1060 Nishikawatsu, Matsue, Shimane 690-0823

The global demand for electrical energy continues to grow, prompting significant interest in fuel cells as a highly efficient device for converting chemical energy from hydrogen and oxygen directly into electrical energy without reliance on fossil fuels. Moreover, fuel cells have the capability to utilize biogas (CH_4-based gas), a renewable resource primarily composed of methane, for electricity generation as seen in Fig.1[1][2].

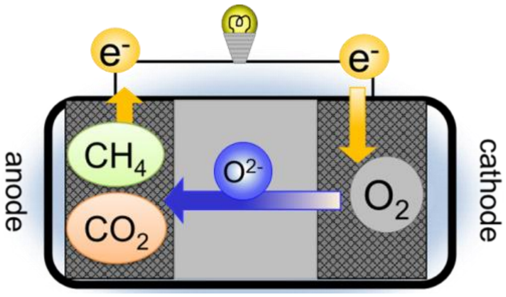

Fig.1 Principle of biogas direct fuel cell. The reforming catalyst in the electrode allows hydrogen to be drawn from methane.

Biogas is produced through the methane fermentation of biomass, a renewable energy source. Hydrogen can be effectively extracted from methane through the Dry Reforming of Methane (DRM) reaction ($CH_4 + CO_2 \rightarrow 2H_2 + 2CO$). Minimizing the activation barriers for the critical steps in DRM, specifically methane dissociation ($CH_4 \rightarrow CH_3 + H$) and carbon dioxide dissociation ($CO_2 \rightarrow CO + O$), is essential for enhancing hydrogen extraction efficiency and thus improving fuel cell efficiency.

My project employed theoretical calculations, specifically density functional theory (DFT), to systematically explore Ni nanoparticle catalysts supported on CeO_2 substrates. I focused on two distinct Ni_4 configurations, designated as "Ni_4 above Ce" and "Ni_4 above O"[3]. My comprehensive computational approach allowed to elucidate the reaction mechanisms at atomic resolution and assess strategies for reducing the activation energy of methane dissociation.

As seen in Fig.2, Results showed that the "Ni_4 above O" structure demonstrated lower activation energy (0.98 eV) compared to the "Ni_4 above Ce" configuration (1.03 eV), suggesting a preferable catalytic configuration. Detailed electron density analyses indicated that a more positively charged Ni_4 cluster, influenced by the electronegativity of substrate atoms beneath the Ni nanoparticles, significantly reduces the activation energy of methane dissociation. Further electronic structure analysis using the projected crystal orbital Hamilton population (pCOHP) method revealed weaker antibonding interactions between CH_3 and Ni atoms in the "Ni_4 above O" structure, leading to enhanced stability and reduced activation energy.

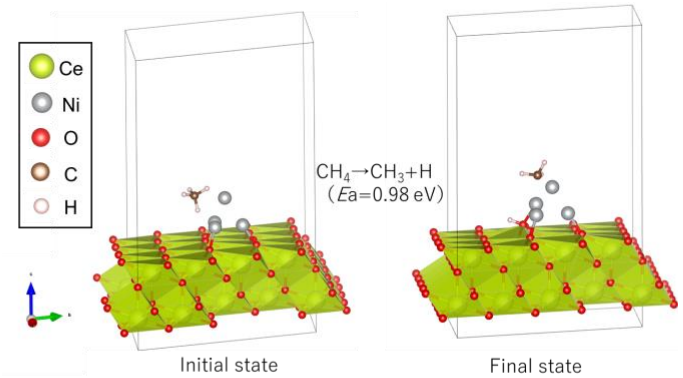

Fig.2 Before and after methane dissociation of the Ni on above O structure as shown by first-principles calculations.

Experimental validation of the computational predictions was achieved through DRM tests using a specially developed flower-like Ni-supported CeO_2 catalyst (Ce(F)). The experimentally determined activation energy for methane dissociation was 0.69 eV, closely matching our DFT-calculated apparent activation energy (0.80 eV) for the "Ni_4 above O" structure. This experimental confirmation significantly validates our theoretical model, highlighting the reliability of DFT calculations in predicting catalytic behaviors.

In conclusion, this project provides critical insights into optimizing Ni-supported CeO_2 catalysts for the DRM reaction, emphasizing the importance of charge distribution and structural configuration. The study offers a viable strategy for future catalyst design, aiming at achieving high efficiency and sustainability in energy production.

Acknowledgments:

This work was supported by JSPS KAKENHI, Fostering Joint International Research (B), Grant Number 20KK0248. Computational resources were provided by the Research Institute for Information Technology at Kyushu University, the Institute for Solid State Physics at the University of Tokyo, and the Cyberscience Center at Tohoku University. Additional support was received from JSPS KAKENHI Grant Numbers JP21K04996 and JP22H05146 (Grant-in-Aid for Transformative Research Areas (A) “Supra-ceramics”), Tateisi Science and Technology Foundation Grant Number KH-018, and Sumitomo Foundation Environmental Research Projects Grant Number 2340007.

References:

[1] T. Fujisaki, K. Ikeda, A. T. Staykov, H. Setiawan, Y. Shiratori, RSC Adv. 2022.

[2] H. Setiawan, M. Sakamoto, T. Fujisaki, S. M. Lyth, Y. Shiratori, Biomass Bioenergy, 2022.

[3] T. Fujisaki, Y. Tsuji, P. H. Tu, T. C. D. Doan, D. S. Rivera Rocabado, A. T. Staykov, K. Yashiro, Y. Shiratori, Phys. Chem. Chem. Phys. 2024

Designing Impurity Doping in Two-Dimensional Materials by First-Principles Calculations

Soungmin Bae

Institute for Materials Research, Tohoku University, 2-1-1 Katahira, Aoba-ku,
Sendai, 980-8577, Japan

Introduction

The critical dimensions of modern semiconductor fabrication have already reached just a few nanometres, and further miniaturization of silicon-based devices is approaching its physical limits. To push integrated circuits into the true nanoscale regime, entirely new device architectures built on two-dimensional (2D) materials are indispensable.

Transition-metal dichalcogenides (TMDCs) with layered crystal structures—most notably MoS_2—retain high electrical conductivity even in monolayer form (< 1 nm), making them strong candidates for next-generation transistor channels. Yet TMDCs suffer from large contact resistance at metal interfaces, so purposeful tuning of their intrinsic properties is essential.

In this study, we systematically explore stable impurity-doped structures and strategies for electrical property control in 2D MoS_2 by means of first-principles calculations.

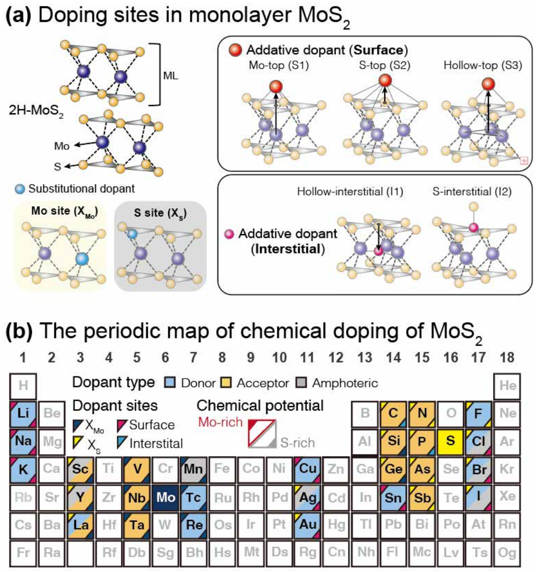

Figure 1. (a) Possible doing sites of 2H-MoS_2 considered in this study. (b) Stable dopant sites predicted for 27 elements from first principles point defect calculations.

Computational Methods

To capture the formation of localized polaron states and to evaluate donor/acceptor transition levels with high fidelity, we performed exhaustive density-functional-theory (DFT) calculations on impurity-doped MoS_2. Roughly twenty dopant elements from the periodic table were surveyed in three configurations—substitutional, surface-adsorbed, and interstitial—while charge states from −2 to +2 were considered. Thermodynamic stability was assessed under varying chemical potentials and Fermi-level positions.

All calculations employed the Vienna Ab initio

Simulation Package (VASP), and defect-formation energies were post-processed with our in-house pydefect workflow.

Discussion

Figure 1 summarizes the energetically preferred configurations. Elements adjacent to Mo or S in the periodic table tend to substitute for Mo or S, respectively. Alkali metals preferentially adsorb on the surface, while small-radius elements such as C and P are stabilized at interstitial sites. Representative electronic structures for $\mathrm{Re_{Mo}}$ and $\mathrm{Nb_{Mo}}$ dopants are plotted in Figure 2. In both cases, carriers introduced by Re or Nb localize strongly around the dopant, forming distinct polaronic states. Similar behaviour was observed for all 27 elements examined, implying that charge transport in doped monolayer $\mathrm{MoS_2}$ is dominated by impurity (hopping) conduction. These insights not only aid the rational design of high-performance TMDC-based devices but also advance our fundamental understanding of $\mathrm{MoS_2}$ electronics.

References

[1] Universal Polaronic Behavior in Elemental Doping of $\mathrm{MoS_2}$ from First-Principles, Soungmin Bae, Ibuki Miyamoto, Shin Kiyohara, Yu Kumagai, ***ACS Nano*** 8, 33988–33997(2024).

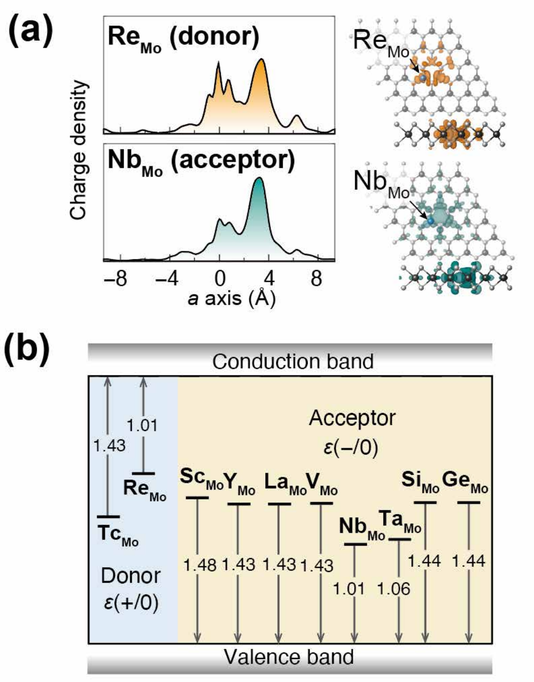

Figure 2. (a) Polaronic (localized) charge distribution of $\mathrm{Re_{Mo}}$ (donor) and $\mathrm{Nb_{Mo}}$ (acceptor) in monolayer $\mathrm{MoS_2}$. (b) Donor/acceptor charge transition levels of dopants in Mo site in monolayer $\mathrm{MoS_2}$.

Understanding of Spin-splitting Phenomena in Altermagnets

Kunihiko YAMAUCHI

Center for Spintronics Research Network, Osaka University, Toyonaka, Osaka 560-8531, Japan

We have investigated spin-splitting phenomena in altermagnetic materials, building on our research initiated last year on altermagnet MnTe [1]. In practice, a combination of first-principles DFT calculations (using the VASP and Wannier90 codes) and ARPES experiments enables us to reveal the electronic structure and uncover the microscopic mechanisms underlying macroscopic material properties.

RuO_2 was initially proposed as a candidate altermagnet that exhibits spin-split band structures in the antiferromagnetic phase, even in the absence of spin-orbit coupling. However, the antiferromagnetic nature of RuO_2 is currently a subject of intense debate. In this study, we elucidated the band structure of the (100), (110), and (101) surfaces of bulk single-crystalline RuO_2. Regardless of surface orientation, the ARPES-derived band structures show semi-quantitative agreement with bulk calculations in the nonmagnetic phase, but exhibit significant discrepancies with those in the antiferromagnetic phase.

These findings suggest the absence of the altermagnetic spin splitting in RuO_2. Moreover, we identified nodal lines near the Fermi energy that give rise to π Zak phase and the topologically protected surface states in nonmagnetic RuO_2 as shown in the figure below. This work is currently being prepared for publication [3].

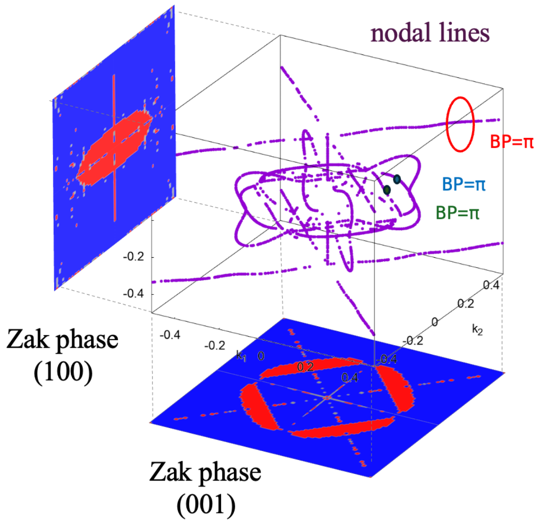

Figure: Nodal-lines and π Zak phase responsible for the topological surface states in nonmagnetic RuO_2.

References

[1] T. Osumi, S. Souma, T. Aoyama, K. Yamauchi, et al., Phys. Rev. B **109**, 115102 (2024).

[2] K. Nakayama, A. Tokuyama, K. Yamauchi, et al., Nature **631**, 54 (2024).

[3] T. Osumi, K. Yamauchi, et al., arXiv:2501.10649 (2025).

First-Principles Calculation on the Adsorption of Ethylene Acrylic Acid Molecules on Chromium Oxide Surfaces

Hiroki IWAI, Yuta TSUJI
Interdisciplinary Graduate School of Engineering Sciences,
Kyushu University, 6-1, Kasuga-koen, Kasuga, Fukuoka, 816-8580, Japan

Hybrid materials that combine metals and polymers are widely utilized across various fields, including aerospace and biomedicine. Specifically, the laminated strips composed of chrome-plated steel and ethylene-acrylic acid (EAA), which are the focus of this study, are employed as protective materials for fiber optic cables. A thorough understanding of the bonding mechanisms between these materials is crucial for improving the long-term stability of the cables. Experimental studies indicate that at the adsorption interface between chrome-plated steel and EAA molecules, two distinct types of coordination bonds, in addition to hydrogen bonding, are formed: (O=)C–O–Cr, which is monodentate, and –C–(O–Cr)$_2$, which is bidentate [1]. In this study, the adsorption energies of EAA molecules on Cr_2O_3 (001) and (012) surfaces, both with a thin layer of chromium hydroxide and without it, were evaluated using density functional theory (DFT). The bonding mechanisms observed in the experiments were corroborated through the DFT calculations at the adsorption interfaces. When coordination bonds were formed, the adsorption interface exhibited greater stability compared to when adsorption occurred solely via hydrogen bonding. However, on the (012) surface with the hydroxide layer, the Cr atoms became coordinatively saturated, preventing the formation of coordination bonds between the EAA molecules and the surface. Furthermore, calculations performed under ferromagnetic conditions, in contrast to antiferromagnetic conditions, revealed minimal differences in the adsorption energy, with negligible structural differences between the two magnetic states. This suggests that the adsorption energy of antiferromagnetic materials can be effectively approximated by that of ferromagnetic materials, with only a minor error.

References

[1] X. Zou, *et al. ACS Appl. Mater. Interfaces*, **14**, 27383 (2022).

First-principles study of surface and defect systems for power electronics materials

Kaori SEINO
Department of Materials Science and Engineering, Kyushu Institute of Technology
Sensui-cho 1-1, Tobata, Kitakyushu, Fukuoka 840-8550, Japan

Power device solutions for highly efficient power are a technical challenge directly related to environmental issues. In addition to Si-based power devices, SiC-based and GaN-based power devices have recently been used. Since high efficiency is also required for power devices that replace silicon, it is essential to minimize the effects of defects that may affect device performance. Moreover, diamond has overwhelming advantages over Si, SiC, and GaN in power electronics, although it is not on the market. For these new power devices to perform as expected, their surface and defect characteristics must be understood.

In this project, we have performed first-principles calculations of surface and defect systems for power electronics materials. For GaN, we consider the atomic diffusion of a Mg atom in p-type GaN via the vacancy mechanism. As a local structure for atomic diffusion of a Mg atoms in GaN, a defect complex which consists from Ga vacancy (V_{Ga}) and a Mg substitutional to Ga site ($\mathrm{Mg}_{\mathrm{Ga}}$) would be a starting configuration of Mg diffusion. Therefore, we first clarify structural and electronic properties of defect systems, V_{Ga}, $\mathrm{Mg}_{\mathrm{Ga}}$, and its complex $\mathrm{Mg}_{\mathrm{Ga}}$-$V_{\mathrm{Ga}}$ by spin-polarized HSE calculations containing 360 atoms using the VASP package [1].

In the case of $\mathrm{Mg}_{\mathrm{Ga}}$-$V_{\mathrm{Ga}}$, the removal of a Ga atom results in four N dangling bonds, and substituting the Ga atom with an Mg atom reduces the number of electrons by one. Therefore, in the neutral charge state of $\mathrm{Mg}_{\mathrm{Ga}}$-$V_{\mathrm{Ga}}$, there are one hole derived from the acceptor atom and four N dangling bonds occupied by a total of five electrons, i.e., possibly four defect states. Accordingly, we can consider high- and low-spin configurations with S=2 and S=0, respectively. Furthermore, the position of V_{Ga} is considered perpendicular or parallel to the c-axis related to Mg impurity. The local electronic structure near the $\mathrm{Mg}_{\mathrm{Ga}}$-$V_{\mathrm{Ga}}$ region, in particular near V_{Ga}, is remarkable as shown in Fig. 1.

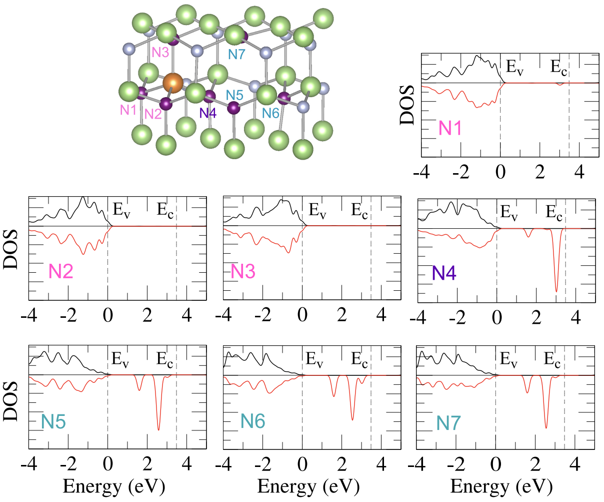

Figure 1: Local atomic configuration of defect complex $\mathrm{Mg}_{\mathrm{Ga}}$-$V_{\mathrm{Ga}}$ in GaN with pDOS of 2p orbitals.

References

[1] K. Seino, K. Shiraishi, and A. Oshiyama, *in preparation*.

Theoretical evaluation of mechanical properties of nano-carbon device structures

Koichi KUSAKABE
Graduate School of Science, University of Hyogo
Kouto, Kamigori-cho, Ako-gun, Hyogo 678-1297

In this study, we investigated nano-carbon and molecular structures and their dynamical properties, as well as layered material structures relevant for the molecular sensing and spintronics applications.

Our design method created material design of a possible Heisenberg spin chain with spin gap, which was realized in a polymerized hydrocarbon molecule called poly-PTM.[1] We have confirmed realization of a new 2D S=3/2 spin system by certifying material stability of the 2D poly-PTM using the density functional theory (DFT) simulation. The magnetic property was determined by construction of the effective Heisenberg Hamiltonian, where its effective exchange interactions were derived by evaluating a low-energy electron Hamiltonian. The localized zero-modes play relevant roles for both the design step and the realization step giving feasible magnetic exchange interaction strength for a quantum computation device.[2]

Topological insulator Bi_2Se_3, which is a layered Van-der-Waals crystal providing a spin-current device. Surface terminations control is shown to be plausible by having various cleaved surfaces, whose topological electronic states are confirmed by our simulations.[3]

Second harmonic generation of $La_4Ge_3S_{12}$ was observed in a recent experiment, whose electronic structures were directly confirmed by our electronic structure calculations.[4] This result again certified relevance of direct comparison of DFT-based simulations with experiments.

Giant Rashba spin-orbit coupling on light-element polar superlattices were designed by an international collaborative work. This investigation focuses staked ultra-thin material structures, whose spintronics properties are newly confirmed.[5]

Mechanical properties of stacked molecular structures, *i.e.* the amyloid-β protein, are analyzed using the nudged-elastic-band method in the DFT simulation. The dynamical properties of a protein molecule at an edge of the fibril are explored, where steric hindrance is important for an elementary deformation process. The size of a residue and occurrence of extra hydrogen bonding are keys to judge probable dissociation process of the fibril.

References

[1] N. Morishita, *et al.*, Appl. Phys. Express **14**, 121005-1-4 (2021).

[2] K. Komatsu, *et al.*, J. Phys. Soc. Jpn. 94, 044704 (2025).

[3] K. Fukumoto, *et al.*, Sci. Rep. 14, 10537 (2024).

[4] H. Ohtsuki, *et al.*, Z. anorg. allg. Chem. e202500029, (2025).

[5] Y. Wicaksono, *et al.*, Phys. Rev. B **110**, L220408 (2024).

Improving Stability of Molecular Dynamics Simulation using Machine-Learning Interatomic Potentials

Kohei Shimamura

Department of Physics,

Kumamoto University, 2-39-1 Kurokami, Chuo-ku, Kumamoto 860-8555

By training on highly accurate first-principles molecular dynamics (FPMD) data, the development of machine-learning interatomic potentials (MLIPs) that maintain the accuracy of FPMD while enabling large-scale and long-time MD simulations has been advancing. Through improvements in training methods, we have been able to construct robust MLIPs over the series of our projects, and we are actively applying them to the calculation of important physical quantities such as thermal conductivity. However, instabilities can still arise during MD simulations. These instabilities typically manifest when MD simulations are performed on systems larger than those represented in the training data. Since the size of systems treatable by FPMD is limited, supplementing training data for larger systems is challenging. Nevertheless, overcoming this issue is essential for handling more realistic systems.

In this study, we aimed to achieve stable MD simulations for one of the graph neural network-type MLIPs, the Allegro model [1], by adopting the Potential Averaging (PA) that we proposed [2]. The PA method belongs to ensemble learning, where multiple MLIPs are treated as a single predictor, and the "averaged forces" computed by these MLIPs are used in the MD simulations. Furthermore, by utilizing the "standard deviation of the forces," it naturally connects to active learning, which allows efficient collection of training data.

We found that, to implement the PA method in the Allegro model, it is necessary to modify not the main body written in Pytorch, but the interface part developed to link Allegro with the MD code LAMMPS, specifically the file pair_allegro.cpp written in C++. Even when MD simulations are performed using MD codes other than LAMMPS, it was possible to run them by modifying only pair_allegro.cpp.

The code validation was conducted using silver chalcogenide systems, for which we had accumulated sufficient knowledge through previous projects. In addition, we use the code developed in this study for a microscopic-level analysis of the supercooled liquid state of Mg alloys. The results of the study on the Mg alloys were presented at the 2025 Spring Meeting of the Physical Society of Japan.

References

[1] A. Musaelian, *et al.*: Nat. Commun. **14**, 579 (2023). [2] D. Wakabayashi, *et al.*: J. Phys. Soc. Jpn., **92**, 074002 (2023).

Quantitative description of cation-dependent electrode potential shift based on liquid Madelung potential

Atsuo YAMADA

Department of Chemical System Engineering,

The University of Tokyo, Bunkyo-ku, Hongo, Tokyo 113-8656

The electrode potential (E) governs the driving force of redox reactions in any electrochemical system. While the Debye–Hückel theory describes electrostatic interactions in dilute solutions, it fails at higher concentrations. To address this, we introduced the concept of the liquid Madelung potential, which explicitly treats electrostatic interactions in electrolyte solutions and successfully reproduces experimental potential shifts [1]. To further improve accuracy, we developed a thermodynamic framework based on MD simulations that considers not only electrostatic interactions but also van der Waals and entropic contributions to the Gibbs energy. This approach was validated for Na^+ and K^+ systems, in addition to the Li^+ system.

Figure 1a shows experimental potential shifts (open circles) as a function of concentration. Smaller cations deviate more from ideal Nernst behavior (dashed line), while calculated shifts (solid circles) agree well with experiment. These shifts stem from a Coulombic penalty caused by substitution of electron-localized solvent with electron-delocalized anions around the cation, which is more pronounced for smaller cations (Figure 1b). The developed computational approach thus provides a general, quantitative framework for potential shifts across alkali cations.

References

[1] N. Takenaka, S. Ko, A. Kitada, A. Yamada, *Nat. Commun*, **15**, 1319 (2024).

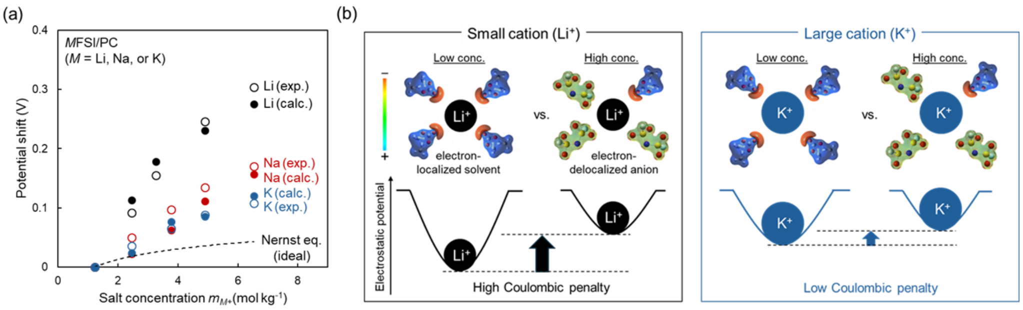

Figure 1 (a) Experimental (open circles) and calculated (solid circles) potential shifts for *M*FSI/PC electrolytes (*M* = Li, Na, or K) as functions of salt concentration (m_{M+}) relative to reference concentration of 1.2 mol kg⁻¹. (b) Schematic illustration explaining the origin of the cation-dependent potential shifts.

Distortion of ultrasmall metal oxides and their electronic state

Akira Yoko

International Center for Synchrotron Radiation Innovation Smart

Tohoku University, Aramaki aza Aoba, 468-1、Aoba-ku, Sendai, Miyagi, 980-8572, Japan

Size effect of materials in nanoscale has been attracting many attentions because of its unique physical properties. Recently, ultrasmall metal oxides can be synthesized by continuous flow hydrothermal method [1,2]. Precisely controlled metal oxide nanoparticles can be obtained with large scale synthesis, and it is currently important to study size effects in ultrasmall region (approximately 1~3 nm) to understand and predict the new properties of those ultrasmall particles.

As one example of the nano-size effect, large magnetic moment of cerium oxide (CeO_x) nanoparticles compared to its bulk has been reported [3,4]. Researchers proposed many possibilities of the origin of unusual magnetism. Although excessive oxygen such as oxygen antisites, interstitial, or Ce vacancy [5] can theoretically contribute to the magnetism in bulk structures, the atomistic structural origin of the size-effect is unclear to date. Here, we propose that the peroxidized structure in vertices of $CeO_{2+\delta}$ nanoparticles attribute to the magnetism in nanoparticles by first-principles calculations of the $Ce_{13}O_{32}$ nanocluster and experimental observation of nanoparticles whose diameter is up to 4 nm synthesized using hydrothermal reaction [1].

We employed density functional theory calculation using VASP package. PBE functional with Hubbard U correction for $4f$ orbitals is applied with on-site potential 5 eV [6]. The electronic density of states (DOS) shows obvious spin splitting in the $Ce_{13}O_{32}$ cluster, which has high symmetry of the arrangement of surface oxygen atoms. It results in a magnetic moment $m = 12.0\ \mu_{\mathrm{N}}$. On the other hand, if we take six oxygen atoms from the cluster and calculate the stoichiometric proper $Ce_{13}O_{26}$ cluster, it does not show any magnetic properties. The results indicate that the surface peroxidization on the nanocluster induce the magnetism.

References

[1] A. Yoko et al., J. Am. Chem. Soc. 146, 16324 (2024).

[2] A. Yoko et al., Precision Chemistry, In press (2025).

[3] M. Coey et al. Nat. Phys., 12, 694 (2016).

[4] K. Ackland and J. M. D. Coey, Phys. Rep. 746, 1 (2018).

[5] A.G. El Hachimi et al., Comput. Mater. Sci. 85, 134 (2014).

[6] M. Nolan et al., Surf. Sci., 576, 217 (2005).

Development of Stretchable Electret Materials for Energy Harvesting with the Aid of Machine Learning

Yuhan Gu, Rui WANG, Kuniko SUZUKI, and Yuji SUZUKI

Department of Mechanical Engineering

The University of Tokyo, Hongo, Bunkyo-ku, Tokyo 113-8656

Electronic devices with skin-like mechanical properties have significant potential in health monitoring and human-machine interface, particularly in wearable and implantable devices [1]. To ensure the overall flexibility of such electronic skin, it is highly desirable to develop intrinsically flexible power sources, such as kinetic energy harvesters using the stretching motions of skin.

Electret is a class of dielectric material with quasi-permanent charges, which can store charges for a long time, even decades [2]. Since electret energy harvesters have a high output power at low frequency with a thinner profile than other principles [3], they are excellent candidates for powering skin electronics.

We recently proposed perfluoro-elastomer FFKM as the base material for stretchable electrets [4]. The cross-linking process is employed for improving the stretchability of elastomer, but it is also used for embedding deep charge traps in the elastomer. By using triallyl isocyanurate (TAIC) as the cross-linking agent, the surface charge density as high as 0.74 C/m^2 has been obtained.

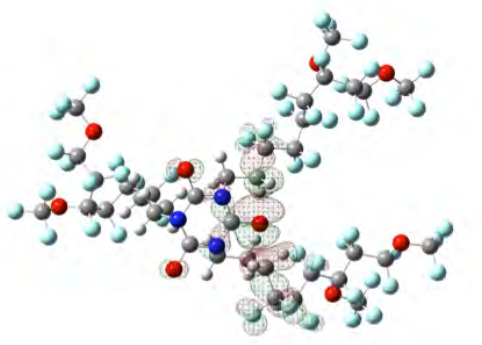

Fig. 1. Preliminary DFT results of cross-linked FFKM with TAIC [4].

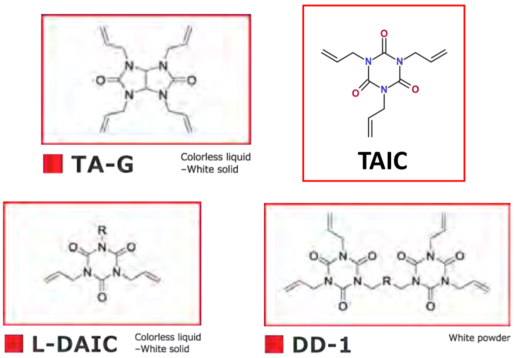

Figure 2. Cross-linking agents studied in this work.

In the present study, we investigate the effect of different cross-linking agents (Fig. 2) on the stretchability and charge stability of cross-linked FFKM.

All the quantum chemical calculations are made with the software GAUSSIAN [5] at the DFT level with the CAM-B3LYP functional, while PCM is combined for solid-state analysis due to the solvation effect correction. The 6-31+G(d,p) basis set is employed to reduce CPU time

Figure 3 shows the distribution of trapped charges in FFKMs. In pristine FFKM, charges are distributed widely in the molecular structure, indicating shallow charge trap. On the other hand, all the cross-linked FFKMs exhibit deep charge trap, and the charges are concentrated in the cross-linking agent. The ionization potential (IP), which is the index of charging performance [2] of those cross-linked FFKMs are 8.57, 8.55, 8.52, and 7.1 eV for DD-1, L-DAIC, TAIC, and TA-G, while that of pristine FFKM is 11.2 eV.

Therefore, FFKM/TA-G should have the highest charging performance. Our physical experiments actually show that FFKM/TA-G gives the highest surface potential after charging and the highest peak temperature in the TSD (thermally stimulated discharge) spectra [6]. This fact proved that DFT-based screening of cross-linking agents is effective for finding high-performance stretchable electrets using FFKM.

This work was supported by JSPS KAKENHI Grant Number JP24H00306. The computation in this work has partially been done using the Supercomputer Center, the Institute for Solid State Physics, the University of Tokyo (ISSPkyodo-SC-2024-Ca-0002).

References

[1] W. Gao, et al., Nature, 529, pp. 509-514 (2016).
[2] Z. Mao, et al., Adv. Mater., 2303827, (2024).
[3] Y. Suzuki, IEEJ Trans. Electr. Electr. Eng., 6, pp. 101-111 (2011).
[4] R. Wang, et al., PowerMEMS 2022, Salt Lake City, pp. 14-17 (2022).
[5] M. Frisch, et al., “Gaussian 09, Rev. A. 1,” Gaussian, Inc. Wellingford, CT, (2009).
[6] R. Wang et al., Adv. Mater., submitted.

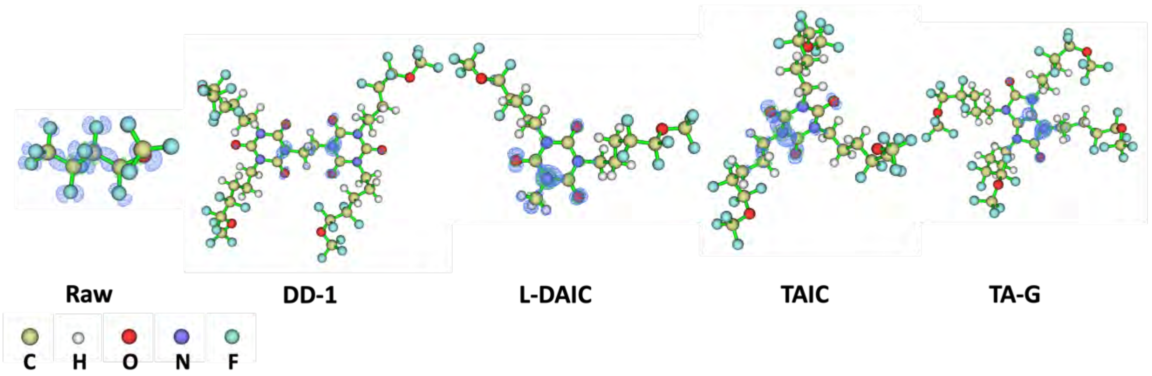

Figure 3. Visualized distribution of trapped charges in FFKMs [6].

Material Design Using Crystal Structure Prediction and First- Principles Calculations

Tomoki YAMASHITA
Department of Electrical, Electronics and Information Engineering,
Nagaoka University of Technology
Kamitomioka-machi, Nagaoka, Niigata, 940-2188

We have studied the structural stability of $\mathrm{Li}_x M_{1-x}\mathrm{Cl}_{2-x}$ (M = Ca, Mg) that can be a candidate material for solid electrolyte of Li-ion batteries. While the synthesis of $\mathrm{LiCaCl_3}$ ($x = 0.5$) has been reported [1], its crystal structure has not yet been elucidated. A crystal structure prediction simulation for $\mathrm{LiCaCl_3}$ was performed using CrySPY [2]. The calculation was performed with 20 atoms, and the structure search was conducted using an evolutionary algorithm with 20 structures per generation up to the 37th generation. Structure optimization and energy evaluation were carried out using the first-principles calculation software VASP. The PBE exchange-correlation functional was employed, and each structure was calculated using a single node. The most stable structure obtained from the search is shown in Fig. 1. The formation energy of this structure, calculated using LiCl and $\mathrm{MgCl_2}$ as reference compounds, is –3.2 meV/atom. Although the value is negative, the result indicates that the energy gain is negligible. These results suggest that, rather than stabilizing in a simple ordered phase, $\mathrm{LiCaCl_3}$ favors a disordered phase that becomes stable above a certain temperature.

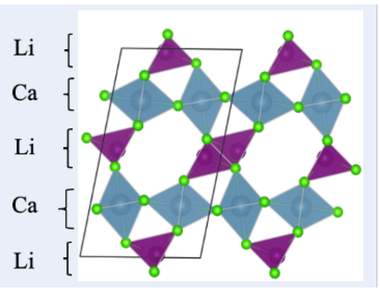

Figure 1: Stable structure of $\mathrm{LiCaCl_3}$ obtained by crystal structure prediction.

Another research topic addressed in this study was the investigation of defect formation in the semiconductor material $\mathrm{Cu_2Sn_{0.5}Ge_{0.5}S_3}$ (CTGS). Formation energies of various defects in CTGS were calculated using VASP. The HSE06 hybrid functional, which provides a good reproduction of the band gap, was employed for the exchange-correlation treatment. The eFNV correction scheme by Kumagai and Oba [3] was applied to account for defect formation energy corrections, as implemented in the pydefect code [4]. First-principles calculations with the HSE06 functional were performed using 16 compute nodes for each calculation. The Cu vacancy defect was found to have a low formation energy and to be the dominant defect. It is also expected to act as a shallow acceptor level, consistent with experimental observations, indicating that it serves as the primary source of holes. Donor levels were identified within the band gap for the (+1/0) charge transition levels of the $\mathrm{Sn_{Cu}}$ and $\mathrm{Ge_{Cu}}$ substitutional defects. Although the band gap can be tuned by varying the Sn/Ge ratio, these donor levels become deeper as the band gap increases, indicating that they may contribute to the reduced power conversion efficiency. In CTGS, the $\mathrm{Sn_{Cu}}$ and $\mathrm{Ge_{Cu}}$ antisite defects form deeper levels as the band gap increases. This indicates that synthesizing the material with a composition ratio that suppresses the formation of these levels, corresponding to a band gap of approximately one eV, may be one of the key conditions for achieving high conversion efficiency.

References

[1] K. Mahendran, S. Nagaraj, R. Sridharan, and T. Gnanasekaran, Journal of Alloys and Compounds **325**, 78 (2001).

[2] T. Yamashita, S. Kanehira, N. Sato, H. Kino, H. Sawahata, T. Sato, F. Utsuno, K. Tsuda, T. Miyake, and T. Oguchi, Sci. Technol. Adv. Mater. Meth. **1**, 87 (2021).

[3] Y. Kumagai and F. Oba, Phys. Rev. B **89**, 195205 (2014).

[4] Y. Kumagai, N. Tsunoda, A. Takahashi, and F. Oba, Phys. Rev. Mater. **5**, 123803 (2021).

Study on the etching mechanism of Si in catalyst-refereed Etching

Daisetsu TOH, Pho Van BUI, Kiyoto KAYAO, Hiroto YAMASAKI, Kouji INAGAKI,
Yoshitada MORIKAWA

Department of Precision Engineering, Graduate School of Engineering,
The University of Osaka, Yamada-oka, Suita, Osaka 565-0871

Si has recently been utilized as a substrate material for X-ray mirrors due to its thermal stability and ease of processing. To achieve high reflectivity and focusing performance, the mirror surface must be atomically smooth. To address this requirement, we propose the application of a novel surface fabrication technique, Catalyst-Referred Etching (CARE). In this method, Si surface was etched via hydrolysis reaction enhanced metal catalyst, leading to atomically smooth surface [1]. In fact, surfaces polished by the CARE method exhibit atomically stepped, extremely smooth surfaces. On the other hand, the etching mechanism of the CARE method requires that hydroxyl (OH) groups exhibit nucleophilicity toward step-edge atoms. However, in the case of Si, where the step-edge atoms are not ionized, OH groups cannot approach the step edges, making it difficult to form stable intermediate states and thereby hindering the progress of etching. To address this issue, we propose the following hypothesis: OH groups formed by the dissociative adsorption of water molecules on the catalyst surface replace hydrogen atoms bonded to step-edge Si atoms, resulting in the formation of OH-terminated step edges, as shown in Fig.1. Through this process, the hydrolysis reaction can proceed in the same manner as previously described, as shown in Fig. 2. Thus, density functional theory (DFT) based calculations for Si(100) have been performed in this study. The calculations were performed by the first-principles approach using the STATE-senri program package. The first-principles simulations were based on the generalized gradient approximation (GGA) with the Perdew-Burke-Ernzerhof (PBE) functional. Ion cores were replaced by ultrasoft pseudopotentials for the Si, H, O, and Pt atoms. Valence wave functions and charge densities were expanded in the plane wave basis sets with cut-off energies of 25 and 225 Ry, respectively. To calculate the reaction pathway, the climbing image nudged elastic band method was adopted. The reaction energy profile for OH termination of step-edge Si atom on Si(100) are shown in Fig. 3. The OH termination required an activation barrier of 0.80 eV, which shows that OH termination proceeds easily. Nest, the height of activation barrier for etching the step edge Si atom via hydrolysis reaction was simulated. The simulation result shown in Fig. 4, indicates that OH termination reduces the potential energy of the intermediate state, lowering the energy barrier from 2.1 eV to 0.52 eV, and thereby promotes the removal of the step-edge Si atom. Our proposed etching mechanism was validated. Furthermore, the simulation results suggest that the presence of a catalyst enables etching of Si even in an environment without dissolved oxygen, leading to the formation of high-precision surfaces, thereby demonstrating the effectiveness of this method.

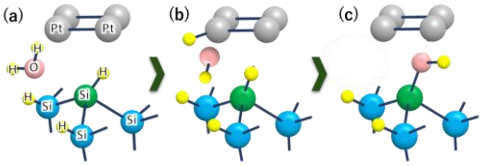

Fig.1 OH terminated step on step-edge Si atom (green marked) on Si(001) surface of (a) intial state, (b) intermediate state and (c) final state

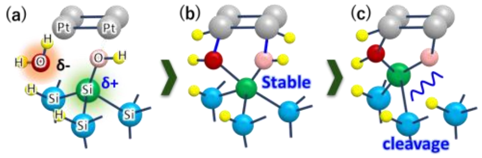

Fig.2 Etcing step on step-edge Si atom teminated by OH of (a) initial state, (b) intermediated state and (c) final state.

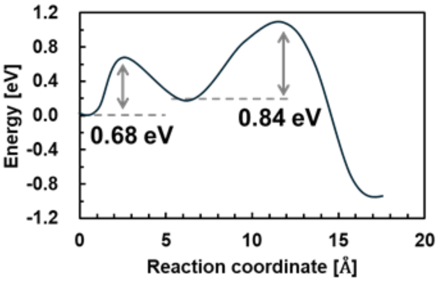

Fig.3 Reaction energy profiles for OH termination on a step-edge Si atom on Si(100)

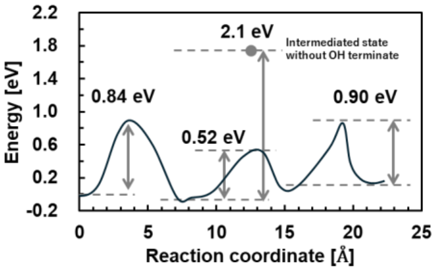

Fig.4 Reaction energy profiles for etching reaction on a step-edge Si atom terminated by OH on Si(100).

References

[1] D. Toh, P. V. Bui, A. Isohashi, N. Kidani, S. Matsuyama, Y. Sano, Y. Morikawa, K. Yamauchi, Rev. Sci. Instrum. Soc. Jpn. **90** 045115 (2019)

Ab Initio Study on Static Structure of White Light Generating Amorphous Molecular Materials

Akihide KOURA

Technical Division, Headquarters for Research and Development Strategy,
Kumamoto University, Kumamoto 860-8555, Japan

In this project, we performed the ab initio molecular dynamics (AIMD) simulations to clarify the static structure of the white light generating amorphous materials [1,2] consisting of $[(\mathrm{RSn})_4\mathrm{S}_6]$ clusters, where the substituents R are methyl (Me), phenyl (Ph), and cyclopentadienyl (Cp). In our simulations, we used eight molecules in a cubic supercell, i.e., numbers of atoms were 208 (Me), 432 (Ph), and 400 (Cp).

Firstly, we carried out AIMD simulations for these three targets. Although the obtained structure factors $S(k)$ seem to be in reasonable agreement with the experimental results, statistics of the intermolecular orientation correlations is insufficient because of only eight molecules.

Secondly, we tried to construct the machine learning interatomic potentials (MLIPs) using the Aenet package [3] to perform large-scale simulations. In this training process, we took not only energy but also interatomic forces and virial tensor into account as parameters of the cost function [4].

To validate the accuracy of MLIP, MLIP-MD simulations with the same size as the FPMD were carried out. Figure 1 shows the partial static structure factors $S_{\alpha\beta}(k)$ and partial radial distribution functions $g_{\alpha\beta}(r)$ of amorphous state consisting of $[(\mathrm{PhSn})_4\mathrm{S}_6]$ clusters obtained by AIMD (black dashed line) and MLIP-MD (red solid line) simulations. Represented result is not the best but a champion data in recent calculations. Peak positions of $S_{\alpha\beta}(k)$ are comparable between AIMD and MLIP-MD, however, some parts of them have slightly different regions. These wrong

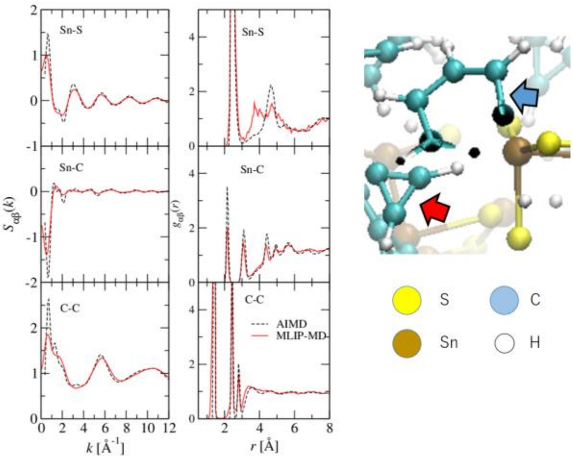

Fig. 1: Partial structure factors $S_{\alpha\beta}(k)$, radial distribution functions $g_{\alpha\beta}(r)$, and a snapshot of $[(\mathrm{PhSn})_4\mathrm{S}_6]$ clusters. Carbon atoms (blue ball) indicated with blue and red arrows are correct and broken phenyls, respectively.

results are easily shown in $g_{\alpha\beta}(r)$. The cores of the clusters consisting of Sn_4S_6 are basically kept their shape, however, the second neighbor of Sn-S at approximately $r = 4$ Å obtained by MLIP-MDs has a strange profile in $g_{\mathrm{SnS}}(r)$. Although a correlation function $g_{\mathrm{CC}}(r)$ by MLIP-MD also has similar profile that obtained by AIMD, the first peak of $g_{\mathrm{CC}}(r)$ by MLIP-MD appears at smaller *r* than that obtained by AIMD. This wrong part of the first peak of $g_{\mathrm{CC}}(r)$ is caused by the C-C-C triangle indicated by the red arrow shown in the right panel of Fig. 1. In this study, such carbon triangles have never appeared in the AIMD simulations, i.e., the triangles are considered to be artificial result which should be solved.

To refine the MLIP-MD simulations, we tested various parameters of energy E, atomic force F, and virial tensor W during training. To perform more robust MLIP-MD simulations, we also used the potential averaging method [5], in which number of MLIPs was up to 30 for averaging potentials.

However, this technique did not sufficiently work for the present target as shown in Fig. 1 so far. So, we are planning to employ the active learning (AL) method. One of our group members try to construct MLIP for the liquid state of lactic acid using AL method. In spite of a smaller number of atomic species comparing with $[(PhSn)_4S_6]$ clusters, it was needed that times of AL was eight.

It is expected that applying AL method to amorphous $[(PhSn)_4S_6]$ clusters will be not easy, however, we plan to continue improving this machine learning technique and clarify the amorphous states of these materials in the future.

References

[1] N.W. Rosemann, *et al.*, J. Am. Chem. Soc. **138**, 16224 (2016).

[2] B.D. Klee, *et al.*, Scr. Mater. **219**, 114851 (2022).

[3] N. Artrith and A. Urban, Comput. Mater. Sci. **114**, 135 (2016).

[4] A. Irie, *et al.*, J. Phys. Soc. Jpn. **90**, 094603 (2021).

[5] D. Wakabayashi, *et al.*, J. Phys. Soc. Jpn. **92**, 074002 (2023).

Interfacial Reaction Study Driven by Mathematical Science, MI and Molecular Dynamics

Ryuhei Sato

Department of Materials Engineering,

The University of Tokyo, 7-3-1 Hongo, Bunkyo-ku, Tokyo 113-8656, Japan

The realization of room-temperature superconductivity is considered one of the holy grails in physics. Polyhydrides with high hydrogen-to-metal (H/M) ratios are among the most promising candidates in terms of superconducting transition temperature (Tc). For instance, CaH_6 exhibits an exceptionally high Tc of 210 K at 160 GPa [1], suggesting that room-temperature superconductivity may be achievable through the exploration of ternary or quaternary compounds within this material class. However, the synthesis of such materials remains a significant challenge. As an example, although CaH_6 was theoretically predicted in 2010 [2], its experimental synthesis was not realized until nearly a decade later [1]. Thus, in addition to predicting stable structures and T_c values, it is crucial to identify feasible synthetic pathways and gain a fundamental understanding of the underlying reaction mechanisms. In this study, we conducted machine learning potential-based molecular dynamics simulations on the CaH_2/H_2 interface to elucidate the reaction mechanism involved in the formation of CaH_6 [3].

During the machine learning potential-based molecular dynamics simulations of the CaH_2/H_2 interface at high pressure and temperature (40 GPa, 1500 K), we observed surface disordering of CaH_2 followed by hydrogen uptake [3]. Upon completion of the reaction, the hydrogen-to-metal ratio in the resulting CaH_x structure converged to approximately 4, and the initially disordered structure was seen to reorganize into an ordered face-centered cubic (FCC) phase. Structural analysis using common neighbor analysis revealed that, during the reaction, the disordered calcium atoms did not exhibit typical crystalline arrangements such as FCC, BCC, or HCP, but rather adopted liquid-like or amorphous configurations. Meanwhile, persistent homology analysis indicated that the hydrogen network around calcium during the reaction closely resembled that of CaH_4. These results suggest that a liquid-phase CaH_4 acts as an intermediate during the hydrogenation process.

This surface-melting hydrogenation reaction ($CaH_2(s) + H_2 \leftrightarrow CaH_4(l)$) can be described by the following free energy relation:

$$\Delta G = \Delta G_{\text{fus}} + \Delta G_{\text{hyd}} + \Delta \gamma_{\text{interface}}$$

Here, ΔG_{fus} denotes the free energy of fusion for CaH_4 (CaH_4(s) ↔ CaH_4(l)), while ΔG_{hyd} represents the free energy change associated with the CaH_2 hydrogenation (CaH_2(s) + H_2 ↔ CaH_4(s)). $\gamma_{\mathrm{A-B}}$ corresponds to the interfacial energy between phases A and B. According to this relation, the surface-melting-assisted hydrogenation becomes favorable under high-pressure conditions because ΔG_{hyd} becomes negative with increasing pressure. In other words, applying a pressure higher than the equilibrium pressure lowers the activation energy for forming the intermediate liquid-phase CaH_x, thereby promoting the overall reaction [3].

References

[1] H. Wang et. al. PNAS 109 (2012) 6463.
[2] L. Ma et. al. PRL 128 (2022) 167001.
[3] R. Sato et. al. ChemRxiv (2024) DOI: 10.26434/chemrxiv-2024-2v5l6

Sulphur Adsorption on Pt Nanoparticles

Takehiko SASAKI and Kotaro MATSUDA
Department of Complexity Science and Engineering, Graduate School of Frontier Sciences,
The University of Tokyo, Kashiwa-no-ha, Kashiwa, Chiba 277-8561

For the use of fuel cells (PEFC) for automobiles, it is important to understand the adsorption states of poisoning speceis on Pt nanoparticles surfaces. Among possible poisoning speceis, sulphur-containing moieties are most important and seeking of removal methods is desired. We are collaborating the research group studying *insitu* measurements of high-energy resolution fluorescence detected X-ray absorption near-edge structure (HERFD-XANES). Various structures of sulphur adsorption states on the surface of platinum nanoparticles were obtained by DFT calculations, where SO_2 is used as the sources of sulphur species.

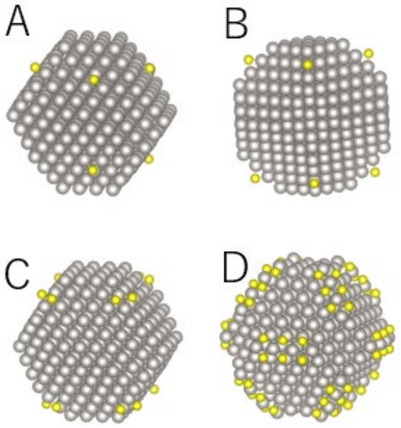

Fig. 1 Sulphur adsorption on Pt nanoparticles. A: hollow site adsorption on (111) terrace. B: Sulphur adsorption on edge. C: Two S atoms on edge. D: Double row- Bridged S atoms.

The Pt nanoparticles are Pt composed of 586 atoms of the cuboctahedron type corresponding to the actual catalyst particle size range of 2.5 nm. DFT calculations were conducted using VASP. The unit cell has a volume of 22.13×44.26×33.19 (Å^3) and contains 215 Pt atoms and sulphur atoms. The energy cutoff was 400 eV and the k-point mesh was 3x2x2. After optimization of this unit cell, cuboctahadral nanoparticle is obtained by symmetry operation, as shown in Fig. 1. The model A corresponds to the S adsorption on the hollow site on (111) terrace with the stabilized energy per one species is -6.00 eV. The model B corresponds to the S adsorption on the edge site (-4.49 eV). The model C corresponds to the two S atoms on the edge site (-5.14 eV). The model D corresponds to the Double row-Bridged S atoms on the edge (-5.34 eV). In previous study [1] adsorption states on the flat (111) terrace were obtained but this study revealed the importance of the edge site.

References

[1] M. Happel *et al.* , J. Phys. Chem. C **115**, 479 (2011).

Divergent Activity Shifts of Tin-Based Catalysts for Electrochemical CO_2 Reduction: pH-Dependent Behavior of Single-Atom Versus Polyatomic Structures

XUE JIA

Advanced Institute for Materials Research (WPI-AIMR),
Tohoku University, Sendai, 980-8577

We have studied divergent activity shifts of Tin-based catalysts for electrochemical CO_2 reduction [1], using large-scale parallel computer simulations

This year, we utilized supercomputing resources to perform high-throughput density functional theory (DFT) calculations and machine-learning force field (MLFF)-accelerated molecular dynamics (MD) simulations to investigate the structure–activity relationship of Sn-based catalysts for electrochemical CO_2 reduction reaction (CO_2RR). This study followed a nine-step research process. **Step 1** involved large-scale data mining of experimental literature from the past decade. **Steps 2–4** focused on analyzing structural information transition from single-atom catalysts (Sn−N_4−C SAC) to polyatomic Sn, surface reconstruction, and machine learning force field (MLFF)-accelerated molecular dynamics simulations. **Steps 5–6** examined pH-dependent activity through electric field simulations and ab initio MD (AIMD) simulations, considering *OCHO dipole moments and the potential of zero-charges (PZCs). **Steps 7–8** developed thermodynamic and kinetic models for CO_2RR, validated by comparing theory with experiments. Finally, **Step 9** conducted high-throughput screening to identify promising M–N–C catalysts for formic acid production under various electrochemical conditions.

Finally, we have revealed an interesting pH-dependent activity divergence in Sn−N_4−C SAC and polyatomic Sn in CO_2RR. Our results indicated that Sn−N_4−C and polyatomic Sn catalysts exhibit opposite trends in the response to the electric fields. Due to differences in local structure, *OCHO adsorbed on Sn−N_4−C SAC exhibits a positive dipole moment, making it more stable under a more negative electric filed (corresponding to an alkaline environment). In contrast, *OCHO with negative dipole moment on polyatomic Sn would be destabilized under alkaline conditions. This is the fundamental cause of the opposite volcano shift on the change of pH levels over Sn−N4−C SAC and polyatomic Sn.

References

[1] Y. Wang, D. Zhang, B. Sun, X. Jia, L. Zhang, H. Cheng, J. Fan, H. Li, Angew. Chem. Int. Ed. **64**, e202418228 (2025).

First-principles study on stability of magnetic materials

Yasutomi TATETSU

Meio University, Biimata, Nago, Okinawa 905-8585

Research and development of automation using AI and robots is accelerating towards the realization of a smart society. Since magnetic materials play a crucial role in the power units of many of these electronic devices, the search for novel magnetic materials with decarbonization in mind is an actively researched field. Furthermore, supported by the remarkable progress in computer hardware and software development, expectations are high for materials exploration using computer simulations. In this study, we applied Neural Network Potentials (NNP), which have recently attracted attention for their ability to perform atomic-level physical simulations in a very short time, to magnetic materials containing Fe, and verified their accuracy by comparing the results with those of first-principles calculations.

For multiple magnetic materials, we applied Matlantis and CHGNet [1, 2], in which NNP is implemented, to perform structural optimization and formation energy calculations. Furthermore, to confirm the reliability of the obtained stable structure and formation energy using NNP, we conducted accuracy verification using the first-principles calculation code OpenMX [3].

We compared the formation energies of each material calculated using OpenMX, Matlantis, and CHGNet. The calculation targets are approximately 200 materials containing Fe, including rare earth permanent magnets. In most materials, the NNP method accurately reproduced the trend of the results calculated with OpenMX. However, in some cases, the formation energies calculated with OpenMX did not match those obtained with the NNP method. These discrepancies tend to appear when formation energies are relatively small, which is a region where high-precision first-principles calculations are required anyway. We believe that detailed analysis is necessary regarding the reasons for the discrepancies. While accuracy verification ultimately requires comparison with high-precision first-principles calculations, the results suggest the potential effectiveness of NNP for high-throughput calculations that require a large amount of computation.

References

[1] S. Takamoto, *et al.*, Nat Commun 13, 2991 (2022); Matlantis (https://matlantis.com/), software as a service style material discovery tool.

[2] B. Deng, *et al.*, Nature Machine Intelligence **5**, 1031–1041 (2023).

[3] http://www.openmx-square.org

Study on physical properties of structural elementary excitations at solid surfaces and interfaces

Hiroyuki KAGESHIMA
Graduate School of Natural Science and Technology, Shimane University
1060 Nishi-Kawatsucho, Matsue, Shimane 690-8504

In this project, we have been focused on physical properties of structural elementary excitations, such as point defects and precursors, of semiconductor surfaces and interfaces [1, 2, 3]. In this year, we have focused on the physical properties of hexagonal boron nitride (hBN) growth on Cu(111) [4]. The calculations were performed based on the first-principles calculation. Program package PHASE/0 was employed [5].

The growth process of hBN on a Cu substrate is, at first glance, a simple phenomenon, in which B and N precursors just aggregate to form hBN islands. However, since hBN is a two-component material, the island shape can vary depending on the relative supply of B and N, which is governed by their chemical potentials. The energy of an island initially increases with size due to the high edge energy but decreases beyond a certain 'critical size', as the inner energy becomes dominant. Under conditions where the critical size is large, intrinsic nucleation becomes more difficult. Therefore, experimental conditions that lead to a larger critical size, controlled via chemical potentials, are desirable for achieving hBN layers with high crystallinity. To investigate this, we studied the relationship between island size, shape, and chemical potential using first-principles calculations, incorporating van der Waals interactions via the vdW-DF2-b86r functional.

To evaluate the critical size, it is necessary to examine the stability of islands at macroscopic scales. However, first-principles calculations are typically limited to systems of microscopic size. In this study, we aimed for higher accuracy by building upon insights from our previous work [3]. We computed the energies of nanoribbons with various widths, featuring both zigzag and armchair edges, as well as islands with different shapes and sizes. From these calculations, we extracted the energies associated with zigzag-edge B and N atoms, armchair-edge B and N atoms, corner B and N atoms, and inner B and N atoms. Using these atomic energy contributions, we then predicted the stability of hBN islands, over a wide range of sizes, including those approaching macroscopic scales.

We first investigated the relationship between island size, chemical potentials, and the resulting stable island shapes. Islands with zigzag edges are generally more stable than those with armchair edges. As a result, the most stable shapes are equilateral triangles and hexagons composed exclusively of zigzag edges. When the chemical potential shifts from a B-rich/N-poor condition to a B-poor/N-rich condition, the stable shape transitions from an equilateral triangle with zigzag B edges, to a hexagon with mixed zigzag edges, and eventually to an equilateral triangle with zigzag N edges.

Furthermore, we found that zigzag-edged equilateral triangles tend to form at smaller sizes, while zigzag-edged hexagons become more favorable at larger sizes. This size-dependent shape transition arises because inner atoms are stabilized by van der Waals interactions with the Cu substrate. As the island grows, the proportion of stable inner atoms increases, reducing the relative contribution of edge energy. This behavior is a distinctive feature of hBN grown on a Cu substrate and does not occur in freestanding hBN. Our finding also highlight a limitation in previous theoretical studies, which overlooked the stabilization effect of inner atoms and thus arrived at incorrect conclusions regarding the most stable island shapes.

Next, we investigated the relationship between critical size and chemical potentials. Under B-rich/N-rich conditions, the critical size becomes small, and can even drop below the size of a single atom when the chemical potentials are excessively high. This implies that islands nucleate rapidly whenever B and N atoms adsorb on the Cu surface, leading to the formation of an amorphous hBN layer. Conversely, under extremely B-poor/N-poor conditions, the critical size approaches infinity, meaning that spontaneous island formation becomes impossible. These findings indicate that a moderately B-poor/N-poor chemical potentials is optimal for promoting the growth of high-quality crystalline hBN layers. Such a condition corresponds to high-temperature growth with a limited supply of B and N precursors, aligning well with the experimental conditions commonly used in practice.

In experiments, equilateral triangular islands are frequently observed. Since subsurface B atoms are calculated to be more stable than those adsorbed on the surface, the Cu surface is likely to become N-rich under typical conditions. As a result, triangles with zigzag N-terminated edges are expected to form. In other experiments, hexagonal islands appear when O_2 is introduced into the source gas. This can be attributed to N reacting with O, thereby reducing the N concentration on the Cu surface and shifting the environment toward N-poor conditions. Similarly, hexagonal islands are also observed when the Cu surface pretreated by electrochemical polishing, which likely leads to surface oxidation and a B-rich condition. These observations are well explained by our theoretical framework, which consistently accounts for the experimental variations.

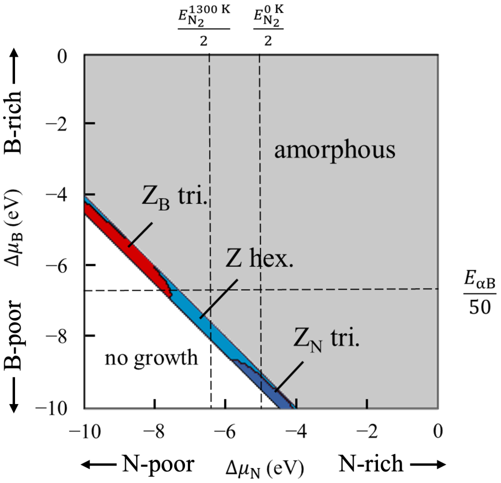

Figure 1: Phase diagram showing the stable shapes of hBN islands at the critical size, as a function of chemical potentials, during growth on the Cu(111) surface.

References

[1] H. Kageshima, T. Akiyama, and K. Shiraishi, Matter. Sci. Semicon. Process. **162** (2023) 107527 (7 pages).

[2] H. Kageshima, T. Akiyama, and K. Shiraishi, Jpn. J. Appl. Phys., 63 (2024) 04SP08 (5 pages).

[3] R. Imamura and H. Kageshima, Jpn. J. Appl. Phys., 63 (2024) 04SP39 (11 pages).

[4] R. Imamura, I. Seo, and H. Kageshima, e-J. Surf. Sci. Nanotechnol. 23 (2025) *advanced online publication* (13 pages).

[5] https://azuma.nims.go.jp

Development of Fast Calculation Codes of Berry Phases in First-principles Calculations and its Application to Energy Conversion Materials

Naoya YAMAGUCHI
Nanomaterials Research Institute (NanoMaRi), Kanazawa University
Kakuma-machi, Kanazawa, Ishikawa 920-1192

This year further development of calculation methods and programs for intrinsic anomalous Hall conductivity (AHC) was carried out. AHC is related to thermoelectric conversion phenomena such as the anomalous Nernst effect, and its intrinsic contribution is based on the Berry curvature of the electronic states of the material. Since the previous year, we have also been developing a computational method for analyzing the layer-by-layer contribution of the AHC by combining the local Berry phase (LBP) method with the hybrid Wannier function method. We have performed applied calculations on various systems such as magnetic topological insulators and magnetic metal thin films and confirmed that the layer-by-layer AHC contribution in magnetic topological insulators and magnetic metal thin films can be analyzed.

On the other hand, in complex material systems, especially those that have defects and impurities, many degenerate points occur due to folding of the electronic band structure in the first Brillouin zone (FBZ), and obtaining the intrinsic AHC is computationally difficult because it requires more k-point sampling than that for perfect crystals. We have developed the LBP method [1] by extending the Fukui-Hatsugai-Suzuki method [2] to metallic systems for intrinsic AHC calculations. In the LBP method, the calculation of the determinant of the overlap matrix that consists of the periodic parts of the Bloch functions between k-points on the edges of the plaquettes is necessary, so basically the occupation numbers within the plaquettes must be the same. When the chemical potential crosses bands, the occupation numbers differ near the intersection point, and they can be approximated by averaging. If there are degenerate points within the plaquette, coarse k-point sampling may result in only one of the bands at a degenerate point contributing to the determinant, leading to numerical instability.

Then, we implemented various methods for calculating determinants in the LBP method using the first-principles calculation code OpenMX [3]. We found that even when degenerate points exist due to the folding of the FBZ, it is possible to evaluate appropriately by successively assessing the properties of overlapping matrices and then providing appropriate minor determinants. We have shown that the proposed method is effective by performing AHC calculations for BCC iron and its supercell systems. In the conventional LBP method, the AHC vibration increased due to the superlattice formation of cells when sampling was performed with the almost same k-point spacing. In the above new method, in BCC iron, it was found that the degree of fluctuation in the results obtained using the primitive cell model, conventional cell model, and supercellized 4-atom model was equivalent, indicating that the AHC vibration, which appears as an error due to superlattice formation of cells, was suppressed. Excessive k-point sampling is no longer necessary, and the required number of k-points can be easily estimated, so it is expected that high-throughput calculations will also be possible. We have developed a new LBP method and have confirmed that the numerical instability can be resolved for various superlattice systems.

References

[1] H. Sawahata, N. Yamaguchi, S. Minami, F. Ishii, Phys. Rev. B **107**, 024404 (2023).

[2] T. Fukui, Y. Hatsugai, H. Suzuki, J. Phys. Soc. Jpn. **74**, 1674 (2005).

[3] http://openmx-square.org.

First-principles calculations of functionalities in Mn_3Sn-based alloys

Katsuhiro Tanaka[1] and Yuta Toga[1,2]
[1] *Department of Physics, University of Tokyo, Bunkyo-ku, Tokyo 113-0033, Japan*
[2] *JSR-UTokyo Collaboration Hub, CURIE, JSR Corporation, Minato-ku, Tokyo 105-8640, Japan*

Several studies have shown that a noncollinear antiferromagnet Mn_3Sn can show physical properties such as the anomalous Hall effect [1] and the tunnel magnetoresistance (TMR) effect [2], which have been observed typically in ferromagnets. In order to pursue the possibility of Mn_3Sn as a material for spintronic devices like thermoelectric devices and magnetic tunnel junctions (MTJs), we have investigated the physical functionalities of Mn_3Sn using first-principles calculations.

Particularly, we have focused on the enhancement of the intrinsic anomalous Hall conductivity (AHC) in Mn_3Sn through elemental substitution in its alloys. We have performed first-principles caluclation of the electronic structure of Mn_3Sn based on the density functional theory (DFT), using the Quantum ESPRESSO package [3]. Based on the results of the DFT calculation, we have constructed a tight-binding model with maximally localized Wannier functions using the Wannier90 package [4]. To calculate the AHC, σ_{xz}, it is needed to integrate the Berry curvature over the Brillouin zone with a dense $\boldsymbol{k}$-point mesh, which often demands a high computational cost.

We have investigated the effects of alloying using the virtual crystal approximation (VCA). In particular, we have simulated the substitutions of In for Sn and Cr for Mn, aiming at achieving the hole doping and tuning the electronic properties. Figure 1 shows the chemical potential dependence of σ_{xz} for the VCA calculations for $Mn_3(Sn, In)$ alloys. We can see a systematic shift of the main peak in the energy-dependent AHC with the increase of the In concentration. This result suggests that the hole doping via In substitution could potentially lead to a significant enhancement of the AHC near the Fermi energy at some specific In ratio. Furthermore, we have observed a similar systematic change in the AHC features as a function of the Cr ratio in the VCA calculations for $(Mn, Cr)_3Sn$ alloys, as shown in Fig. 2. These VCA results indicate that the hole doping through elemental substitution at both of the Sn and Mn sites will be a possible route for tuning the AHC in Mn_3Sn system. Since the VCA approach has limitations in precisely describing the electronic properties of the materials with element substitutiion, it will be also necessary to employ some other

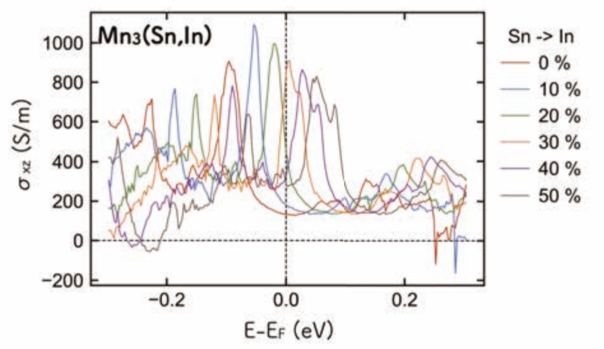

Figure 1: Calculated energy dependence of the anomalous Hall conductivity, σ_{xz}, of $Mn_3(Sn, In)$ alloys for various In ratios.

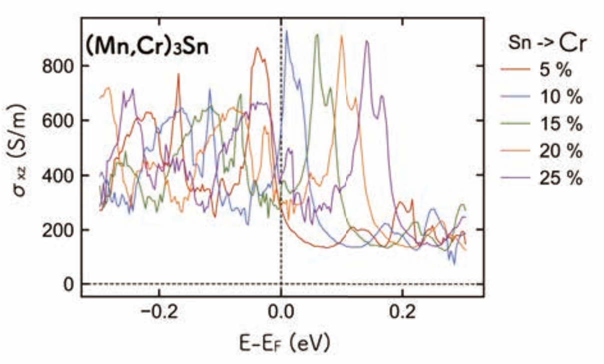

Figure 2: Calculated energy dependence of the anomalous Hall conductivity, σ_{xz}, of $(\mathrm{Mn},\mathrm{Cr})_3\mathrm{Sn}$ alloys for various Cr ratios.

methods like supercell calculations for more quantitative predictions.

Apart from the effect of elemental substition on the AHC, we have also investigated the potential of $\mathrm{Mn_3Sn}$ as a magnetic electrode of the MTJs. Constructing the MTJs using $\mathrm{Mn_3Sn}$, we have performed first-principles calculations of the TMR effect as well as the electronic structures of the MTJs.

References

[1] S. Nakatsuji, N. Kiyohara, and T. Higo, Nature **527**, 212 (2015).

[2] X. Chen et al., Nature **613**, 490 (2023).

[3] P. Giannozzi et al., J. Phys.: Condens. Matter **21**, 395502 (2009); P. Giannozzi et al., J. Phys.: Condens. Matter **29**, 465901 (2017).

[4] G. Pizzi et al., J. Phys. Cond. Matt. **32**, 165902 (2020).

Electronic state analysis on molecular thin film surface

Kaori Niki

Graduate school of science

Chiba University, Yayoi-cho, Inage-ku, Chiba 263-8522

Introduction

To reduce CO_2 emissions, catalyst development for CO_2 reduction has been actively pursued. We aimed to realize a CO_2 reduction catalyst using inexpensive metals and investigated the electronic states involved in the conversion process from CO_2 to CO on the ZrO_2 surface.

Method

We performed density functional theory (DFT) calculations using the Vienna Ab initio Simulation Package (VASP) version 6.4.1 [1,2]. The exchange correlation effects were described by the spin-polarized generalized gradient approximation (GGA) within the revised Perdew-Burke-Ernzerhof (RPBE) formalism [3]. We chose the surfaces of monoclinic ZrO_2(001), containing (2*2*2) elemental unit cells, and tetragonal ZrO_2(101), containing (2*1*2) elemental unit cells as slab models.

Results

It was found that the adsorption energy of CO2 on ZrO2 is lowest at oxygen vacancy sites. At this time, CO2 is bended when it is adsorbed as C fills the vacancy site. It was also found that electrons are exchanged between the vacancy sites of CO2 and ZrO2. It was found that the CO2 is separated into CO and OH when hydrogen atoms, which are added in the experiment, are adsorbed. Furthermore, when H is added, OH becomes H2O and is desorbed. At that time, the energy is more stabilized when new CO2 is adsorbed onto the defects than when defects are generated in ZrO2. This clarified at the electronic state level that a cycle of CO reduction is generated.

It was also found that, between a monoclinic surface and a tetragonal surface, more energy is required to generate H2O on the tetragonal surface. This clarified that the reduction cycle does not establish itself on the tetragonal surface, resulting in a smaller amount of reduction [4].

Conclusion

By performing VASP calculations, we clarified the structural changes of CO_2 and the electron transfer processes between CO_2 and the vacancy of ZrO_2.

References

[1] G. Kresse and J. Hafner, Phys. Rev. B **47**, 558 (1993).

[2] G. Kresse and D. Joubert, Phys. Rev. B **59**, 1758 (1999).

[3] J. P. Perdew, K. Burke, and M. Ernzerhof, Phys. Rev. Lett. **77**, 3865 (1996).

[4]A. Omata *et al.*, e-Journal surf. Sci. Nanoteh. **22**, 327 (2024).

First-principles study of surface atomic structure and chemical properties of intermetallic compounds

Kazuki Nozawa
Department of Physics and Astronomy, Kagoshima University,
1-21-35, Korimoto, Kagoshima 890-0065

This fiscal year, we have studied the adsorption structure of Pentacene (Pn) on the Ag-In-Yb quasicrystal (QC) surface, and the hydrogen and acetylene adsorption on the trace-amount Pd-doped $Al_{13}Fe_4$ intermetallic compound surface. These calculations were carried out using the VASP code.

In recent years, quasi-periodic molecular arrangements of Pn have been obtained by depositing Pn on the icosahedral Ag-In-Yb QC surfaces. To get insight into the details of the quasi-periodic Pn layer, we studied the stable adsorption structure of Pn on the two-fold and five-fold surfaces of the Ag-In-Yb QC. The atomic positions of the surface atoms were extracted from the X-ray diffraction experimental data, and the surface was approximated using a disk-shaped cluster with a diameter of 2.2 nm and a thickness of 0.8 nm to be treated within the ordinary DFT calculation. The simulation cell contains about 700 atoms. Because the calculated force acting on the atoms is incorrect, especially at the cluster edge, we identified the stable adsorption positions by manually varying the Pn molecule. We found that Pn is stable in the Yb-rich region. However, some typical motifs observed by STM experiments have not been explained by the calculated stable adsorption sites. We are currently investigating the possibility of a surface point defect at some Yb sites.

$Al_{13}Fe_4$ is a periodic approximant to decagonal QCs. The monoclinic unit cell contains 102 atoms, occupying 20 inequivalent atomic sites: Al(1)-Al(15) and Fe(1)-Fe(5). The surface was modeled by a symmetric slab model composed of seven atomic layers and a 1.55 nm thick vacuum layer. We previously studied the bulk and surface structure of $Al_{13}Fe_4$, where a single Pt atom is introduced per unit cell. This year, we studied the case where the Pd atom was introduced and confirmed that Pd occupying the Fe(1) site is exposed on the surface, as is the case with Pt. We also studied the adsorption of acetylene and hydrogen on this surface. The calculations for acetylene adsorption are almost completed, and the acetylene molecule tends to be stable on the Al_5Fe flower-like motif, which is a fragment of the puckered layer separated by cleavage.

First-principles molecular dynamics simulations for confined water

Tatsuhiko Ohto

Graduate School of Engineering, Nagoya University, Furo-cho, Chikusa-ku, Nagoya, 464-8603 Aichi, Japan

Water plays a crucial role in geological, biological, and technological processes. Nanoscale water confinement occurs in many of these settings, including sedimentary rocks, water channel proteins, and applications like desalination and water purification membranes. The structure and properties of water in nanoconfinement can differ significantly from bulk water, exhibiting, for instance, modified hydrogen bonds, dielectric constant, and phase transitions. Despite the importance of strongly nanoconfined water, experimentally elucidating the nanoconfinement effect on water, such as its orientation and hydrogen bond (H-bond) network, has remained challenging. Here, we study two-dimensionally nanoconfined aqueous electrolyte solutions with tunable confinement from nanoscale to angstrom-scale sandwiched between a graphene sheet and CaF2. We employ heterodyne-detection sum-frequency generation (HD-SFG) spectroscopy, a surface-specific vibrational spectroscopy capable of directly and selective probing water orientation and H-bond environment at interfaces and under confinement. Remarkably, the vibrational spectra of the nanoscale confined water can be described quantitatively by the sum of the individual water surface signals from the CaF2/water and water/graphene interfaces until the confinement reduces to angstrom-scale (< ~8 Å). Ab initio molecular dynamics simulations confirm our experimental observation. These results manifest that interfacial, rather than nanoconfinement effects, dominate the water structure until angstrom-level confinement.

References

[1] Y. Wang et al., arXiv:2310.10354v2

Material search and spin-orbit coupling induced properties at artificial interfaces and multilayers

Kohji NAKAMURA

Graduate School of Engineering, Mie University, Tsu Mie 5148507

Search of promising thin films with desired magnetic properties is an important goal in the field of spintronics. We here report on three examples calculated by using full-potential linearized augmented plane-wave (FLAPW) method [1].

Enhancement of interfacial perpendicular magneto-crystalline anisotropy (iPMA) at Fe/MgO: We demonstrated that large iPMA and low Gilbert magnetic damping constant (α) at Fe/MgO interface are achieved by substituting N-anions at MgO barrier interface. The iPMA is enhanced by four times and the α is reduced by 65% compared to the pristine Fe/MgO. The mechanism is explained by a band realignment at Fermi level (E_F), where the Fe $d_{\pm1}$ orbitals at the interface are pushed above and below E_F but the Fe $d_{\pm2}$ orbitals remain at E_F by the N-anion substitution.

Enhancement of spin Hall conductive (SHC) in Graphene/MoS$_2$: Generation and controlling of spin current in two-dimensional (2D) materials such as graphene are challenging due to small intrinsic SOC of the 2D materials. We predicted the finite SHC of 25 Ω^{-1}cm^{-1} in van der Waals heterostructure of graphene/MoS$_2$. By applying positive external-electric-field, we find that the SHC increase up to 170 Ω^{-1}cm^{-1} while application of negative external-electric-field hardly affects the SHC. The underlying mechanism is explained in terms of spin Berry curvature in Dirac-cone bands of graphene in the heterostructure, where the size of band gap is modulated sensitively by the magnitude of external-electric-field.

Code development for angle-dependent X-ray magnetic circular dichroism (AD-XMCD): Method to calculate AD-XMCD spectra was successfully developed and applied to $L1_0$-ordered FeX and CoX (X = Ni, Pt) alloys systematically. By changing incident angles and magnetic moments from [001] to [100], we demonstrated the modification of XMCD spectra at the L_2 and L_3 edges. We find that this originates from the changes in magnetic dipole and orbital moments that depend on the angle variation.

References

[1] K. Nakamura et.al., Phys. Rev. B **67**, 014420 (2003).

Prediction of properties of organic ferroelectrics and piezoelectrics by first-principles calculation

Shoji ISHIBASHI
National Institute of Advanced Industrial Science and Technology (AIST)
Tsukuba, Ibaraki 305-8568

In response to the application of an electric field, the refractive index varies linearly for certain class of materials. This effect is known as the Pockels effect and is one of the second-order nonlinear optical effects. In the present study, we simulated the Pockels effect in organic ferroelectric crystals of croconic acid (CRCA) and 5,6-dichloro-2-methylbenzimidazole (DC-MBI) [1].

Simulations were carried out in the following three modes: (1) with a clamped cell and clamped atomic positions (an optimized structure at $E = 0$), (2) with a clamped cell and relaxed atomic positions at E, and (3) with a relaxed cell and relaxed atomic positions at E. In the first mode, the response to electric field application is purely electronic. In the second mode, the ionic response was included. For the third mode, the piezoelectric effect was also added to the electronic and ionic responses. A dielectric constant ε at an electric field of E was evaluated using the formula $\varepsilon = 1 + (1/\varepsilon_0)(\mathrm{d}P/\mathrm{d}E)$, where ε_0 is the vacuum permittivity. Electric polarization values P were calculated at $E, E \pm 0.1, E \pm 0.2$ (MV cm^{-1}). By applying linear regression to the relationship between E and P, $\varepsilon(E)$ values were obtained. Pockels coefficients r_{ijk} were evaluated by applying linear regression to $1/\varepsilon(E)$. For CRCA, E values were sampled as $0, \pm 1, \pm 2$ (MV cm^{-1}) while for DC-MBI, simulations were also carried out at ± 3 (MV cm^{-1}) because its electro-optic response was small. For these organic crystals, the van der Waals interaction is critical, and two types of van der Waals density functionals vdW-DF-cx and rVV10 were used. These functionals reproduce the lattice parameters of CRCA and DC-MBI successfully [2]. All the calculations were performed using the QMAS code.

Table 1: Percentages from piezoelectric, ionic and electronic contributions.

	piezoelectric	ionic	electronic
CRCA*	32.2	57.7	10.1
CRCA†	24.4	61.8	13.8
DC-MBI*	54.1	24.5	21.4
DC-MBI†	58.5	21.0	20.5

* vdW-DF-cx, † rVV10

For CRCA and DC-MBI, the r_{333} values are obtained as 17.0 and 2.7 (pm/V) with the vdW-DF-cx functional while as 12.4 and 2.0 (pm/V) with the rVV10 functional, respectively. Percentages from piezoelectric, ionic and electronic contributions are shown in Table 1. It is shown that the ionic contribution is important particularly for CRCA. These calculated results are reasonable compared with the experimental ones [1].

References

[1] K. Sunami, S. Horiuchi, S. Ishibashi, and J. Tsutsumi: Adv. Electron. Mater. **11**, 2400346 (2025).

[2] S. Ishibashi, S. Horiuchi, and R. Kumai: Phys. Rev. Mater. **5**, 094409 (2021).

Electronic structures of doped carbon nanotubes

Yoshitaka FUJIMOTO
School of Engineering, Kyushu University, Fukuoka 819-0395

Carbon nanotubes (CNTs) are candidate materials for next generation nanoelectronics devices because they show unique and excellent electronic properties such as long mean free path and high carrier mobility. It has been often reported that the doping with heteroatoms can enhance the chemical reactivity of CNTs, and a variety of applicable systems such as catalyst and sensors are proposed using doped CNTs [1]. It has been reported that the boron-doped graphene can strongly bind with harmful NO_x molecules, which suggests the possibility to fabricate the harmful NO_x sensors [2, 3]. The B-doped (10,0) CNTs can adsorbe the toxic CO molecule, and it is revealed that the conductivity of the B-doped CNTs is largely changed by the adsorption of the CO molecule [4, 5]. Pyridine-type nitrogen-doped CNT is another candidate material for development of highly sensitive gas sensors. The adsorption properties of ammonia and water molecules to pyridine-type N-doped graphene have been studied and the ammonia and water molecules are adsorbed strongly to pyridine-type N-doped graphene [6].

We here report the adsorption properties of toxic molecules to the pyridine-type N-doped CNTs for designing high-performance gas sensors. We firstly exmaine the adsorption properties of toxic molecules (CO, NO, and NO_2) on the pyridine-type N-doped (11,0) CNTs. It is found that three kinds of molecules (CO, NO and NO_2) are adsorbed with relatively large adsorption energies of $|E_a| > 2$ eV. Here, the adsorption energy E_a is defined by $E_a = E_{tot} - E_{pyr} - E_{mol}$, and E_{tot}, E_{pyr} and E_{mol} are the total energies of pyridine-type N-doped (11,0) CNT with and without the molecule and of the isolated molecule, respectively. In the case of the adsorption of the CO molecule, the C atom of the CO molecule binds with three N atoms in the pyridine-type N defects, forming tetrahedral coordinations. For the adsorption of NO molecules, the N atom of the NO molecule is adsorbed with the N atom in the pyridine-type defect, whereas for the NO_2 molecule, the desorption takes place at the pyridine-type defect: the NO_2 molecule attached to the N atom in the pyridine-type defect is desorbed as an NO molecule, and the remaining O atom of the NO_2 molecule is adsorbed to the N atom in the pyridine-type defect.

We next study the transport properties of the pristine and pyridine-type N-doped (11,0) CNTs. There is an energy band gap of ~ 1 eV in the pristine (11,0) CNT, and its conductance shows a quantized value at the outsides of the energy gap. When pyridine-type N defects are introduced to the nanotube, the acceptor states emerge around the valence-band maximum and the Fermi energy of the pyridine-type N-doped CNT relatively moves to the edge of the valence bands. As a result, the pyridine-type N-doped CNT should become a p-type semiconductor. When a CO molecule is adsorbed to the pyridine-type N-doped CNT, the conductance spectrum is sizably modified: the conductances overall decrease. We also study the conductance variation at the Fermi energy for adsorption of various molecules. Three kinds of molecules (CO, NO, and NO_2) are distinguishable from one another for the adsorptions to the pyridine-type N defect due to the relatively large changes of the conductance.

In summary, we have examined the effects of the introduction of pyridine-type N defects and the adsorption of molecules on the atomic structures, energetics and transport properties of (11,0) CNTs using the first-principles electronic transport study. The CO, NO, and NO_2

molecules bind to the pyridine-type N-doped (11,0) CNTs with relatively large adsorption energies. The introduction of the pyridine-type defects into semiconducting (11,0) CNT should give rise to a *p*-type transport property. Three kinds of molecules (CO, NO, and NO_2) are distinguishable from one another for the adsorptions to the pyridine-type N defect because of the relatively large changes of the conductance. The pyridine-type N-doped CNT could become a highly sensitive sensor material to detect toxic CO and harmful NO_x molecules.

References

[1] Y. Fujimoto, Micromachine **15**, 1172 (2024).

[2] Y. Fujimoto and S. Saito, Chem. Phys. **478**, 55 (2016).

[3] Y. Fujimoto and S. Saito, Appl. Surf. Sci. Adv. **1**, 100028 (2020).

[4] Y. Fujimoto and S. Saito, J. Electrochem. Soc. **169**, 037512 (2022).

[5] Y. Fujimoto, J. Electrochem. Sci. Eng. **12**, 431 (2022).

[6] Y. Fujimoto and S. Saito, JPS Conf. Proc. **4**, 012002 (2015).

Electronic structure analysis of spin devices using first-principles calculation

Hideo KAIJU, Mizuki MATSUZAKA, Koki HORIGANE, and Chika HASHIMOTO
Faculty of Science and Technology, Keio University
Yokohama, Kanagawa 223-8522, Japan

Magnetic tunnel junction (MTJ), which consists of a thin insulation layer sandwiched by two magnetic layers, exhibits a large tunnel magnetoresistance (TMR) effect [1,2]. The TMR effect strongly depends on not only the materials of an insulation layer and magnetic layers, but also the lattice matching between the insulation layer and magnetic layers. In a recent study, a significant TMR ratio of 631% was achieved in lattice-matched FeCo/MgO/FeCo MTJs at room temperature [3].

In this study, we compare TMR ratios based on the materials of insulation and magnetic layers and the lattice matching, to clarify the mechanism of the TMR effect. We investigate the tunneling transmittance and conductance of electrons, and TMR ratios in good lattice matched MgO-based MTJ, $SrTiO_3$-based MTJ, and InP-based MTJ, in which Fe or FeCo is used for magnetic layers, using first-principles calculations.

We used Quantum ESPRESSO for first-principles calculations. The calculations are performed based on density functional theory, plane wave approximation, and pseudopotential model. First, we performed structural relaxation for each MTJ in parallel magnetization. The supercells of MgO-, $SrTiO_3$-, and InP-based MTJs are shown in Figure 1. Then, we calculated the tunneling transmittance and conductance in parallel and antiparallel magnetizations using the Landauer-Büttiker method. Finally, we calculated the TMR ratio for each MTJ from the obtained conductance. The calculations are MPI-parallelized in each step especially for *k* points.

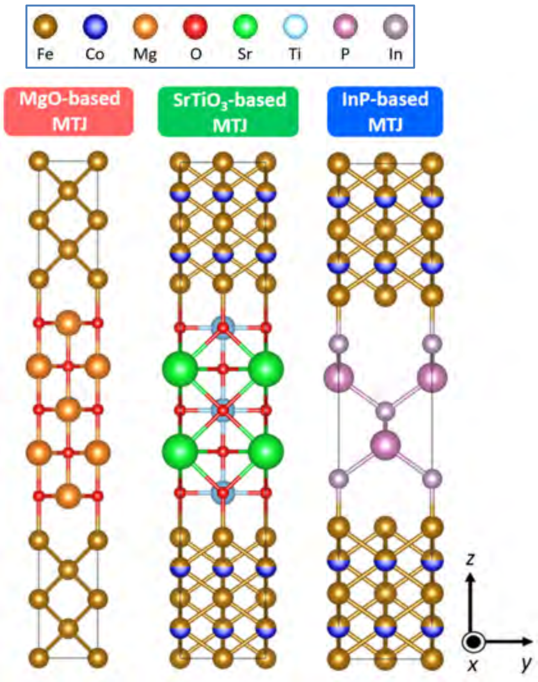

Figure 1: Supercells of MgO-, $SrTiO_3$-, and InP-based MTJs.

Table 1 shows the conductance G_P and G_{AP} in parallel and antiparallel magnetizations, respectively, and TMR ratio for MTJs. We obtain relatively small TMR ratios of 229%, 324%, 100% and 426% in Fe/SrTiO$_3$/Fe, FeCo/SrTiO$_3$/FeCo, Fe/InP/Fe and FeCo/InP/FeCo MTJs, whereas large TMR ratios of 8920% and 6420% in Fe/MgO/Fe and FeCo/MgO/FeCo MTJs, respectively. Figure 2 shows the $k_{||}$-resolved conduction spectra of majority spins in parallel magnetization. The conductance of majority spins at Γ point is dominant in MgO-based MTJs, in contrast to the conductance of minority spins or at non-Γ point is enhanced in SrTiO$_3$-based and InP-based MTJs. We clarified the robust conduction through the Δ_1 band of majority spins contributes to large TMR ratios in MgO-based MTJs, whereas the suppression of the conduction through the Δ_1 band of majority spins as well as the enhancement of the conduction through other bands leads to the decrease of TMR ratios in SrTiO$_3$-based and InP-based MTJs.

Table 1: Conductance in both parallel and antiparallel magnetizations, respectively, and TMR ratio for MTJs.

MTJs	G_P ($\Omega^{-1}\mu m^{-2}$)	G_{AP} ($\Omega^{-1}\mu m^{-2}$)	TMR ratio
Fe-MgO	0.508	0.00564	8920%
Fe-SrTiO$_3$	51.4	15.7	229%
Fe-InP	64.9	32.6	100%
FeCo-MgO	0.673	0.0103	6420%
FeCo-SrTiO$_3$	20.8	4.92	324%
FeCo-InP	41.5	8.03	416%

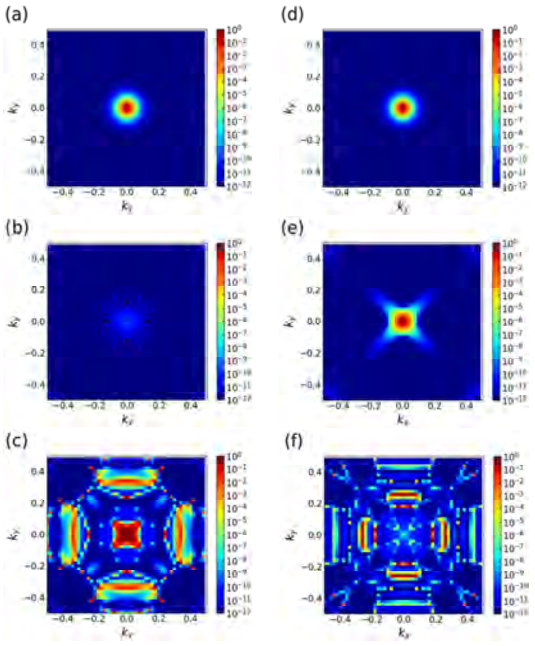

Figure 2: $k_{||}$-resolved conduction spectra (in units of Ω^{-1}) of majority spins in parallel magnetization for (a) Fe/MgO/Fe, (b) Fe/SrTiO$_3$/Fe, (c) Fe/InP/Fe, (d) FeCo/MgO/FeCo, (e) FeCo/SrTiO$_3$/FeCo, and (f) FeCo/InP/FeCo MTJs.

References

[1] S. S. P. Parkin *et al.*, *Nat. Mater.* **3**, 862 (2004).

[2] S. Yuasa *et al.*, *Nat. Mater.* **3**, 868 (2004).

[3] T. Scheike *et al., Appl. Phys. Lett.* **112**, 112404 (2023).

Ab initio calculation of the rotation effect of oxygen octahedron in Ca_2MnO_4 on electronic properties

Kazuma NAKAMURA
Quantum Physics Section, Kyushu Institute of Technology
1-1 Sensui-cho, Tobata, Kitakyushu, Fukuoka, 804-8550

Domain walls in transition-metal oxides are expected to have new functions due to their local structure, and have been actively studied in recent years. One example is Ca_2MnO_4 (CMO), which is known to have the freedom to rotate the oxygen octahedron around the *c*-axis, resulting in the formation of multiple phases. In CMO, the rotation of the octahedron tends to result in domain boundaries. At high temperatures (above 1,050 K), CMO has a highly symmetric structure without oxygen octahedral rotation [$I4/mmm$, Fig. 1(a)], and at low temperatures it is known that it can coexist with multiple phases in which the oxygen octahedron is rotated. The low-temperature phases are classified according to the difference in the stacking pattern in the *c*-axis direction of the MnO_2 layers composed of oxygen octahedra, and are known to be a structure with in-phase rotation [$Acam$, Fig. 1(b)] and a structure with anti-phase rotation [$I4_1/acd$, Fig. 1(c)]. In this study, we focus on the effect of the oxygen octahedral rotation of CMO on the low-energy electronic properties.

Ab initio spin-polarized density functional calculations were performed using Quantum Espresso [1] for the three structures identified in the experiment shown in Fig.1 (left). These structural models were aligned to a 56-atom superlattice so that the electronic structures could be compared. In addition, several structural models differing in spin arrangement, rotation pattern of oxygen octahedra, and rotation angle are generated, and the band-structure calculations were performed. Transport properties were calculated using BoltzTraP2 [2].

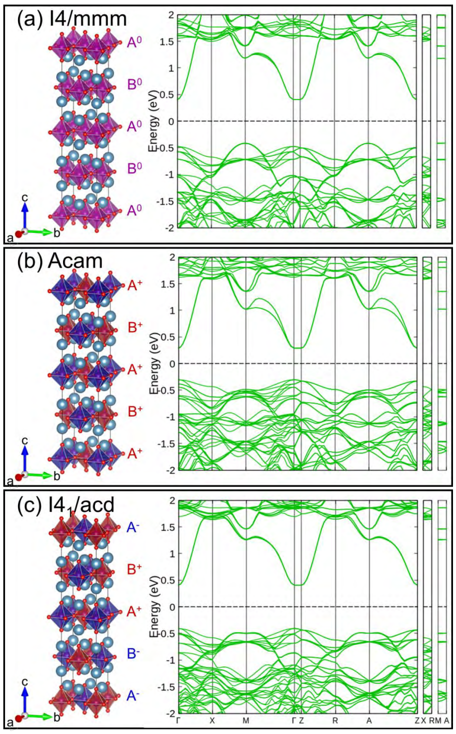

Figure 1: **Three crystal structures (left) and antiferromagnetic band structure (right) of Ca_2MnO_4: (a) $I4/mmm$, (b) $Acam$, (c) $I4_1/acd$. Ca (blue), Mn (purple), O (red). The colors of the oxygen octahedra indicate the rotation state [no rotation (purple), clockwise (blue), counterclockwise (red)].**

Figure 1 (right) are the calculated band structures by spin-polarized density functional calculations for the three basic structures. We

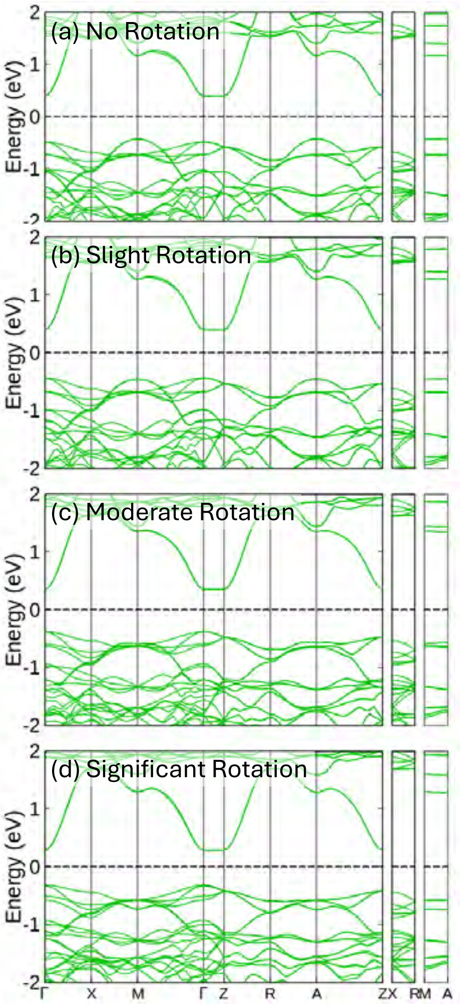

Figure 2: **Antiferromagneitc C-type band structures for structural models (28-atom system) with different rotation angles: (a) 0°, (b) 4.6°, (c) 9.1°, (d) 13.5°.**

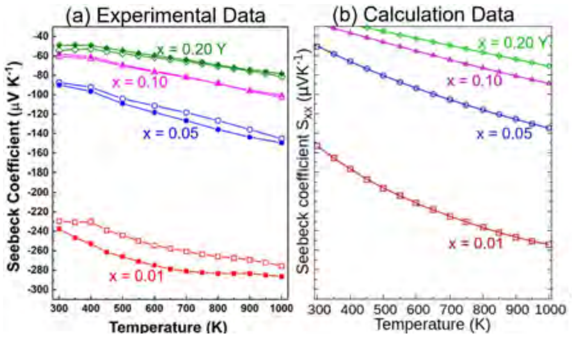

Figure 3: **Temperature dependence of the Seebeck coefficient. (Left) Experimental results for polycrystalline** $\mathrm{Ca}_{2-x}Ln_x\mathrm{MnO}_4$ **(*Ln* = La or Y doped). (Right) Theory. The scale of the y-axis is the same.**

found that the C-type (AFC), in which the magnetization of adjacent Mn atoms in the $\mathrm{MnO_2}$ plane is arranged antiferromagnetically, is stable. $I4/mmm$ has an indirect band gap of 0.82 eV between the Γ point and the M point, while $Acam$ and $I4_1/acd$ have a direct band gap at the Γ point, which are 0.59 eV and 0.81 eV, respectively. This result is consistent with the experimental and other calculations. Also, when focusing on the band at the top of the valence band near the M point, $I4/mmm$ and $Acam$ form a parabolic band, while $I4_1/acd$ has a band structure with a flattened parabola. We found that these details are not due to the rotation pattern and result from the rotation angle itself.

Figure 2 compares the AFC band structures for four rotation angles of the oxygen octahedron, (a) 0°, (b) 4.6°, (c) 9.1°, and (d) 13.5°. The band gap at the Γ point decreased (0.88 eV, 0.84 eV, 0.73 eV, and 0.60 eV, respectively), and the shape of the band at the top of the valence band at the M point changed. From the above, we conclude that the electronic structure of CMO is greatly affected by the rotation angle.

The transport properties were investigated: Temperature dependence of the Seebeck coefficient under electron doping is shown in Fig. 3. The Seebeck coefficient decreases with temperature, being insulating behavior. It can be seen that the calculated values in the in-plane direction show a reasonable agreement with the experiment. The different colors in the figure represent the difference in the doping amount. The doping dependence of the Seebeck coefficient is also consistent with the experiment.

References

[1] P. Giannozzi et al. *J. Phys.: Condens. Matter* **21**, 395502 (2009).

[2] G. K. H. Madsen, J. Carrete, and M. J. Verstraete. *Comput. Phys. Commun.* **231**, 140 (2018).

Advances in Catalytic Theory and Predictive Modeling Enabled by Large-Scale Parallel Computing

Di ZHANG

Advanced Institute of Material Research,

Tohoku University, 2 Chome-1-1 Katahira, Aoba Ward, Sendai, Miyagi 980-8577

We utilized the ISSP massive parallel computer system to perform simulations on single-atom and dual-atom M-N-C catalysts, focusing on ORR and OER performance modeling across different pH conditions, spin state simulations, and data-driven catalyst design. VASP software on ISSP was primarily used for DFT calculations and first-principles molecular dynamics simulations. The main achievements are summarized below.

Unlocking New ORR Mechanisms in M–N–C Catalysts with Massive Parallel Simulations: Using the ISSP supercomputer, we performed large-scale first-principles modeling combined with pH-coupled microkinetic simulations and synchrotron spectroscopy to reveal a new ORR pathway in weak-binding M–N–C catalysts.We identified oxygen adsorption at the metal–nitrogen bridge site as a key step (**Fig. 1**), altering scaling relations, electric field responses, and kinetic barriers. These findings redefine the catalytic behavior of weak-binding SACs and open new directions for clean energy applications. [1]

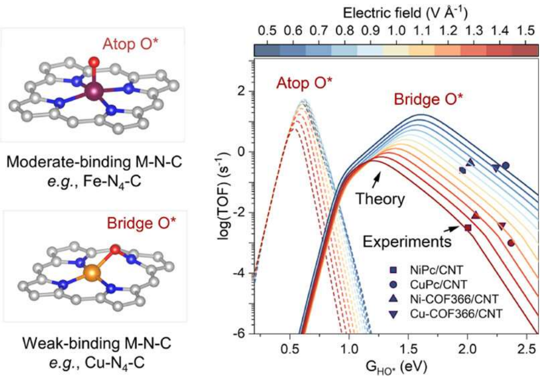

Fig. 1: New ORR Mechanisms on weak-binding M–N–C Catalysts

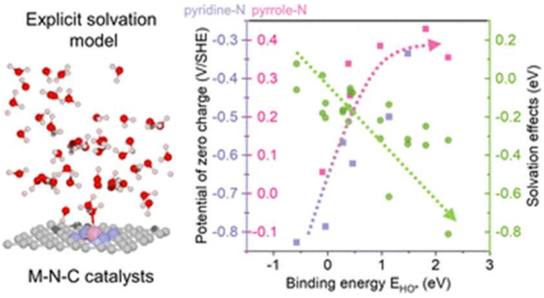

Fig. 2 PZC and solvation effect of M-N-C catalysts

We employed large-scale ab initio molecular dynamics and DFT simulations to reveal how the potential of zero charge (PZC) and solvation effects govern the activity of M–N–C catalysts. Our results show that PZC and solvation vary with metal type and nitrogen coordination, fundamentally impacting key reaction intermediates and pH-dependent behaviors (**Fig. 2**). This work highlights the necessity of including these effects for accurate modeling and rational catalyst design. [2]

We integrated high-throughput supercomputing with precise synthesis to accelerate the discovery of single-atom catalysts (SACs) for water purification (**Fig. 3**). Large-scale computational screening of 43 metal–N₄ structures enabled the rapid identification of high-performance candidates, leading to the synthesis of an Fe–SAC with record-high Fenton-like activity and outstanding long-term stability. This work demonstrates the power of combining supercomputing-driven prediction with controlled synthesis for next-generation catalyst development.[3]

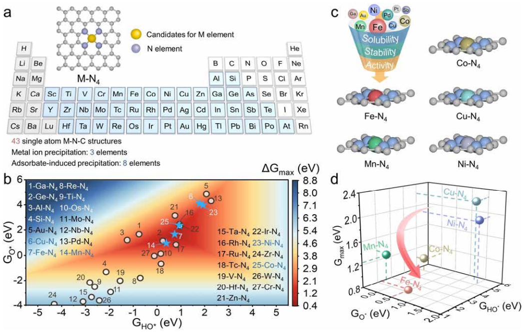

Fig. 3 The discovery of single-atom catalysts (SACs) for water purification.

Using DFT simulations, we elucidated how a built-in magnetic field modulates the spin state of Co centers in molecular M–N–C electrocatalysts, driving major enhancements in ORR and OER performance. Spin-state transitions from low- to high-spin states, validated by computation and experiment, lead to a one-order increase in turnover frequency and 4000% magnetocurrent boost. This approach offers a universal platform for spin-controlled catalyst design.[4]

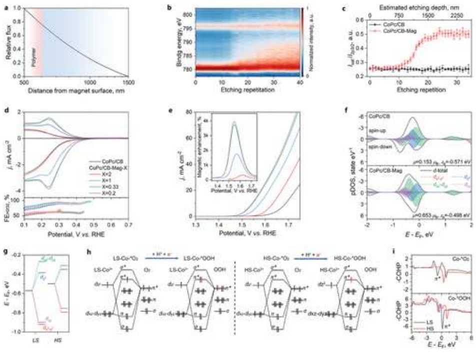

Fig.4 DFT calculations with a magnetic field-integrated electrocatalyst.

References

[1] J. Am. Chem. Soc. 2025, 147, 7, 6076–6086.

[2] J. Mater. Chem. A, 2024, 12, 13742-13750.

[3] Angew. Chem. Int. Ed. 2025, e202500004.

[4] Advanced Materials 2024, 36, 45, 2408461

DFT and Multireference Calculations of Zeolites, High-Entropy Alloys, and Framework Materials

Quan Manh PHUNG
Graduate School of Science, Department of Chemistry
Nagoya University, Furocho, Chikusa, Nagoya, Aichi 464-8601

We have utilized the Supercomputer System B to study various chemical systems, using mainly density functional theory (DFT) and ab initio methods (CASSCF/CASPT2). DFT calculations were performed with VASP and OpenMX, while CASSCF/CASPT2 calculations were done with OpenMolcas. In addition, we perform classical molecular dynamics simulations with GROMACS.

1. Zeolites [1]

We studied the homolytic and heterolytic methane hydroxylation in copper zeolites, $[CuOCu]^{2+} + CH_4 \rightarrow CH_3OH + [Cu\text{-}Cu]^{2+}$. The investigation employed a combination of DFT and CASSCF/CASPT2 calculations to provide detailed mechanistic insight.

2. Mesoporous materials [2]

Various mesoporous materials, particularly high-entropy alloys (HEA), have been studied with DFT. The studies focused on catalytic processes, such as hydrogen evolution reaction (HER), oxygen reduction reaction (ORR), and methanol reduction reaction (MOR).

The catalytic properties of some metal-organic frameworks (MOFs) and covalent-organic frameworks (COFs) have been investigated mainly with DFT and MD simulations.

References

1. M. Han, T. Nagaura, H. N. Nam, Z. Yang, A. Alowasheeir, Q. M. Phung, T. Yanai, J. Kim, S. M. Alshehri, T. Ahamad, Y. Bando, Y. Yamauchi, *Small*, **2025**, Accepted.
2. Q. M. Phung, T. Yanai, D. Plessers, B. F. Sels, R. A. Schoonheydt, K. Pierloot, *ACS Catal.*, **2025**, *15*, 1249.

Materials exploration loop with materials informatics.

Yosuke HARASHIMA
Graduate School of Science and Technology, Nara Institute of Science and Technology
Takayama-cho, Ikoma, Nara 630-0192

In this study [1], we proposed a new materials exploration method called the Covariance Linkage Assimilation method for Unobserved Data Exploration (CLAUDE), which combines a multivariate Gaussian-based data assimilation technique with Bayesian optimization. The goal is to improve the efficiency of finding optimal material properties using limited experimental and simulation data.

Materials informatics often suffers from the scarcity of property-specific experimental data, while simulation data, though abundant, may have systematic errors. Data assimilation techniques have been successful in fields like weather forecasting and are now being adapted for materials science. Bayesian optimization has also become a key tool for efficient material discovery.

The proposed method uses a posterior distribution derived from multivariate Gaussian distribution instead of the conventional Gaussian process regression. It can handle missing data via direct likelihood formulation, enabling the assimilation of multiple datasets. Monte Carlo sampling of the posterior distribution allows Bayesian optimization without requiring full data matching between experiments and simulations.

We demonstrated as follows.
1. Optimization of Example Functions: We tested CLAUDE on example models and demonstrated that the method more efficiently found the maximum value compared to ordinary Bayesian optimization. Incorporating simulation data exploration alongside experimental data exploitation significantly accelerated optimization.
2. Practical Application to Photocatalysts: The method was applied to predict the bandgap of $(\mathrm{Sr}_{1-x_1-x_2}\mathrm{La}_{x_1}\mathrm{Na}_{x_2})(\mathrm{Ti}_{1-x_1-x_2}\mathrm{Ga}_{x_1}\mathrm{Ta}_{x_2})\mathrm{O}_3$, an important photocatalytic material. Using a combination of first-principles calculations and limited experimental measurements, the assimilation model accurately predicted bandgap values even at compositions not included in the original dataset. Experimental validation confirmed the predictions, capturing effects like atomic hybridization and non-linear bandgap shifts.

The proposed assimilation method significantly improves search efficiency and prediction accuracy in materials exploration, especially when experimental data are scarce. The successful demonstration with photocatalyst bandgaps highlights the method's practical utility. CLAUDE is positioned as a powerful tool for accelerating materials discovery through intelligent data integration.

References

[1] Y. Harashima, *et al.*: arXiv:2408.08539 (2024); `https://github.com/yy-harashima/CLAUDE`.

Computational Investigation of Multi-Exciton Generation Mechanism by Large-Scale Excited-State Method

Takatoshi Fujita
National Institutes for Quantum Science and Technology
Anagawa, Inage-ku, Chiba 263-8555

We have been developing the large-scale excited-state methods based on the fragment molecular orbital (FMO) method and the GW/Bethe-Salpeter equation method. Recently, we extended the FMO-based GW/BSE method to calculate the electronic couplings relevant to the singlet fission process. This development enables the first-principles investigation of multi-exciton generation processes in molecular aggregates based on the first-principles calculations.

In parallel, we developed a computational procedure to characterize the excited states in molecular aggregates. Characterizing the excited states is essential for understanding photophysical and photochemical processes. In this study, we propose a method to reconstruct the total transition density matrix (TDM) and natural transition orbitals (NTOs) from the FMO method. By expressing NTOs as linear combinations of fragment molecular orbitals, we introduce novel measures to quantify the extent of collectivity and delocalization of excited states. As an application, we characterized the low-energy excited states in a pentacene cluster. First, we derived the Frenkel exciton and Wannier-Mott exciton states as limiting cases of the FMO-based excited-state Hamiltonian. We compared the wave function obtained from FMO with those of the Frenkel and Wannier-Mott exciton states in terms of collectivity and delocalization. We suggest that the excited states of the pentacene cluster exhibit intermediate properties between the Frenkel and Wannier-Mott exciton states.

Furthermore, as an application of our multi-scale approach [1], we have elucidated the role of charge-transfer (CT) state manifold in the exciton dissociation processes in donor/acceptor blends. Understanding the relationship between the energy levels and the charge photogeneration in donor/acceptor blends is crucial to improving the power conversion efficiency of organic solar cells. Here, we investigate the exciton dissociation dynamics in poly(3-hexylthiophene) (P3HT)/[6,6]-phenyl-C61-butyric acid methyl ester (PCBM) blends by employing the ensemble-averaged wave packet dynamics and the Marcus-Levich-Jortner rate equation. To improve the accuracy of the wave packet dynamics method, we introduced reorganization and temperature corrections and validated these methods against the hierarchical equation of motion method. Our analyses reveal that higher-energy CT states, often overlooked in conventional models, play a significant role in facilitating exciton dissociation. These results highlight the importance of considering the entire CT-state manifold in understanding the charge photogeneration dynamics in donor/acceptor blends.

References

[1] T. Fujita, M. Nozaki, submitted.

Search for high temperature superconductivity in hydrides

Takahiro ISHIKAWA
Department of Physics, The University of Tokyo
7-3-1 Hongo, Bunkyo-ku, Tokyo 113-0033

Lanthanum hydride (La-H) shows superconductivity at 260 K at 170 GPa [1, 2]. Recently, the superconducting critical temperature T_c was reported to increase further to 550 K through repeated cooling and heating of the sample [3]. The large enhancement of the superconductivity has been speculated to be caused by the reaction of La-H with other materials existing in the sample chamber of the diamond anvil cell. Dominant candidates for the materials are nitrogen (N) and boron (B), originating from a hydrogen-source material (NH_3BH_3) used for the synthesis of hydrides, and platinum (Pt), gold (Au), and gallium (Ga), originating from electrodes.

In this study, assuming a reaction between La-H and Pt, we searched for thermodynamically stable phases in the La-Pt-H system at 20 GPa using a high-speed construction method of a formation-enthalpy convex hull (CH) diagram that integrates evolutionary algorithms (EA), first-principles calculations based on the density functional theory (DFT), and universal neural network potential (UNNP) calculations [4]. At each generation for the CH construction, a few thousand structures created by EA are rapidly optimized by the UNNP calculations implemented in Matlantis [5], and only several dozen structures appearing near CH are extracted. Then, the structural optimizatios are performed for the extracted structures using the DFT calculations implemented in the Quantum ESPRESSO (QE) code [6], executed on the ISSP supercomputer, and the convex hull is subsequently updated. For the stable compounds, we calculated the electron-phonon coupling constant λ and the logarithmic averaged phonon frequency ω_log using the QE code and estimated T_c based on the Allen-Dynes formula [7]. Our exploration revealed that $LaPtH_6$ exhibits the highest Tc of 18.67 K at 20 GPa [8], with no evidence supporting the previously reported superconductivity at 550 K.

References

[1] M. Somayazulu *et al.*: Phys. Rev. Lett. **122**, 027001 (2019).

[2] A. P. Drozdov *et al.*: Nature **569**, 528 (2019).

[3] A. D. Grockowiak *et al.*: Front. Electron. Mater. **2**, 837651 (2022).

[4] T. Ishikawa *et al.*: Phys. Rev. B **109**, 094106 (2024).

[5] Matlantis (https://matlantis.com/), software as a service style material discovery tool.

[6] P. Giannozzi *et al.*: J. Phys.: Condens. Matter **21**, 395502 (2009).

[7] P. B. Allen and R. C. Dynes: Phys. Rev. B **12**, 905 (1975).

[8] T. Ishikawa *et al.*: http://arxiv.org/abs/2502.06821 (2025).

Structural and electronic properties of gold nanotubes

Shota ONO
Muroran Institute of Technology, Muroran, Hokkaido 050-8585, Japan

Carbon nanotubes (CNTs) are created by rolling up the graphene. The chiral vector determines the structure of CNTs and also their electronic properties. The properties of different nanotubes have been investigated by rolling up other 2D materials. Recently, Kashiwaya et al. have reported the creation of goldene, which is 2D gold with a hexagonal structure [1]. The goldene has been expected to be useful for miniaturizing electronic devices to the nanoscale.

In this project, we have studied the structural and electronic properties of gold nanotubes (GNTs). Based on first-principles calculations, we calculated the strain energy $\Delta E(n,m) = E(n,m) - E_{\rm 2D}$, where $E(n,m)$ and $E_{\rm 2D}$ are the total energy per atom of the (n,m) GNT and the goldene. The continuum elasticity theory predicts $\Delta E(n,m) \propto R^{-2}$ with the GNT radius R. We have shown that the inverse square law does not hold for GNTs (see Fig. 1). This is due to the enhanced strain energy in specific GNTs. The specific chiralities were identified by imposing the Bloch and geometric boundary conditions to the electronic structure of goldene having a hexagonal shape of the Fermi surface. We also confirmed that the electronic states on the Fermi surface exhibit an in-plane character. These factors result in an increase in the strain energy.

These research findings were reported in Ref. [2]. Another study regarding other 2D materials conducted last year was also completed, and its results were reported in Ref. [3].

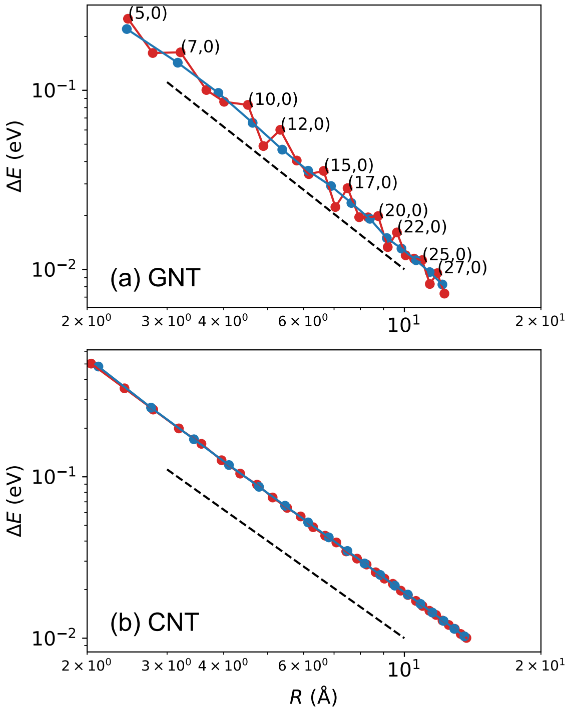

Figure 1: The strain energy $\Delta E(n,m)$ as a function of R for (a) GNTs and (b) CNTs with the chiral indices $(n,0)$ and (n,n).

References

[1] S. Kashiwaya et al., Nat. Synth **3**, 744 (2024).

[2] S. Ono and H. Yoshioka, Phys. Rev. B **111**, 085414 (2025).

[3] S. Ono and R. Pawar, Phys. Rev. Materials **8**, 094002 (2024).

Modeling ultrafast electron dynamics: Case studies of elemental metals and carbon nanostructures

Shota ONO
Muroran Institute of Technology, Muroran, Hokkaido 050-8585, Japan

In the field of ultrafast dynamics, it is still a challenge to interpret the transient optical responses within the femtosecond timescale. In this project, we have studied (i) the transient luminescence of 15 elemental metals [1] and (ii) the transient absorption spectra of few-walled carbon nanotubes (CNTs) [2].

For the case (i), we interpreted the luminescence dynamics of light metals; 3*d*, 4*d*, and 5*d* transition metals; and noble metals [1]. To understand the different decay rate of infrared luminescence among these metals, we calculated the electron-phonon (e-ph) coupling constant by using the density-functional perturbation theory implemented to the Quantum Espresso. Based on the two-temperature model between hot electrons and phonons, we estimated the decay rate of non-equilibrium electrons. We have confirmed that the calculated decay rate agrees with the experiments (see Fig. 1). The disagreement between the theory and experiments for Al and Be will be due to the creation of non-equilibrium phonons during the relaxation.

For the case (ii), we interpreted the absorption dynamics for bundled few-walled CNTs [2]. To understand the anomalously enhanced decay constant at a specific energy, we constructed an analytical model that relates the absorption decay with the electron temperature decay. By considering the van Hove peaks in the electron density-of-states, we have found that our model captures the overall feature of the absorption dynamics. The dimensionality of electron dynamics in bundled few-walled CNTs and van der Waals heterostructures of CNTs covered with boron nitride nanotubes was also investigated.

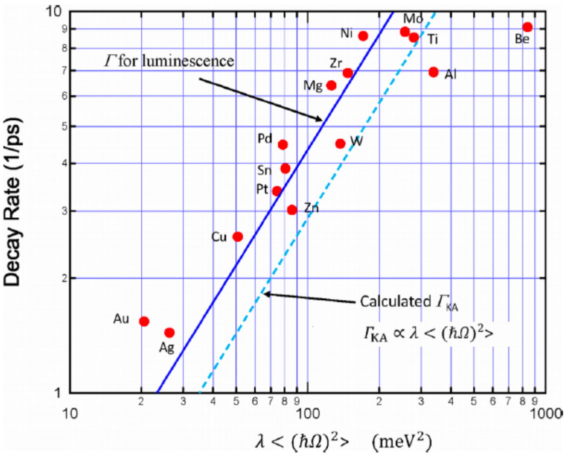

Figure 1: Correlation between the luminescence decay rate at 0.6 eV and the e-ph coupling constant for 15 elemental metals. The blue dashed line represents the values calculated by the temperature model. The values multiplied by 1.5 are shown by a solid line [1].

References

[1] T. Suemoto, S. Ono et al., Phys. Rev. B **111**, 035150 (2025).

[2] G. Noyama et al., Carbon Trends **20**, 100510 (2025).

Theoretical Simulation of Subcycle Reciprocal-Space Images of Electron Density Driven by a Strong Laser Field

Yasushi SHINOHARA[1,2]

[1]*Photon Science Center,*

The University of Tokyo, Hongo, Bunkyo-ku, Tokyo 113-8656.

[2]*NTT Basic Research Laboratories,*

NTT Corporation, 3-1 Morinosato Wakamiya, Atsugi, Kanagawa 243-0198.

We have investigated the response of insulators to strong light fields using time-dependent density functional theory (TDDFT) [1]. When the field strength becomes comparable to the intrinsic electric field within the material, the system exhibits extremely nonlinear responses that cannot be described by perturbative expansions. To accurately capture these dynamics, it is necessary to solve the time-dependent Kohn-Sham equation directly in real time. The SALMON-TDDFT code [2] provides a platform for solving the Kohn-Sham equation for crystalline solids, molecules, and atoms. In this study, we performed simulations using system B at SCC-ISSP.

We conducted TDDFT simulations to obtain subcycle reciprocal-space images of the electron density in monolayer hexagonal boron nitride (hBN) and graphene under an intense electric field. The corresponding real-space electron densities were derived via spatial Fourier transforms. The applied electric field was linearly polarized, with a full width at half maximum (FWHM) duration of 14 fs, a photon energy of 0.4 eV, and a peak intensity of 1 TW/cm².

Under the influence of the peak electric field, the electron distribution becomes significantly distorted. In monolayer hBN, the low-frequency components of the reciprocal-space electron density exhibit oscillations that vary nearly linearly with the applied field strength. Our simulations suggest that these dynamics correspond to electron hopping between two distinct B–N bonds in response to the field. In contrast, graphene does not show such linear field-dependent oscillations.

References

[1] Erich Runge and E. K. U. Gross, Phys. Rev. Lett. 52, 997 (1984).

[2] https://salmon-tddft.jp/, M. Noda, S.A. Sato, et al., Computer Physics Communications. 235, 356 (2019).

Calculation of electronic states for improving characteristics at the channel interface of power MOSFETs

Hironori YOSHIOKA
Advanced Power Electronics Research Center,
National Institute of Advanced Industrial Science and Technology (AIST), Tsukuba, Ibaraki 305-8568

In order to reduce loss in power electronics equipment, it is extremely important to understand and control the electronic state at the channel interface between the gate insulator and the semiconductor of the MOSFETs. For example, in SiC MOSFETs, which have recently been put to practical use, the channel mobility at the SiO_2/SiC interface is very low (10~100 $cm^2V^{-1}s^{-1}$), but the fundamental causes are not fully understood or elucidated.

The fact that channel mobility varies greatly depending on the SiC crystal plane {(0001) or (11-20)} has been a major mystery for 20 years [1]. We have clarified that this is due to the extreme localization of the conduction band wave function at the (0001) interface [2]. Using density functional theory (DFT), we calculated the wave function at the conduction band edge of SiC slabs and found that the wave function of the 4H-SiC (0001) slab is uniquely localized very close to the interface (< 0.5 nm) when an electric field is applied. This is related to the long crystal periodicity specific to the [0001] direction. By comparing the electric field dependence of the distance (z) of the wave function from the interface with the electric field dependence of the mobility obtained experimentally, we showed that the difference in z can explain the difference in mobility between the (0001) and (11-20). In other words, it can be said that the (0001) has smaller z by the unique localization at the interface and then has a lower mobility because of frequent scattering from interface defects.

Conventional simulations based on the effective mass approximation have been used to predict the characteristics of semiconductor devices, but we have shown that the unique localization of the wave function shown by DFT calculations cannot be reproduced by the effective mass approximation. In other words, DFT calculations are essential for predicting the properties of the SiO_2/SiC interface.

DFT calculations were performed using the ISSP supercomputer. Using the RSDFT (Real-space density functional theory) code [3], we applied an electric field of about 1 MV/cm, which is close to the situation for the inversion electrons in MOSFETs, and calculated the wave function attracted to the interface. Norm-conserving pseudopotentials and GGA by PBE were used. The H/amorphous SiO_2/4H-SiC/H slab structures, which were terminated with H atoms, were used. The (0001) and (11-20) SiC were used as the interface. z was calculated from the expectation value of the position of the wave function.

In [2], DFT calculations were performed with a slab thickness of 3 nm. For this thickness, the confinement effect by the finite thickness slab results in a non-negligible error in the calculation of z, compared to calculations for a sufficiently thick slab. Therefore, in FY2024, re-calculation was performed with a slab thickness of 11 nm (maximum number of atoms: 1,323). In addition, the E-k dispersion was calculated by setting the k-points finely, and the effective mass was calculated from the second derivative.

Even when the slab thickness increased, the qualitative trend did not change, and z was smaller for the (0001) plane. The effective mass did not change significantly from the bulk upon application of an electric field. We were able to quantitatively show that the difference in mobility between the (0001) and (11-20) can be largely explained by the difference in z and the anisotropy of the effective mass. We presented the results at [4] in November 2024.

References

[1] H. Yoshioka, J. Senzaki, A. Shimozato, Y. Tanaka, and H. Okumura, Appl. Phys. Lett. **104**, 083516 (2014).

[2] H. Yoshioka, J. Iwata, and Y. Matsushita, Appl. Phys. Lett. **122**, 222104 (2023).

[3] J. Iwata *et al.*, J. Comp. Phys. 229, 2339 (2010).

[4] H. Yoshioka, J. Iwata, and Y. Matsushita, 先進パワー半導体分科会第 11 回講演会, invited, (2024).

Modeling of the Ammonia Decomposition Reaction and Nitriding on Metal Surfaces

Peijie FENG, Minhyeok LEE, and Yuji SUZUKI
Department of Mechanical Engineering, School of Engineering,
The University of Tokyo, 7-3-1 Hongo, Bunkyo-ku, Tokyo 113-8656

Ammonia is a promising green energy carrier for the next generation, but employing it directly as a fuel is challenging due to its low flammability and potential NOx emissions [1]. Moreover, our previous study [2] showed that ammonia catalytically decomposes on iron-based materials, forming iron nitride, which in turn enhances ammonia decomposition more effectively than pure iron surfaces. To model the dynamics of the nitriding process in conjunction with surface decomposition, understanding the reaction mechanisms at the atomic level is indispensable. Considering both accuracy and computational complexity, we employed a density functional theory (DFT)-based first-principles approach using Vienna Ab-initio Simulation Package (VASP) to calculate the possible underlying surface reactions.

Due to the diversity of iron nitrides, which includes not only solid solutions of α- and γ-iron, but also γ’, ε, and ζ iron nitrides, the systematic modeling and computation of these atomic interfaces remain a challenging task. To address this, we embarked on building a framework to systematically explore surface reactions on all possible forms of iron and iron nitrides.

First, the low Miller indices were computed for α-Fe, ε-Fe, γ-Fe, γ’-Fe_4N, and ε-Fe_3N, which include (001), (100), (010), (110), (101), (011), (111), (211), (121), (112), (102), (012), (120), (210), (021), (201), and (221). Table 1 illustrates the results obtained after systematic interface modeling and computation. Based on the most stable facet identified, surface reactions were subsequently computed on these facets.

The catalytic activities of iron and iron nitrides were first examined by comparing the adsorption energy of nitrogen atoms [3], which serves as an indicator of promoting ammonia decomposition. Because modeling the facet

Table 1: Systematic examination of the surface energies of iron and iron nitrides involved in the phase transformations during ammonia-induced nitriding.

	α-Fe	γ-Fe	ε-Fe	γ’-Fe_4N	ε-Fe_3N
Computed Facets	10	11	20	16	48
The most stable facet	(110)	(001)	(001)	(001)	(101)
Surface Energy (eV)	0.163	0.169	0.204	0.125	0.189

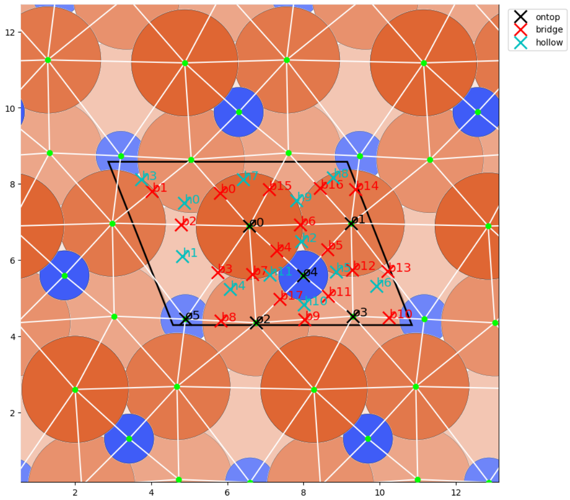

Fig. 1: The identified adsorption sites on ε-Fe_3N, 101 facet. The orange and blue circle represent the Fe and N atoms, respectively, with lighter colors indicating atoms located further from the interface. The black lines illustrate the unit cell and the "x" mark represents the identified adsorption sites in a unit cell.

with adsorbates requires meticulous examination of all possible adsorption sites, we developed a program using the Python Materials Genomics (pymatgen) package [4]. As a result, all possible adsorption sites were identified by considering both the periodicity and symmetry of the facet as shown in Fig. 1. In addition to ε-Fe_3N, adsorption sites were also identified for α-Fe and γ'-Fe_4N. The computational results show that nitrogen atoms preferentially adsorb at hollow sites formed by neighboring iron atoms. For ε-Fe_3N, as shown in Fig. 1, the sites marked h0, h7, and h9 can form stable adsorption configurations. Among these sites, the h0 site exhibits the most stable adsorption, with an adsorption energy of −6.41 eV. A similar computation performed on α-Fe revealed that the adsorption energy is slightly lower than that of ε-Fe_3N, with a value of −6.56 eV. This indicates that ε-Fe_3N may exhibit greater reactivity when iron is nitrided to a certain extent and ε-Fe_3N is formed.

In conclusion, the most stable facets were identified for α-Fe, ε-Fe, γ-Fe, γ'-Fe_4N, and ε-Fe_3N. Subsequently, a program was developed to identify adsorption sites, enabling a systematic examination of the adsorption energies of various adsorbates. The most stable adsorption sites for nitrogen atoms were then determined, and the corresponding adsorption energies were used to estimate their reactivity in catalyzing ammonia decomposition. ε-Fe_3N is predicted to be more reactive than the un-nitrided α-Fe. Future work will include a more detailed investigation of the reaction pathways.

References

[1] M.V. Manna, P. Sabia, R. Ragucci, M. de Joannon, Fuel **264**, 116768 (2020).
[2] P. Feng, M. Lee, D. Wang, Y. Suzuki, Int. J. Hydrog. Energy **48**, 75 (2023).
[3] E. Skúlason et al., Phys. Chem. Chem. Phys. **14**, 1235-1245 (2012).
[4] P. S. Ong. et al., Comput. Mater. Sci. **68**, 314-319 (2013).

First-principles calculation of dielectric constant in oxide-based phosphor

Kenji HIRATA

National Institute of Advanced Industrial Science and Technology (AIST) 807-1, Shuku, Tosu, Saga 841-0052

Recently, it was discovered that $SrAl_2O_4$:Eu^{2+}, which is $SrAl_2O_4$ doped with europium, emits light due to energy generated by static electricity.[1] Since static electricity can cause malfunctions in electronic devices, both in manufacturing environments and in next-generation mobility applications, the development of a general-purpose visualization technique for static electricity is highly desirable. As a result, this material has attracted considerable attention as a potential static electricity visualization material. In this study, the dielectric constant of the oxide phosphor $SrAl_2O_4$:Eu^{2+} was estimated using first-principles calculations in order to investigate the mechanism underlying its electrostatic emission. Furthermore, calculations were performed on the energy levels of oxygen vacancies, which are deeply involved in the emission mechanism.

A supercell was created by expanding $SrAl_2O_4$ unit cell 2×1×2 times, and one strontium site was replaced with Eu (Fig. 1). The dielectric constant of $SrAl_2O_4$:Eu^{2+} without oxygen vacancies was estimated to be approximately 5.3, and it was found that the introduction of oxygen vacancies tends to increase this value. The chemical potential of oxygen was calculated in order to determine the energy levels of oxygen vacancies. The phase diagram of the Sr-Al-O system was estimated in chemical potential space, which was consistent with previous reports. [2] The present results will be utilized in future studies to calculate the energy levels of oxygen vacancies with greater accuracy.

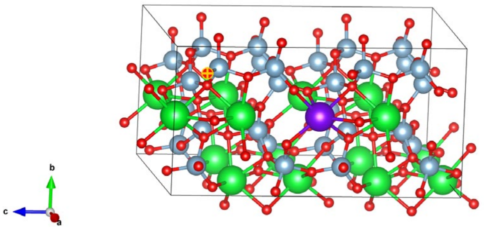

Fig. 1. Supercell model of $SrAl_2O_4$:Eu^{2+}. Purple, green, blue, and red spheres represent Eu, Sr, Al, and O atoms, respectively.

References

[1] K. Kikunaga and N. Terasaki, Sci. Rep. **12**, 8524 (2022).

[2] E. Finley, A. M. Tehrani, and J. Brgoch, J. Phys. Chem. C **122**, 16309 (2018).

Phase transformation and electric state of high entropy alloys

Yoko Yamabe-Mitarai
Frontier Science Graduate School,
The University of Tokyo, Kashiwa-no-ha, Kashiwa, Chiba 277-8561

High-entropy alloys (HEAs) have been attracting attention as new-generation structural and functional materials since this new paradigm was proposed in 2004 [1]. Most HEAs have a single face-centered-cubic (fcc), body-centered-cubic (bcc) structure, or their mixtures. Not many examples of HEAs with the hexagonal-close-packed (hcp) structure have been studied. We are applying to find HEAs with hcp structure experimentally and a few alloys were found to have an hcp structure [2].

Among the hcp-HEAs, equiaxed single-phase hcp phase was successfully developed in TiZrAl, TiZrHf, and TiZrHfAl. The deformation mechanism was investigated using a strain jump test and slip analysis after deformation. The hcp-HEAs indicated high strength compared with conventional Ti alloys, even though the slip system is the same as that of conventional Ti alloys. A strong solid-solution strengthening effect of HEAs was suggested by strong multi-elemental interaction and short-range order from macroscopic analysis. To investigate whether strong multi-elemental interaction or short-range order formation occurs, an electron charge of density was calculated using DFT. A supercell model with 128 atoms was used to indicate the solid solution phase. Special Quasirandom Structure was used to simulate random atomic positions. The internal coordinate was optimized using Quantum Espresso (QE). The electron charge density was calculated on the optimized coordinates. The results indicated that the strong bonding between some specific elements is expected to improve strength [3].

The second topic is the adhesion behavior of the oxide layer on Ni to understand the stability of the protective oxide layer. Some alloying elements drastically decreased interfacial energy, improving the adhesion between Ni and the oxide layer [4].

References

[1] B. Cantor et. al., A. J. B. Vincent, Mater. Sci. Eng. A, **375-377**, 213 (2004).

[2] Y. Yamabe-Mitarai et. al., JALCOM, **911**, 164849 (2022)

[3] S. J. Liang, T. Yoshino, R. Matsumoto, R. Sahara, Y. Toda, S. Matsunaga, G. Miyamoto, Y. Yamabe-Mitarai, Mater. Sci. Eng. A, **929**, 148143 (2025).

[4] M. Negami, R. Morihashi, T. Yoshino, R. Sahara, Y. Yamabe-Mitarai, Corros. Sci, **237**, 112329 (2024).

Theoretical design of bistable functional materials based on calculations for diradical-solid interaction

Kohei TADA

Department of Materials Engineering Science, Graduate School of Engineering Science, Osaka University, Toyonaka, Osaka 560-8531, Japan

Molecules with all paired-electrons are called closed-shell molecules, while other molecules that has unpaired electrons are called open-shell molecules. The highest occupied molecular orbital (HOMO) of closed-shell molecules is generally bonding and the lowest unoccupied molecular orbital (LUMO) is antibonding; therefore, the HOMO-LUMO gap is generally large. As the covalent bonds in the closed-shell molecule weaken, the HOMO-LUMO gap narrows, the electrons are localised on each atom and show the properties of unpaired electrons. These unpaired electrons occupy the degenerate orbitals. Such open-shell molecules are called diradical molecules.

The degree of localisation is featured by diradical character (y value) and the y value is widely used in molecular design [1]. The relationship between y value and electronic properties of the molecules is shown in Fig 1. The variation in localisation will cause magnetism change. The HOMO-LUMO gap is affected by the y-variation, and redox properties will be changed. The design of bistable molecular materials can be achieved by establishing a closed-/open-shell controlling This study aims to establish a theoretical basis for the control by molecule-solid interactions.

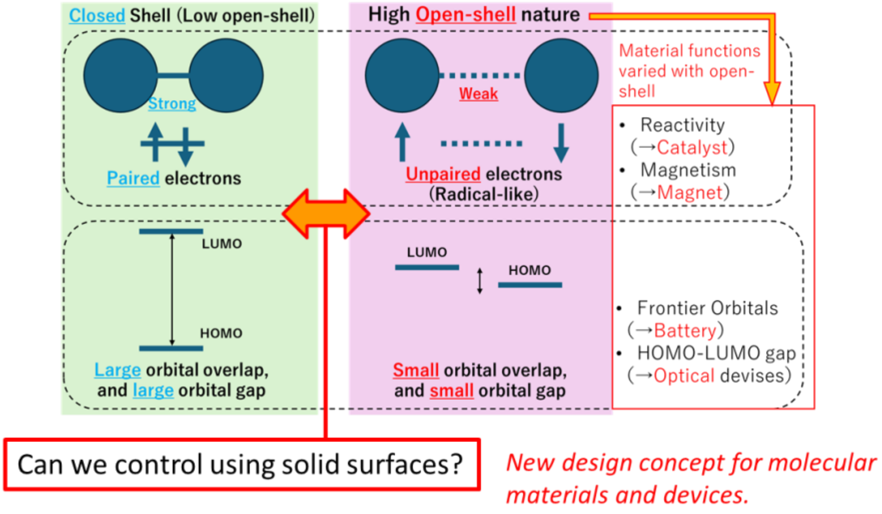

Fig. 1: Schematic view of study concept.

A method to estimate *y*-values of molecule-solid composite systems with realistic costs has been developed by the author (AP-DFT/plane-wave method) [2,3]. Electronic state optimisation via DFT/plane-wave was performed by the VASP code, and the y-values were calculated by the developed code using the optimised electron densities. System B (ohtaka) was used for the investigation of theoretical models, and system C (kugui) was used for the application to real systems.

For “control,” it is necessary to find both “increasing” and “decreasing” mechanisms. A systematic study using diatomic adsorption model of Au, Ag, and Cu showed that the oxide surface have (1) a mechanism to increase y-value due to orbital polarisation effect and (2) a mechanism to decrease y-value due to electron transfer; the balance between these two opposing mechanisms determines whether the y-value is increased or decreased by surface adsorption (Fig. 2) [4]. The former effect is dominant in Au adsorption, while the latter effect is dominant in Ag adsorption. This result was selected as an issue cover of *Chemistry*.

As an application to real systems, we investigated metal-organic-framework (MOF) materials based on a Ru binuclear complex (Ru_2-MOF). It was found that the electron distribution around the Fermi level of Ru_2-MOF is strongly dependent on the magnetic state [5]. This indicates that the conductivity would be related with their magnetic properties.

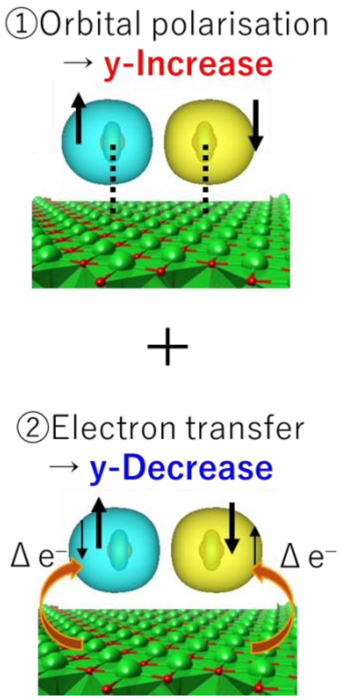

Fig. 2: *y*-Modification effects by oxide surfaces.

References

[1] T. Stuyver, B. Chen, T. Zeng, P. Geerlings, F. De Proft, R. Hoffinann, Chem. Rev. **119**, 11291 (2019).

[2] K. Tada, Y. Kitagawa, T. Kawakami, M. Okumura, S. Tanaka, Chem. Lett. **50**, 392 (2021).

[3] K. Tada, H. Ozaki, K. Fujimaru, Y. Kitagawa, T. Kawakami, M. Okumura, Phys. Chem. Chem. Phys. **23**, 25024 (2021).

[4] K. Tada, K. Masuda, R. Kishi, Y. Kitagawa, Chemistry **6**, 1572 (2024).

[5] N. Amamizu, K. Tada, R. Kishi, W. Kosaka, H. Miyasaka, Y. Kitagawa, Chem. Lett. **53**, upae230 (2024).

Theoretical investigation to design of novel Na-ion battery materials with low environmental impact and high durability

Kohei TADA

Department of Materials Engineering Science, Graduate School of Engineering Science, Osaka University, Toyonaka, Osaka 560-8531, Japan

Sodium-ion battery (SIB) systems are candidates for sustainable energy storage systems. The Na-containing layered transition metal oxide materials can be synthesized easily and have high capacity, making them the most extensively studied materials for cathode materials of SIB systems. Among the layered structures, P2-type $Na_{2/3}(Mn_{2/3}Ni_{1/3})O_2$ (P2-type Na-NMO)is an attractive material because its theoretical capacity and working potential are comparable to those of the cathode materials of lithium-ion battery systems [1]. However, the P2-structure is metastable at higher potential range, and schemes to retain the structure during cycling must be discussed. Recently, it is shown that milling the materials increases durability [2]; however, the mechanism is still unknown. Furthermore, life cycle assessment analysis showed the environmental impact belonging to Ni is high [3]. Hence, to achieve low environmental impact and high durability systems, theoretical investigations is needed.

In this project, density functional theory (DFT) calculations were performed (1) to investigate the mechanism of high durability in milling samples, and (2) to design low Ni-containing materials. The calculations were performed by VASP programme implemented in ohtaka (system B) and kugui (system C).

The P2-type structure transitions to a more stable layered structure (O2 structure) by layer-sliding, and the O2 structure transferred to a rock-salt structure, resulting in redox-inactivation [4]. Our DFT calculations showed that the P2-type structure will quickly transitions to the O2-type structure. Therefore, for clarifying the mechanism of high durability of milling sample, we should investigate not only bulk structure but also other pieces.

Then, I assumed the difference of surface energy would be a reason, and the surface energies of P2- and O2-type NMOs were estimated using the total energies of oxides such as NiO and MnO. The calculated results show a clear difference on the (100) surface energy. The P2-type structure would be stabilized by milling due to the increase of the exposed (100) surface area.

A faster method than DFT calculations, such as machine learning interatomic potential (MLIP) calculation, is needed to study the change in potential due to the substitution of Ni in NMO with other elements. DFT calculations were performed for several substituents (Mg, Zn, Cu, Sn), and the calculated results were compared with the predicted results of MLIP calculations. From the comparison, I found that the CHGNet potential has good agreement with DFT. Furthermore, the DFT calculation showed that an O-redox mechanism of the P2-structure; it indicates if milling process could introduce the Ni-defects and the defect density could be controlled, the NMO material with low Ni amount and high capacity will be obtained. These results will be presented at Pacifichem2025.

References

[1] N. Yabuuchi, K. Kubota, M. Dahbi, S. Komada, Chem. Rev. **114**, 11636 (2014).

[2] R. Kataoka, N. Taguchi, K. Tada, A. Machida, N. Takeichi, Batteries & Supercaps **6**, e202200462 (2022).

[3] R. Yokoi, R. Kataoka, T. Masese, V. Bach, M. Finkbeiner, M. Weil, M. Baumann, M. Motoshita, Res. Conservation Recycl. **204**, 107526 (2024).

[4] P.-F. Wang, Y. You, Y.-X. Yin, Y.-S. Wang, L.-J. Wan, L. Gu, Y.-G. Guo, Angew. Chem. Int. Ed. **55**, 7445 (2016).

Exploration of photonic hypermaterials with complete-gap

Nayuta TAKEMORI
Department of Physics,
Osaka University, Toyonaka,Osaka 560-0043,JAPAN

In this study, we investigated the formation mechanisms of photonic band gaps in two-dimensional quasiperiodic structures using large-scale parallel computations. We focused on three representative tilings—the Hexagon-Boat-Star (HBS) tiling, the square-triangle tiling [1], and the Ammann-Beenker tiling [2]—and constructed photonic crystal models by placing air cylinders at each vertex on a dielectric background.

The simulations were performed using a custom-built photonic band structure solver based on the plane-wave expansion method. We adopted the Ho method [3] to ensure accurate eigenvalue convergence and employed the MAGMA GPU-based eigensolver to accelerate the diagonalization of large sparse matrices. These techniques enabled us to compute the photonic band structures efficiently across various geometrical configurations and material parameters.

Our results [4] revealed the existence of complete photonic band gaps in the square-triangle and HBS tilings. By introducing secondary air cylinders at the centers of star prototiles, we were able to significantly enhance the gap width. This work paves the way for more efficient designs in photonic technologies, with potential applications in optical sensors and novel laser systems.

References

[1] M. E. Zoorob et al., *Nature* **404**, 740 (2000).

[2] D. T. Roper, D. M. Beggs, M. A. Kaliteevski, S. Brand and R. A. Abram, Journal of Modern Optics **53** 407–416 (2006).

[3] K. M. Ho, C. T. Chan, and C. M. Soukoulis, *Phys. Rev. Lett.* **65**, 3152 (1990).

[4] N. Takemori and A. Yamamoto, *J. Phys.: Condens. Matter, submitted*

Magnetic properties of ferromagnetic Fe lattice induced by He atoms trapped in vacancy

Kazuhito Ohsawa
Institute for Applied Mechanics, Kyushu University,
Kasuga-koen 6-1, Kasuga, Fukuoka 816-8580

Introduction

Iron (Fe) and its alloys are important structural materials in advanced fusion reactors. Vacancies (V) and vacancy type lattice defects are nucleated in the plasma facing materials (PFMs) used in the fusion reactors under the irradiation circumstance. Such vacancy type lattice defects are considered to be remarkable trap sites of helium (He) atoms. According to first-principle calculations, more than 30 He atoms can be accommodated in a single vacancy. So, the effects of the vacancy-helium (V-He) complexes, vacancy trapping one or multiple He, have been investigated in the field of the PFMs for safe operation of the fusion reactors. Rare gas, such as He, does not make chemical bonding with other elements. However, He atoms trapped in a vacancy physically presses the Fe lattice, and it causes stress field. In the present report, we focused on the magneto-volume effect around the V-He complexes, that is, variation of magnetic moment of Fe atoms derived from the stress field owing to the He atoms trapped in a Fe vacancy.

Simulation method

First-principle calculations based on density functional theory are performed by Vienna ab-initio simulation package (VASP) with generalized gradient approximation (GGA) and projector augmented wave method (PAW). We used supercell in which one vacancy was introduced into 128 Fe atoms (4x4x4 bcc lattice). The cut-off energy of plane wave was 500eV. In the present simulations, Fe atoms are supposed to be ferromagnetic elements.

Binding energy E_b between single or multiple He atoms and vacancy was estimated, as follows.

$$E_b=E[\mathrm{Fe}_{m-1}\mathrm{VHe}_n]+nE[\mathrm{Fe}_m]-E[\mathrm{Fe}_{m-1}\mathrm{V}]-E[\mathrm{Fe}_m\mathrm{He}] \qquad (1)$$

where E is cohesive energy of supercell. For example, the supercell $\mathrm{Fe}_{m-1}\mathrm{VHe}_n$ is composed of m-1 Fe atoms, one vacancy V, and n He atoms trapped in the Fe vacancy. Similarly, supercell Fe_m is perfect Fe lattice, $\mathrm{Fe}_{m-1}\mathrm{V}$ is supercell including a vacancy. $\mathrm{Fe}_m\mathrm{He}$ represents supercell including a He located at an interstitial lattice site. In the present simulations, the total number of Fe atoms is m=128.

Results and discussion

There are two typical interstitial sites, T-site and O-site, in bcc lattice, as shown in Fig. 1. An interstitial He atom at T-site is more stable than that at O-site. We searched stable structures of single and multiple He atoms trapped in the Fe vacancy, as shown in Fig. 2. In the case of single He, it is located at the center of the Fe vacancy. While, multiple He atoms in the vacancy are located at positions separated from other atoms as far as possible. The reason why such structures are selected is that He is rare gas which does not make chemical bonding.

Binding energies are shown in Fig. 3, which is almost proportional to the number of He atoms. Fig. 4 shows the relation between average magnetic moment of Fe atoms and volume expansion of Fe lattice. The magnetism of Fe lattice is larger, as the number of He atoms trapped in the Fe vacancy increases. This result indicates that magneto-volume effect is observed around Fe-V complex. We expect that this study will be applied to development of a new non-destructive inspection method to detect He aggregation in ferromagnetic materials

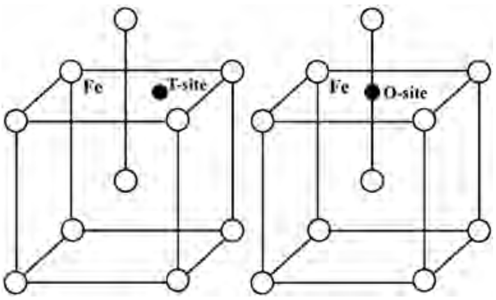

Fig. 1: Schematic view of T-site and O-site in bcc lattice.

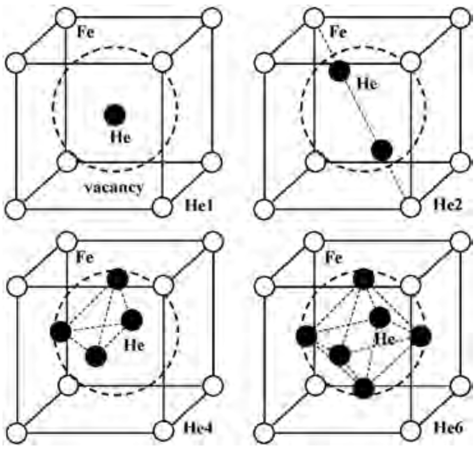

Fig. 2: Schematic view of stable structure of He atoms in Fe vacancy.

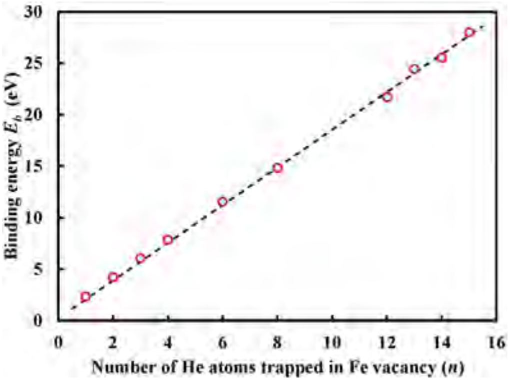

Fig.3: Binding energy for single and multiple He atoms trapped in Fe vacancy.

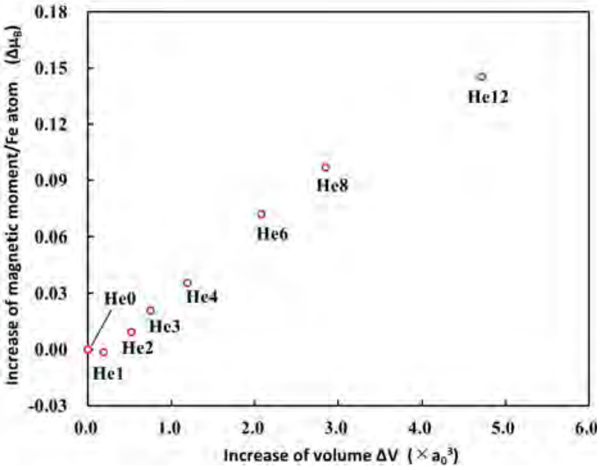

Fig. 4: Relation between average magnetic moment of Fe atoms and volume expansion of Fe supercell.

Evaluation of a New Methodology for Emission Spectra of Light-Element Materials

Masahito Niibe,[a,b] Takeru Nakashima,[c] Yoko Saito,[c] Yasunobu Ando,[c] Teruyasu Mizoguchi,[d] and Iwao Matsuda[a]

[a] *ISSP, The University of Tokyo, 5-1-5Kashiwa-no-ha, Kashiwa, Chiba 277-8581*

[b] *LASTI, University of Hyogo, 3-1-2 Koto, Kamigori, Hyogo 678-1205*

[c] *IIR, Institute of Science Tokyo, Yokohama, Kanagawa 226-8501*

[d] *IIS, The University of Tokyo, Komaba, Tokyo 153-8505, Japan*

X-ray emission spectroscopy (XES) is a method for spectroscopic analysis of X-rays emitted from atoms excited by means such as X-rays, electron beams, and particle beams during the relaxation process of the excitation [1]. XES can directly identify the valence electronic states and track the chemical reactions occurring at the surface. This usability potentially leads to the prediction of new substances and to design functional materials through combinations of material informatics and computational simulations.

Especially, XES is less commonly performed than X-ray absorption spectroscopy (XAS) due to limitations in measurement equipment. Therefore, *ab-initio* simulations play a crucial role; however, there are relatively few *ab-initio* codes designed for simulating XES. We have focused on this difficulty and found the new methodology to simulate XES for light-element materials.

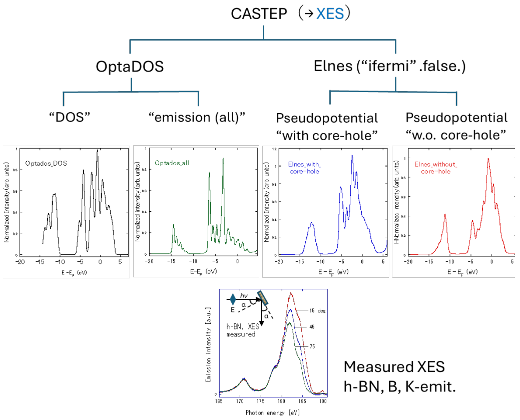

Fig.1: Schematic comparison of the applications of ELNES and OptaDOS for XES, and their treatment of core-hole effects.

In this study, we evaluate a new methodology for simulating XES of light-element materials through a series of material calculations using the facilities of the Supercomputer Center, ISSP. The methodology involves applying CASTEP's conventional ELNES [2] approach to XES simulations, while neglecting core-hole effects. To verify this approach, we compare the XES results obtained using our methodology with those from OptaDOS [3] and assess the impact of core-hole effects in light-element materials, which is shown schematically in Fig.1. Additionally, we compare both simulation

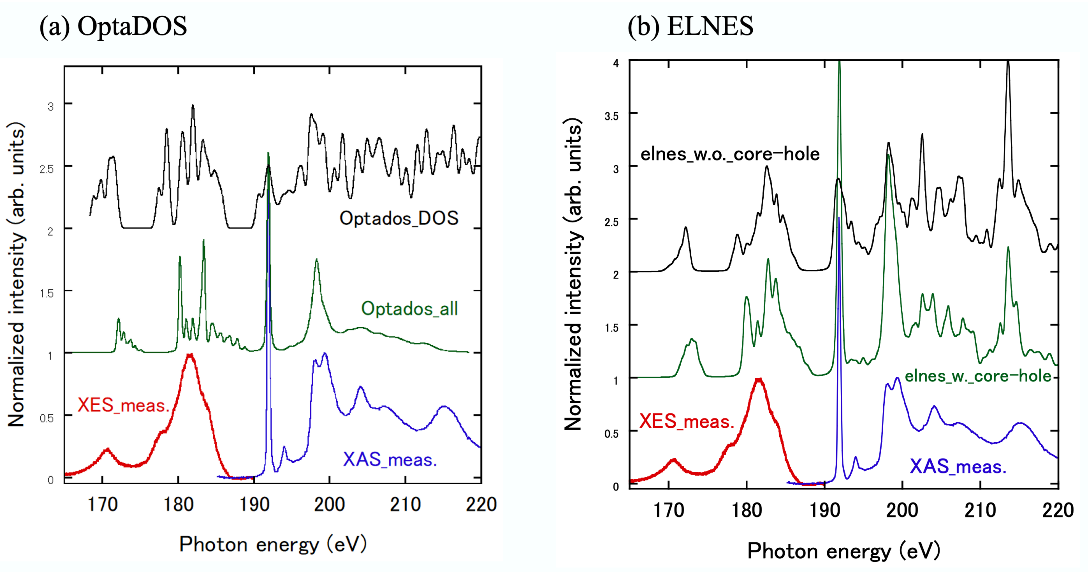

Fig.2: Measured and calculated XES and XAS spectra near the B K-edge of h-BN powder. In both (a) and (b), the red and blue lines indicate the measured XES and XAS, respectively. The green and black lines represent the calculated XES or XAS spectra. (a) shows the simulation results obtained using the OptaDOS method, while (b) shows those using the CASTEP-ELNES method. CASTEP-ELNES method without core-hole effect showed the good agreement with experimental XES spectra. The energy axes of the calculated spectra near the Fermi edge were shifted to almost coincide with the measured spectra.

results with experimental data to evaluate the accuracy and validity of our methodology. For some light-element material, we confirmed that our methodology successfully reproduces the experimental XES spectra. Figure 2 shows the measured and calculated XES and XAS spectra near the B K-edge of h-BN powder as example of our calculations. This study is currently under review [4].

References

[1] A. Meisel, G. Leonhardt, R. Szargan, “X-ray spectra and chemical binding” Springer-Verlag, New York (1989).

[2] M. C. Payne, M. P. Teter, D. C. Allan, *et al.*, Rev. Modern Phys. **64**, 1045 (1992).

[3] A. J. Morris, R. J. Nicholls, C. J. Pickard, and J. R. Yates, Comput. Phys. Commun. **185**, 1477 (2014).

[4] M. Niibe, T. Nakashima, Y Saito, *et al.*, e-J. Surf. Sci. Nanotechnol. *under review.*

Clarification of adhesion mechanism at interface between plasma-treated fluoropolymer and CuO using DFT+U method

Yuji OHKUBO, Kota YAMAGUCHI, and Kouji INAGAKI
Graduate School of Engineering,
Osaka University, 2-1 Yamadaoka Suita, Osaka 565-0871

Polytetrafluoroethylene (PTFE) has very low relative dielectric constant and dielectric loss tangent is considered as a suitable dielectric of high frequency printed wiring boards. However, PTFE has low adhesion property, so adhering PTFE to copper foil is difficult. We have achieved generation of oxygen-containing functional groups and adhesion strength of 0.98 N/mm between PTFE and Cu when PTFE was Helium-plasma-treated at over 200°C under atmospheric pressure [1]. The adsorption energies of fluorinated molecules with C–OH, C=O, $\mathrm{C{-}OO^{\cdot}}$ generated by plasma treatment on Cu(111) surface were calculated to investigate the functional groups that contribute to adhesion improvement [2]. However, X-ray Photoelectron Spectroscopy (XPS) spectra indicates that the copper foil surface is naturally oxidized to CuO by atmospheric oxygen. In this report, we calculate the adsorption energies of fluorinated molecules on the CuO(111) surface, taking into account the natural oxidation of the copper foil, and clarify the functional group that contributes to adhesion improvement.

The calculations were performed using the STATE (Simulation tool for atom technology) code based on Density functional theory (DFT) with plane-wave basis and ultra-soft pseudopotentials. The standard DFT fails to obtain the correct electronic structure of CuO due to the strong electron correlation and antiferromagnetic behavior. Therefore, in this study, we used the DFT+U method, which has been reported to accurately describe the structure of CuO by considering on-site Coulomb repulsion among localized d-d electrons by incorporating an extra energetic penalty for delocalization. The exchange-correlation functional used was the generalized gradient approximation (GGA) based on the Perdew–Burke–Ernzerhof (PBE) formulation. The wave function and the charge density of cutoff energies were 36 Ry and 400 Ry, respectively. K point mesh was 9 × 9 × 9 when CuO bulk is calculated.

The adsorption energy (E_{ads}) per molecule was calculated from the relation

$$E_{\mathrm{ads}} = (E_{\mathrm{surf}} + E_{\mathrm{mol}}) - E_{\mathrm{mol/surf}} \qquad (1)$$

where E_{surf} is the energy of the naked surface slab; E_{mol} is the energy of the isolated fluorinated molecules; $E_{\mathrm{mol/surf}}$ is the total energy of the adsorbate–substrate system.

Transition state energies (E_{a}) were calculated using the CI-NEB method to determine the activation energies of various adsorption reactions. The activation energies (E_{act}) were calculated using the following equation.

$$E_{\mathrm{act}} = E_{\mathrm{a}} - E_{\mathrm{ini}} \qquad (2)$$

Table. 1. E_{ads} of fluorinated molecules on CuO(111) surface and E_{act} of various reactions.

	E_{ads} [eV]			E_{act} [eV]
	Adsorption site			
molecule	$\mathrm{Cu_{3c}}$	$\mathrm{Cu_{4c}}$	$\mathrm{O_{3c}}$	
$\mathrm{CF_3{-}CF_3}$	0.00	0.00	0.00	-
$\mathrm{CF_3{-}CF_2{-}OH}$	0.08	-	0.50	-
$\mathrm{CF_3{-}CF{=}O}$	0.00	0.00	0.00	-
$\mathrm{CF_3{-}CF_2{-}OO^{\cdot}}$	0.65	0.14	0.08	-
$\mathrm{CF_3{-}CF_2^{\cdot}}$	-	-	2.37	-
$\mathrm{CF_3{-}CF_2{-}O^{\cdot}}$	1.79	-	-	-
$\mathrm{CF_3{-}CF_2^{\cdot} + F}$	-	-	0.87	2.39
$\mathrm{CF_3{-}CF_2{-}O^{\cdot} + H}$	1.31	-	-	0.00
$\mathrm{CF_3{-}CF_2{-}O^{\cdot} + O}$	0.83	-	-	1.15

Table. 2. E_{ads} of fluorinated molecules on nonstoichiometric CuO(111) surface.

molecule	E_{ads} [eV]
$\mathrm{CF_3{-}CF_3}$	0.00
$\mathrm{CF_3{-}CF_2{-}O^{\cdot} + H}$	1.66
$\mathrm{CF_3{-}CF{=}O}$	0.14
$\mathrm{CF_3{-}CF_2{-}OO^{\cdot}}$	2.29
$\mathrm{CF_3{-}CF_2{-}O^{\cdot}}$	3.23

where E_{ini} is the energy of the initial state.

Table 1 shows the calculated E_{ads} of fluorinated molecules on CuO(111) surface and E_{act} of various reactions. The [+] in **Table 1** indicates that the F, H, or O atoms in the fluorinated molecule dissociated and adsorbed on the CuO(111) surface.

$\mathrm{CF_3{-}CF_3}$ was not adsorbed at either site ($E_{\mathrm{ads}} = 0$ eV). In addition, when the F atom dissociates from $\mathrm{CF_3{-}CF_3}$ and $\mathrm{CF_3{-}CF_2^{\cdot}}$ adsorbs, the activation energy is very large, indicating that $\mathrm{CF_3{-}CF_3}$ cannot adsorb on the CuO(111) surface. This is consistent with the experimental result that untreated PTFE cannot adhere to copper foil[1]. The adsorption energies of fluorinated molecules with oxygen-containing functional groups (C–OH, C=O, C–OO$^{\cdot}$) introduced by plasma treatment are all lower than 1 eV, indicating that they do not contribute significantly to adhesion. On the other hand, the adsorption energy of $\mathrm{CF_3{-}CF_2{-}O^{\cdot}}$ was as high as 1.79 eV. When the H atom dissociates from $\mathrm{CF_3{-}CF_2{-}OH}$ or the O atom dissociates from $\mathrm{CF_3{-}CF_2{-}OO^{\cdot}}$ and $\mathrm{CF_3{-}CF_2{-}O^{\cdot}}$ adsorbs, the activation energies are 0.00 eV and 1.15 eV, respectively. These reactions are likely to proceed under the thermocompression conditions (320°C) used to bond the plasma-treated PTFE and copper foil [1]. Therefore, –OH and –OO$^{\cdot}$ are thought to contribute to adhesion improvement by dissociating and adsorbing H and O atoms during thermal compression.

The adsorption energy of $\mathrm{CF_3{-}CF_2^{\cdot}}$ was the highest at 2.37 eV. The adsorption state of $\mathrm{CF_3{-}CF_2^{\cdot}}$ on a stoichiometric CuO(111) surface is equivalent to that of $\mathrm{CF_3{-}CF_2{-}O^{\cdot}}$ on a nonstoichiometric CuO(111) surface with an oxygen vacancy. Since the adsorption energy is expected to increase significantly when oxygen vacancies exist on the CuO(111) surface, the adsorption energy on the nonstoichiometric CuO(111) surface was also calculated.

Table 2 shows that the adsorption energy increases significantly if oxygen vacancies exist on the CuO(111) surface. Oxygen vacancies are thought to be created by diffusion of oxygen atoms into the bulk (Cu or $\mathrm{Cu_2O}$ layer) through thermal compression [3].

References

[1] M. Nishino et al., *RSC adv.*, **13** (2023) 25895–25903.

[2] 西野実沙 他, 日本接着学会 第 60 回年次大会講演要旨集 (2022) 50–51.

[3] S. Y. Lee et al., *Appl. Surf. Sci.* **206** (2003) 102–109.

Ab-initio study on phonon localization and phonon-assisted electron transport in multilayer 2D materials

Kenji TSURUTA, Kosuke TAKAHASHI, Ryusei TERASAKA, Yuri FUKAYA,
Masaaki MISAWA,[a] and Satoshi OHMURA[b]
*Department of Electrical and Electronic Engineering, Okayama University,
Okayama 700-8530, Japan*
[a] *Department of Intelligent Mechanical Engineering, Fukuoka Institute of Technology,
Fukuoka 811-0295, Japan*
[b] *Department of Civil and Environmental Engineering, Hiroshima Institute of Technology,
Hiroshima 731-5193, Japan*

The current operating frequency of telecommunication devices is in the GHz band and, with increasing demand for communication, the range expected will be toward THz regime in the future. The objective of this research is thus to investigate and design materials for devices operating in the THz band. Specifically, by introducing defects in a bilayer structure of graphene and boron nitride (BN), we aimed to control the localization of phonons by using defects as channels. We also investigated a phonon-induced electron transport between carbon nanotubes (CNTs) and boron nitride nanotubes (BNNTs) in CNTs and BNNTs heterostructures. Ultrafast photo-induced charge transfer from CNTs to BNNTs through electron channels and the subsequent formation of radial phonons at the interface of van der Waals heterostructures has been demonstrated through ultrafast time-resolved electron diffraction measurements [1].

In this study, first-principles calculations based on density functional theory were performed using the Vienna Ab initio Simulation Package (VASP) and Phonopy [2] to perform phonon analysis. Simulation models of graphene and BN bilayer structures and CNTs and BNNTs heterostructures were created and the phonon dispersion relations were calculated by VASP and Phonopy using these models as inputs to analyze each vibrational mode.

The results of phonon analysis show that the introduction of defects in the graphene resulted in localized phonon modes in the BN layer underneath the defects [3], which may lead to turning on/off the localization of phonon states. In the study of CNT and BNNT heterostructure, we compared the electronic band structure at the ground state with that for the structure where the BNNT layer was displaced according to phonon modes excited with large out-of-plane displacement. We found that by exciting the phonon mode, the electronic band of the BNNT shifts to the lower energy side and overlaps with the near-ultraviolet absorption band of the CNT, allowing electrons to undergo interlayer transition. Also, the wave functions of the shifted bands were found to spatially overlap between CNTs and BNNTs. As a typical case among the transfer mode assisted by the phonon excitations, figure 1 shows a CNT (20,0) – BNNT (29,0) heterostructure subjected to one of the phonon modes as well as the wave function distribution overlapping between CNT and BNNT.

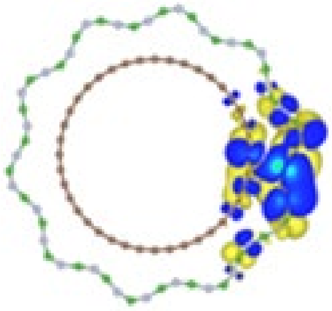

Fig. 1 Wave function in a CNT (20,0) – BNNT (29,0) heterostructure subjected to a phonon mode.

References

[1] Y. Saida *et al.*, *Nat. Commun.* **15**, 4600 (2024).
[2] A. Togo *et al.*, *J. Phys.: Condens. Matter* **35** ,353001 (2023)
[3] K. Takahashi *et al.*, in *Abstract Book of the 10th International Symposium on Surface Science (ISSS-10)*, 3P31 (2024).

Structural analysis of metal oxide quasicrystal thin films

Junji YUHARA
School of Engineering, Nagoya University,
Furo-cho, Chikusa-ku, Nagoya, Aichi 464-8603

We have studied metal oxide quasicrystal ultra-thin films [1] using massively parallel computer simulations. This year, we focused on the structural analysis of honeycomb structure ultrathin Ce-Ti-O films on Pt(111) [2]. The density functional calculations were conducted using VAPS 5.4.4.

After deposition of 0.5 ML Ce and 0.8 ML Ti on Pt(111)/sapphire(0001), following with annealing in oxygen atmosphere and vacuum, an arrangement of dodecagonal clusters, which consists of triangles and squares marked in white, were locally observed in STM image (Fig. 1). In addition, there are some purple triangles and green trapezoids which have an unequal distance to the clusters marked in white, leading it to be recognized as OQC-related structure.

For the OQC-related structure of the ultrathin Ce-Ti-O film, Ce corresponds to Ce^{3+}. Titanium appears as Ti^{2+} ions, as the XPS and XAS spectra indicate. The elemental atomic composition was determined based on the experiment, proposing a low-density model, as shown in Fig. 2. This model's stability and STM simulation are calculated using VASP. Surface atomic density is estimated through XPS and Rutherford backscattering spectroscopy.

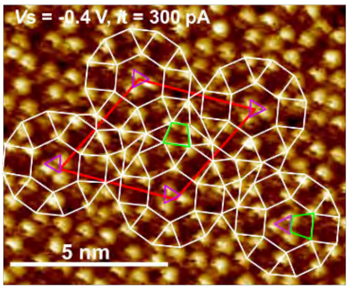

Fig.1: STM image of OQC-related structure of ultra-thin Ce-Ti-O film.

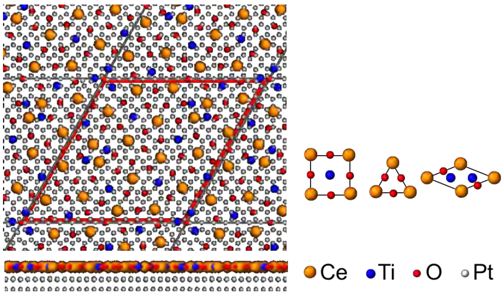

Fig.2: Schematic structural model of OQC-related structure of ultra-thin Ce-Ti-O film.

References

[1] J. Yuhara, K. Horiba, R. Sugiura, X. Li, T. Yamada, Phys. Rev. Mater. **4**, 103402 (2020)

[2] X. Li, S. Yamada, Y. Yamada, M. Yoshida, Y. Hashimoto, T. Matsushita, W. Ma, E. Gaudry, and J. Yuhara, J. Phys. Chem. C **128**, 20238 (2024)

Theoretical study of work function and band gap of double-perovskite

Kazume NISHIDATE
Graduate School of Science and Engineering, Iwate University
4-3-5 Ueda, Morioka, Iwate, 020-8551

In our course of study, we found that the origin of the optical band gap of 1.0 eV of the double perovskite $\mathrm{Ba_2PrBiO_6}$ may originate in its defect structure, namely, $\mathrm{Pr_{Bi}}$ surface defect[1]. This year, we mainly focus on the surface electronic state of $\mathrm{TiO_2}$ rutile photocatalyst as a reference, since its work function and electronic structures are fairly well-known compared to those of the double perovskite, and therefore, it gives us a guide to construct the model systems. We employed GGA with U method to suppress the underestimation tendency of the band gap. We constructed (110) surface slab consisting of four 3×3 layers of $\mathrm{TiO_2}$ with the vacuum region of 20 Å.

When we apply the U= 10 eV, the calculated band gap, 2.9 eV, is almost equal to that of the experimental one, 3 eV. However, the crystal field energy splitting of the t_{2g} and the e_g becomes somewhat blurred, consistent with the reported result[2]. Next, we evaluated projected DOS for each atom of layers. We found that the DOS of the topmost surface oxygen shows similar energy distribution as that of the oxygen in the $\mathrm{TiO_2}$ bulk. On the other hand, the $3d$ state of the topmost Ti is significantly modified due to the lack of the surrounding oxygen atoms breaking its crystal field symmetry. The projected DOS for the Ti at the subsurface shows a similar energy distribution as that of the Ti in the $\mathrm{TiO_2}$ bulk system. Therefore, we can conclude that the electronic structure of (110) $\mathrm{TiO_2}$ slab already becomes bulk-like in the subsurface region. Next, we studied surface defects. When we introduce the $\mathrm{V_O}$ by subtracting an oxygen atom from the topmost layer, we observed defect-induced states 0.66 eV above the VBM (valence band maximum). The interstitial Ti at the subsurface, Ti_i, creates defect induced states 0.35 eV above the VBM. Adsorption of hydrogen on the topmost oxygen, OH defect, creates an energy state just above the VBM. We are currently inspecting the validity of our findings compared with the reported experimental results.

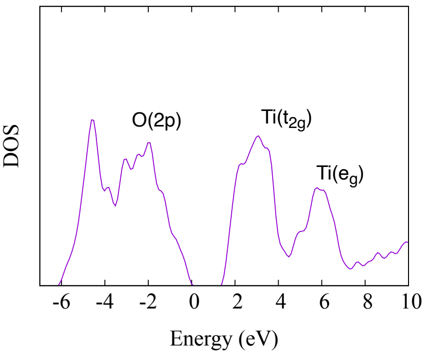

Figure 1: DOS of Rutile (110) surface

References

[1] K. Nishidate, M. Matsukawa, A. Matsushita, Y. Li, D.C. Roy, and M. Hasegawa,: Surf. and Int. **24**, 103914 (2024).

[2] M. E. Arroyo-de Dompablo, A. Morales-Garcia, and M. Taravillo, J. Chem. Phys, **135**, 054503 (2011)

Development of a multi-GPU quasiparticle self-consistent *GW* calculation code

Masao OBATA

Institute of Science and Engineering, Kanazawa University, Kanazawa, Ishikawa 920-1192

The quasi-particle self-consistent *GW* (QSGW) method is a powerful approach for first-principles electronic structure calculations, surpassing the one-shot G_0W_0 approach [1]. However, its computational cost is significantly higher due to the requirement for off-diagonal elements of the self-energy Σ, unlike G_0W_0 calculations. Additionally, the self-consistent procedure demands considerable computational time. The main computationally intensive parts are the computation of Σ and screened Coulomb interaction W, which scale with the fourth power of the system size and the square of the k-points.

In this study, we applied a multi-GPU implementation to the QSGW code ecalj [2] to extend its application range by accelerating computation. Our approach utilizes GPU-accelerated math libraries with OpenACC programming. The math libraries are accessed through wrapper functions providing a unified interface for GPU and CPU versions. These wrapper functions, implemented using Fortran module coding and the C preprocessor, enable easy switching between GPU and CPU computations. This implementation avoids code duplication, ensuring that most of the code is common to both CPU and GPU versions. By utilizing math libraries, we have facilitated the implementation of mixed-precision calculations such as TensorFloat-32 (TF32). As a benchmark, for an interface system with 40 atoms (Type II superlattice $(\mathrm{InAs})_{10}/(\mathrm{GaSb})_{10}$), the computation of Σ and W using 4 GPUs was completed in 2.9 hours (0.9 hours with TF32). In comparison, the same calculation on a CPU (512 cores) required 34 hours, achieving a speedup of 12 times and 38 times with TF32. Although QSGW calculations consume significant memory due to the expansion coefficients of W and wavefunction products, the introduction of batch partitioning methods enables robust calculations for large-scale systems.

References

[1] M. van Schilfgaarde et al., Phys. Rev. Lett., 96, 226402 (2006).

[2]ecalj:https://github.com/tkotani/ecalj

Theoretical Study on Electronic Properties in New Nanoscale Surfaces and Interfaces

Katsuyoshi KOBAYASHI
Department of Physics, Ochanomizu University
2-1-1 Otsuka, Bunkyo-ku, Tokyo 112-8610

Recently, there has been a report of spirally grown graphene [1]. This year, we calculated the electronic state and electron transmission properties of spirally structured graphene. Figure 1 shows a structure of a finite-width graphene which changes its direction by 120 degrees. A triangular structure is inserted between two finite-width graphenes. Figure 2 shows an energy band structure of a spiral structure which has this triangular structure as the unit cell. The tight-binding method is used. Only the transfer energy between nearest-neighbor atoms is considered. The unit of energy is the transfer energy. The figure shows the case where the triangular unit cell consists of 9 carbon atoms. This corresponds to the width of 6 atoms of the straight graphene. The energy bands are symmetrical with respect to the zero energy line with a phase shift by π. This result can be understood from the triangular structure in Fig. 1.

The atoms in a triangle are divided into A and B sublattices. We assign the boundary atoms as A sublattices. Inside the triangle, A sublattice atoms have only B sublattice atoms next to them, and vice versa. In a spiral structure, which is a periodic structure of triangles, the boundary A sublattice atoms have adjacent A sublattice atoms in the neighboring triangles. Therefore, in the tight-binding equation, if the sign of the amplitudes of the A sublattice atoms of one triangle and that of the B sublattice atoms of the neighboring triangles are simultaneously inverted, it is also the solution with the energy having the reverse sign. In this case, a phase mismatch arises between the boundary A sublattice atoms of adjacent triangles, which is resolved by the Bloch phase π.

Figure 3 shows the electron transmission property calculated as a function of energy. The transmission probability between two straight graphenes through a spiral graphene is calculated. The rotation angle of the spiral graphene is that of 10 triangular unit cells. The transmission probability is close to zero in the band gap region of the energy bands of the spiral graphene. Outside the band gap, the transmission probability is close to unity. It implies that electrons travel well through the spiral structure. First-principles calculations of wider graphene are found in Ref. [2].

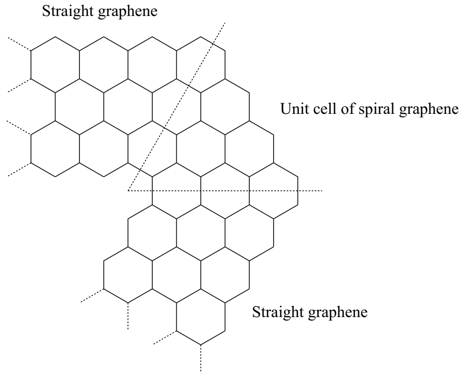

Figure 1: Atomic structure of a graphene spiral structure. The figure shows a triangular unit cell of a spiral graphene connected to two straight graphenes.

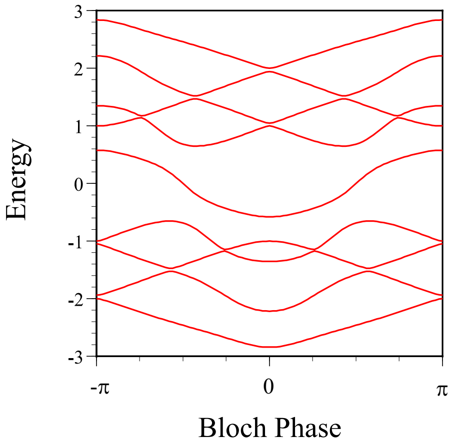

Figure 2: Band structure of a spiral graphene.

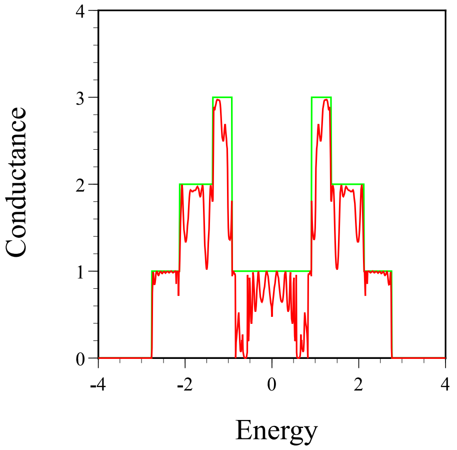

Figure 3: Electrical condunctance through a spiral graphene. The unit of conductance is $2e^2/h$. The green line shows the number of conduction channels.

References

[1] H. Sun, X. Kong, H. Park, F. Liu, Z. Lee, F. Ding, Adv. Mater. **34** (2022) 2107587.

[2] Z. Zhou, L. Yan, X.-M. Wang, D. Zhang, J.-Y. Yan, Results in Phys. **35** (2022) 105351.

Photocatalytic versus Thermal Reaction Pathways of CO_2 Methanation over Single Ru–Ni/ZrO_2 Catalyst Proved by DFT Calculations

Masahito Sasaki, Keisuke Hara, Tomoki Oyumi, and Yasuo Izumi

Graduate School of Science, Chiba University, Yayoi 1-33, Inage-ku, Chiba 263-8522

Photocatalytic CO_2 reduction into fuels and/or valuable chemicals creates new C neutral cycle. Major problem to apply this technique in sustainable society is slow formation rates of fuels and/or value-added chemicals that are governed by photon number of the light reaching the earth [1].

In this report, the formation rates were increased both by increasing irradiated photons and by effective additive to photocatalyst. The effect of irradiated UV–visible light intensity on photocatalysis was evaluated. We previously reported one of the best photocatalytic CO_2 methanation activity using Ni/ZrO_2 photocatalyst: 0.98 mmol h^{-1} g_{cat}^{-1} irradiated by UV–visible light @186 mW cm^{-2} [2]. Therefore, the effect of single Ru doped onto Ni/ZrO_2 photocatalyst on CH_4 formation rate was also evaluated.

In the evaluation, reaction pathway including the activation energy was important based on density functional theory calculations using Vienna Ab Initio Simulation Package code version 6.4.1. The supercomputer of ISSP was ultimately essential for the searches of reaction pathway for each step from CO_2 to CH_4 over the composite surface of the best photocatalyst using climbing-image nudged elastic band method mostly owing to the CPU comprising more than 128 cores at ISSP.

When the UV–visible light intensity was increased from 186 mW cm^{-2} [2] to 713 mW cm^{-2}, the CO_2 methanation rate increased from 0.98 to 2.9 mmol h^{-1} g_{cat}^{-1} using Ni/ZrO_2 photocatalyst. Furthermore, by doping single Ru (1.0 wt %) to Ni/ZrO_2, the CO_2 methanation rate even increased to 8.9 mmol h^{-1} g_{cat}^{-1} @713 mW cm^{-2}.

DFT calculation results were summarized in Schemes 1 and 2 using single Ru–Ni/ZrO_2 photocatalyst (Panels A and B) in comparison to Ni/ZrO_2 photocatalyst (Panel B′). Scheme 1 corresponded to photocatalytic CO_2 methanation irradiated at 186 mW cm^{-2} or photocatalyst cooled in water bath irradiated at 568 mW cm^{-2}. The activation energy was the highest: 1.17 eV from adsorbed CO_2 to OCOH species at O vacancy site at ZrO_2 surface [3] using both single Ru–Ni/ZrO_2 and Ni/ZrO_2 (Scheme 1B and B′). In fact, under these photocatalytic reaction conditions, photocatalytic CO_2 methanation rates were essentially equivalent either using single Ru–Ni/ZrO_2 or Ni/ZrO_2.

Scheme 2 corresponded to photocatalytic CO_2 methanation irradiated by UV–visible light at 713 mW cm^{-2}, without water cooling. Under the reaction conditions, the catalyst was heated by light energy and the charge separation and resulting red-ox reactions over ZrO_2 surface became negligible compared to thermal steps over Ru and/or Ni (Scheme 2A). Under such reaction conditions, single Ru atom on Ni nanocluster lattice adsorbed CO_2 (Scheme 2B(b) and (b′)) and facilitated the dissociation to CO and O (species c), whereas over Ni cluster surface free from Ru, the weakly-adsorbed CO_2 was much more difficult to dissociate (Scheme 2B′(b) and (c)). This accounted for the rate difference of 2.9 mmol h^{-1} g_{cat}^{-1} using Ni/ZrO_2 versus 8.9 mmol h^{-1} g_{cat}^{-1} using single Ru–Ni/ZrO_2 @713 mW cm^{-2}. The reaction pathway illustrated in Scheme 2A and B was also supported by predominantly adsorbed CO species over single Ru–Ni/ZrO_2 under UV–visible light (Scheme 2A(c–e)) observed by FTIR.

References

[1] T. Loumissi, R. Ishii, K. Hara, T. Oyumi, I. Abe, C. Li, H. Zhang, R. Hirayama, K. Niki, T. Itoi, and Y. Izumi, *Angew. Chem. Int. Ed.* **63**, e202412090 (2024).

[2] H. Zhang, T. Itoi, T. Konishi, and Y. Izumi, *Angew. Chem. Int. Ed.* **60**, 9045–9054 (2021).

[3] K. Hara, M. Nozaki, T. Hirayama, R. Ishii, K. Niki, and Y. Izumi, *J. Phys. Chem. C*, **127**, 1776–1788 (2023).

Scheme 1. Proposed photocatalytic reaction pathway and corresponding free energy calculations of CO_2 photoreduction to proceed over (A, B) single Ru–Ni/ZrO_2 and (B') Ni/ZrO_2.

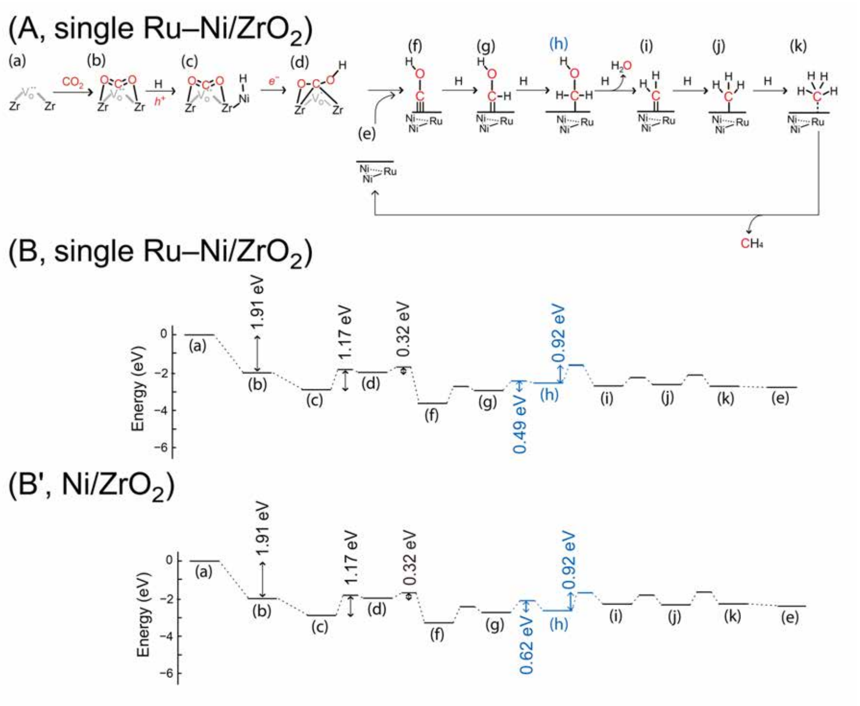

Scheme 2. (A) Proposed thermal reaction pathway and corresponding free energy calculations of CO_2 reduction using (B) Ni/ZrO_2 and (B') single Ru–Ni/ZrO_2.

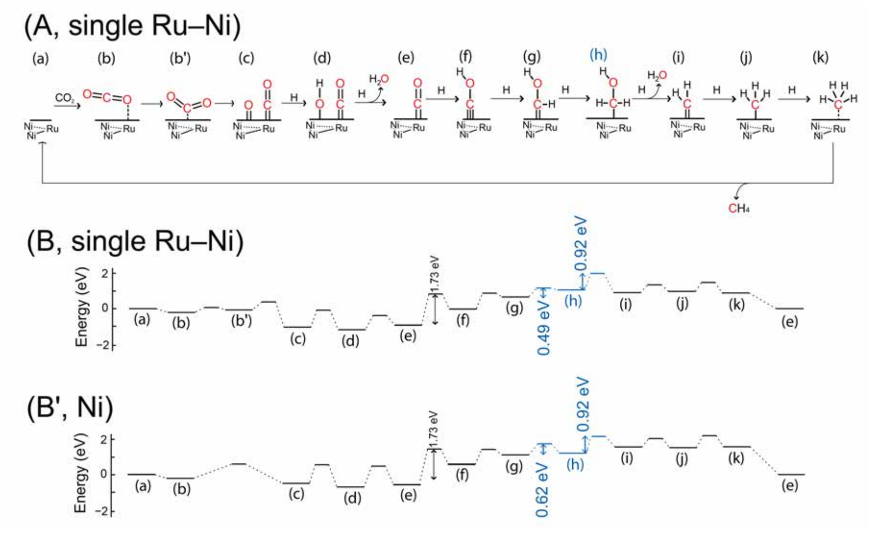

First-principles study of multi-orbital and multi-layer compounds

Hirofumi Sakakibara

Faculty of Engineering, Tottori University, Tottori, Tottori 680-8552

Since the discovery of the Ruddlesden-popper type bilayer nickelate superconductor $La_3Ni_2O_7$ (Fig.1 (a)) [1], related studies and publications have explosively increased. One of this extreme scientific interest may originate the similarity with high-T_c cuprates, because the first example of such cuprates is the single layer Ruddlesden-popper type oxide. A clear similarity is that both compounds are strongly-correlated-electron systems since the main layer is formed by oxidized transition metal (Cu and Ni). On the other hand, the biggest difference is the number of active orbital degrees of freedom, namely, the minimum model of bilayer nickelate may consists of total four orbitals, the $d_{x^2-y^2}$ and $d_{3z^2-r^2}$ orbitals in each layer [2]. Our previous calculation using fluctuation-exchange approximation (FLEX) has shown that the superconducting symmetry in La3Ni2O7 is $s\pm$ with reversed sign between the bonding and anti-bonding bands like as iron-pnictide ones [2]. These bonding is formed by the $d_{3z^2-r^2}$ orbitals facing between the layers.

One of the problems in FLEX calculation is that the incompleteness of the treatment for electron-correlation. A complementary approach is the Density Matrix Renormalization Group (DMRG), in which the numerically exact solution can be obtained. However, DMRG is much consuming about the computational resource, the model should be much simplified compared to our original two-dimensional and multiorbital-multilayer model. To overcome this difficulty, we have derived a one-dimensional ladder model to mimic the bilayer model. In the first paper, we have calculated the two-orbital Hubbard ladder model in which all of the interorbital interactions are omitted (only the intraorbital interaction "U" is activated). The conclusion throughout the analysis of spatial pair correlation function is that this model is favorable for the superconductivity. However, although this model may capture the essence of superconducting transition in La3Ni2O7, there remain a simple problem that whether if the interorbital interactions such as Hund's coupling change the conclusion? To clarify this point, we have additionally derived a *t-J* ladder model, having the lower computational costs to include Hund's coupling. The conclusion is that superconductivity is favorable in this model, and the Hund's coupling may stabilize the superconductivity [4].

Another significant problem is how to theoretically predict a new bilayer superconductor. Until now, all of the bulk nickelates need to be pressurized to exhibit superconductivity (exceptions are the thin-film nickelates, not only the infinite layered ones [5] but also the Ruddlesden-popper type ones [6]). Therefore, to discover a nickelate superconductor free from pressure is a good aim. One well-known empirical rule is that the chemical bonds connecting the NiO2 layer should be straight if the superconductivity occurs. To clarify this hypothesis, we have proposed an oxychloride nickelate $Sr_3Ni_2O_5Cl_2$ (Fig. 1(b))[7] and theoretically evaluated the possibility of supercondutivity. Firstly, we have determined the energetically most stable structure at ambient pressure (= 0 GPa external pressure) using VASP code. The obtained structure has *I*4/*mmm* space group symmetry. Subsequently, we have calculated the phonon dispersion (Fig. 1 (c)) and checked the absence of imaginary mode, which means that the *I*4/*mmm* structure of $Sr_3Ni_2O_5Cl_2$ is dynamically stable at ambient pressure. This theoretical prediction about the symmetry of the crystal structure has been experimentally proven by Yamane *et al.* [8]. We have also constructed a low-energy tight-binding model through the maximally localized Wannier function, including the derivation of onsite interaction parameters using constrained Random Phase Approximation (cRPA) method. We have also applied FLEX approximation to this model to conclude that $Sr_3Ni_2O_5Cl_2$ probably exhibit the superconductivity. Unfortunately, there is still no report that superconductivity is observed in $Sr_3Ni_2O_5Cl_2$. The absence of superconductivity may be because of the stacking faults between layers [8]. The experimentally estimated band gap is much small, implying that $Sr_3Ni_2O_5Cl_2$ is intrinsically metallic, consistent with our first-principles calculation.

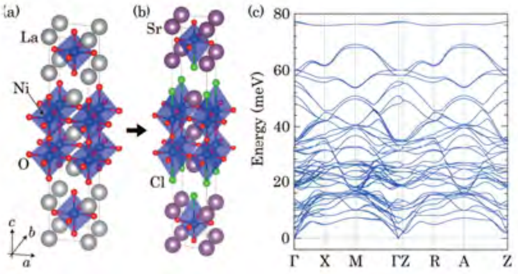

Fig. 1: crystal structure of (a)$La_3Ni_2O_7$ and (b)$Sr_3Ni_2O_5Cl_2$, and phonon dispersion of the latter (cited from Ref. [7]).

References

[1] H. Sun *et al.*, Nature (London) **621**, 493 (2023).

[2] H. Sakakibara, N. Kitamine, M. Ohi, and K. Kuroki, Phys. Rev. Lett. **132**, 106002 (2024).

[3] T. Kaneko, H. Sakakibara, M. Ochi, K. Kuroki, Phys. Rev. B **109**, 045154 (2024).

[4] M. Kakoi, T. Kaneko, H. Sakakibara, M. Ochi, and K. Kuroki, Phys. Rev. B **109**, L201124 (2024).

[5] D. Li et al., Nature (London) **572**, 624 (2019).

[6] E. K. Ko et al., Nature (London) **638**, 935 (2025).

[7] M. Ochi, H. Sakakibara, H. Usui, and K. Kuroki, Phys. Rev. B **111**, 064511 (2025).

[8] K. Yamane et al., Acta Cryst. **C81** (2025).

A theoretical study on an oxidation process at a metal surface

Satoshi Hagiwara
Center for Computational Sciences,
University of Tsukuba, Tennodai, Tsukuba 277-8581

Corrosion reaction at the metal/water interface is one of the significant chemical reactions for controlling material lifetimes. During corrosion reaction, the breakdown of protective oxide passivation layers on host materials occurs due to the migration of environmental Cl ions through the passivation layer. The accumulated Cl ions at the interface mechanically break a metal/oxide junction. Therefore, we carried out the DFT calculations using the Al(111)/α-Al_2O_3(0001) interface to reveal the details of the Cl ion insertion [1]. Moreover, we developed the surface stress calculation method under a finite bias voltage using the effective screening medium (ESM) method [2] and applied it to the Al(111) surface [3]. Here, we explain the results of surface stress.

We performed all calculations by using the open-source package QMAS (Quantum MAterials Simulator) code [4]. To simulate the bias-voltage dependence of surface stress, we combined the macroscopic stress and stress density calculation methods with ESM, which is easily done through the Green's function satisfying the Poisson equation. In this study, we used the vacuum/slab/metal boundary condition of ESM.

The result of macroscopic surface stress quadratically depends on the bias-voltage, which agrees with that of thermodynamic Gokhshtein's equation [5]. The local stress analysis using stress density reveals that the outermost layer behaves as a capacitor. The inner layer contribution to the bias-voltage dependence of surface stress cannot be neglected. Thus, enough thickness of the surface slab is necessary to determine the surface stress precisely. This method will be useful to discuss the mechanical effect on the passivation film breakdown.

References

[1] S. Hagiwara, and M. Otani et al., Corr. Sci. under review. [2] M. Otani and O. Sugino, Phys. Rev. B **73**, 115407 (2006). [3] S. Hagiwara, S. Ishibashi, and M. Otani, Phys. Rev. B **110**, 155409 (2024). [4] https://qmas.jp/. [5] A. Y. Gokhshtein, Russ. Chem. Rev. **44**, 921 (1975).

First principles study on the thermoelectric properties of goniopolar compounds

Hidetomo USUI

Department of Applied Physics,

Shimane University, Nishikawatsu-cho, Matsue, Shimane 690-8504

Goniopolar compounds exhibit both p-type and n-type characteristics depending on direction. Due to this anisotropic nature, these compounds have been investigatedas candidates for transverse thermoelectric materials. For example, the goniopolar thermoelectric material Re_4Si_7 exhibits a relatively high figure of merit $Z_{xy}T$ ~ 0.7 [1]. Mg_3Bi_2 is another goniopolar thermoelectric material, which shows $Z_{xy}T$ of 0.06 at 300K [2]. This value is not particularly high, indicating the need for further optimization.

In this study, we analyzed the thermoelectric performance of Mg_3Bi_2 using first-principles calculations to understand the origin of its relatively high performance. The Quantum ESPRESSO package [3] was used to calculate the electronic and phonon structures of Mg_3Bi_2. The electron relaxation time was evaluated by assuming electron-phonon scattering, using the EPW code [4]. We calculated the electrical resistivity, and the Seebeck coefficient within Boltzmann transport theory, using the calculated relaxation time.

The goniopolarity of Mg_3Bi_2 originates from its band dispersion around the Fermi level. Its band structure features both Dirac cone-like valence and conduction bands at the Γ point, as well as multi-valley bands near the L* point. We found that Mg_3Bi_2 exhibits a long relaxation time, which is favorable for thermoelectric performance. However, the Seebeck coefficient is relatively low due to the closed band gap.

We conclude that opening the band gap is essential to enhancing the Seebeck coefficient and improving transverse thermoelectric performance.

References

[1] M. R. Scudder *et al.*, Energy Environ. Sci. **14**, 4009 (2021).

[2] Y. Goto *et al.*, Chem. Mater. **36**, 2018 (2024).

[3] P Giannozzi *et al.*, J.Phys.:Condens.Matter **29**, 465901 (2017).

[4] H. Lee *et al.*, npj Comput. Mater. **9**, 156 (2023).

Impurity control of chalcogenides by surface-modification

Ken-ichi SHUDO

Fac. of Eng/Sci, Yokohama Nat'l Univ.

Tokiwadai 79-5, Hodogaya-ku Yokohama 2408501

We measured electronic states of layered material such as chalcogenides and topological insulators, experimentally by means of ultraviolet photoemission spectroscopy (UPS) and metastable-atom electronic spectroscopy (MAES). While the spectra of the former method involve the density of state near the surface with a few nanometer depth, those of the latter the spectra only reflect the electronic states whose wavefunctions protrude into vacuum. Thus, we calculated the electronic states of MoS_2 with impurity and defects in the top-most layer, and that of Bi_2Se_3. Several layers of those materials stand for the slab model, and the electronic states are obtained using a first-principle density functional package Vienna Ab initio Simulation Package (VASP). The top panel in Fig.1 indicates the slab of $TiSe_2$ with vacuum layer at the right-hand. The local density in each slice parallel to the surface was projected, into energy distribution as shown in main panel of Fig.1. The special localizations specific to the near-surface region and to the vacuum region are both going to be discussed with the basis of the experimental data.

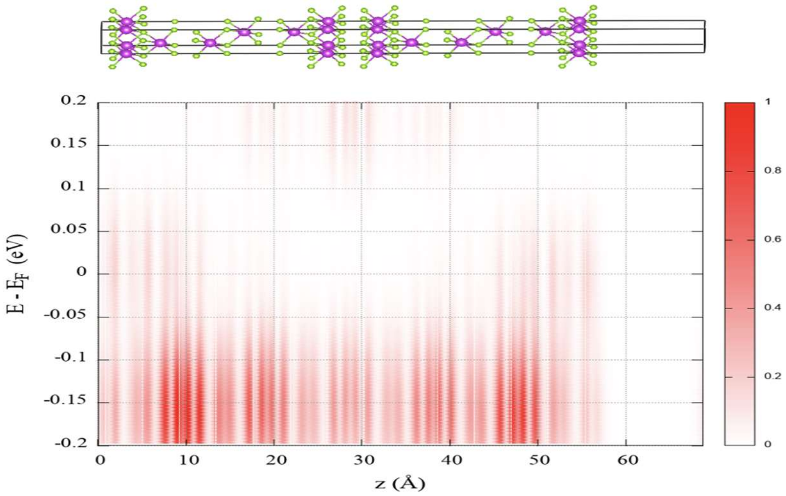

Fig. 1: Spatial distribution of density of state near the surface of Bi_2Se_3. This slab is the case without any defect.

First-principles lattice defects engineering for atomic-scale multiferroics

Takahiro SHIMADA and Susumu MINAMI
Graduate School of Engineering, Kyoto University,
Kyoto daigaku-Katsura, Nishikyo-ku, Kyoto 616-8540

Recent advancements in nanotechnology have driven the need for functional materials that exhibit electromechanical responses at the atomic scale. In this context, this work investigates the electromechanical behavior of an isolated oxygen vacancy in a paraelectric oxide, $BaHfO_3$, using *ab initio* finite electric field calculations based on density functional theory (DFT). Our results unveil a previously unrecognized localized electromechanical phenomenon—negative electrostriction—centered around a single oxygen vacancy.

We models a neutral oxygen vacancy in $BaHfO_3$ using the 5 x 3 x 3 supercell including a relatively large number of atoms up to 225. We simulate the structural and electronic properties under applied finite electric fields up to 15 MV/cm using the VASP code [1] based on the modern theory of polarization [2] with the supercomputers. We explicitly include the effect of electric field on force and stress in order to obtain the equilibrium structure under finite electric fields. The results indicate that, although the pristine $BaHfO_3$ does not exhibit a net polarization, the introduction of an oxygen vacancy leads to a local dipole moment and strain distribution under the electric field. Remarkably, the strain response along the field direction is compressive (negative), a stark contrast to typical positive electrostriction observed in conventional dielectrics.

Further detailed analysis reveals that this negative electrostriction originates from the localized defect states and associated electrons near the vacancy. Under the electric field, these electrons shift in the direction opposite to the field, creating an asymmetric charge distribution. This in turn causes an uneven displacement between the adjacent hafnium atoms, generating localized compressive strain. The calculated electrostrictive coefficients ($Q_{11} = -0.040$ m^4/C^2, $Q_{12} = 0.019$ m^4/C^2) further confirm the negative electrostriction nature, and the local dielectric permittivity near the vacancy is estimated to be ~129—substantially larger than the host material (~43).

This work emphasizes the engineering implications of these findings. First, it shows that oxygen vacancies—commonly treated as passive defects—can be reinterpreted as active electromechanical elements at the atomic scale. Second, since oxygen vacancies can be selectively introduced and manipulated (e.g., via ion irradiation or scanning probe techniques), they present a viable route for constructing ultra-compact and tunable electromechanical devices. Furthermore, unlike conventional materials that require complex processing to achieve miniaturization, the approach demonstrated here relies solely on point defect engineering.

This work has been published in *Journal of Applied Physics* [3].

References

[1] G. Kresse and J. Hafner, Phys. Rev. B **48**, 13115 (1993).

[2] I. Souza, J. Íñiguez, and D. Vanderbilt, Phys. Rev. Lett. **89**, 117602 (2002).

[3] Y. Ikeda, S. Minami, and T. Shimada, J. Appl. Phys. **136**, 214101 (2024).

First-Principles calculation of transverse thermoelectric conductivity in the D0$_3$-type Heusler compound Fe$_3$Si

Susumu MINAMI, Takahiro SHIMADA

Department of Mechanical Engineering and Science,
Kyoto University, Nishikyo-ku, Kyoto 615-8540

The anomalous Nernst effect (ANE), which generates a transverse voltage from a longitudinal temperature gradient in magnetic materials, has gained renewed interest for energy harvesting applications[1]. The intrinsic component of ANE can be understood through the Berry phase concept, with topological electronic structures such as Weyl nodes and nodal lines inducing large Berry curvature. Fe$_3$Si is particularly promising due to its high Curie temperature (820 K[2]) and lack of rare or toxic elements. We performed first-principles calculations based on density functional theory using the VASP for the D03-type Heusler compound Fe$_3$Si. A Wannier function was constructed to calculate the Berry curvature and transverse thermoelectric (TE) properties. The anomalous Hall conductivity (σ_{xy}) and transverse TE conductivity (α_{xy}) were evaluated using Berry curvature formalism with 200×200×200 k-point sampling.

The calculated total magnetic moment was ~5.07 μB/f.u., and σ_{xy} and α_{xy} reached about 500 Ω^{-1}cm^{-1} and 1.5 AK^{-1}m^{-1} at room temperature, consistent with experimental values[3,4]. With hole doping ($E = E_F$ - 0.22 eV), σ_{xy} exhibited a sharp peak reaching ~1500 Ω^{-1}cm^{-1}, while α_{xy} increased to ~5 AK^{-1}m^{-1}. This value is comparable to other well-known ANE materials with topological electronic structures. We identified a clear correspondence between the nodal line network in Fe$_3$Si and large Berry curvature distribution in the Brillouin zone. The nodal lines form ring shapes on the $k_i = 0$ plane and connect near the X point. Our analysis revealed that the density of states composed of nodal lines (D_{NL}) shows peaks that directly correlate with enhanced transverse TE conductivity, specifically attributable to a "Van Hove singularity" in the D_{NL}.

Our first-principles study demonstrates that Fe$_3$Si exhibits α_{xy} of 1.5 AK^{-1}m^{-1} at room temperature, which increases to ~5 AK^{-1}m^{-1} with hole carrier doping[5]. From an experimental perspective, tuning the D_{NL} peak to the Fermi energy through chemical doping or external fields could lead to improved ANE performance in Fe$_3$Si-based materials.

References

[1] M. Mizuguchi and S. Nakatsuji, Sci. Tech. Adv. Mater. **20**, 262 (2019).

[2] Y. Nishino, S.-Y. Inoue, S. Asano, and N. Kawamiya, Phys. Rev. B **48**, 13607 (1993).

[3] Y. Hamada, et al.,, Appl. Phys. Lett. **119**, 152404 (2021).

[4] Y. Wang et al., Appl. Phys. Lett. **125**, 081901 (2024).

[5] S. Minami, S. Hogaki, and T. Shimada, Phys. Rev. Mater. **8**, 075403 (2024).

Atomic-level surface architecture of nanocellulose

Shuji FUJISAWA

Graduate School of Agricultural and Life Sciences ,

The University of Tokyo,Yayoi 1-1-1, Bunkyo-ku, Tokyo 113-8657

The surface molecular structure of nanocellulose has remained poorly understood, primarily due to the hurdles in resolving atomic-level details of its surfaces. Nuclear magnetic resonance (NMR) is a powerful method to unveil the surface structure, but conventional solid-state ^{13}C NMR faces a significant challenge stemming from its low sensitivity at natural abundance. Here, we present first detailed surface architecture of nanocellulose using dynamic nuclear polarization (DNP) enhanced solid-state NMR [1]. DNP-NMR can significantly enhance the detection of surface molecules and their dipolar interactions, enabling detailed analysis of the spatial distribution and substitution positions of the functional groups on the nanocellulose surface. Furthermore, we quantitatively characterized the molecular conformations present in the entire CNF and identified the preferred molecular conformation exhibited specifically on the nanocellulose surface, which was reinforced by molecular dynamics simulations and density functional theory calculations. his combined technique is applicable not only to P-CNF but also to various types of CNF previously reported, such as surface carboxylated- and sulphated-, and aminated-CNFs. Therefore, our approach fills a critical gap in understanding the surface structure and material properties of CNF, and thus can help tailor CNF properties for specific applications in materials science, biotechnology, environmental engineering, and beyond.

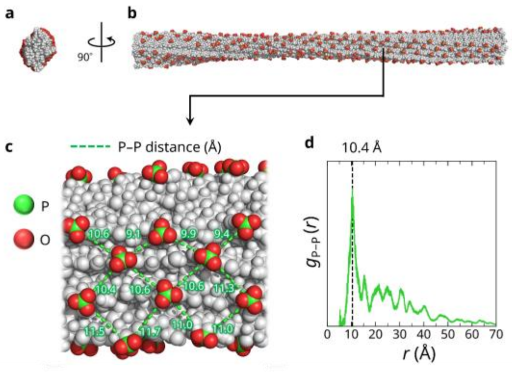

Fig. 1: Distance between phosphorus atoms on the surface of P-CNF. (a,b) Equilibrated structure of a CNF created by MD simulation. (c) enlarged view of the chemical structure (d) Radial distribution function between the phosphorus atoms

References

[1] D. A. Hall et al. Science **276**, 930 (1979)

Revisiting the conventional superconducting theory: Toward nearly uniform electron systems

Ryosuke AKASHI
National Institutes for Quantum Science and Technology

The first-principles calculation of superconducting transition temperatures has long been an intriguing goal in the materials science. Its applicability to phonon-mediated superconductors [1] has been recently improved with the first-principles Eliashberg theory [2, 3, 4] and density functional theory for the superconductors (SCDFT [5, 6, 7]). Its extension to electronic correlation effects such as charge and spin still remains difficult. To include the dynamical charge fluctuation (plasmon) effect one needs to faithfully execute the Eliashberg equation with full dependence of the electron self energy on the wavenumber and frequency, but it is numerically demanding. In the computationally cheaper counterpart, SCDFT, how to properly include the self energy with the formally static DFT is under debate, even in the uniform electron gas [9]. As particular interests are featured in the enhancement of superconductivity in nearly uniform electron systems [11], a efficient code for analyzing the superconducting properties for nearly uniform electrons is needed.

We developed a code to calculate the self energy efficiently for superconducting calculations in the uniform system, aiming at future extension to nearly-uniform cases. The self energy in the GW_0 approximation is defined as follows:

$$\Sigma(\mathbf{k}, i\omega) = -T\sum_{\nu}\int \frac{d\mathbf{q}}{(2\pi)^3} G(\mathbf{k}-\mathbf{q}, i(\omega-\nu))W_0(\mathbf{q}, i\nu), \tag{1}$$

with

$$G(\mathbf{k}, i\omega) = \left[1 - G_0(\mathbf{k}, i\omega)\Sigma(\mathbf{k}, i\omega)\right]^{-1} G_0(\mathbf{k}, i\omega),$$
$$G_0(\mathbf{k}, i\omega) = \frac{e^{i0^{+}\omega}}{i\omega - (k^2 - k_{\mathrm{F}}^2)/2}. \tag{2}$$

Here k_{F} denotes the Fermi wavenumber. To execute the Matsubara summation efficiently, we implemented a method using the intermediate representation [12], thanks to which the number of frequency grid points were reduced from $O(\beta)$ to $O(\log\beta)$ $(\beta = 1/T)$. Figure 1

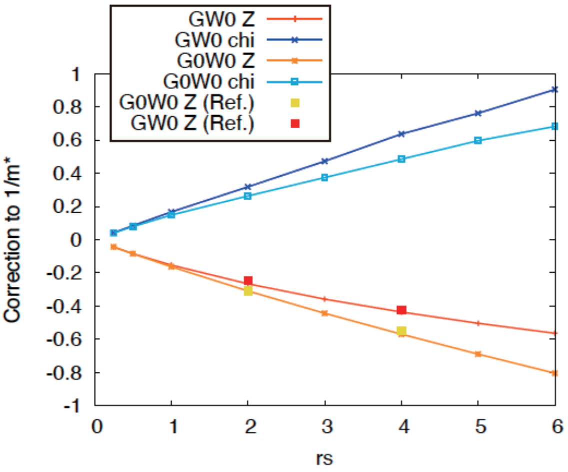

Figure 1: The GW_0 self-energy correction to the inverse effective mass in the uniform electron gas. “Z” and “chi” are contributions coming from the antisymmetric and symmetric parts of the self energy with respect to Matsubara frequency, respectively. The $\mathrm{G}_0\mathrm{W}_0$ results are taken from Ref. [9]. “Ref” points are from Ref. [10]

shows the self-energy correction to the electron normal-state effective mass. The application of this GW_0 self energy to the Eliashberg equations [4] at extremely low temperature and extension to nearly uniform systems are under way.

Also, we have recently pointed out a nearly free electron-like character of the electronic states in a pressure-induced high-temperature superconductor H_3S [11]. We deepened the analysis by examining the Kohn-Sham (KS) wavefunctions. We calculated the band structure in the cubic ($Im\bar{3}m$) phase at 200GPa. Figure 2 depicts the accumulated squared norm of the plane-wave coefficients

$$\sum_{|\mathbf{G}'|<|\mathbf{G}|} |c_n(\mathbf{k}+\mathbf{G}')|^2 \qquad (3)$$

for the KS eigenstates $\psi_{n\mathbf{k}}(\mathbf{r}) = \sum_{\mathbf{G}} c_n(\mathbf{k}+\mathbf{G})e^{i(\mathbf{k}+\mathbf{G})\cdot\mathbf{r}}$ The band index n is labeled in ascending order in theKS energy. The steep increase from zero to $\gtrsim 0.95$, which is exhibited by all the bands shown, indicates that the corresponding KS state is dominated by a single plane wave. The same features were also seen in other k points; H, N and the point marked by arrow (not shown). This result shows that in this system, the electronic states indeed lose their atomic-orbital character and are rather well represented by the nearly uniform electron theory [13]. The first-principles calculations were performed using Quantum Espresso [14] with norm conserving pseudopotentials from *Pseudo dojo* [15].

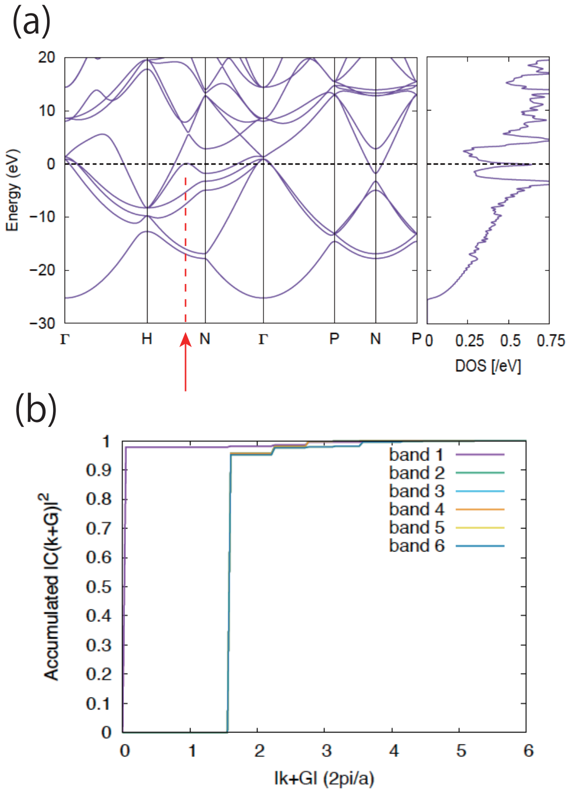

Figure 2: (a) Electronic band structure and density of states (DOS) of H_3S at 200GPa. Dashed horizontal line indicates the Fermi level, whereas vertical line indicates the cut of the van-Hove line that is responsible for the peak in the DOS. (b) Accumulated squared plane-wave coefficients of the KS states at Γ point.

References

[1] J. Bardeen, L. N. Cooper, and J. R .Schrieffer, Phys. Rev. **108** (1957) 1175.

[2] G. M. Eliashberg, Zh. Eksp. Teor. Fiz. **38**, (1960) 966.

[3] A. B. Migdal, Zh. Eksp. Teor. Fiz. **34**, (1958) 1438.

[4] A. Sanna *et al.*, J. Phys. Soc. Jpn. **87**, (2018) 041012.

[5] M. Lüders *et al.*, Phys. Rev. B **72** (2005) 024545.

[6] M. A. L. Marques *et al.*, Phys. Rev. B **72** (2005) 024546.

[7] A. Sanna, C. Pellegrini, and E. K. U. Gross, Phys. Rev. Lett. **125** (2020) 057001.

[8] F. Essenberger *et al.*, Phys. Rev. B **90** (2014) 214504.

[9] R. Akashi, Phys. Rev. B **105** (2022) 104510 .

[10] B. Holm and U. von Barth, Phys. Rev. B **57** (1998) 2108.

[11] R. Akashi, Phys. Rev. Research **6** (2024) 033012.

[12] H. Shinaoka, *et al.*, Phys. Rev. B **96** (2017) 035147.

[13] R. Akashi, in preparation.

[14] P. Giannozzi *et al.*, J. Phys. Condens. Matter **29** (2017) 465901.

[15] G. Pizzi *et al.*, J. Phys. Condens. Matter **32** (2020) 165902.

Ab-initio MD simulation for molten Rb_2AgI_3

Shuta TAHARA
Department of Liberal Arts and Sciences,
Chukyo University, 101-2 Yagoto Honmachi Showa-ku, Nagoya, Aichi 466-8666

We have been carried out experimental and theoretical studies with an interest in the diffusion mechanism of Ag ions diffusing in solids, such as AgI and $RbAg_4I_5$ and its molten phases [1-3]. Although Rb_2AgI_3, the subject of this study, is not a superionic conductor, it is an interesting material for studying the conductive environment of Ag ions in materials by comparing it with $RbAg_4I_5$, which is a superionic conductor in the RbI-AgI system. Since Rb_2AgI_3 and $RbAg_4I_5$ have different structures in the solid state, we thought that comparing the structures and physical properties in the high-temperature molten state would be more appropriate for investigating the effect of differences in composition on the Ag ion conductive environment than comparing the two solid states. In this project, we carried out AIMD simulations of molten Rb_2AgI_3. Figure 1 shows a comparison of our previous experimental data for molten Rb_2AgI_3 with the results of this simulation. We plan to analyze ion diffusion by checking whether the ionic conductivity derived from the ion diffusion coefficient matches the experimental data.

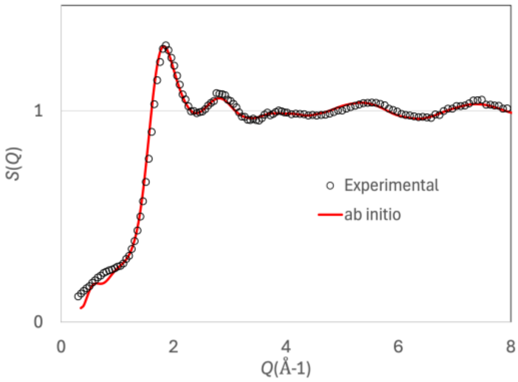

Fig. 1: Structure factors of molten Rb_2AgI_3. Open circles and red curve indicate experimental data and AIMD of this study, respectively.

References

[1] S. Tahara and T. Fukami, J. Phys. Soc. Jpn. **84**, 024602 (2015).

[2] S. Tahara et al., J. Chem. Phys. **143**, 044509 (2015).

[3] S. Tahara, et al., EPJ Web conf. **151**, 03006 (2017).

Optical properties and dielectric functions parameterization in UV-visible spectroscopy data analysis of $LiNbO_2$

Takayuki MAKINO
Graduate School of Engineering, University of Fukui
Bunkyo 3-9-1, Fukui, Fukui 910-8507

Lithium niobate crystallizes into a three-dimensional structure ($LiNbO_3$) or a metastable $LiNbO_2$ modification. Epitaxial growth techniques enable $LiNbO_2$ thin-film growth [1]. This material exhibits intriguing properties, such as superconductivity [2]. Its previously unknown band gap in stoichiometric $LiNbO_2$ was recently quantified by us [3]. However, the optical properties of delithiated $LiNbO_2$ remain unclear. Experimental data conversion from UV-visible spectroscopic data into complex dielectric functions [$\tilde{\epsilon} = \epsilon_1 + i\epsilon_2$ (or the complex index of refraction $\tilde{n} = n + ik$)], is crucial for material analysis. This also plays a significant role in comparative studies with theory using high-performance computers.

Several approaches for the abovementioned conversion are documented [4]. The numerical inversion can estimate dielectric functions at each wavelength but poses challenges as an inverse problem [5]. Using, *e.g.*, the Newton-Raphson method, this approach requires precise knowledge of material properties and layer thickness, risks inaccuracies without these details. Challenges include multiple possible solutions and requires well-chosen initial values for the root search. Recently, a deep learning-based method has been adopted, improving robustness and efficiency [6].

A second approach employs physics-based models to describe optical properties with meaningful parameters. While insightful, this method incurs high computational costs due to complex function structures. A third approach, which we adopt here, parameterizes dielectric functions using Lorentz functions for continuous modeling, avoiding the abovementioned limitations and ensuring smooth interpolation between spectral points.

In the simplest case, by letting us take ℓ thickness of the sample and λ wavelength, measured quantities such as transmission (T) and reflectivity (R) are expressed as functions of n and k as shown below.

$$T = (1 - R)^2 \exp(-\frac{4\pi k\ell}{\lambda}),$$

and

$$R = \frac{(n-1)^2 + k^2}{(n+1)^2 + k^2}.$$

Because we now consider the film-on-substrate (two-layer) case, the relevant equations become significantly complicated. Explicit notations of the related equations in two layer model can be found elsewhere [6].

Strictly speaking, the aforementioned Lorentz oscillator (peak) is an equation related to the dielectric constant. However, to avoid the complexity of deriving both the complex refractive index and the complex dielectric constant, the equation for the Lorentz oscillator concerning the complex refractive index is presented here. The related equation reads:

$$\tilde{n} \propto \frac{1}{\omega_j^2 - \omega^2 + i\gamma\omega},$$

where ω, ω_j, γ denotes photon energy, peak energy and a broadening, respectively.

Due to typically broad measured photon energy range, spectroscopic data analysis leads to challenges in optimizing high-dimensional parameter spaces. Its challenge with high-dimensional problems make MCMC (Markov-chain Monte Carlo) method more effective. Tools like STAN offer user-friendly environments for these tasks. Additionally, Likhachev's criteria, such as the information criterion, improve reliability by determining the optimal number of peaks [4].

Photometric spectra were obtained via a UV-visible spectrometer, and numerical computations were performed using STAN (https://mc-stan.org). In implementing the proposed approach, we used 6 peaks. Figure 1 presents the converted result from measured quantities, i.e., complex dielectric function in delithiated $\mathrm{LiNbO_2}$ film at room temperature. The delithiation degree is *ca.* 50%.

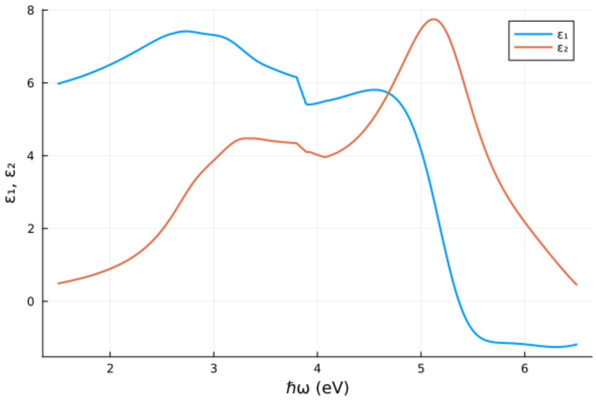

Figure 1: Complex dielectric functions (ϵ_1, ϵ_2) of delithiated $\mathrm{LiNbO_2}$ thin film

The transition from stoichiometric to delithiated $\mathrm{LiNbO_2}$ induces a blueshift due to the role of delithiation in hole doping, i.e., a degenerate semiconductor with the Burstein effect [7]. Delithiation also causes inhomogeneity-related broadening, more pronounced than in the stoichiometric case.

Comparisons between measured dielectric functions and ab-initio calculations are underway, utilizing density functional theoretical methods via Quantum ESPRESSO to model electronic structures, and RESPACK for many-body effects such as electron-hole correlations [8].

In summary, we have discussed dielectric function parameterization, including measured quantity conversions, introduced three approaches, explained the reasoning behind our selected method, and reported dielectric functions of delithiated $\mathrm{LiNbO_2}$.

References

[1] T. Soma, K. Yoshimatsu, and A. Ohtomo: Science Advances **6** (2020) eabb8570.

[2] E. R. Ylvisaker and W. E. Pickett: Phys. Rev. B **74** (2006) 075104.

[3] T. Kurachi, T. Yamaguchi, E. Kobayashi, T. Soma, A. Ohtomo, and T. Makino: Physica B **621** (2021) 413259.

[4] D. Likhachev: Thin Solid Films **636** (2017) 519.

[5] G. E. Jellison and F. A. Modine: Appl. Phys. Lett. **69** (1996) 371.

[6] K. Saeki and T. Makino: Jpn. J. Appl. Phys. **62** (2023) 081002.

[7] E. Burstein: Phys. Rev. **93** (1954) 632.

[8] K. Nakamura, Y. Nohara, Y. Yosimoto, and Y. Nomura: Phys. Rev. B **93** (2016) 085124.

Structural analysis of single layer borophene and boride on Ni surfaces

Takeshi NAKAGAWA

Interdisciplinary Graduate School of Engineering Sciences,
Kyushu university, 6-1 Kasuga koen, Kasuga, Fukuoka 816-8580

We performed a structural search and analysis of boron deposited on Ni(111). Owing to boron's electron deficiency and the structural variability associated with its hexagonal network—particularly with respect to defect concentration—two-dimensional boron films exhibit considerable complexity. Surface boride formation introduces additional challenges for structural characterization. To explore stable configurations, we employed a crystal structure prediction based on particle-swarm optimization (CALYPSO) [1], combined with first-principles calculations using VASP, across a wide range of boron–nickel compositions. Our calculations identify B_{13} overlayer borophene and Ni_7B_3 boride structures as energetically favorable. Among these, the B_{13} structure exhibits better agreement with low-energy electron diffraction (LEED) and scanning tunneling microscopy (STM) results. Phonon dispersion analysis further confirms the dynamical stability of B_{13}, with all phonon modes displaying real (positive) frequencies.

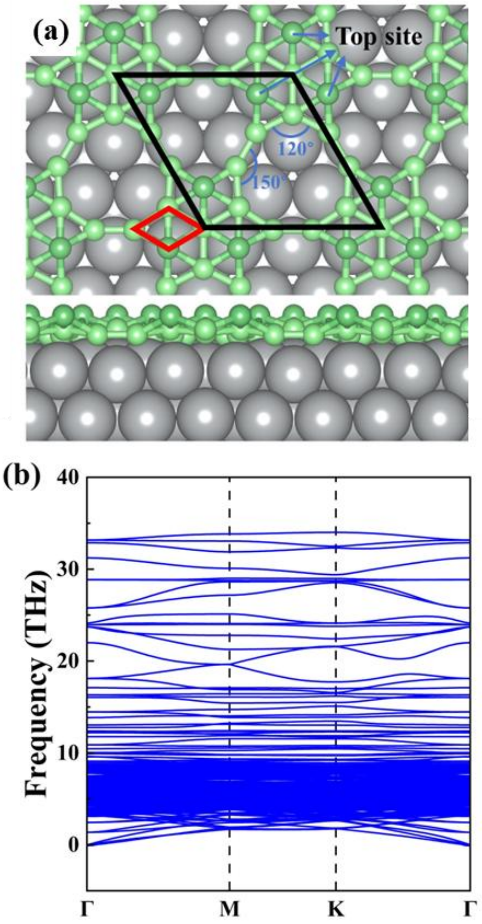

Fig. 1: (a) A predicted structural model of B_{13} on Ni(111). (b) Phonon dispersion for B_{13} on Ni(111).

References

[1] Y. Wang, J. Lv, L. Zhu, Y. Ma, Phys. Rev. B **82**, 094116 (2010).

Interfacial phonon modes at grain boundaries in single-layer graphene/hexagonal boron nitride

Masaaki MISAWA
Department of Intelligent Mechanical Engineering, Fukuoka Institute of Technology
3-30-1 Wajiro-higashi, Higashi-ku, Fukuoka 811-0295

With the development of surface acoustic wave devices, there is a need for more advanced technology to control phonon propagation. To establish a methodology to control ultra-high frequency phonons in the THz band based on nanoscale structures, we conducted a first-principles calculations with the following objectives. (1) Exploring localized phonon modes at grain boundaries (GBs). (2) Controlling phononic properties using vdW heterojunction. All calculations are performed using VASP [1] and PHONOPY [2] codes.

Phonon dispersion relations of the single-layer graphene containing armchair-GB (SLG) and that stacked with hexagonal boron nitride (G/BN) systems were analyzed. In the SLG system, the four interfacial phonon modes (three in-plane and one out-of plane modes) localized at the GB were introduced (Figure 1). On the other hand, in the G/BN system, the nine interfacial phonon modes (seven in-plane and two out-of plane modes) were detected (Figure 2). Some of them, the BN layer oscillates simultaneously with the GB in SLG. These results suggest the possibility of introducing GB-localized phonons in the desired frequency band using stacking structures.

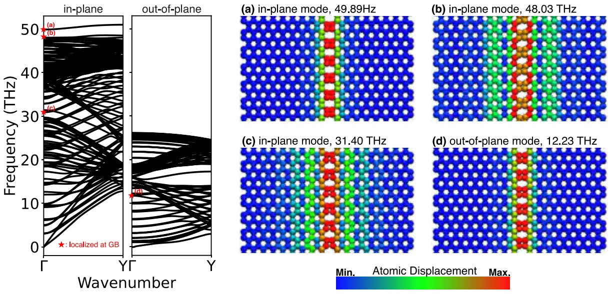

Figure 1: Phonon dispersion relation and atomic displacement of the localized phonon modes in the SLG system.

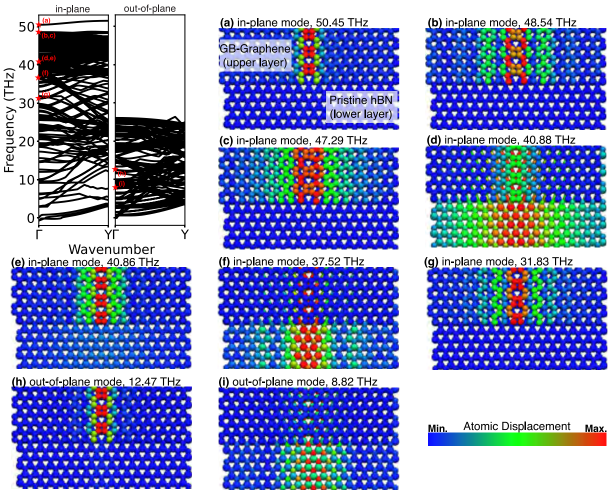

Figure 2: Phonon dispersion relation and atomic displacement of the localized phonon modes in the G/BN system. the upper graphene layer is displayed only in the upper half of the images.

References

[1] G. Kresse and D. Joubert, Phys. Rev. **59**, 1758 (1999).

[2] A. Togo, J. Phys. Soc. Jpn. **92**, 012001 (2023).

First-principles Calculation of Tungsten Alloy

Shoya Kawano

Department of Electrical and Electronic Engineering, Kyushu Institute of Technology,
Kitakyushu, Fukuoka, 804-8550

Tungsten is widely used as a heating element, electrode, and electron-emitting material in X-ray sources and other high-temperature applications. Among these applications, there is growing interest in enhancing heater performance by raising its electrical resistivity. It has been found that adding ruthenium (Ru) to tungsten increases its electrical resistivity fourfold. This demonstrates that alloying tungsten with suitable elements can effectively raise its resistivity. Accordingly, optimizing both the type and concentration of alloying elements in tungsten is essential for industrial applications.

First, we conducted a resistivity simulation for pure tungsten, which crystallizes in the body-centered cubic (bcc) structure. Using Quantum ESPRESSO [1] and Perturbo [2], we calculated the temperature-dependent resistivity of pure tungsten; the results are shown in Fig. 1 (solid line denotes calculated values; dashed line denotes data-book values). The close agreement confirms that first-principles methods can reliably predict tungsten's electrical resistivity. The average electron relaxation time (scattering lifetime) determined from these calculations was 16 fs. Applying the same methodology to Au yields a relaxation time of 24 fs [3], consistent with Au's lower resistivity and validating our pure-W results.

Next, we modeled W–Ru alloys for which experimental resistivity data are available. In these alloys, Ru atoms randomly substitute for W sites within the bcc lattice. To capture this disorder, we generated numerous candidate structures using the cluster-expansion method implemented in ATAT [4] and computed each structure's formation enthalpy. Enthalpy decreases with increasing Ru concentration, indicating favorable Ru dissolution in W and agreeing with experimental observations. When we attempted to compute electron–phonon scattering lifetimes for these structures, however, low-concentration Ru alloys exhibited dynamical instabilities in phonon calculations, preventing a direct calculation of their resistivities.

We therefore approximated the relaxation time in W–Ru alloys as no greater than that of pure tungsten. Under this assumption, we calculated the electrical conductivity of the alloys using BoltzTraP2 [5]. Figure 2 shows the resistivity as a function of

Ru concentration, with black circles for individual configurations and red circles for ensemble averages. The averaged values exhibit a clear upward trend with increasing Ru content. Experimentally, a 4 % Ru alloy has a resistivity of approximately 22 μΩ·cm; our results reproduce this trend, though they slightly underestimate the absolute values because of the constant-lifetime assumption. Nevertheless, our calculations successfully capture the effect of alloying on tungsten's resistivity.

References

[1] https://www.quantum-espresso.org/

[2] https://perturbo-code.github.io/

[3] J. I. Mustafa et. al., Physical Review B **94** (2016).

[4] A. van de Walle, M. Asta and G. Ceder, Calphad **26** (2002).

[5] https://arxiv.org/abs/1712.07946

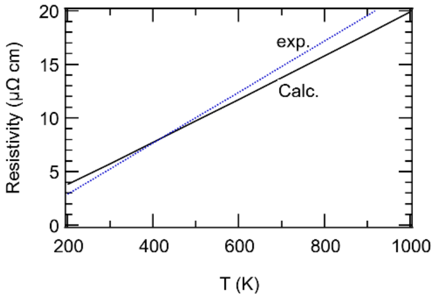

Fig. 1: Electrical resistivity of pure tungsten

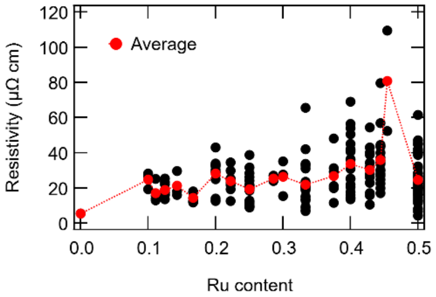

Fig. 2: Electrical resistivity of W-Ru calculated using the relaxation time of pure tungsten ($W_{1-x}Ru_x$, $x \leq 0.5$). Black circles indicate the electrical resistivity of each structure produced, and red circles indicate the average value for each composition.

Relative stabilities of In-induced surface reconstructions on the Si(111) surface

Tsuneo FUKUDA

Department of Physics and Electronics, Graduate School of Engineering,

Osaka Metropolitan University, 1-1 Gakuen-cho, Nakaku, Sakai, Osaka 599-8531

Indium-induced atomic structures on the Si(111) surface were studied by first-principles calculations. Experimental and theoretical studies on In-induced silicon surface have attracted much attention because of the implication of various condensed matter physics, such as charge density waves, Peierls transition, and two-dimensional superconductivity to name a few. To understand the physics behind the Si-In system, it is crucial to accurately determine the atomic structure and electronic states.

The aim of this project is to determine relative stability of surface atomic structures as a function of In and Si coverages based on first-principles scheme. We used VASP (=Vienna Ab initio Simulation Package) for this project and various calculation parameters that affect the total energies of surface structures were systematically studied in detail for several surface reconstructions and chemical potentials were compared. The parameters and surface reconstruction studied are listed in Table 1.

The lattice parameter of bulk Si was $0.72 \pm 0.01\%$ larger than the experimental parameter extrapolated to 0 K, and that cohesive energy was $1.7\% \pm 0.2\%$ smaller than experimental value, respectively. These errors are due to the cutoff energies and the number of k points.

Table 1:Calculation Parameters and Surface reconstrcutions

Potential	PBE [1]
Cutoff Energy	382-500 eV
Electronic Convergence	<1E-6 eV
Structure Convergence	<0.1 eV/nm
Slab layers	3-8 DL
k-points	0.015-0.055 Ang^{-1}
Surface Reconstruction (Superstructure)	$\sqrt{3} \times \sqrt{3}R30°(\sqrt{3}\text{-}\alpha)$ $\sqrt{31} \times \sqrt{31}$R9° $4 \times 1(8\times 2)$ $\sqrt{7} \times \sqrt{7}$ $\sqrt{7} \times \sqrt{3}$-rect

For the In-induced surface structures, all the structures shown in Table 1 were stable. However, the formation energies depended on the number of k points, the cutoff energies, and the number of layers in the slab, and no systematic trend was observed in the range of a few tens of meV. Thus, the relative stability of each structure varies depending on the choice of these calculation parameters. We are currently trying to find a method of selecting correct grand state energies and appropriate for the In-Si system [2].

References

[1] J.P. Perdew, K. Burke, M. Ernzerhof, Phys. Rev. Lett. **77** 3865 (1996).

[2] T. Fukuda, in preparation

DFT calculations of adsorbed molecules captured by metal-organic films on Cu(111)

Noriyuki TSUKAHARA
National Institute of Technology, Gunma College
Toriba-machi, Maebashi, Gunma, 371-8530

In this study, I verified that the porous 2D metal-organic network (2D-MON) film on the metal surface can trap adsorbed atoms and molecules, enabling control of the size of metal clusters and molecular oligomers in the pores.

Element-specific cluster formation in the pore of the 2D-MON.

From STM measurements, when Ag, In, and Pd atoms are deposited on the 2D-MON on Ag(111), indium clusters grow at the center of the pores, while Ag and Pd clusters grow from the 2D-MON. The present DFT calculations show that an In adatom in the pores interact with the 2D-MON repulsively, whereas Ag and Pd adatoms interact attractively. The location where the metal adatoms aggregate is determined by the interaction between the metal adatom and the 2D-MON. [1]

Formation of specific HCOOH oligomer in the pore of the 2D-MON.

HCOOH molecules aggregate one-dimensionally on Cu(111). From STM measurements, when HCOOH molecules are trapped in the present 2D-MON on Cu(111), tetramer chains tend to be selectively formed in the pores, and both ends of the tetramer chain are located at the specific sites in the pore. Figure 1 shows the position dependence of the adsorption energy of a HCOOH molecule in the pore, and attractive interaction occurs between the 2D-MON and the HCOOH molecule. A chain grows from this HCOOH molecule, and the other end of the tetramer chain also interacts attractively with the 2D-MON. [2]

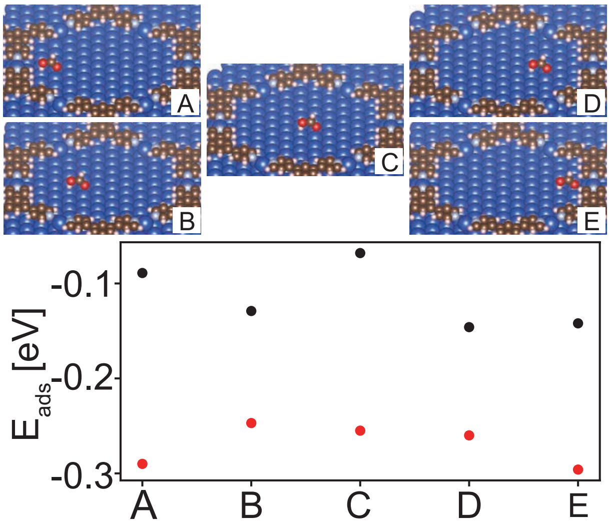

Figure 1: Position dependence of the adsorption energy of a HCOOH molecule in the pore. Black and red dots indicates the calculated results without and with vdW correction, respectively.

References

[1] N. Tsukahara, R. Arafune, and J. Yoshinobu: Jpn. J. Appl. Phys. **63**, 065504 (2024).

[2] N. Tsukahara and J. Yoshinobu: *in preparation*

Search and realization of novel electronic properties of surfaces and interfaces and of nanostructures

Takeshi INAOKA
Department of Physics and Earth Sciences, Faculty of Science,
University of the Ryukyus, 1 Senbaru, Nishihara, Okinawa 903-0213

Advances in supercomputers have made it possible to calculate the electronic structure of organic crystals composed of large molecules. Using the van-der-Waals density functional theory, we have been investigating the electronic structure of x-form phthalocyanine (Pc) crystals doped with iodine (I) atomic chains. The Pc is a planar π-conjugated macrocyclic molecule which can include an atom of various species at its center position, such as Si or Li, as mentioned below. The x-form crystal is constituted of a square-lattice arrangement of molecular chains with double period and with molecular planes normal to the stacking direction. Doped I atoms form atomic chains between these molecular chains.

We employ the program package 'Vienna Ab initio Simulation Package' (VASP) [1-4] on system B (ohtaka).

(I) x-SiPcI crystals

In last year's study [5], we found that the SiPc chains act to form equally spaced I atomic chains, while the I atoms try to create trimerized chains. These effects compete with each other, but the trimerization effect is larger. The trimerized I atomic chains are not metallic . However, since the distance between neighboring trimers is not so large compared to the bond length of the trimer, application of uniaxial compression in the stacking direction could create equally spaced I chains and thereby conduction bands. In this study, with a gradual increase in uniaxial compressive strain, we perform structural optimization and trace changes in the electronic structure. Since SiPc molecules are stacked with double period, and I atomic chains are trimerized, we assume an x-form SiPcI crystal with 6-fold period in the stacking direction.

In the stable structure, the lattice constant c_0 of the unit cell in the c-axis direction is 19.12 Å, the bond length of each trimer is 3.00 Å, and the distance between adjacent trimers is 3.55 Å. In order to apply uniaxial compressive strain in the stacking direction, we gradually decrease c_0, and perform structural optimization at each c_0 value. In this process, the bond distance of the trimer almost remains unchanged, but the distance between neighboring trimers decreases, and at c_0=18.00Å, the I atomic chains are equally spaced at 3.00Å. Figure 1 shows the electron density distribution (a) before and (b) after application of uniaxial compressive strain. The compressive strain changes the distribution localized in each trimer to that extending over the entire I chain.

Our band analysis along this process clearly shows how the Peierls gap associated with the trimerized I chains gradually reduces and finally closes above the Fermi level E_F. When I atoms are equally spaced, the structure becomes doubly periodic in the stacking direction. Analysis of band dispersion shows that a band with extremely strong dispersion originating from the p_z orbitals of the I

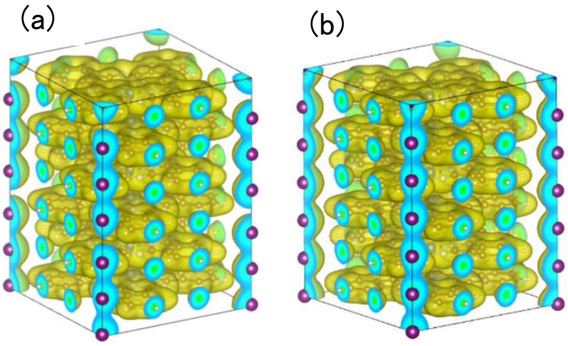

Fig.1 Electron density distribution of x-SiPcI crystals (a) before and (b) after uniaxial compression is applied. This compression changes trimerized I chains to equally spaced ones.

atoms crosses E_F, indicating that the conduction band is formed by uniaxial compressive strain. The effective mass ratio and the one-dimensional electron density are $m^*/m_0=0.11$ and $n_{1D}=1.00\times10^7$/cm, respectively. From the strain dependence of the total energy, the uniaxial compressive stress required for formation of conduction bands is estimated to be about 1.6 GPa.

(II) x-LiPcI crystals

Teruya et al. showed that Mott insulators of x-LiPc can be converted to metals of x-LiPcI and vice versa by chemical I doping and dedoping [6]. Here, we describe the progress of our theoretical study of x-LiPcI crystals.

Figure 2 exhibits the band dispersions on the Γ-Z line in the stacking direction in the Brillouin zone. The dispersive bands near and above E_F originate from p_z-orbital overlapping between neighboring stacked molecular planes. The double period in the stacking direction is reflected in the band structure. A pair of bands b193 and b194 with strong dispersion are formed by band folding at the Z point, and b193 crosses E_F, which indicates that this is a metallic band. Without I doping, the Fermi level E_F comes just at the band folding point of b193 and b194 at the Z point. As stated in last year's report as for a single x-LiPc chain, each of these two degenerate states at the band folding point is occupied by an unpaired electron. This corresponds to the appearance of Mott insulators in x-LiPc. On I doping, since I atomic chains receive electrons from x-LiPc molecular chains, the Fermi level E_F shifts down from the band folding point, and the band b193 becomes metallic. Figure 3 exhibits the electron density distribution of the state on b193 just below E_F circled green in Fig. 2. We can see the p_z orbital overlap between the neighboring stacked molecules at each position of C atoms nearest to the center Li atom. This overlap contributes to electrical conductivity in the stacking direction.

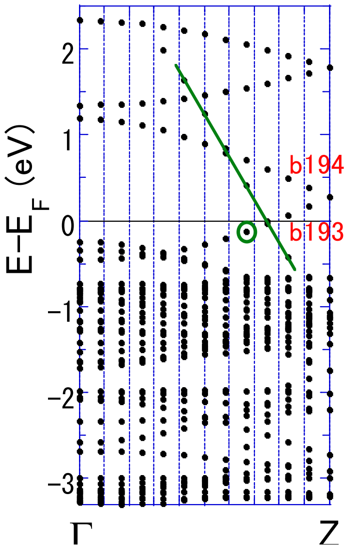

Fig. 2 Band dispersions of x-LiPcI crystal on the Γ-Z line.

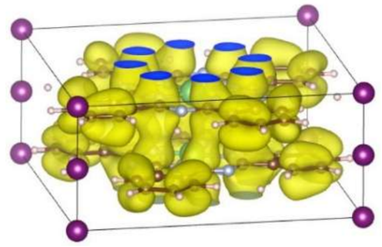

Fig. 3 Electron density distribution (isosurfaces) of the state circled green in Fig. 2.

If we consider equally spaced I chains, we have a metallic band originating from I atomic chains, as lined green in Fig. 2. However, Raman spectroscopy analysis indicates that the I chains are in a pentameric arrangement as I_5^-. If we consider ten-fold periodicity in the stacking direction and perform structural optimization, we would find that pentamerized chains are more stable than equally spaced chains, and that the resulting band of I chains is not metallic.

References

[1] G. Kresse and J. Hafner: Phys. Rev. B **47**, 558-561 (1993).

[2] G. Kresse and J. Furthmüller: Comput. Mat. Sci. **6**, 15-50 (1996).

[3] P. E. Blöchl: Phys. Rev. B **50**, 17953 (1994).

[4] J. Klimeš, D. R. Bowler, and A. Michaelides: Phys. Rev. B **83**, 195131 (2011).

[5] T. Inaoka, AIP Advances **14**, 085016 (2024).

[6] R. Teruya et al.: Angew. Chem. Int. Ed. **61**, e202206428 (2022).

Ab initio molecular dynamics study of inorganic polymer

Yoh-ichi Mototake, Yoshifumi Amamoto, Hiroyuki Kumazoe,
Hidetoshi Morita, Hayato Okubo
Graduate School of Social Data Science,
Hitotsubashi University, Chome-1 Naka, Kunitachi, Tokyo, 186-0004

To model, predict and control pattern dynamics involving chemical reactions, such as the formation of SiC polycrystalline ceramics from precursor polymers (Figure), it is necessary to integrate and model phenomena with different chemical bonding states and temporal and spatial scales, such as chemical reactions involving changes in chemical bonds and structure formation of global patterns from atoms and molecules. Although modeling such pattern dynamics must be integrated, no method has yet been established to model such pattern dynamics. Therefore, we aim to develop a machine learning modeling framework to realize it.

The purpose of this project is to generate a simulation-based dataset to develop a machine learning model that reproduces the formation process of SiC polycrystalline ceramic from the precursor polymer.

Originally, we planned to collect a dataset of multi-scale material formation processes involving chemical reactions based on existing simulation methods such as first-principles molecular dynamics calculations using neural potentials. However, we found that it is very difficult to reproduce the formation of thousands of molecules and their networking and crystallization processes using existing methods, no matter how coarse-grained the simulations are. Therefore, we developed an informatics framework to construct an entire dataset by combining partially simulated data. This year, we realized to start creating the dataset based on this framework.

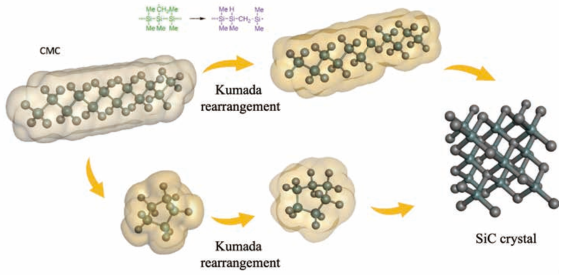

Figure: SiC polycrystal formation process by precursor polymer method [1,2,3].

References

[1] S. Yajima, J. Hayash, and M. Omori, Chem. Lett., 931（1975）.

[2] S. Yajima, J. Hayashi, M. Omori and K. Okamura, Nature, 261, 683（1976）.

[3] K. Shiina and K. Kumada, J. Org. Chem., 23, 139（1958）

First-principles study of Si, Ge, and nanodiamond materials

Hana Pratiwi KADARISMAN
Nanomaterials Research Institute (NanoMaRi), Kanazawa University
Kakuma machi, Kanazawa, Ishikawa 920-1192

1. **The OH-termination on Si and Ge surfaces**

Termination of semiconductor surfaces influences the stability and affects the chemical reactivity of the materials. Previously, we found the persistent spin helix on diamond 111 surface [1] after introducing the OH (hydroxyl termination on its surface. These results motivated us to investigate the impact of OH termination on the other group IV semiconductors, specifically Si and Ge surfaces.

This year, we performed first-principles calculation of OH-terminated Si and Ge surfaces. Our goals are to observe and analyze the electronic properties of the Si and Ge after OH-termination on its surface. Moreover, we also investigate the spin-orbit coupling property of OH-terminated Si, and Ge surfaces. First-principles electronic structure calculations were carried out based on the density functional theory using the OpenMX[2] code. The spin orbit coupling was included in this computation.

The results show that the OH-termination on silicon and germanium surfaces induces spin splitting at the conduction band minimum (CBM) and valence band maximum (VBM), for the silicon and germanium surfaces, respectively. Based on these findings, we discuss the possibility of OH-terminated silicon and germanium for the spintronic application.

2. **NV center in nanodiamond**

We performed the first-principles calculation of NV center in nanodiamond using Openmx [2] code. To simulate the nanodiamond structure, a large number of carbon atoms is required, which demands substantial computational resources. The computational demands of this study were efficiently handled using the ISSP supercomputer. We expect the difference shapes of nanodiamond structure may produce the difference stabilities and electronic properties. To investigate these further, additional calculations and analyses are necessary.

References

[1] H. P. Kadarisman, N. Yamaguchi, and F. Ishii: Appl. Phys. Express **16** (2023) 023001.

[2] http://openmx-square.org

Analyses of semiconductor surface processes by machine-learning based potentials

Kouji INAGAKI
Graduate School of Engineering, Osaka University
Yamadaoka 2-1, Suita, Osaka 565-087

The mechanochemical method, a type of ultra-precision surface processing, uses a synergistic effect of mechanical interaction and chemical reaction processes, but the mechanism is not clear. A proper understanding of the mechanism is essential for efficient improvement of the processing method.

The objective of this study is to establish and apply a method to analyze the mechanism by large-scale Molecular Dynamics (MD) calculations using the Machine Learning Potential (MLP). In contrast to other studies, where MLPs that use structures close to stable atomic structures as training data have been used to search for new materials with metastable structures, this study aims to develop MLPs that employ more training data at the boundaries of bond formation and bond breaking for highly accurate simulations of processing phenomena. In order to collect training data, we proposed a method to collect training data from atomic structures where bond formation/breakage occurs by performing MD calculations at high temperatures using a provisional MLP.

An application was developed to extract structures from trajectories of MD calculations, and the method was evaluated using the example of a diffusion process of H adsorbed on a Si(001) surface. After preparing the initial training data, an iterative MLP refinement process consisting of MLP generation, MD execution, and additional training data was performed. This repetition reduced the frequency of calculation crashes due to non-physical breakdowns caused by imperfections in the MLP during MD, confirming the effectiveness of the method.

However, the occurrence of non-physical breakage could not be reduced to zero, and additional learning data is considered necessary. Furthermore, the learning data collection application we developed required a large amount of storage space, making it difficult to collect learning data on a larger scale. We plan to improve the learning data collection application in the future.

References

[1] K. Inagaki, The 72th JSAP Spring Meeting 2025 14p-K507-9.

Electronic structure of aqueous polymers

Osamu TAKAHASHI, Nanami SHIMA, Risa OKADA, and Yuika WATARI
Graduate School of Science, Hiroshima University, Kagamiyama, Higashi-hiroshima, Hiroshima 739-8526

Membrane technology to produce fresh water from seawater and contaminated water is extremely attractive because it is low energy and simple to implement [1]. Recently, self-assembled liquid crystalline membrane materials with uniform pore size in the nano or sub-nano class have been developed. By controlling the hydrophilic groups in the films, liquid crystalline films with different separation capacities can be produced. In order to develop membranes with more effective separation ability, it is important to understand the nature of water in the pores, i.e., the structure of hydrogen-bonded water in the nanochannel.

Soft X-ray emission spectroscopy (XES) measurements were performed to investigate the structure of water in the pores of liquid crystal films. In the case of liquid crystal membranes (ILCs) with benzyltriethylammonium groups, observed spectra of the water in the membranes resembles that in $MgSO_4$ solution when compared to that in NaCl solution, suggesting that this explains the water permeability [2]. In the present study, we constructed membrane models of two types of liquid crystal membranes with triethylammonium and imidazolium groups (Figure 1) as typical examples of membranes by molecular dynamics (MD) simulations. In addition, X-ray emission spectroscopy (XES) calculations were performed to explore the structure of water in the pores.

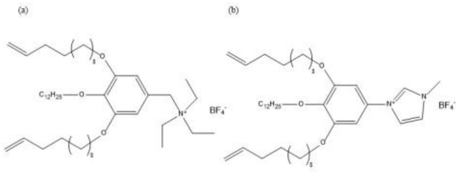

Fig.1 Molecular structure of ILC. (a) benzyl-triethylammonium and (b) benzylimidazorium system.

Structures of model ILCs were constructed by MD simulations using Gromacs [4] following Ref. [3]. Using a snapshot of MD simulations, a water molecule was sampled randomly and surrounding atoms within 6Å were picked up. Dangling chemical bonds were terminated by hydrogen atoms. A geometry at the center water molecule was optimized, and vibrational frequencies were obtained by Hessian matrices. Initial positions and velocities for hydrogen atoms in the water molecule were sampled quantum mechanically. Core-hole induced MD simulations were propagated within 20 fs. For obtained trajectories XES calculations were performed using density functional theory code deMon2k [5]. XES spectral calculations were performed along with a scheme of semi-classical Kramers-Heisenberg theory [6]. To resolve entanglements of potential energy surface and the transition moment curves genetic algorithm were applied [7].

We focus on the double peaks seen around 528 and 529 eV, which are attributed to the $1b_1$ state of water. In our previous study [8], these peaks originate from two different structures that induce different dynamics. The peak structures differ depending on the type of solution and the membrane structure. In water in the membrane, the relative intensity of the double peaks is independent of the water concentration (experimentally corresponding to the water pressure in the membrane). In the case of the triethylammonium system, the intensity between the double peaks tends to be higher at 3M. This reflects the difference in dynamics resulting from the various hydrogen bonding modes. In the case of the imidazolium system, the spectrum is independent of the water concentration. These differences may reflect differences in the hydrophilicity of the functional groups. The water in the membrane is more similar to that in the $MgSO_4$ solution, providing a qualitative explanation for the permeability of the membrane.

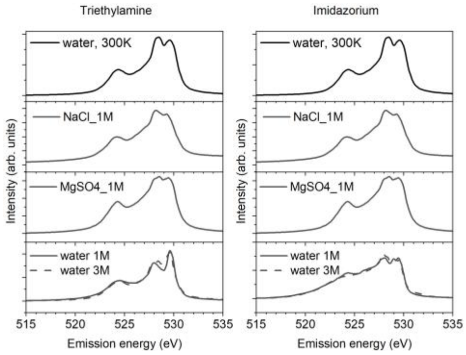

Fig.2: Calculated XES spectra of water, 1M NaCl solution, 1M $MgSO_4$ solution, and ionic liquid crystal with benzyltriethylammonium and imidazorium functionals.

References

[1] M. Henmi et al., Adv. Mater., **24**, 2238 (2012).

[2] R. Watanabe et al., Ang. Chem. Int. Ed., **59**, 23461 (2020).

3) Y. Ishii et al., Sci. Adv., **7**, eabf0669 (2021).

4) M.J. Abraham, et al., SoftwareX, **1-2**, 19 (2015).

5) A. M. Köster et al., deMon2k ver.5 (2018).

6) M. P. Ljungberg et al., Phys. Rev. B, **82**, 245115 (2010).

7) L. G. M. Pettersson et al., Theor. Chem. Acc., 140, 162 (2021).

8) O. Takahashi et al., Phys. Rev. Lett., 128, 086002 (2022).

Machine Learning-based DFT Calculation of Lignin Adsorption and Oxidative Activity on Ni/CeO₂ (111)

TEPPEI NUNOURA and ZHIHE ZHAO

Department of Environment Systems, Graduation School of Frontier Science,
The University of Tokyo, Kashiwa-no-ha, Kashiwa, Chiba 277-8581

To explore the adsorption behavior of lignin on Ni-loaded CeO_2 (111) surfaces, we integrated machine learning techniques to automatically generate and screen over 100 adsorption configurations. Through structural optimization, we identified the most stable adsorption structures and utilized the results to evaluate the oxidative potential of the catalyst toward lignin.1

In this study, we performed ab initio calculations to investigate the lignin adsorption behavior of Ni-loaded CeO_2 (111) surfaces. The theoretical framework was established using the PBE functional within the Vienna Ab initio Simulation Package.

We first identified the thermodynamically stable (111) surface of CeO_2 and modeled Ni cluster loading on this surface. Using a machine learning-assisted workflow, we generated and screened over 100 different lignin adsorption configurations, enabling high-throughput identification of the most stable structures. Among the 300 adsorption configurations, Guaiacol showed the highest oxidative reactivity on the Ni/CeO_2 (111) surface than syringol and p-hydroxyphenol.

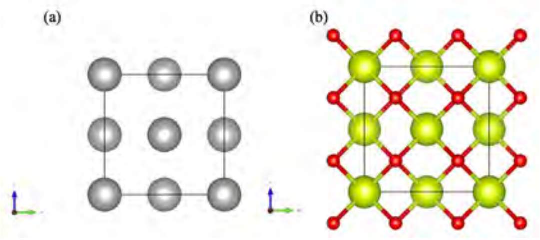

Fig.1 (a) Ni cluster crystal structure is face-centered cubic; (b) CeO_2 crystal cell (before cleavage)

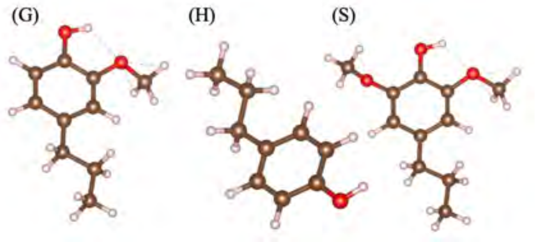

Fig.2 Guaiacyl (G), Hydroxyphenyl (H), and Syringyl (S) unit of lignin.

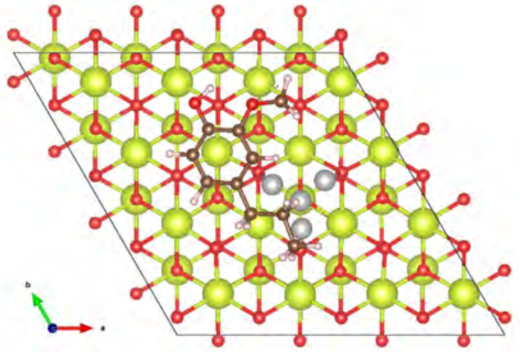

Fig.3 Guaiacyl (G) adsorbed on Ni/CeO_2 (111).

References

[1] Xie, Jin.; et al. *ACS Catal.* **2023**, *13* (14), 9577–9587.

Theoretical Analysis of H-terminated Si Atomic Layer Nanoribbons

Junhuan LI, Kenta ARIMA
Graduate School of Engineering,
The University of Osaka, Yamada-oka, Suita, Osaka 565-0871

Our goal was to predict the electrical and optical properties of silicon atomic layer nanoribbons (SiNRs), which we are attempting to form using our group's unique experimental techniques [1]. Density functional theory calculations were performed using the STATE [2] code with ultrasoft pseudopotentials.

Our computational model starts with bulk silicon as the initial material. Si nanosheets with atomic-layer thickness were generated by cleaving along the Si(111) plane. These sheets were then cut along the armchair direction to form armchair Si nanoribbons (ASiNRs). Examples of hydrogen-terminated ASiNRs are shown in Figure 1. The ribbons in Figures 1(a−c) have different thicknesses but the same width, defined as the number of dimer lines across the ribbon, which is 7 in this case.

Structural optimization was performed for the models, including hydrogen atoms. A plane-wave basis set was used to expand wave functions and charge density with cutoff energies of 36 Ry and 400 Ry, respectively. The Brillouin zone integration was done with a uniform grid of 30 *k* points along the edge direction. The electronic structures of ASiNRs were simulated using the optimized models. Our preliminary results show that the bandgap of the ribbons is strongly dependent on their thickness and decreases with increasing width.

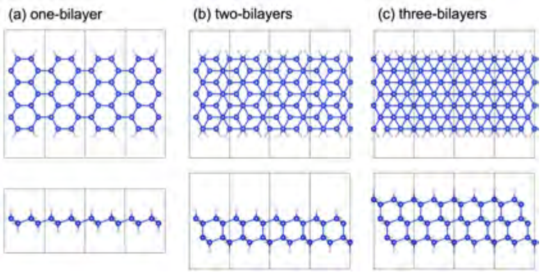

Fig. 1: Three atomic configurations of ASiNRs: (a) one-bilayer, (b) two-bilayers, and (c) three-bilayers.

References

[1] Z. Ma, S. Masumoto, K. Kawai, K. Yamamura, and K. Arima, Langmuir **38**, 3748 (2022).

[2] J. Li, K. Inagaki, and K. Arima, Phys. Rev. Res. **6**, 013252 (2024).

Electronic Structure of WO_3

Takahiro Maehira
Faculty of Science, University of the Ryukyus, Nishihara, Okinawa 903-0213

The monocarbides of transition elements from the group-IVB, -VB, and -VIB columns of the Periodic Table are well known for their great hardness and strength, high melting temperatures, metal-like thermal and electrical resistivities, nonstoichiometry, and superconducting properties [1, 2]. Most experimental and theoretical efforts to understand the fundamental properties of these technologically important materials have focused thus far on the group-IVB and -VB carbides, all of which crystallize with the cubic rocksalt structure. The compound WO_3 has eight phases: a low temperature phase is cubic WO_3. We studied simple cubic WO_3 with a space group of Pm3m which contains one molecule in the unit cell. The lattice parameter a is 3.838 Å, respectively [3]. The calculation for the energy band structures was carried out by using the OpenMX code(`http://www.openmx-square.org/`). First, we discuss the calculated results for WO_3 as shown in Figure 1, in which we depict the energy band structure along the symmetry axes in the Brillouin zone, which is shown in Figure 1, in the energy region from -10.0 to 10.0 eV. The Fermi level E_{F} is at 0.0 eV. for WO_3 and indicated by dashed lines in Figure 1. With respect to the energy band structure near E_{F}, we emphasize that there is always hybridization between the W 5d and O 2p states in WO_3. The total number of holes is equal to that of electrons, which represents that WO_3 is a compensated metal. Since the lowest twelve bands are fully occupied, as shown in Figure 1, the next three bands are partially occupied, while higher bands are empty. This compound is compensated metal because of having two chemical units in the unit cell. We move to discuss the Fermi surface of WO_3. Three bands cross the E_{F}, therefore WO_3 has three Fermi surfaces in Figure 2. The color on the Fermi surface illustrates the distribution of the Fermi velocity components. Fermi surfaces for WO_3 centered at the Γ points, respectively. The 7th band has one lattice-like hole sheet centered at the each Γ point. Red-shift indicate the increase of the admixture of Fermi velocity components. The Fermi surfaces were calculated with FermiSurfer [4].

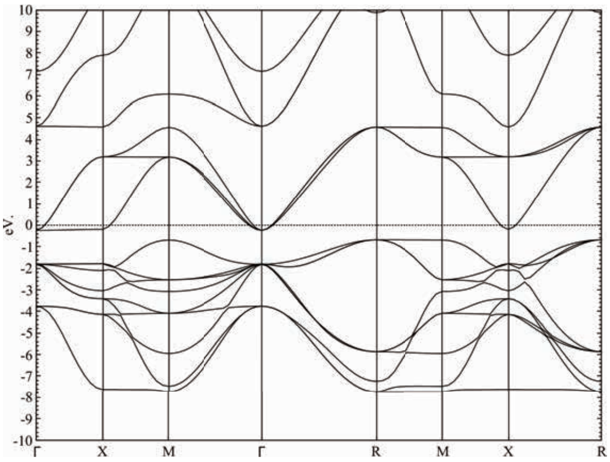

Figure 1: The energy band structure for WO_3, the symmetry points and axis for the simple cubic structure. E_{F} indicates the position of the Fermi level.

WO_3-type structures can be described as ABX_3 perovskites in which the A-cation site is unoccupied. They therefore have the general composition BX_3, where B is normally a cation and X is a bridging anion. The chemical diversity of such structures is very broad,

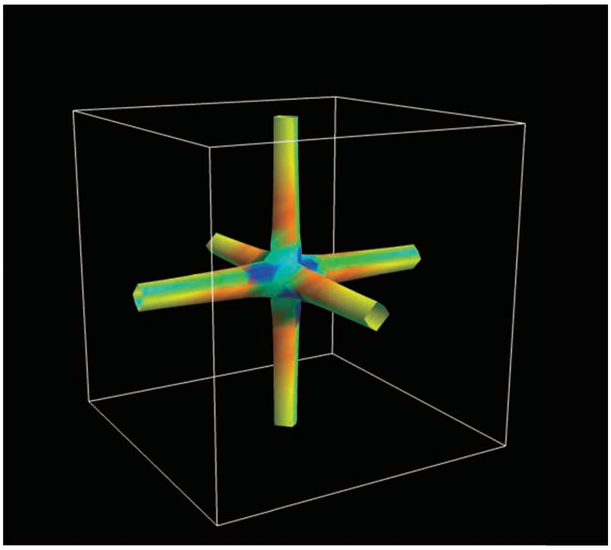

Figure 2: The Fermi surface for WO_3 centered at Γ point. Colors indicate the Fermi velocity components on the Fermi surface.

ranging from simple oxides and fluorides, such as WO_3 and AlF_3, to more complex systems in which the bridging anion is polyatomic, as in the Prussian blue-related cyanides such as $Fe(CN)_3$ and $CoPt(CN)_6$. The calculated total density of states (DOS) for WO_3 is shown in Figure 3, in the energy region from -10.0 to 10.0 eV. The total density of states for WO_3 is shown by the solid black line and the s, p, d and f states are shown by the solid color lines, respectively. This figure tells us that the DOS of the d states is higher than that of the f states at the Fermi level.

References

[1] L. E. Toth: *Transition Metal Carbides and Nitrides.*, Academic, New York(1971).

[2] E.K. Storms: *The Refractory Carbides.*, Academic, New York(1967).

[3] L.S. Palatnik, O.A. Obol'yaninova, M.N. Naboka, N.T. Gladkikh : Inorg. Mater.(1973)718.

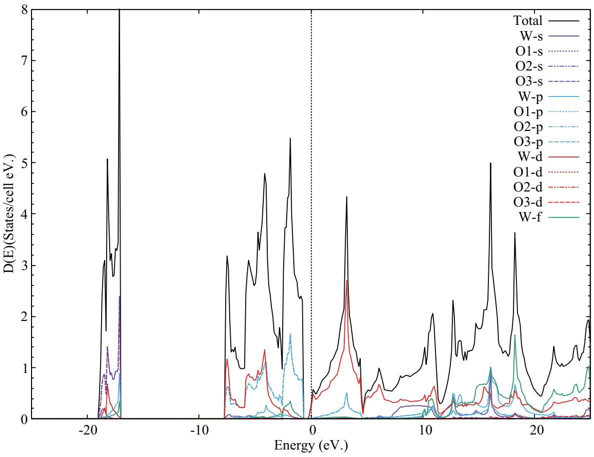

Figure 3: The density of states for WO_3. E_F indicates the position of the Fermi level shown by the dashed line.

[4] R. Kubo: J. Phys. Soc. Jpn. **12** (1957) 570.